Detailed Studies of Light Transport in Optical Components of Particle Detectors

Von der Fakultät für Mathematik, Informatik und Naturwissenschaften
der RWTH Aachen University zur Erlangung des akademischen Grades
eines Doktors der Naturwissenschaften genehmigte Dissertation

vorgelegt von

Diplom-Physiker

Erik Dietz-Laursonn

aus Gera

Berichter: Universitätsprofessor Dr. Thomas Hebbeker
Privatdozent Dr. Oliver Pooth

Tag der mündlichen Prüfung: 22.08.2016

Abstract

Scintillator- and fibre-based particle detectors are an indispensable tool in high-energy particle physics, medical physics and other fields of application. The potentially very low light yield, down to a few photons, of the optical detector components in combination with the inevitable light transport to photodetectors necessitate an optimal design and detailed understanding of such detectors. Thus, very detailed simulations are needed, which require a very accurate modelling of the optical physics (optics, scintillation, wavelength-shifting effects,...), of the optical material properties, and of the optical components. To allow for a reliable usage also by less experienced users, the necessary complexity and flexibility of a suitable simulation framework must not lead to an increasing danger of user mistakes. Additionally, the required effort for creating or modifying a detailed simulation has to be minimised in order to allow for the fast creation of flexible simulation setups.

In the scope of this thesis, these challenges have been addressed by developing the general simulation framework GODDeSS. It is an extension of the particle-physics simulation tool Geant4 and allows for the easy simulation of optical detector components, especially combinations of scintillators, optical fibres, and photodetectors. To achieve this, the creation of simulated setups is automated as much as possible: The material properties of the optical detector components are specified via easy-to-read text files and new object classes allow for an easy creation of scintillator tiles, optical fibres, reflective wrappings and paints, and photodetectors with basically a single line of code per created object. This results in an increase of flexibility and at the same time in a reduction of complexity. The user can create extensive setups within a few lines of code and typical mistakes are avoided, as the peculiarities of Geant4 regarding the configuration of the optical physics processes are treated automatically by the GODDeSS framework. All this makes GODDeSS an excellent approach to simplify the detailed simulations of optical detector components, which are necessary for designing modern particle detectors and for understanding their response.

This thesis introduces the GODDeSS framework, its classes, and its functionality. Furthermore, the extensive efforts to validate it against manufacturer data as well as against test measurements with prototype setups will be presented. Additionally, detailed simulations have been performed in order to investigate the optical properties of optical fibres and of the characteristics of the response of detector modules.

Zusammenfassung

Szintillator- und Faser-basierte Teilchendetektoren sind ein unerlässliches Werkzeug in der Hochenergie-Teilchenphysik, der Medizinphysik und anderen Anwendungsgebieten. Die Kombination aus der potentiell sehr geringen Lichtausbeute der optischen Detektorbauteile, bis zu einigen wenigen Photonen, und dem unvermeidlichen Lichttransport zu Photodetektoren macht sowohl ein optimales Design als auch ein detailliertes Verständnis solcher Detektoren nötig. Daher werden sehr detaillierte Simulationen gebraucht, welche eine sehr genaue Modellierung der optischen Physik (Optik, Szintillation, wellenlängenschiebende Effekte,...), der optischen Materialeigenschaften und der optischen Bauteile voraussetzen. Um eine verlässliche Nutzung auch durch unerfahrene Nutzer zu ermöglichen, dürfen die nötige Komplexität und Flexibilität von adäquaten Simulations-Frameworks nicht zu einer erhöhten Gefahr von Nutzerfehlern führen. Zusätzlich muss der Aufwand, der nötig ist um eine detaillierte Simulation zu erstellen oder zu modifizieren, minimiert werden, um die schnelle Erzeugung von flexiblen Simulationen zu ermöglichen.

Im Rahmen dieser Arbeit wurden diese Herausforderungen mit der Entwicklung des vielseitigen Simulations-Frameworks GODDeSS angegangen. Dabei handelt es sich um eine Erweiterung von Geant4, einem Simulationswerkzeug für die Teilchenphysik, die die leichte Simulation von optischen Detektorbauteilen, insbesondere Szintillatoren, optische Fasern und Photodetektoren, ermöglicht. Um dies zu erreichen, wurde die Erzeugung von simulierten Aufbauten soweit wie möglich automatisiert: Die Materialeigenschaften der optischen Detektorbauteile werden mittels leicht verständlichen Textdateien definiert und neue Objektklassen ermöglichen die Erzeugung von Szintillatorkacheln, optischen Fasern, reflektierenden Hüllen und Anstrichen sowie von Photodetektoren mit einer einzelnen Code-Zeile pro erzeugtem Objekt. Dies hat eine Erhöhung der Flexibilität bei gleichzeitiger Verringerung der Kompatibilität zur Folge. Der Nutzer kann umfangreiche Aufbauten in wenigen Code-Zeilen erzeugen, wobei typische Fehler vermieden werden, da die Besonderheiten von Geant4 bezüglich der Konfiguration der optischen Prozesse automatisch durch das GODDeSS Framework gehandhabt werden. All das macht GODDeSS zu einem exzellenten Ansatz zur Vereinfachung der detaillierten Simulationen von optischen Detektorkomponenten, welche für das Konstruieren von modernen Teilchendetektoren und für das Verstehen ihres Ansprechverhaltens nötig sind.

Die vorliegende Arbeit stellt das GODDeSS Framework, seine Klassen und seine Funktionsweise vor. Des weiteren werden die umfangreichen Bemühungen präsentiert, es gegen Herstellerdaten und Testmessungen mit Prototypmodulen zu validieren. Zusätzlich wurden detaillierte Simulationen durchgeführt, um die optischen Eigenschaften von optischen Fasern und die Charakteristika des Ansprechverhaltens von Detektormodulen zu untersuchen.

Annotations

In this document, electric charges are always given in units of the *elementary charge* $e = 1.602 \cdot 10^{-19}$ C [1], i.e. the electric charge of electrons is -1, meaning $-1\,\mathrm{e} = -1.602 \cdot 10^{-19}$ C.

If not specified differently, the name of the *particles* also represents their *anti-particles*, e.g. when talking about muons also anti-muons are referred to (e.g.: $\mu = \mu^{\pm}$).

Throughout this document, the term *energy* of particles always refers to the *(relativistic)* ***kinetic*** *energy* of the particles, as long as it is not specified in a different way.

Important variables, which are used often within this document, are introduced and summarised in table A.1, which can be found in appendix A.

In this document, *bold and italic words* are used to guide through the text: important ***informations*** are highlighted by italic script, whereas important **discriminations** are highlighted by bold script.

All the work that is described in this document has been done by the author. Exceptions are explicitly stated in the text.

A **preliminary version** of the studies that will be presented in the sections 8.1, 9.4.1, and 9.4.3 was already published in [2].

Abbreviations

DNA	**D**eoxyribo**N**ucleic **A**cid
ESA	**E**uropean **S**pace **A**gency
Geant	**Ge**ometry **an**d **t**racking [3]
GODDeSS	**G**eant4 **O**bjects for **D**etailed **De**tectors with **S**cintillators and **S**iPMs [4]
LUT	**L**ook-**U**p **T**able (especially in Geant4)
MC	**M**onte **C**arlo
MET	**M**issing **E**nergy in the **T**ransverse plane
MIP	**M**inimum **I**onising **P**article
MPV	**M**ost **P**robable **V**alue of a distribution (mainly used for Landau distributions)
PDE	**P**hoton **D**etection **E**fficiency
QDC	**Charge**-to-**D**igital **C**onverter
RMS	**R**oot **M**ean **S**quare
WLS	**W**ave**L**ength-**S**hifting

Scientific experiments:

ALICE	**A** **L**arge **I**on **C**ollider **E**xperiment [5]
AMS	**A**lpha **M**agnetic **S**pectrometer [6]

ANTARES	**A**stronomy with a **N**eutrino **T**elescope and **A**byss environmental **RES**earch [7]
ATLAS	**A** **T**oroidal **L**HC **A**pparatu**S** [8]
CERN	**C**onseil **E**uropéen pour la **R**echerche **N**ucléaire [9] (= European Organisation for Nuclear Research)
CMS	**C**ompact **M**uon **S**olenoid [10]
LHC	**L**arge **H**adron **C**ollider [11]
LHCb	**L**arge **H**adron **C**ollider **b**eauty [12]
MICE	**M**uon **I**onisation **C**ooling **E**xperiment [13]

Medical imaging methods:

CT	**C**omputed **T**omography
PET	**P**ositron **E**mission **T**omography
SPECT	**S**ingle **P**hoton **E**mission **C**omputed **T**omography
ToF-PET	**T**ime-**o**f-**F**light **P**ositron **E**mission **T**omography

Detector components:

AMD	**A**achen **M**uon **D**etector [14]
ECAL	**E**lectromagnetic **CAL**orimeter
HCAL	**H**adronic **CAL**orimeter
MTT	**M**uon **T**rack fast **T**ag [2, 15]
RICH	**R**ing **I**maging **Ch**erenkov detector
TRD	**T**ransition **R**adiation **D**etector
TRT	**T**ransition **R**adiation **T**racker

Photodetectors:

APD	**A**valanche **P**hoto**D**iode
GAPD	**G**eiger-mode **A**valanche **P**hoto**D**iode
HPD	**H**ybrid **P**hoton **D**etectors
MCP	**M**icro**C**hannel **P**late
PMT	**P**hoto**M**ultiplier **T**ube
SiPM	**Si**licon **P**hoto**M**ultiplier (also referred to as MPPC (**M**ulti-**P**ixel **P**hoton **C**ounter) or PPD (**P**ixelated **P**hoton **D**etectors))

Materials:

fPMMA	**f**luorinated PMMA
PMMA	**P**oly**M**ethyl**M**eth**A**crylat ($(C_5O_2H_8)_n$)
PS	**P**oly**S**tyrene ($(C_8H_8)_n$)
PVT	**P**oly**V**inyl**T**oluene
PWO	lead tungstate (**P**b**WO**$_4$)

Contents

1 Motivation **1**

2 Interactions of Particles in Matter **5**
2.1 Electromagnetic Interactions of Traversing Massive Particles in Matter . . . 5
2.1.1 Interaction with Atomic Electrons (Excitation, Ionisation) 5
2.1.2 Interaction with Nuclei (Multiple Scattering) 10
2.1.3 Radiative Energy Loss 10
2.2 Electromagnetic Interactions of Photons in Matter 15
2.2.1 Photoelectric Effect 16
2.2.2 Compton Scattering 17
2.2.3 Pair Production 17
2.3 Non-Electromagnetic Interactions of Traversing Massive Particles in Matter . 18
2.3.1 Strong Interaction 18
2.3.2 Weak Interaction 19
2.4 Particle Cascades 20
2.4.1 Electromagnetic 20
2.4.2 Hadronic 21
2.5 Behaviour of Optical Photons at Surfaces 22

3 Particle Detection and Optical Detector Elements **27**
3.1 Principles of modern Particle Detectors 27
3.2 Optical Detector Elements 31
3.2.1 Wavelength-Shifting (WLS) Materials 31
3.2.2 Scintillating Materials 32
3.2.3 Optical Fibres 36
3.2.4 Photodetectors 39

4 Simulations in Physics and Detector Construction **47**
4.1 Physics Simulations 47
4.2 Geant4 49
4.2.1 Basic Principles 49
4.2.2 Physics and Particle Types 50
4.2.3 Geometry and Materials 51
4.2.4 Optical Surfaces 52
4.2.5 Primary Particles 54
4.2.6 User-defined Actions 54
4.2.7 Peculiarities 55
4.2.8 Geant4 Extensions 61

5 The GODDeSS package **63**
5.1 The GODDeSS Framework . . . 63
5.1.1 Object Classes . . . 65
5.1.2 Solved Challenges and Remaining Issues . . . 71

6 Consistency Check of Material Property Input and Physics Processes **73**
6.1 Emission Spectra . . . 74
6.2 Decay Times . . . 75
6.3 Scintillation Light Yield . . . 77
6.4 Reflectivity Spectra . . . 79
6.5 Bulk Attenuation Length for Optical Photons . . . 80
6.6 Scintillator Gamma Ray Attenuation Length . . . 82
6.7 Influence of Surface Roughness . . . 85
6.8 Reflectivity (Fresnel Equation) . . . 89
6.9 Energy Change during the WLS Process . . . 90
6.10 Cherenkov Spectrum . . . 91
6.11 Application of LUT Surfaces . . . 95
6.12 Fibre Trapping Efficiency . . . 97
6.13 Fibre Bending Loss . . . 100

7 Adapting GODDeSS to Reality **105**
7.1 Exit Characteristics of Light from Optical Fibres . . . 105
7.2 Fibre Signal Attenuation Length . . . 108

8 Validation against Measurements with Prototype Modules **113**
8.1 Hodoscope Measurements of Prototype Modules . . . 113
8.1.1 Experimental Procedure . . . 114
8.1.2 Analysis and Comparison . . . 115
8.2 Test-Beam Measurements of Prototype Modules . . . 126
8.2.1 Experimental Procedure . . . 126
8.2.2 Analysis and Comparison . . . 128

9 Detailed Studies **133**
9.1 Trapping Efficiency of Optical Fibres . . . 133
9.2 Signal Attenuation Length of Optical Fibres . . . 143
9.3 Exit Characteristics of Light from Optical Fibres . . . 146
9.3.1 Fibre Type . . . 146
9.3.2 Fibre Length . . . 148
9.3.3 Finish of the Fibre End Face . . . 149
9.3.4 Distance between the Fibre End and the Photodetector . . . 151
9.3.5 Equality of the Refractive Indices of Cladding and Surroundings . . . 157
9.4 Optical Readout Options . . . 157
9.4.1 Signal Height . . . 158
9.4.2 Timing . . . 162
9.4.3 Special Fibre Layouts . . . 171

10 Conclusion **177**
10.1 Summary . . . 177
10.2 Outlook . . . 179

A Appendix: Important Quantities **181**

B Appendix: Fibre Trapping Efficiency **183**

C Appendix: Code Examples **187**
C.1 Geant4 . . . 187
C.2 GOODDeSS . . . 189
C.2.1 Installation and Usage . . . 189
C.2.2 How To . . . 194

D Appendix: Implementation of Material Properties **199**
D.1 Elements . . . 199
D.2 Materials . . . 199
D.3 Physics Processes . . . 210

E Appendix: Influence of the Path Segmentation on the Birks Correction **211**

F Appendix: Adjustments to the Hodoscope Software **213**
F.1 Data Acquisition . . . 214
F.2 Data Reconstruction . . . 217

G Appendix: Config Data for the Hodoscope Measurements **219**

List of Figures **223**

List of Tables **227**

List of Equations **229**

Bibliography **231**

1. Motivation

Historically, detectors for high-energy particles have been developed and utilised in the field of high-energy particle physics. There, the first discoveries have been made using particle detectors like *cloud chambers* (e.g. positron and muon discovery [16, 17]), *bubble chambers* (e.g. weak neutral current discovery [18]), and *emulsions* (e.g. charged pion discovery [19]). Nowadays, the application of detectors for high-energy particles is not restricted to the field of particle physics any more, but they can also be found in other fields, e.g. medical imaging. This is possible, as the technologies for the detection of particles and for the determination of their properties have significantly been improved since the days of the bubble chambers.

Besides the pure detection of radiation, e.g. with rather simple devices like the Geiger-Müller tube [20], more specialised detectors also allow for the identification of different particle types and the determination of their properties. Thus, modern particle detectors are able to distinguish between high-energy photons (γ), leptons (e, μ, τ, ν), and hadrons or jets (consisting of hadrons). Which particles are observable, is something that totally depends on the *design* of each detector as well as the *environment* it is used within. Neutrinos, for example, do not interact inside "normal-sized" particle detectors, as they do not interact electromagnetically or strongly and the weak interaction has very low cross sections. Thus, neutrinos can only be observed (indirectly) in very large-scale detectors that are specialised on neutrino detection. In other detectors, there is either no possibility to detect neutrinos or they only contribute to the missing (transverse) energy (MET), which can be calculated in (nearly) hermetic detectors. The other (charged) leptons can, in general, easily be detected by electromagnetic interactions, just like high-energy photons. However, tauons decay almost immediately ($\tau_\tau \approx 0.29\,\text{ps}$ [1]), which makes a very precise tracking and particle identification necessary to identify the tauons from their decay products. The detector's ability to identify hadrons depends on its radiation environment. Whereas single hadrons can in principle be identified by determining their mass, an identification of single hadrons is not possible in very high-energy collision experiments like in the ATLAS [8] or CMS [10, 21] experiments at LHC [11] at CERN [9].[1] There, the initial quarks have such high energies that they hadronise to jets consisting of many hadrons (and leptons) travelling roughly in the same direction. In this case, a very good tracking capability of the detector can allow for the identification of b-jets, jets that started with a b-quark, as the lifetime of b-hadrons is in the right range to result in an observable distance between the creation point of the primary interaction products and the decay point of the b-hadron. However, also within jets, the identification of single particles is possible, if the detector is highly segmented. This has e.g. been done with the particle-flow algorithms for particle identification at CMS [23].

[1] In contrast, the ALICE [5] and LHCb [12] experiments at LHC are in particular designed for hadron identification (especially from heavy ion collisions or b-mesons, respectively), therefore, hadrons from high-energy collisions can be distinguished and thus be identified there [22].

A *good and reliable reconstruction* of the physics objects from the corresponding detector response is essential for a meaningful analysis of the data provided by the detector. This is likewise true for large-scale searches for new physics, like the μ and/or γ identification in the recent discovery of the Higgs boson [24–26] or e.g. the ongoing searches for extra dimensions [27] and Z' [28], as well as for every-day-applications like the photon identification in medical imaging devices, e.g. (ToF-)PET scanners [29]. Thus, a *good design and understanding* of the detector is indispensable.

To enable modern detectors to fulfil their tasks, they consist of many small components, which carry out different tasks and exploit many different physical processes. There are detectors that are based on *chemical particle detection* like e.g. the Homestake experiment for solar neutrino detection via ^{37}Cl - ^{37}Ar conversion [30]. Other experiments use *Cherenkov radiation* like e.g. the IceCube experiment [31] in Antarctica, the Super-Kamiokande experiment [32] in Japan, or the ANTARES [7] and KM3NeT [33] experiments in the Mediterranean Sea. Yet others work with *transition radiation* like e.g. the transition radiation tracker (TRT) of the ATLAS experiment or the transition radiation detector (TRD) of the AMS-02 [6] and the ALICE experiments.[2] Nevertheless, the by far most widely-used physical processes in modern particle detectors and detector parts are the *excitation and ionisation* processes of charged particles[3], which are exploited by basically three types of material: *Gases* are used in ionisation chambers like e.g. in the muon detection system of the CMS experiment [36] or in radiation detectors based on the Geiger-Müller tube. *Scintillators* are widely used in calorimeters, e.g. of (ToF-)PET scanners or particle physics experiments like ALICE, ATLAS, CMS (cf. figure 1.1) and LHCb [37] at CERN as well as in fibre trackers of experiments like LHCb [38] or MICE [13]. *Semiconductors* can be found e.g. in the tracking detectors of the ALICE, ATLAS, CMS and LHCb experiments at CERN as well as in modern light-sensitive detector elements.

This thesis concentrates on *optical particle detection*, i.e. via optical photons that have been created by scintillation, Cherenkov radiation, or transition radiation.[4] Scintillating materials are cheap (compared to semiconductors) as well as low-maintenance (compared to gases) and allow to make the deposited energy visible and mensurable. As a disadvantage, the optical light, which has been created within the scintillating material, has to be transported to photodetectors, before the optical signal can be transformed into a measurable electrical signal. Therefore, the detector response to one and the same traversing particle, decisively depends on the amount of light that is reaching the photodetector. This is critically dependent of the *optical properties* as well as the combination of the optical components. The possible variations include attenuation lengths, refractive indices, surface conditions, reflectivities, dimensions, photodetector type and position, and the possible use of optical fibres. Additionally, the light yield of optical detector components can be very low (in the few photon range), which increases the possible influence of the mentioned optical factors on the measured signal. As a result, it is not trivial to understand the response of an existing detector or to predict and optimise the detector response during the design process. A crit-

[2] Detailed descriptions of the working concepts of detectors based on Cherenkov radiation, transition radiation, and chemical reactions can be found in [1, 34, 35].

[3] These particles can be either primary particles (from the original beam) or secondary particles (which have been produces in interactions).

[4] Detailed descriptions of the working concepts of gaseous detectors and semiconductor detectors can be found in [1, 39, 40] and [1, 39, 41, 42], respectively. Semiconductor-based detectors in their function as photodetectors are also introduced in subsection 3.2.4.

ical precondition for successfully doing so is therefore a *detailed study and understanding* of the light propagation and its affecting processes in the optical components of the detector. Hence, these topics have been studied in detail in this thesis.

The work for this thesis has been performed in the scope of design studies for upgrade proposals for two experiments the host-institute (Physics Institute III, RWTH Aachen University) is contributing to. These are namely the studies on the MTT-upgrade [2, 15] for CMS at CERN and on the AMD-upgrade [14] for the Pierre Auger Observatory [43]. The *general simulation framework* GODDeSS has been developed for this purpose (cf. chapter 5) and can in principle be applied to every optical particle detector, especially those using combinations of scintillators, optical fibres and optical photodetectors (especially Silicon PhotoMultipliers (SiPMs)), which is a very good and widely used choice for particle detection nowadays (e.g. [44–51]).

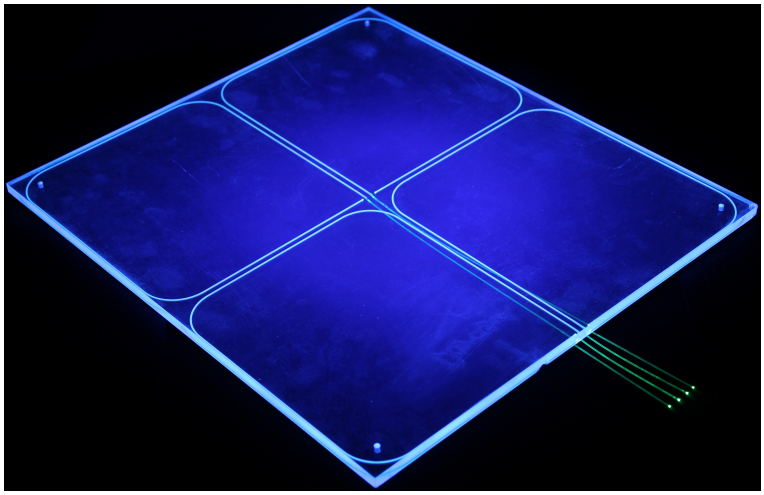

Figure 1.1.: $454 \times 404.6 \times 9\,\mathrm{mm}^3$ scintillator tile with embedded WLS fibres as it is used in the HCAL of the CMS detector. Photographed by Markus Merschmeyer and Florian Scheuch, Physics Institute III, RWTH Aachen University.

2. Interactions of Particles in Matter

In the previous chapter, the particles, which are relevant with respect to particle detection, have been presented. These particles can be detected, when they are interacting with matter within detector volumes. In this chapter, the relevant interactions, which these particles undergo when traversing matter, will be described. Knowing, understanding, and considering these interactions is crucial in order to understand or simulate the detector response to traversing particles.

In MC simulations (cf. chapter 4), complex physical correlations are often approximated by parametrised functions including fit parameters from measurements. This will not be discussed in this chapter. In case of the particle-physics simulation framework Geant4, which has been used in the scope of this thesis, information on this topic can be found in [52].

Important variables, which are used often within this chapter, are introduced and summarised in table A.1, which can be found in appendix A.

2.1. Electromagnetic Interactions of Traversing Massive Particles in Matter

When traversing matter, *massive charged particles* interact *electromagnetically* with the matter's atoms. This leads to a *continuous loss of energy*, which is composed of contributions of several different processes. Additionally, the particles can be *deflected* as well as *emit radiation*. The following summary of the relevant processes is based on [1, 53, 54].

2.1.1. Interaction with Atomic Electrons (Excitation, Ionisation)

Traversing charged particles can interact with the atomic electrons within matter and transfer energy to them.[5] Thereby, the electrons can be lifted to excited states or even be knocked out of the atoms. The description of the *energy loss* of the traversing particles depends on the particle species, i.e. if the particles are electrons/positrons or heavier particles.

[5] The scattering angle is very small for these interactions (for heavy particles with $m_e \ll m_{particle}$).

Heavy Particles

The mean energy loss of *heavy charged particles* with mass m and charge z can be described by the *Bethe-Bloch equation* [1, 53], which depends on prefactors, *particle properties*, *material properties* as well as some corrections:

$$\left(\frac{\mathrm{d}E}{\mathrm{d}x}\right)_{\text{ion.}} = -\frac{4\pi N_\mathrm{A}\alpha^2\hbar^2}{m_\mathrm{e}} \cdot \frac{z^2}{\beta^2} \cdot \rho\frac{Z}{M} \cdot \left(\ln\left(\frac{(\beta\gamma)^2}{\sqrt{1+2\gamma m_\mathrm{e}/m+(m_\mathrm{e}/m)^2}} \cdot 2\frac{m_\mathrm{e}c^2}{I_\text{eff}}\right) - \beta^2 - \frac{\delta(\beta\gamma)}{2}\right). \quad (2.1)$$

It contains the mean excitation energy I_eff and the $\beta\gamma$-dependent density effect correction δ, which will be described below in the paragraph "Mean Excitation Energy" and "Density Effect Corrections", respectively. Calculation rules for materials that do not only consist of one element can be found in the paragraph "Material Layers, Mixtures, and Chemical Compounds".

The behaviour of the Bethe-Bloch equation is illustrated in figure 2.1. It is characterised by a broad minimum, whose absolute minimum value is located at $\beta\gamma$-values between 3 and 4, depending on the material. A particle in this energy region is therefore called "Minimum Ionising Particle" (MIP). Typical values are 2.02 MeV/cm and 12.74 MeV/cm for MIP muons in organic scintillator (polyvinyltoluene (PVT)) and lead, respectively.

The Bethe-Bloch equation is valid for a wide particle velocity region ($0.1 \lesssim \beta\gamma \lesssim 1000$ [1]) and for a wide range of charged particles (heavier than electrons and up to light nuclei). In this region, it describes the particle's mean energy loss in intermediate-Z materials with a

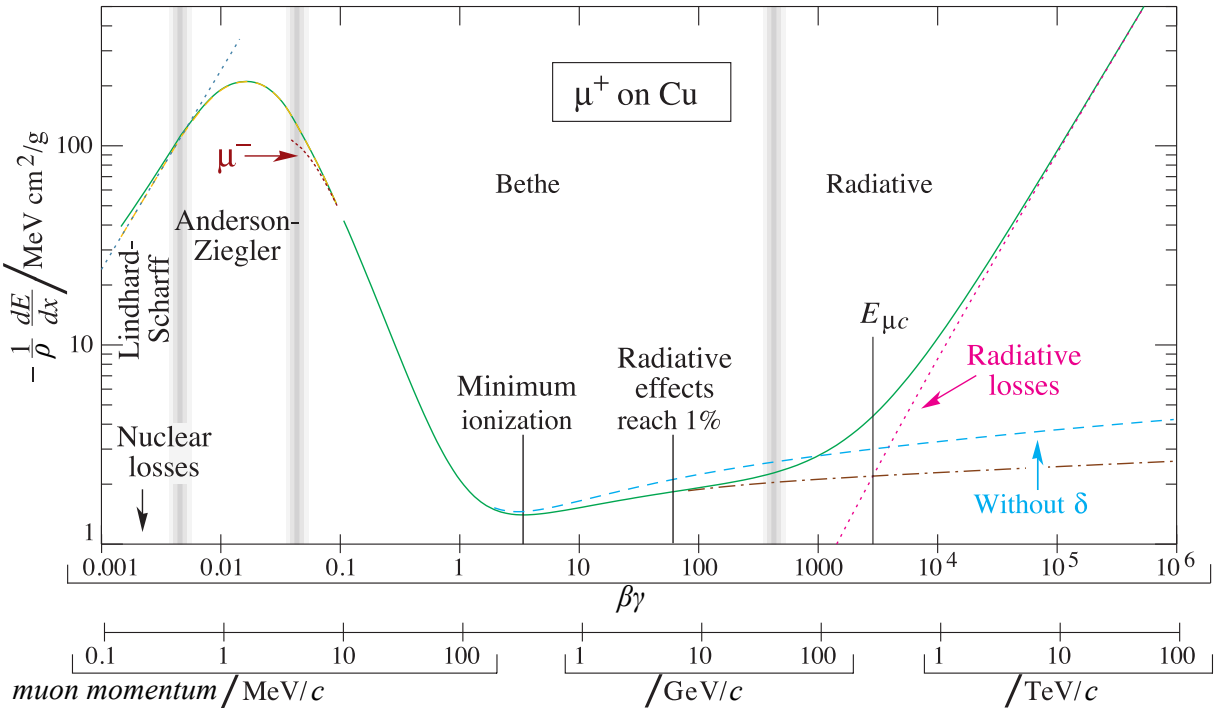

Figure 2.1.: The mean energy loss of muons in matter (using the example of copper), depending on their $\beta\gamma$-factor or momentum (adapted from [1]). δ represents the density effect corrections.

high accuracy of a few percent. At higher velocities, above the critical energy $E_{\mu c}$ (cf. paragraph "Bremsstrahlung" of subsection 2.1.3), energy loss via Bremsstrahlung becomes dominant. For lower velocities, corrections have to be applied to take the influence of the electron's atomic binding into account. In case of heavier particles, like e.g. ions, correction terms have to be applied, which consider the particles' dimensions as well as higher-order photon couplings. For lighter hadrons, these corrections can be neglected, as they only lead to significant changes in energy regions where Bremsstrahlung is already dominating.

Values for the mean energy loss of muons for different particle energies in various materials and the chemical elements can be found in [55]. When using this data, it is important to be aware that the density effect corrections, which can have a significant impact on the energy deposition (figure 2.1 shows the energy loss logarithmically!), are already considered in the values given there.

Electrons and Positrons

Just like heavy particles, *electrons and positrons* lose energy by interactions when traversing matter. For low energies, below the critical energy, energy losses by ionisation dominate, although other processes also contribute (cf. figure 2.2). Additionally, because of their small mass, Bremsstrahlung becomes dominant for higher (but still relatively low ($\gtrsim 10\,\mathrm{MeV}$ [1])) energies.

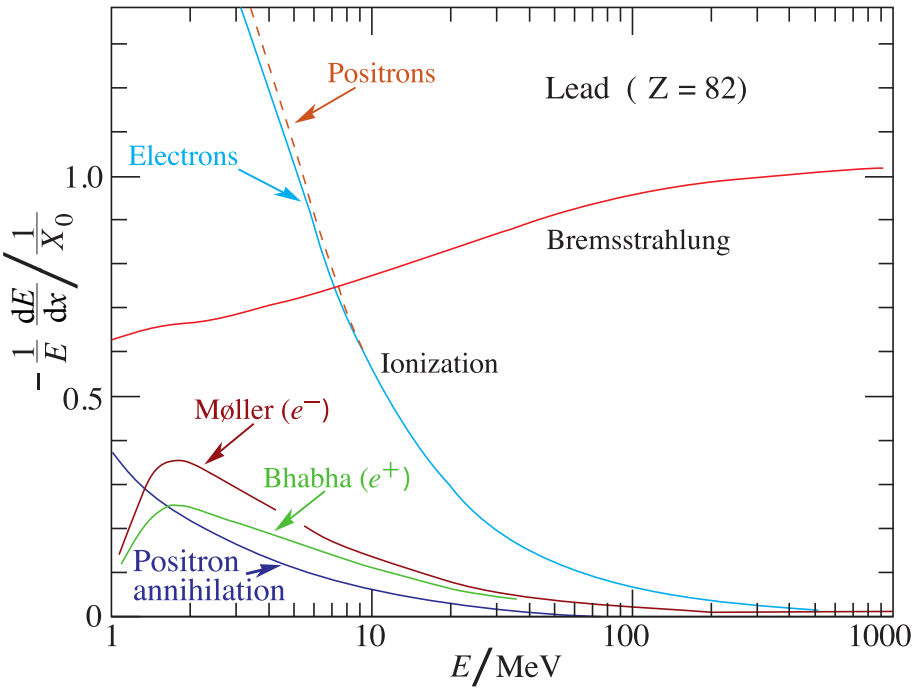

Figure 2.2.: The mean energy loss of electrons and positrons in matter (using the example of lead), depending on their energy E (adapted from [1]). It should be noted that the mean energy loss per particle energy is shown, in contrast to figure 2.1. The radiation length X_0 is the distance within a material after which the energy of a high-energy particle would have decreased to 1/e of its initial value because of Bremsstrahlung (cf. paragraph "Bremsstrahlung" of subsection 2.1.3).

To determine an equation giving the mean energy loss, the same methods as for heavy particles are used, i.e. assuming interactions on quasi-free atomic electrons, considering screening and density effects, and neglecting the shell correction. The result differs from the result for heavy particles, because the collision partners have the same mass and quantum-mechanical effects have to be considered, because of the *particle spin* and the *indistinguishability* of the collision partners in case of electron-electron interactions. It can be written as [1, 53, 54]

$$\left(\frac{\mathrm{d}E}{\mathrm{d}x}\right)_{\text{ion. } e^{\pm}} = -\frac{4\pi N_\mathrm{A}\alpha^2\hbar^2}{m_\mathrm{e}} \cdot \frac{1}{\beta^2} \cdot \rho\frac{Z}{M} \cdot \left(\ln\left(\beta\gamma \cdot \sqrt{\frac{\gamma-1}{2}}\frac{m_\mathrm{e}c^2}{I_\mathrm{eff}}\right) + D_\pm - \delta(\beta\gamma)\right), \quad (2.2)$$

with

$$D_- = \frac{1-\beta^2}{2} - \frac{2\gamma-1}{2\gamma^2}\ln 2 + \frac{1}{16}\left(\frac{\gamma-1}{\gamma}\right)^2$$

$$D_+ = \ln 2 - \frac{\beta^2}{24}\left(23 + \frac{14}{\gamma+1} + \frac{10}{(\gamma+1)^2} + \frac{4}{(\gamma+1)^3}\right).$$

Here, D_- is valid for electrons, whereas D_+ has to be used for positrons. The mean excitation energy I_eff, the density effect correction δ and calculation rules for materials that do not only consist of one element will be described in the following paragraphs.

Mean Excitation Energy

Using the correct mean excitation energy is one of the difficulties when determining the mean ionisation energy. As figure 2.3 shows, there is no simple correlation between Z and I_eff.

It can roughly be approximated via $I_\mathrm{eff} \approx Z \cdot 10\,\mathrm{eV}$ or $I_\mathrm{eff} \approx Z^{0.9} \cdot 16\,\mathrm{eV}$ [53], but it is a better choice to use the values that can be found in [55].

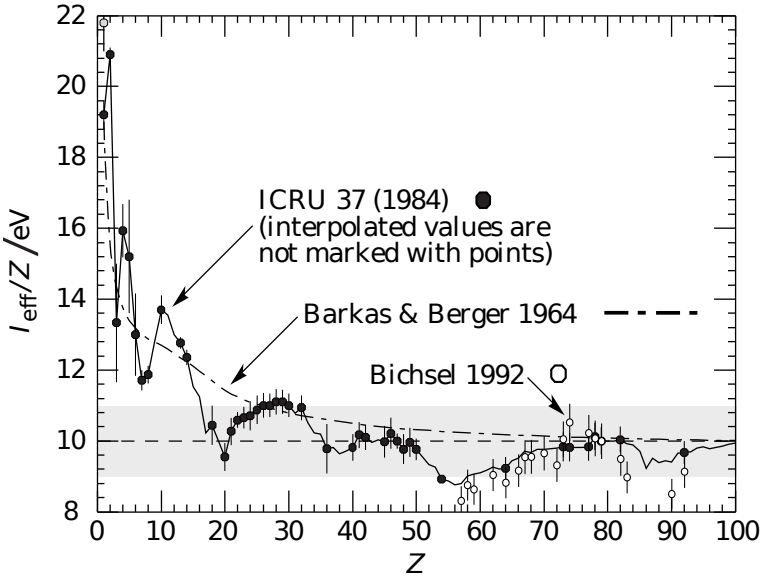

Figure 2.3.: Mean excitation energy of different materials (adapted from [1]). The grey point in the upper left corner is for liquid H_2, the corresponding black point for H_2 gas.

Density Effect Corrections

Because of *polarisation in the material*, the extension of the particle's electric field is limited and thus, the mean energy loss is reduced. As the total polarisation increases with the electron density of the material, the correction is much larger for liquids or solids than for gases. For high energies ($\beta\gamma \gtrsim 100$ [53]), the density effect correction can be approximated by [1]

$$\frac{\delta}{2} \approx \ln\left(\beta\gamma \cdot \frac{\hbar\omega_\mathrm{p}}{I_\mathrm{eff}}\right) - 0.5. \tag{2.3}$$

Values for the plasma frequency ω_p of the chemical elements can be found in [55]. A more precise equation for the density effect, which is also valid for $\beta\gamma < 100$, can be found in [1].

Material Layers, Mixtures, and Chemical Compounds

In many applications, the energy loss via ionisation has to be determined not within a material consisting of only one chemical element, but within material layers, mixtures, or chemical compounds. In this case, the equations (2.1) and (2.2) have to be modified. Literature [54, 56, 57] generally refers to *Bragg's additivity rule*

$$\left(\frac{1}{\rho}\frac{\mathrm{d}E}{\mathrm{d}x}\right)_{\text{ion., tot}} = \sum_j \frac{m_j}{m_\mathrm{tot}}\left(\frac{1}{\rho}\frac{\mathrm{d}E}{\mathrm{d}x}\right)_{\text{ion., }j} \quad\Leftrightarrow\quad \left(\frac{\mathrm{d}E}{\mathrm{d}x}\right)_{\text{ion., tot}} = \sum_j \frac{V_j}{V_\mathrm{tot}}\left(\frac{\mathrm{d}E}{\mathrm{d}x}\right)_{\text{ion., }j}. \tag{2.4}$$

Here, m_j/m_tot is the fraction by weight of the jth element and V_j/V_tot is the jth element's fraction by volume. This method returns good results for high particle energies [54], despite the fact that the $I_{\text{eff, }j}$ of the different components are underestimated, because electrons are bound more tightly in chemical compounds, and that the density corrections $\delta_j(\beta\gamma)$ do not have much physical relevance, because they depend on the electron density.

Alternatively, there are also tables containing values for $I_{\text{eff, tot}}$ and $\omega_{\text{p, tot}}$ for the chemical elements as well as for many mixtures and chemical compounds (e.g. [55, 58]).

Fluctuation of the Energy Loss

The so far mentioned equations describe the mean energy loss $\overline{\Delta E}$ of particles by ionisation. However, the energy-loss process is of *statistical nature*, as the total energy loss is the sum of several independent interactions. Thus, the "real" energy loss ΔE follows a distribution $f(\Delta E, \Delta x)$, which depends on the thickness of the material layer Δx. For **thick material layers** ($\Delta E \sim E$), where the number of interactions is large, the energy-loss distribution can be described by a *Gaussian distribution* around the mean energy loss [54]

$$f(\Delta E, \Delta x) \sim \exp\left(-\frac{\left(\Delta E - \overline{\Delta E}\right)^2}{2\sigma^2}\right), \tag{2.5}$$

with its variance

$$\sigma^2 = \frac{1-\beta^2/2}{1-\beta^2} \cdot \frac{4\pi N_\mathrm{A}\alpha^2\hbar^2c^2}{1+2\gamma m_\mathrm{e}/m+(m_\mathrm{e}/m)^2} \cdot \rho\frac{Z}{M} \cdot \Delta x,$$

which is proportional to the thickness of the material layer. In case of **thin material layers** ($\Delta E \ll E$), where the number of interactions is small and thus rare hard interactions have a significant impact, $f(\Delta E, \Delta x)$ can be described by a *Landau distribution* with its most probable value (MPV) for the energy loss [1, 53]

$$\Delta E_\mathrm{mpv} = \frac{2\pi N_\mathrm{A}\alpha^2\hbar^2}{m_\mathrm{e}} \cdot \frac{1}{\beta^2} \cdot \rho\frac{Z}{M} \cdot \Delta x \cdot \left(\ln\left(\frac{4\pi N_\mathrm{A}\alpha^2\hbar^2c^2}{I_\mathrm{eff}^2} \cdot \gamma^2 \cdot \rho\frac{Z}{M} \cdot \Delta x\right) - \beta^2 + 0.2 - \delta(\beta\gamma)\right) \quad (2.6)$$

For high particle energies ($\beta\gamma \gtrsim 100$ [53]), this becomes

$$\Delta E_\mathrm{mpv} = \frac{2\pi N_\mathrm{A}\alpha^2\hbar^2}{m_\mathrm{e}} \cdot \frac{1}{\beta^2} \cdot \rho\frac{Z}{M} \cdot \Delta x \cdot \left(\ln\left(\frac{4\pi N_\mathrm{A}\alpha^2c^2}{\beta^2\omega_\mathrm{p}^2} \cdot \rho\frac{Z}{M} \cdot \Delta x\right) + 0.2\right),$$

because of equation (2.3). In both cases, ΔE_mpv increases with increasing thickness of the material layer.

2.1.2. Interaction with Nuclei (Multiple Scattering)

In contrast to interactions with the atomic electrons, which have been described in the previous section, interactions of heavy particles (with $m_\mathrm{e} \ll m_\mathrm{particle} \ll m_\mathrm{nucleus}$) with the nuclei result in *negligible energy losses* but *significant scattering* angles. For many consecutive nuclear scattering processes, the total scattering angle with respect to the particle's direction of flight is Gaussian distributed[6] around 0 ° with an RMS of [1, 53, 54]

$$\theta = z \cdot \frac{13.6\,\mathrm{MeV}}{c\beta p}\sqrt{2 \cdot \frac{x}{X_0}}\left(1 + 0.038\ln\left(\frac{x}{X_0}\right)\right). \quad (2.7)$$

This equation is valid for particles with charge z and momentum p, traversing a scattering medium with thickness x and radiation length X_0[7]. It is accurate to $\leq 11\,\%$ for $10^{-3} < x/X_0 < 100$ [1] and describes multiple scattering of particles in a single material.

In case of particles traversing many different material layers and mixtures, summing up the squares of the different θ contributions does not return the correct combined result. Instead, θ has to be determined for a combined radiation length X_0 of the whole setup, (cf. paragraph "Bremsstrahlung" of subsection 2.1.3).

2.1.3. Radiative Energy Loss

In addition to transferring energy to particles forming the matter, traversing charged high-energy particles also lose energy by *emitting photons*. The most important processes are described in this subsection.

[6] Less frequent "hard" scattering processes lead to non-Gaussian tails [1].
[7] The radiation length X_0 is defined in paragraph "Bremsstrahlung" of subsection 2.1.3.

Cherenkov Radiation

If a charged particle traverses matter, it temporarily polarises the atoms next to its trajectory by inducing dipoles. For particle velocities below the effective speed of light in the material ($v_{\text{part}} = \beta c < v_{\text{phot}} = c/n$, where n is the material's refractive index (cf. section 2.5)), the polarisation, reorientation of the dipoles, and depolarisation happen so fast that the overall effect vanishes. For $v_{\text{part}} > v_{\text{phot}}$ (Cherenkov threshold), these processes happen very slowly, thus, the total polarisation is asymmetric and an *overall dipole field* remains (cf. figure 2.4(a)) and radiation is emitted. As n is a function of the frequency of the light (cf. section 2.5), the Cherenkov threshold is only exceeded for certain energy or wavelength ranges. As a consequence, Cherenkov radiation is also only emitted in these ranges.

The Cherenkov radiation is emitted under the Cherenkov angle θ_{C} with respect to the particle's direction. As can be derived from geometrical considerations (cf. figure 2.4(b)), It is given by:

$$\cos\theta_{\text{C}} = \frac{1}{n\beta}. \tag{2.8}$$

The mean number of Cherenkov photons that is produced by a particle with charge z per path length x and photon energy E_γ or photon (vacuum, cf. section 2.5) wavelength λ is given by[8] [1]

$$\frac{\mathrm{d}^2N}{\mathrm{d}x\,\mathrm{d}E_\gamma} = \frac{\alpha z^2}{\hbar c}\left(1 - \frac{1}{\beta^2 n^2(E_\gamma)}\right) \quad \text{or} \quad \frac{\mathrm{d}^2N}{\mathrm{d}x\,\mathrm{d}\lambda} = \frac{2\pi\alpha z^2}{\lambda^2}\left(1 - \frac{1}{\beta^2 n^2(\lambda)}\right). \tag{2.9}$$

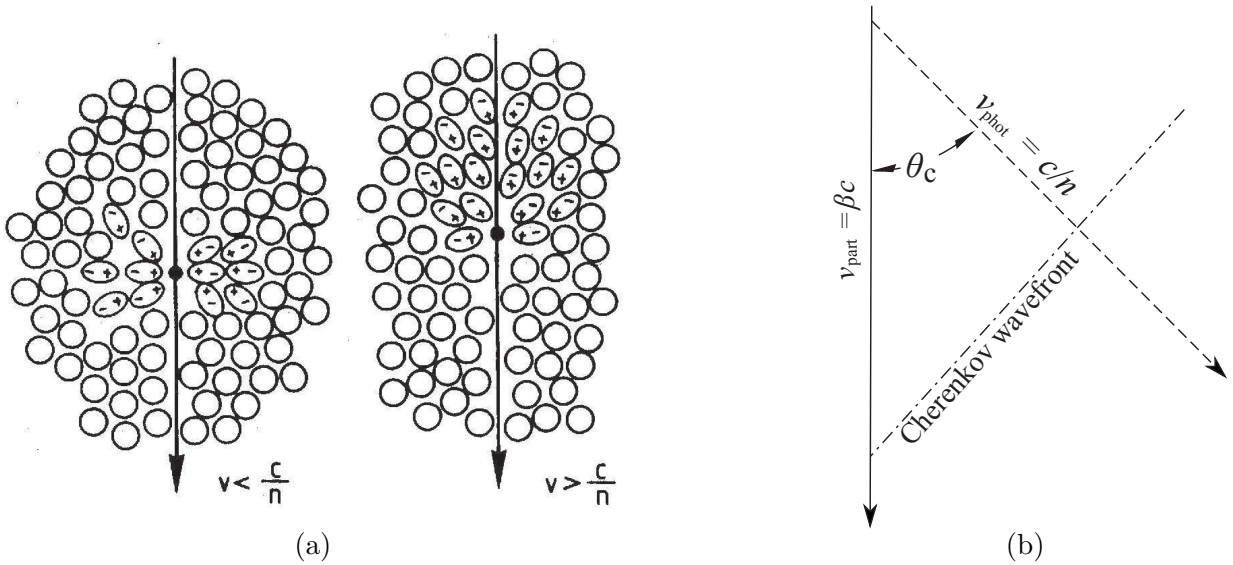

Figure 2.4.: **(a):** Illustration of the polarisation of slow and fast particles in matter (adapted from [53]). In case of fast particles (i.e. $v_{\text{part}} > v_{\text{phot}} = c/n$), an overall dipole field remains. **(b):** Geometry of the development of Cherenkov radiation [1].

[8] Under the assumption of $n = \text{const}$, integrating equation (2.9) leads to a divergent number of photons if the considered upper photon energies are not restricted. This would result in a large number of high-energy Cherenkov photons and thus in a significant energy loss of the traversing particle. As this does not match the observations, the Cherenkov radiation has to be limited to a reasonable energy range. This is not necessary, if the realistic refractive index spectrum is used, as the refractive index tends to one for high photon energies (cf. section 2.5) and, thus, limits the Cherenkov emission spectrum to lower energies.

From this equation, the particle's mean energy loss by Cherenkov radiation can be determined by integrating over the E_γ or λ range, on which $n(E_\gamma)$ or $n(\lambda)$ fulfils the Cherenkov criterion [54]:

$$\left(\frac{\mathrm{d}E}{\mathrm{d}x}\right)_{\text{Cherenkov}} = -\int\limits_{\beta n>1}\left(\frac{\mathrm{d}^2N}{\mathrm{d}x\,\mathrm{d}E_\gamma}\cdot E_\gamma\right)\mathrm{d}E_\gamma = -\int\limits_{\beta n>1}\left(\frac{\mathrm{d}^2N}{\mathrm{d}x\,\mathrm{d}\lambda}\cdot\frac{2\pi\hbar c}{\lambda}\right)\mathrm{d}\lambda. \tag{2.10}$$

However, the energy loss due to Cherenkov radiation is relatively low compared to the energy loss via other processes (in particular: ionisation), usually much less than 1 % and up to $\approx 5\,\%$ [54] in light gases (e.g. hydrogen or helium). Typical values are ~ 335 photons/cm and $\sim 770\,\mathrm{eV/cm}$ for MIP muons ($\beta\gamma = 3.5$) in typical organic scintillators ($n = 1.58$) when considering optical Cherenkov photons ($1.5\,\mathrm{eV} \leq E_\gamma \leq 3.1\,\mathrm{eV}$).

Bremsstrahlung

Another radiative energy loss of charged particles traversing matter is via Bremsstrahlung. This occurs, because the particles interact with the *Coulomb field* of the nuclei and are thus *deflected*. The photons are mainly emitted at small angles with respect to the particle's trajectory. The average emission angle is [54]

$$\theta_{\text{mean}} = \frac{mc^2}{E_{\text{part}}} = \frac{1}{\gamma},$$

where E_{part} is the energy of the particle and m is its mass.

Energy loss by Bremsstrahlung is *dominant for high particle energies* (cf. figures 2.1 and 2.2). The full description is quite complex, as the actual probability of Bremsstrahlung depends on many factors:

- The probability of Bremsstrahlung depends on the effective distance between the particle and the nucleus. In classical description, the charge of the nucleus is partly screened by the charge of the atomic electrons, if the effective distance of the interaction is much larger than the atomic radius ("complete screening"). Thus, the effective charge, which influences the interacting particle, is smaller than in case of a short effective distance ("no screening"). Even if the classical description is no longer applicable in quantum mechanics, the concept of the effective interaction distance can nevertheless be introduced. The screening can be approximated as "complete" for particle energies $E \gg mc^2/(\alpha Z^{1/3})$ [54], except for the emission of high-energy photons.

- Additionally to the Coulomb field of the nuclei, which gives a Z^2 proportionality, the Coulomb field of the atomic electrons has to be taken into account. This results in an additional proportionality of $\approx Z$, which varies because of screening.

However, the energy loss by Bremsstrahlung is dominant for energies that are sufficiently high to approximate the screening as "complete" (except for high-energy photon emission).

In this case, the mean energy loss per distance is proportional to the initial energy of the particle, thus the particle's energy decreases exponentially:

$$\left(\frac{\mathrm{d}E}{\mathrm{d}x}\right)_{\text{brems}} = -\frac{E}{X_0} \quad \Rightarrow \quad E = E_0 \cdot e^{-x/X_0}. \tag{2.11}$$

X_0 is the so-called *radiation length*. After traversing a distance of X_0 within a material, the particle's energy has decreased to $1/e$ of its initial energy. X_0 depends on the material the particle is traversing and the particle's properties themselves. For particles with mass m and charge z, it can be written as [54]:

$$\frac{1}{X_0} = 4\frac{N_\mathrm{A}\hbar^2\alpha^3}{c^2} \cdot \frac{z^2}{m^2} \cdot \frac{\rho}{M} \cdot \phi(Z). \tag{2.12}$$

The actual shape of $\phi(Z)$ depends on the applied corrections and can (at first approximation) be described as [53, 54]

$$\phi(Z) \approx Z(Z+1)\ln\left(\frac{183}{Z^{1/3}}\right) \tag{2.13}$$

This approximation is in reasonable agreement with data (except for high-energy photon emission), but there are several different modifications, e.g. depending on the energy range. A comprehensive description including the effects due to atomic and nuclear form factors for light and heavy elements results in [1, 54]:

$$\phi(Z) \approx (a(Z) - \chi(Z))\, Z^2 + b(Z) \cdot Z \tag{2.14}$$

with

$$\chi(Z) = \alpha^2 Z^2 \left(\frac{1}{1+\alpha^2 Z^2} + 0.20206 - 0.0369\,\alpha^2 Z^2 + 0.0083\,\alpha^4 Z^4 - 0.002\,\alpha^6 Z^6\right)$$

and

Z	1	2	3	4	> 4
$a(Z)$	5.31	4.79	4.74	4.71	$\ln(184.15\,Z^{-1/3})$
$b(Z)$	6.144	5.621	5.805	5.924	$\ln(1194\,Z^{-2/3})$

.

For material layers, mixtures, and chemical compounds, the radiation length can be calculated via [54]

$$\frac{1}{\rho\, X_0} = \sum_j \frac{m_j}{m_{\text{tot}}} \cdot \frac{1}{\rho_j\, X_{0\,j}} \quad \Leftrightarrow \quad \frac{1}{X_0} = \sum_j \frac{V_j}{V_{\text{tot}}} \cdot \frac{1}{X_{0\,j}}. \tag{2.15}$$

Here, m_j/m_{tot} is the fraction by weight of the jth component, V_j/V_{tot} is the jth component's fraction by volume, and the sum over j adds up all material components. Values of the radiation length X_0 for electrons can be found in [55].

In order to determine whether Bremsstrahlung has a significant impact on the total energy loss of a particle, the *critical energy* E_c can be used as an indicator. It is the energy of a particle,at which the mean energy loss by ionisation equals that by Bremsstrahlung. It

depends on the material (e.g. the aggregation state) and can be approximated for electrons and positrons by [1]

$$E_{\mathrm{c,\,e,\,solid}} = \frac{610\,\mathrm{MeV}}{Z + 1.24} \qquad E_{\mathrm{c,\,e,\,gas}} = \frac{710\,\mathrm{MeV}}{Z + 0.92}.$$

A more accurate description (which is valid not only for electrons and positrons) is [54]

$$E_{\mathrm{c}} = 2.66\,\mathrm{MeV} \cdot \left(Z \cdot \frac{\rho / \frac{\mathrm{g}}{\mathrm{cm}^3}}{M / \frac{\mathrm{g}}{\mathrm{mol}}} \cdot X_0/\mathrm{cm} \right)^{1.11}. \tag{2.16}$$

Values of the radiation length X_0 for electrons (which can easily be converted to values for other particles) and of the critical energy for electrons and muons can be found in [55]. For electrons/photons, the radiation length X_0 is $\approx 43\,\mathrm{cm}$ in typical organic scintillators (PVT). As $X_0 \sim m^2$ and the muon, the next heavier particle, has a mass of $m_\mu \approx 200 \cdot m_e$, its critical energy is in the above 100 GeV range. Therefore, energy loss via Bremsstrahlung is mainly important for electrons. The values for (MIP) muons in PVT are $X_0 \approx 17\,\mathrm{km}$, $E_{\mathrm{c}} = 1195\,\mathrm{GeV}$, and $\left(\frac{\mathrm{d}E}{\mathrm{d}x}\right)_{\mathrm{brems}} \approx 190\,\mathrm{eV/cm}$. However, for muons with a kinetic energy of 1 TeV, which can e.g. be created in the collisions at LHC, the energy loss via Bremsstrahlung is not unimportant any more ($\left(\frac{\mathrm{d}E}{\mathrm{d}x}\right)_{\mathrm{brems}} \approx 0.6\,\mathrm{MeV/cm}$)

Transition Radiation

In addition to their energy loss due to ionisation and the previously described radiation effects, charged particles traversing matter lose energy via transition radiation. This happens, if a particle with charge z crosses the boundary between *materials with different refractive indices*, a so-called radiation layer. In this case, asymmetries in the temporary polarisation of the atoms next to the particle's trajectory occur. The resulting *overall dipole field* leads to the emission of radiation, also for particle velocities below the Cherenkov threshold.

The full description of the energy distribution is rather complicated (cf. e.g. [54]). About half of the energy is emitted by photons with $0.1 \leq \hbar\omega/\gamma\,\hbar\omega_{\mathrm{p}} \leq 1$ [1]. For energies with $\hbar\omega > \gamma\,\hbar\omega_{\mathrm{p}}$, the spectrum rapidly decreases, whereas photons with low energies experience absorption in operational detectors consisting of many radiator layers. The photons are emitted in a cone, which has a maximum intensity for an angle θ_{max} with respect to the particle's trajectory, which can be determined by [59]

$$\sin\theta_{\mathrm{max}} = \frac{1}{\beta\gamma}.$$

Examples of the angular distribution of the emitted photons can be found in [59]. The total energy per boundary that is emitted in one direction with respect to the particle's trajectory is given by [54]

$$E = z^2\gamma\frac{\alpha\hbar}{3}\frac{(\omega_{\mathrm{p},2} - \omega_{\mathrm{p},1})^2}{\omega_{\mathrm{p},2} + \omega_{\mathrm{p},1}}, \tag{2.17}$$

where $\omega_{\mathrm{p},1}$ and $\omega_{\mathrm{p},2}$ are the plasma frequencies of the two materials forming the boundary. Values for the plasma frequency ω_{p} of the chemical elements can be found in [55]. Typical values for the emitted energy of a MIP ($\beta\gamma = 3.5$) per boundary are $\approx 0.35\,\mathrm{eV}$ for a PVT-air boundary and $\approx 1.05\,\mathrm{eV}$ for a lead-air boundary. Thus, transition radiation is generally not relevant for scintillator-based optical detector components.

2.2. Electromagnetic Interactions of Photons in Matter

Unlike the massive particles, photons do not continuously lose energy when traversing matter and interacting with it. Instead, in every interaction, photons are *either absorbed or scattered*. Thus, a photon beam rather loses photons (i.e. intensity) than photon energy when interacting with matter. After traversing a distance x within matter consisting of a compound material, a mixture, or a chemical element (as special case with $j = 1$), the intensity I of a photon beam with an initial intensity I_0 can be described with the total cross section for photonic process σ_{tot} as [53, 54]

$$I = I_0 e^{-\mu x} \qquad \text{with the } \textit{attenuation coefficient} \qquad \mu = N_{\text{A}} \frac{\rho}{M} \cdot \sigma_{\text{tot}}. \tag{2.18}$$

For material layers, mixtures, and chemical compounds, the photon attenuation is [54]:

$$\mu_{\text{tot}} = N_{\text{A}} \sum_j \left(\frac{V_j}{V_{\text{tot}}} \cdot \frac{\rho_j}{M_j} \cdot \sum_k \sigma_{jk} \right) = \sum_j \frac{V_j}{V_{\text{tot}}} \cdot \mu_j \quad \Leftrightarrow \quad \left(\frac{\mu}{\rho} \right)_{\text{tot}} = \sum_j \frac{m_j}{m_{\text{tot}}} \cdot \left(\frac{\mu}{\rho} \right)_j . \tag{2.19}$$

Here σ_{jk} is the cross section for photonic process k with the atoms of the jth constituent element, m_j/m_{tot} is the fraction by weight of the jth component, and V_j/V_{tot} is the jth component's fraction by volume.

The most important processes that contribute to the attenuation coefficient are described below. Figure 2.5 shows, which effect dominates, depending on the photon energy E_γ and the atomic proton number Z of the material.

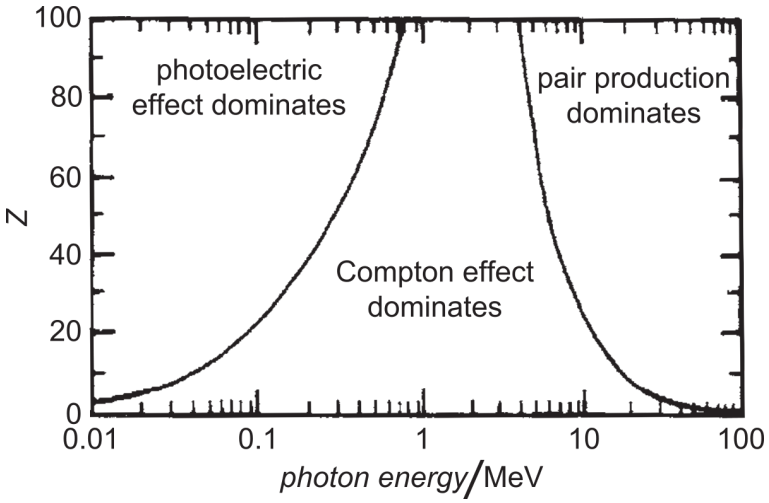

Figure 2.5.: The dominating interaction processes of photons in matter, depending on the photon energy E_γ and the atomic proton number Z of the absorber material. Adapted from [53].

2.2.1. Photoelectric Effect

Atomic electrons, i.e. electrons that are bound to a nucleus, can *absorb photons*. During this process, the electron gains the energy E_γ that the photon carried and is lifted to an excited state or, if the photon's energy exceeds the electron's binding energy, is emitted from the atom. The latter case is referred to as photoelectric effect. The nucleus, as the third collision partner, takes the recoil momentum. Therefore, the cross section for this process strongly increases with the strength of the binding between electron and nucleus and is, thus, much higher for the inner electron shells of an atom than for the outer shells. Therefore, *characteristic absorption edges* can be observed, when the photon energy is in the region of the binding energy of the electron shells. Additionally, the shell's energetic substructure due to *fine-structure splitting* leads to additional, less distinct absorption edges. The effect of absorption edges is illustrated in figure 2.6.

In the **non-relativistic** energy region ($E_\gamma \ll m_\mathrm{e}c^2$), the total cross section σ_phot of the photoelectric effect can be described using the Born approximation [53, 54]:

$$\sigma_\mathrm{phot} = \frac{8\sqrt{2}}{3\pi}\alpha^6\lambda_\mathrm{e}^2 \cdot Z^5 \left(\frac{m_\mathrm{e}c^2}{E_\gamma}\right)^{3.5}. \tag{2.20}$$

In case of heavy elements (i.e. large values of Z) or photon energies around the absorption edges, this approximation cannot be used and the cross section has to be calculated using the exact wave functions. Alternatively, higher-order parametrisations containing fit parameters from measurements can be used. This is especially done for MC simulations.

In the **relativistic** case ($E_\gamma \gg m_\mathrm{e}c^2$), the cross section becomes [53]

$$\sigma_\mathrm{phot} = \frac{\alpha^6}{\pi}\lambda_\mathrm{e}^2 \cdot Z^5 \frac{m_\mathrm{e}c^2}{E_\gamma}. \tag{2.21}$$

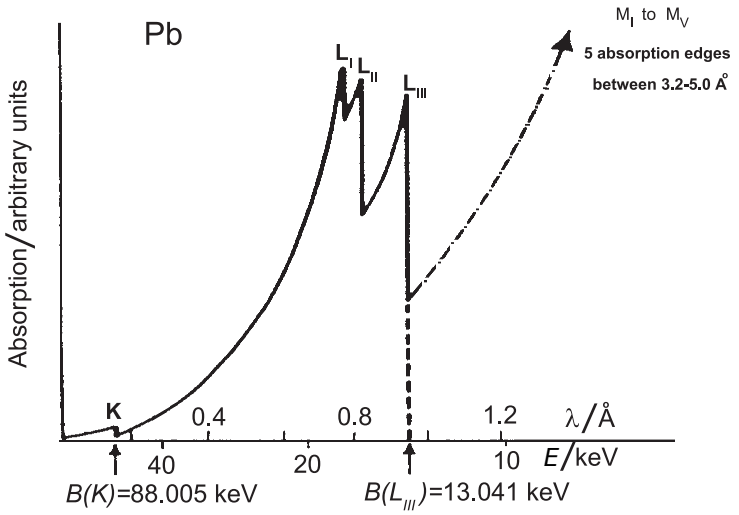

Figure 2.6.: Illustration of the absorption edges of the photoelectric effect close to the electron shell's binding energies B using the example of lead [54].

2.2.2. Compton Scattering

Because of momentum conservation, free electrons cannot absorb photons. If a photon interacts with a *(quasi)free electron*, it is *scattered* and loses some of its energy E_γ to the slow electron or gains some energy from the fast electron (inverse Compton effect).

For photons in matter, the atomic electrons can be considered as free electrons, if their binding energy can be neglected. This approximation is generally done when calculating the total cross section σ_{comp} of Compton scattering. The reason is that for low-Z materials the binding energy of the K-shell electrons is low compared to the considered photon energies, whereas for high-Z materials, the strongly bound K-shell electrons only represent a small fraction of all electrons. For low photon energies ($E_\gamma \lesssim 100\,\text{keV}$ [54]) or for the differential cross section, the binding has a larger impact and has to be considered.

With $\epsilon = E_\gamma/(m_\text{e}c^2)$, the total cross section for Compton scattering off an atom is [53, 54]:

$$\sigma_{\text{comp}} = \frac{\alpha^2}{2\pi}\lambda_\text{e}^2 \cdot Z \left(\frac{1+\epsilon}{\epsilon^2} \left(\frac{2\,(1+\epsilon)}{1+2\epsilon} - \frac{\ln(1+2\epsilon)}{\epsilon} \right) + \frac{\ln(1+2\epsilon)}{2\epsilon} - \frac{1+3\epsilon}{(1+2\epsilon)^2} \right). \tag{2.22}$$

Compton scattering of photons off other charged particles than electrons is possible, too. But it has a strongly suppressed cross section, as the Compton wavelength is proportional to $1/m$ (cf. table A.1), where m is the mass of the considered particle, i.e. the photon's partner for Compton scattering in this case.

2.2.3. Pair Production

If the photon energy E_γ exceeds the needed threshold, a photon within the *Coulomb field* of a charged particle with mass m can be converted into a pair of a charged particle with mass m_{pair} and its anti-particle. The threshold consists of the mass of the two created particles as well as the recoil energy, which is transferred to the source particle of the Coulomb field (because of momentum conservation) [54]:

$$E_\gamma \geq 2\, m_{\text{pair}}\, c^2 \left(1 + \frac{m_{\text{pair}}}{m} \right). \tag{2.23}$$

For photons in matter, the most probable process is the production of electron-positron pairs in the Coulomb field of a nucleus. For photon energies with $m_\text{e}c^2 \ll E_\gamma \ll m_\text{e}c^2/(\alpha Z^{1/3})$ [60], the **screening** of the nucleus by its electrons can be **neglected**[9] (cf. "Bremsstrahlung" of subsection 2.1.3). In this case, the cross section for pair production in the Coulomb field of the nucleus can be calculated via [53, 54]

$$\sigma_{\text{pair, nuc}} = \frac{\alpha^3}{\pi^2}\lambda_\text{e}^2 \cdot Z^2 \left(\frac{7}{9} \ln\left(2\frac{E_\gamma}{m_\text{e}c^2} \right) - \frac{109}{54} + \frac{129}{80}\frac{m_\text{e}c^2}{E_\gamma} \right). \tag{2.24}$$

[9] "For low energies the photon must come relatively close to the nucleus to make pair production probable, which means that the photon sees only the 'naked' nucleus." [61]

In case of **complete screening** of the nucleus by its electrons ($E_\gamma \gg m_e c^2/(\alpha Z^{1/3})$ [60]), the cross section for pair production in the Coulomb field of the nucleus becomes energy-independent and can approximately be expressed by the material's radiation length X_0 [53, 54]:

$$\begin{aligned}\sigma_{\text{pair, nuc}} &= \frac{\alpha^3}{\pi^2}\lambda_e^2 \cdot Z^2 \left(\frac{7}{9}\ln\left(\frac{183}{Z^{1/3}}\right) - \frac{1}{54}\right) \\ &\approx \frac{7}{9}\frac{\alpha^3}{\pi^2}\lambda_e^2 \cdot Z^2 \ln\left(\frac{183}{Z^{1/3}}\right) \\ &\approx \frac{7}{9}\cdot\frac{M}{\rho N_A}\cdot\frac{1}{X_0}.\end{aligned} \tag{2.25}$$

Furthermore, the total cross section for pair production also has to consider a correction for (suppressed) pair production in the Coulomb field of an atomic electron and the screening effects in this case, as well as radiation corrections. With an empirical equation, the total cross section for pair production in the Coulomb field of an atom can be described as [54]:

$$\begin{aligned}\sigma_{\text{pair}} &= \sigma_{\text{pair, nuc}} + \sigma_{\text{pair, e}} \\ &= \left(1 + \frac{1}{Z}\left[\frac{3+\alpha Z}{9}\cdot\ln\left(\frac{E_\gamma}{2m_e c^2}\right) - 0.00635\cdot\ln^3\left(\frac{E_\gamma}{2m_e c^2}\right)\right]\right)\sigma_{\text{pair, nuc}}.\end{aligned} \tag{2.26}$$

Of course, not only the production of an electron-positron pair is possible. If the photon carries enough energy, e.g. a muon-antimuon pair can be produced. However, the cross section for this process is strongly suppressed, as the Compton wavelength of heavier particles is much smaller (cf. table A.1).

2.3. Non-Electromagnetic Interactions of Traversing Massive Particles in Matter

Besides the electromagnetic interactions, which have been described in the previous section, also *strong* and *weak interactions* can occur when particles traverse matter. They are summarised in this section, based on [53] for the strong and [34] for the weak interaction.

2.3.1. Strong Interaction

In addition to electromagnetically and weakly, *hadronic particles* and *nuclei* can also interact strongly. In the inelastic case, the particles turn into a different species, as their quark content is changed. At the same time, secondary hadronic particles can be created, if the energy of the interacting particle is high enough.

For low particle energies, both, the elastic and the inelastic strong cross section ($\sigma_{\text{el.}}$ and $\sigma_{\text{inel.}}$, respectively), are strongly depending on the particle's energy. For high energies, they

can be approximated as being energy-independent. Thus, when additionally neglecting the cross section's dependence of the interacting particle (e.g. protons, pions, kaons,...), the absorption probability P of high-energy hadrons traversing the distance x within matter can be described by

$$P = e^{-x/\lambda_\mathrm{I}} \tag{2.27}$$

with the *nuclear interaction length* λ_I that is defined as [53, 62]

$$\frac{1}{\lambda_\mathrm{I}} = N_\mathrm{A}\frac{\rho}{M}\cdot\sigma_\mathrm{inel.}. \tag{2.28}$$

For material layers, mixtures, and chemical compounds, this results in

$$\left(\frac{1}{\rho\,\lambda_\mathrm{I}}\right)_\mathrm{tot} = \sum_j \frac{m_j}{m_\mathrm{tot}}\cdot\left(\frac{1}{\rho\,\lambda_\mathrm{I}}\right)_j \quad\Leftrightarrow\quad \frac{1}{\lambda_{\mathrm{I},\,\mathrm{tot}}} = \sum_j \frac{V_j}{V_\mathrm{tot}}\cdot\frac{1}{\lambda_{\mathrm{I},\,j}}. \tag{2.29}$$

Here, m_j/m_tot is the fraction by weight of the jth component, V_j/V_tot is the jth component's fraction by volume, and the sum over j adds up all material components. By replacing $\sigma_\mathrm{inel.}$ with the total hadronic cross section $\sigma_\mathrm{tot.} = \sigma_\mathrm{el.} + \sigma_\mathrm{inel.}$ the *nuclear collision length* λ_T can be obtained. λ_I can roughly be approximated with [63]

$$\lambda_\mathrm{I} \approx 35\,\frac{\mathrm{g}}{\mathrm{cm}^2}\cdot\frac{\left(M/\frac{\mathrm{g}}{\mathrm{mol}}\right)^{1/3}}{\rho}.$$

Values of λ_I and λ_T can be found in [55]. Typical values of λ_I are 78.80 cm and 20.27 cm for organic scintillators (PVT) and the inorganic scintillator lead tungstate (PWO), respectively.

2.3.2. Weak Interaction

As the weak interaction is "weak" (i.e. has very low cross sections), its contribution is only important for particles that are uncharged (no electromagnetic interaction) and leptonic (no strong interaction). The only known particles that meet these requirements are *neutrinos*. They can be detected via weak interactions with nuclei or atomic electrons , which can result in a change of the chemical composition of the detector volume as well as in the emission of an electromagnetically interacting particle.

As the cross sections of the weak interaction are very small (the probability of a neutrino interaction when traversing 10 m of solid iron is below 10^{-7} % [34]), very large interaction volumes are needed, if it is desired to detect neutrinos (cf. e.g. the IceCube experiment [31] or the Super-Kamiokande experiment [32]). In "normal-sized" particle detectors, neutrino detection is practically not possible. To circumvent this problem, the neutrino energy or momentum can be inferred from the *missing energy or momentum* in the detector, if the centre-of-mass energy of the interaction is known.

2.4. Particle Cascades

When high-energy particles interact with matter, new particles are created, which in general also possess high energies. Thus, particle cascades or showers can form. They can roughly be divided into electromagnetic and hadronic cascades. Detailed information can e.g. be found in [1, 54, 63] for the electromagnetic and in [1, 62, 63] for the hadronic case. Information from these sources has been summarised below.

2.4.1. Electromagnetic

For high-energy electrons, *Bremsstrahlung* is the dominant process of energy loss. At the same time, *pair production* dominates the interactions of high-energy photons. Combining this, high-energy electrons/photons will induce cascades of (mainly) electrons and photons when interacting with matter. Using a very simple model of the development of such cascades (incident energy E_0, electrons with energies E_e above the critical energy E_c emitting photons after one radiation length X_0, photons with energies $E_\gamma > E_c$ creating electron-positron-pairs after $1\,X_0$, energy is shared equally between the particles at each step), important properties can roughly be determined:

⇒ The number N of particles in one step of the cascade as well as their energy E depends on the position x in the material: $N \approx 2^{(x/X_0)} \approx E_0/E$.

⇒ The creation of new particles stops when all charged particles fall below the critical energy E_c. Thus, the total number of particles created in the cascade is $N_{tot} \approx 2E_0/E_c$[10] and the position of the shower maximum in units of X_0 can be approximated with $x \approx \ln(E_0/E_c)/\ln 2$.

⇒ To absorb 95 % of the cascade, the material should be about 15-20 X_0 thick.

The realistic description of the development of an electromagnetic cascade is much more complicated. Nowadays, this is mainly done by Monte Carlo simulations (cf. chapter 4). An accurate description is e.g. needed for the understanding of detector responses or to determine the lateral extent of the cascade. The latter can be characterised by the *Molière radius* R_M with [1, 54, 63]

$$R_M \approx X_0 \cdot \frac{21\,\text{MeV}}{E_c}. \tag{2.30}$$

As it is proportional to the radiation length X_0, the Molière radius behaves for material layers, mixtures, and chemical compounds like X_0 does. It is found that 90 %/95 % of the cascade is contained in a cylinder around its axis with a radius of [1, 54, 63]

$$r_{90\%} = R_M \qquad r_{95\%} = 2 \cdot R_M.$$

Typical values of the radiation length X_0 and the Molière radius for electrons (which can easily be converted to values for other particles, cf. paragraph "Bremsstrahlung" of sub-

[10] Here the "geometric series" has been used.

section 2.1.3) can be found in [55]. For electrons/photons, the radiation length X_0 is $\approx 43\,\text{cm}$ in typical organic scintillators (PVT) and 0.89 cm in the inorganic scintillator lead tungstate (PWO), which is one reason why the latter is e.g. used in the electromagnetic calorimeter (ECAL) of the CMS experiment [36].

2.4.2. Hadronic

When high-energy hadrons traverse matter and perform *strong interactions*, they create new hadrons. As long as their energy is high enough, these secondary hadrons create new hadrons, too. Thus, hadronic cascades develop, similar to the electromagnetic cascades.

The description of hadronic cascades is more complicated than the description of electromagnetic cascades and is also mainly done by Monte Carlo simulations nowadays. It is found that the extent of a hadronic cascade can be described by the nuclear interaction length λ_I (cf. subsection 2.3.1), which is much larger than the radiation length X_0 for most materials used in detectors. For the energy range of a few GeV to a few 100 GeV, the material thickness that is needed to absorb 95 % of the cascade can be approximated by [62]

$$x_{95\%} \approx x_\text{max} + 2.5\,(E/\text{GeV})^{0.13}\,\lambda_\text{I}, \tag{2.31}$$

with the position of the cascade's maximum

$$x_\text{max} \approx (0.2\ln(E/\text{GeV}) + 0.7)\,\lambda_\text{I}.$$

This approximation agrees with experimental data within 10 %. An alternative approximation is [62]

$$x_{95\%} \approx (1 + 1.35\ln(E/\text{GeV}))\,\lambda_\text{I}.$$

As $x_{95\%}$ varies between $6.2\,\lambda_\text{I}$ and $10.3\,\lambda_\text{I}$ for 100 GeV and 1 TeV hadrons, respectively, HCALs have to be constructed from materials that possess as low λ_I-values as possible, e.g. by using a sampling calorimeter design. For the lateral extent of the cascade it can be approximated that 95 % of the cascade is contained in a cylinder around its axis with a radius of

$$r_{95\%} \approx \lambda_\text{I}. \tag{2.32}$$

Typical values of λ_I are $\approx 79\,\text{cm}$ and $\approx 20\,\text{cm}$ [55] for organic scintillators (PVT) and inorganic scintillators (PWO), respectively. From this point of view, inorganic scintillators would be the preferable choice for hadronic calorimeters. Nevertheless, hadronic calorimeters are usually designed as *sampling calorimeters* with alternating (high-density) absorber (e.g. $\lambda_{\text{I, copper}} \approx 15\,\text{cm}$) and (organic) scintillating layers. This fact has various reasons, like the lower costs and better shaping properties of organic scintillators or the improved depth information of sampling calorimeters.

The secondary hadrons are mainly charged and neutral pions and only to a minor degree kaons, protons, neutrons, and other hadrons. About one third of these secondary particles are neutral pions, which quickly decay into two high-energy photons and thereby trigger

electromagnetic sub-cascades in the hadronic cascade. Therefore, hadronic cascades have an *electromagnetic fraction*, which can be approximated as [1, 62, 63]

$$f_{\mathrm{em}} = 1 - \left(\frac{E}{E_0}\right)^{k-1}, \tag{2.33}$$

where E is the initial energy of the primary hadron, E_0 is the minimal necessary energy for inelastic interactions and varies between 0.7 GeV (for iron) and 1.3 GeV (for lead) [63], and the parameter k varies between 0.80 and 0.87 [1], depending on the mean neutral pion multiplicity and the energy loss due to neutral pions in a single interaction. Both parameters have to be obtained experimentally for a given calorimeter configuration.

Additionally, a fraction f_{ion} of the energy within a hadronic cascade is deposited via electromagnetic interactions of the charged hadrons and another fraction f_{inv} cannot be detected because of escaping neutral particles and muons or as energy is used to overcome nuclear binding energies. The invisible fraction can be estimated to $f_{\mathrm{inv}} \approx 20\,\%$ to $40\,\%$ [1, 63], depending on the material and the initial particle energy.

2.5. Behaviour of Optical Photons at Surfaces

Additionally to the interactions that have been described before, there are other effects that photons undergo within matter: the *optical effects* like *refraction* and *reflection* at surfaces between different materials. These effects are especially important for photons with energies/wavelengths in the optical range ($\sim 1.5\,\mathrm{eV}$ to $\sim 3.1\,\mathrm{eV}$ or $\sim 400\,\mathrm{nm}$ to $\sim 800\,\mathrm{nm}$), which can be created because of Cherenkov radiation as well as wavelength-shifting and scintillation effects (cf. subsections 2.1.3, 3.2.1, 3.2.2) during the traversal of charged particles through matter. Optical effects occur in the *wave description* of electromagnetic radiation and cannot be explained in its particle description, similar to diffraction and interference effects.

The magnitude of refraction and reflection of electromagnetic waves depends on the *refractive index* n of the material in which the wave is propagating. In **macroscopic** description, the speed of light (i.e. the phase velocity v_{phase} of electromagnetic waves) is lower in material than in vacuum. As the photon energy $E_\gamma = h\nu$ and momentum $p_\gamma = {}^{E_\gamma}/_{c} = {}^{h\nu}/_{c}$ do not change, the wave's frequency ν has to stay the same and thus its wavelength λ has to change:

$$\nu = \frac{v_{\mathrm{phase,\,vac}}}{\lambda_{\mathrm{vac}}(\nu)} = \frac{v_{\mathrm{phase,\,mat}}}{\lambda_{\mathrm{mat}}(\nu,\, v_{\mathrm{phase,\,mat}})}. \tag{2.34}$$

Microscopically (cf. e.g. [64]), the electromagnetic wave causes forced oscillations of the atomic electrons. These *induced oscillating dipoles* then emit electromagnetic waves with the same frequency ν, wavelength λ_{vac}, and phase velocity $v_{\mathrm{phase,\,vac}}$ as the original wave, but with a *phase delay*. The superposition of the original wave with its secondary waves creates a new effective wave with the same frequency. As illustrated in figure 2.7, with each new atomic layer that emits new secondary waves inside the material, the phase shift between the original and the effective wave continuously changes. This corresponds to a

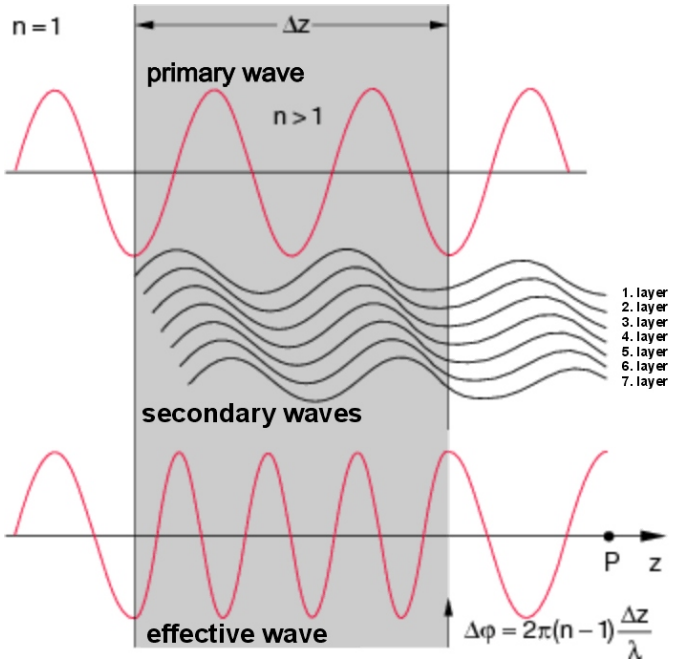

Figure 2.7.: Illustration of the microscopic origin of the refractive index (adapted from [67]): Secondary waves are emitted by oscillating dipoles, which have been induced by the original wave. The superposition of the original wave with the increasing number of secondary waves causes an increasing phase shift between the effective and the original wave, i.e. a difference in wavelength and thus (because of the constant frequency) a different speed of light in matter.

deviation between the wavelength λ_{mat} of the effective wave and the original wave[11] and is equivalent to a phase velocity of the effective wave $v_{\text{phase, mat}}$ inside the material that differs from the vacuum phase velocity (cf. equation (2.34)).[12] Outside, behind the material, no further secondary waves are emitted and the effective wave returns to its vacuum velocity and wavelength again.

The proportional factor between $v_{\text{phase, vac}} = c$ and $v_{\text{phase, mat}}$ is the refractive index [66]:

$$n(\nu) = \frac{c}{v_{\text{phase, mat}}(\nu)} = \frac{\lambda_{\text{vac}}(\nu)}{\lambda_{\text{mat}}(\nu,\, v_{\text{phase, mat}})}.$$

The refractive index (or other optical properties) can often also be found as a function of λ. In this case, λ always represents the wavelength in vacuum λ_{vac} rather than λ_{mat}.

In the microscopic model, it is possible to determine the refractive index by approximating the atomic electrons as *harmonic oscillators* (cf. e.g. [64] or [68]). This allows for explaining the frequency dependence of the refractive index and leads to [69]

$$n^2(\omega) = 1 + \frac{e^2}{\epsilon_0 m_{\text{e}}} \sum_j \frac{N_j}{\omega_j^2 - \omega^2 + i\gamma_j\omega} = 1 + \frac{e^2}{\epsilon_0 m_{\text{e}}} \sum_j \frac{N_j \left(\omega_j^2 - \omega^2 - i\gamma_j\omega\right)}{\left(\omega_j^2 - \omega^2\right)^2 - (\gamma_j\omega)^2} \tag{2.35}$$

[11] Helpful animation (with German explanations) illustrating this effect can be found here: [65].
[12] The velocity of the individual superposing waves, which form the effective wave, remains unchanged and equals c also within material.

with $\omega = 2\pi \cdot \nu$. Here, e is the electron's charge and j represents electrons with different resonance frequencies ω_j[13], damping constants γ_j, and number N_j of electrons per unit volume. As equation (2.35) consists of a real and an imaginary part, the refractive index can be written as [69]:

$$n(\omega) = n'(\omega) - ik(\omega). \tag{2.36}$$

It can be shown (c.f. e.g. [64]) that the *real part* n' is responsible for the different *phase velocity* in matter, i.e. for dispersion and refraction, whereas the *imaginary part* k is responsible for the *attenuation* of the wave, i.e. for absorption.

The general behaviour of n' and k are illustrated in figure 2.8, using the example of water. For transparent materials, i.e. for frequency ranges on which the material is transparent, the refractive index is a monotonically increasing function of the photon frequency [71]:

$$\frac{\mathrm{d}n'}{\mathrm{d}\omega} \geq 0. \tag{2.37}$$

This behaviour is referred to as *normal dispersion*. The contrary case is called anomalous dispersion and occurs in frequency regions of resonant absorption. These appear for electromagnetic waves with frequencies ω that match the resonance frequency ω_j of the atomic electrons. For electromagnetic waves with frequencies that are far off ω_j, the refractive index tends to one[14], i.e. there is no or only little effect. Therefore, they are referred to as optical effects, as they mainly play a role for *optical photons* (which happen to possess the "right" frequencies).[15]

At the surface between two regions with different refractive indices, a part of the electromagnetic wave is reflected and the other part is refracted. This change of direction can be understood by the *Huygens-Fresnel principle* [74, 75]: When being hit by an electromagnetic wave, the surface (as every point of the wave front) emits new so-called elementary waves. In case of reflection, these elementary waves propagate with the same phase veloc-

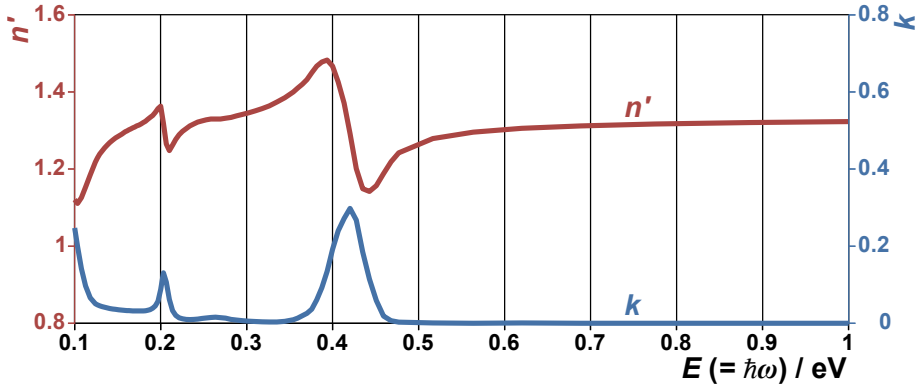

Figure 2.8.: The complex refractive index of water for the energy range from 0.1 eV to 1 eV (adapted from [70]): The red curve represents the real part n', the blue curve illustrates the imaginary part k.

[13] For conductive surfaces, the resonance frequencies ω_j approaches 0.

[14] More correctly, for $\omega \gg \omega_j$, the refractive index becomes $n(\omega) = \sqrt{1 - (\omega_\mathrm{p}/\omega)^2}$ [69], cf. e.g. aluminium (figure D.4).

[15] In fact, the optical effect can also be used for "non-optical" photons but with a much smaller impact, e.g. for refractive x-ray lenses (cf. e.g. [72] and [73]).

ity as the original wave front and thus form a reflected wave that departs from the surface under the same angle as the original wave approached. In case of refraction, the elementary waves propagate with a different phase velocity and thus the new wave that they form has a different direction than the original wave. Figure 2.9 illustrates these effects.

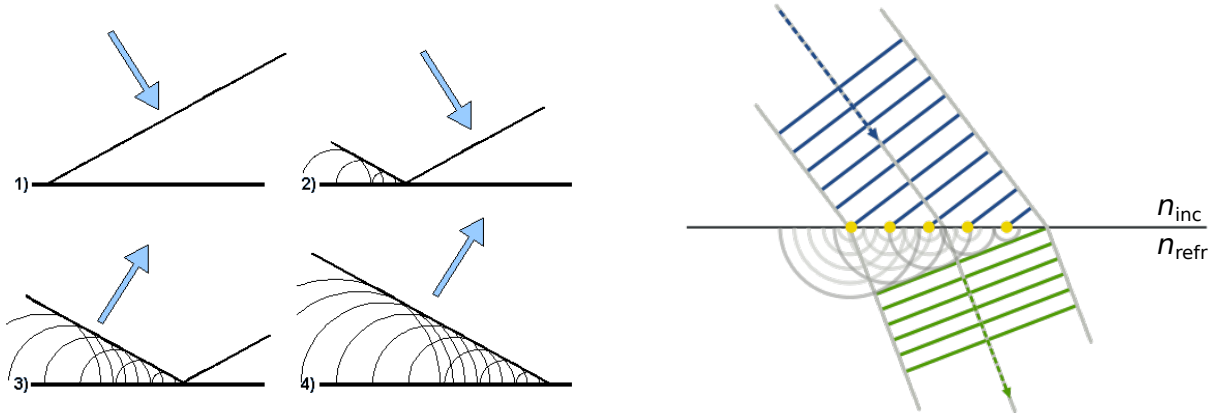

(a) (b)

Figure 2.9.: Huygens-Fresnel principle to depict the behaviour of electromagnetic waves when being reflected **(a)** or refracted **(b)** at surfaces. Taken from [75].

The rules for the change of the direction of the electromagnetic wave in case of refraction and reflection as well as the fraction of reflected and refracted wave intensity (i.e. the probability that a single photon is reflected or refracted in the particle description) can be derived from the Maxwell equations (cf. e.g. [76]). The well-known results[16] are the *reflection law* between the reflection angle α_{refl} and the incidence angle α_{inc}:

$$\alpha_{\text{refl}} = \alpha_{\text{inc}}, \tag{2.38}$$

Snell's law[17] between the refraction angle α_{refr} and the incidence angle α_{inc}

$$n_{\text{refr}} \sin \alpha_{\text{refr}} = n_{\text{inc}} \sin \alpha_{\text{inc}}, \tag{2.39}$$

and the *Fresnel equations*[18,19], describing the fraction R of the reflected and the fraction T of the refracted (= transmitted) wave intensity [76]:

$$\begin{aligned} R_{\parallel} &= \frac{\left|E_{\parallel\,\text{refl}}\right|^2}{\left|E_{\parallel\,\text{inc}}\right|^2} = \left|\frac{n_{\text{refr}} \cos \alpha_{\text{inc}} - n_{\text{inc}} \cos \alpha_{\text{refr}}}{n_{\text{refr}} \cos \alpha_{\text{inc}} + n_{\text{inc}} \cos \alpha_{\text{refr}}}\right|^2 \\ R_{\perp} &= \frac{\left|E_{\perp\,\text{refl}}\right|^2}{\left|E_{\perp\,\text{inc}}\right|^2} = \left|\frac{n_{\text{inc}} \cos \alpha_{\text{inc}} - n_{\text{refr}} \cos \alpha_{\text{refr}}}{n_{\text{inc}} \cos \alpha_{\text{inc}} + n_{\text{refr}} \cos \alpha_{\text{refr}}}\right|^2 \\ R &= \frac{\left|E_{\parallel\,\text{refl}}\right|^2 + \left|E_{\perp\,\text{refl}}\right|^2}{\left|E_{\parallel\,\text{inc}}\right|^2 + \left|E_{\perp\,\text{inc}}\right|^2} = \frac{R_{\parallel}\left|E_{\parallel\,\text{inc}}\right|^2 + R_{\perp}\left|E_{\perp\,\text{inc}}\right|^2}{\left|E_{\parallel\,\text{inc}}\right|^2 + \left|E_{\perp\,\text{inc}}\right|^2} \end{aligned} \tag{2.40}$$

[16] For these equations, the angles are measured from the perpendicular and not from the surface itself.
[17] Snell's law is in principle valid for complex refractive indices. Whereas only the real version of the equation has a physical meaning, the complex version can e.g. be used for mathematical transformations.
[18] To obtain correct results, the Fresnel equations have to be used with complex refractive indices, unless the refractive indices' imaginary part is negligible.
[19] The Fresnel equations in this form are valid for all surfaces, also for metal surfaces. [77]

$$
\begin{aligned}
T_{\parallel} &= \left|\frac{n_{\text{refr}}\cos\alpha_{\text{refr}}}{n_{\text{inc}}\cos\alpha_{\text{inc}}}\right| \frac{\left|E_{\parallel\,\text{refr}}\right|^2}{\left|E_{\parallel\,\text{inc}}\right|^2} = \left|\frac{n_{\text{refr}}\cos\alpha_{\text{refr}}}{n_{\text{inc}}\cos\alpha_{\text{inc}}}\right| \left|\frac{2n_{\text{inc}}\cos\alpha_{\text{inc}}}{n_{\text{refr}}\cos\alpha_{\text{inc}} + n_{\text{inc}}\cos\alpha_{\text{refr}}}\right|^2 \\
T_{\perp} &= \left|\frac{n_{\text{refr}}\cos\alpha_{\text{refr}}}{n_{\text{inc}}\cos\alpha_{\text{inc}}}\right| \frac{\left|E_{\perp\,\text{refr}}\right|^2}{\left|E_{\perp\,\text{inc}}\right|^2} = \left|\frac{n_{\text{refr}}\cos\alpha_{\text{refr}}}{n_{\text{inc}}\cos\alpha_{\text{inc}}}\right| \left|\frac{2n_{\text{inc}}\cos\alpha_{\text{inc}}}{n_{\text{inc}}\cos\alpha_{\text{inc}} + n_{\text{refr}}\cos\alpha_{\text{refr}}}\right|^2 \\
T &= \left|\frac{n_{\text{refr}}\cos\alpha_{\text{refr}}}{n_{\text{inc}}\cos\alpha_{\text{inc}}}\right| \frac{\left|E_{\parallel\,\text{refr}}\right|^2 + \left|E_{\perp\,\text{refr}}\right|^2}{\left|E_{\parallel\,\text{inc}}\right|^2 + \left|E_{\perp\,\text{inc}}\right|^2} = \frac{T_{\parallel}\left|E_{\parallel\,\text{inc}}\right|^2 + T_{\perp}\left|E_{\perp\,\text{inc}}\right|^2}{\left|E_{\parallel\,\text{inc}}\right|^2 + \left|E_{\perp\,\text{inc}}\right|^2}.
\end{aligned}
\tag{2.41}
$$

Here "$\parallel$" refers to the parts of the electromagnetic wave that are polarised parallel to the surface, whereas "$\perp$" refers to the parts polarised perpendicular to the surface.

Additionally, a result of equation (2.39) is the *total reflection* of an electromagnetic wave in case of $n_{\text{inc}} > n_{\text{refr}}$, if the incidence angle equals or exceeds the critical angle

$$
\alpha_{\text{crit}} = \arcsin\left(\frac{n_{\text{refr}}}{n_{\text{inc}}}\right). \tag{2.42}
$$

In this case, the reflectivity is 100 %, independent of the Fresnel equations. This is an important effect for *loss-less light trapping* and *guiding* in optical detector parts (cf. section 3.2).

3. Particle Detection and Optical Detector Elements

In the previous chapter, the interactions of particles traversing matter have been presented. They provide the physical basis for the detection of such particles with a detector. This chapter will summarise the general working principle of modern particle detectors and introduce their optical detector elements, which are used for particle detection nowadays.

Due to the variety of factors influencing these components, the detailed understanding of their response requires detailed simulations (cf. chapter 4). This is particularly true for optical detector components with their potentially low light yield.

3.1. Principles of modern Particle Detectors

The detector design critically depends on several factors, such as the *type of particles* that are to be detected, the *detector's task* (i.e. the observables that are to be determined), the *environment* the detector has to work in (e.g. high or low radiation rates), appropriate *material or component combinations*, *geometrical restrictions*, and *expenses*. Hence, some representative detector designs will be presented in the section, using representative examples. These detector designs have in common that *optical detector components* play an important role in all of them.

Vertex-Enclosing Detectors

The Compact Muon Solenoid (CMS) [10] and (Time-of-Flight) Positron Emission Tomography ((ToF-)PET) scanners [29] are examples of detectors that are built around the source (vertex) of the particles to be detected.

CMS is a multi-purpose detector, which is operated at the Large Hadron Collider (LHC) [11], a proton-proton collider ring at CERN [9]. The primary purpose of CMS is to find physics beyond the Standard Model by examining particle collisions. For that purpose, all particles have to be detected, identified, and their properties have to be determined. This is basically achieved by particle tracking, momentum determination, energy determination and muon tagging. As the full particle spectrum in a wide energy range (from few GeV to few TeV) is expected to occur within CMS, this purpose can only be satisfied with a detector design that

consists of several layers, which are (in the particles' direction of flight): particle tracker, ECAL, HCAL, magnet coil (for momentum determination via trajectory bending), and muon detector. Because of the fact that all particles originate from the interaction point of the colliding beams, the detector layers of CMS are arranged onion-skin-like around it. This is illustrated in figure 3.1(a). The detector was designed to be as hermetic as possible, but it is not fully hermetic because of geometrical restrictions, e.g. by the beam pipe of the collider ring, by cabling and mechanical support, or by the composition of the full detector from several detector sectors.

Within many parts of the CMS detector, optical components can be found [21, 36]: The ECAL consists of the inorganic scintillator PWO and the HCAL contains the PS-based and PVT-based organic scintillators SCSN-81 (Kuraray) and BC-408 (Saint-Gobain [78]), respectively. The very-forward detector parts are located within a very high radiation environment and thus, no scintillators but radiation-hard quartz fibres are used to detect traversing particles via Cherenkov radiation. Combinations of WLS fibres and light-guiding fibres are used to collect the light from the active optical detector volumes and to allow for a spatial separation of them and their readout modules with the photodetectors. The latter is necessary in order to keep the detector as compact as possible.

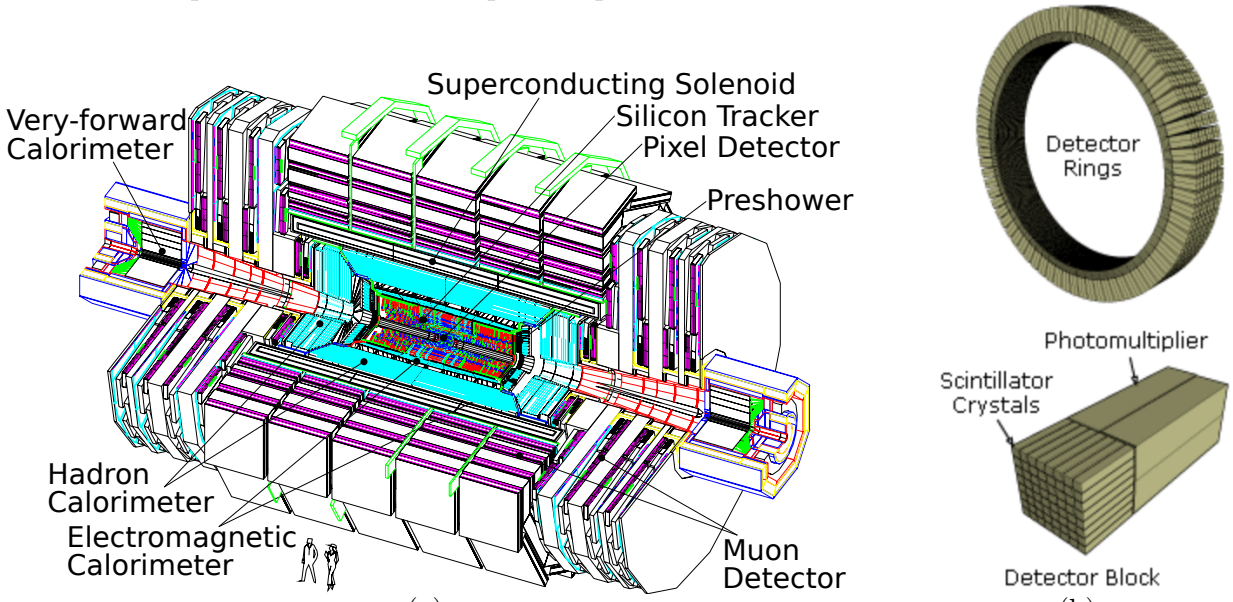

Figure 3.1.: Schematic illustration of the detector design of **(a)** the CMS detector (adapted from [36]) and **(b)** medical (ToF-)PET-scanners (adapted from [79]).

(ToF-)PET scanners are particle detectors used in medical imaging. A positron-emitting radioactive isotope is introduced into the part of the (human) body that is to be visualised. The emitted positrons annihilate with electrons of the tissue and two photons are created, each with an energy of 511 keV and departing from the interaction point back-to-back. By identifying pairs of photons that fulfil these features, the interaction points can be reconstructed and thus a three-dimensional visualisation of the isotope's distribution within the body can be generated. As only photons (of a specific energy) need to be detected, (ToF-)PET scanners usually only consist of a calorimeter, which is able to absorb the photons and measure their energy. The calorimeter parts form a detector ring (cf. figure 3.1(b)) to allow for the detection of both photons belonging to a pair. This detector design is far

from being hermetic, simply because there has to be enough free space reserved for the patient. At a justifiable radiation exposure of the patient, this dramatically limits the event rate that (ToF-)PET scanners can obtain. The calorimeter parts usually consist of the inorganic scintillators LSO (Lu_2SiO_5), LYSO ($Lu_{1.8}Y_{0.2}SiO_5$), or LaBr(Ce) and are readout by PMTs or SiPMs [29]. As the calorimeter is the only detector part, there is usually no necessity to separate the active detector volumes and the photodetectors.

Vertex-Non-Enclosing Detectors

A different detector design is used, if it is not necessary or not possible to build the detector around the particle source. Examples are the LHCb [12] and the Alpha Magnetic Spectrometer (AMS-02) [6].

LHCb is another detector located at the LHC, but it does not need to cover the full particle spectrum. It concentrates on b-mesons, which mostly traverse close to LHC's beam pipe after they have been created in the proton-proton collisions. Therefore, the detector layers of LHCb do not surround the interaction point, but have only been installed close to the beam pipe (cf. figure 3.2(a)). Optical components can be found in the calorimeters (organic scintillator, WLS fibres, and PMTs), the RICH (radiators, mirrors, and HPDs creating, collecting, and detecting Cherenkov radiation), and in the tracker (after the planned upgrade: scintillating fibre tracker with SiPMs).

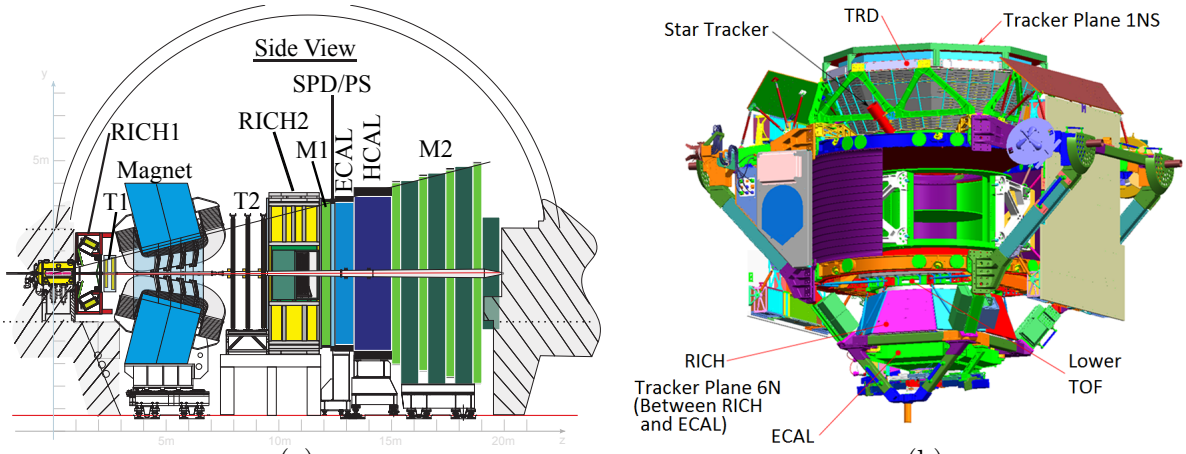

(a) (b)

Figure 3.2.: **(a):** Schematic illustration of the detector design of the LHCb detector (adapted from [38]) containing Ring Imaging Cherenkov detectors (RICH1, RICH2) for particle identification, the tracker system (T1, T2), the electromagnetic and hadronic calorimeters (ECAL, HCAL) with their trigger detectors Scintillating Pad Detector (SPD) and Preshower (PS), and the muon system (M1, M2). **(b):** Schematic illustration of the detector design of the AMS-02 detector (adapted from [6]) with the Transition Radiation Detector (TRD) for $e^{\pm}$ identification, the Time-of-Flight System (ToF) for triggering purpose, the tracker system, the Ring Imaging Cherenkov detector (RICH) for particle identification, and the electromagnetic calorimeter (ECAL).

AMS-02 is located on the International Space Station (ISS) and searches for high-energy cosmic rays. Therefore, there is no defined interaction point, i.e. a vertex-enclosing detector design is not possible and AMS-02 restricts itself to a limited field of view (cf. figure 3.2(b)). The heavier particles are identified by combining the information of the tracker, the ECAL, and the RICH detector, thus no HCAL or muon system is necessary. Nevertheless, optical detector components are contained in several parts of AMS-02: organic scintillators in the Time-of-Flight System and the Anti-Coincidence Counter, scintillating fibres in the ECAL, WLS and light-guiding fibres in the Anti-Coincidence Counter, and radiators and mirrors in the RICH.

Large-Scale Detectors

The Pierre Auger Observatory [43] and the IceCube experiment [31] are examples for a detector design that is used if normal-size detector volumes are insufficient.

The **Pierre Auger Observatory** is a surface-based detector for ultra high-energy cosmic rays ($10^{17}\,\text{eV} \leq E \leq 10^{21}\,\text{eV}$). High-energy cosmic particles colliding with atmospheric particles initiate cascades of secondary particles. These atmospheric showers can e.g. be investigated by detecting the secondary particles that reach the ground distributed over an area of few km^2 or the fluorescence light of air molecules that have been excited during the shower. Each alternative allows for the determination of the initial energy of the primary particle. The Pierre Auger Observatory is located in Argentina, near the city of Malargüe, and combines 27 fluorescence telescopes surveying the sky and 1660 water-Cherenkov-tanks, which cover about $3000\,\text{km}^2$ with a distance of 1.5 km between each other. This is illustrated in figure 3.3(a). Inside the water-filled tanks, traversing charged secondary particles from the atmospheric showers create Cherenkov radiation, which is detected by PMTs. The active detector volume of the fluorescence telescopes is the atmosphere itself, the optical fluorescence photons are collected via mirrors and detected by PMTs.

The purpose of the **IceCube** experiment is to detect cosmic neutrinos and determine their origin in the universe. Neutrinos can only be detected via charged secondary particles from

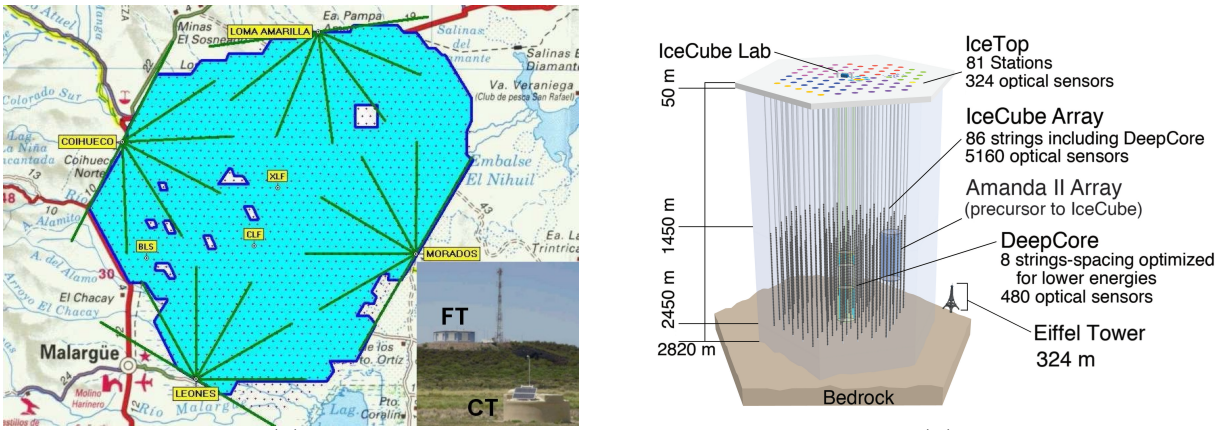

(a) (b)

Figure 3.3.: Schematic illustration of the detector design of **(a)** the Pierre Auger Observatory (with its fluorescence telescopes (FT) and water-Cherenkov-tanks (CT), adapted from [80]) and **(b)** the IceCube detector (adapted from [31]).

(weak, cf. subsection 2.3.2) neutrino interactions. As neutrino interactions are extremely unlikely, very large sensitive detector volumes are needed. Therefore, IceCube is located at the South Pole, using $1\,\mathrm{km}^3$ of ice as detector volume. Inside this volume, high-energy charged secondary particles are created from neutrino interactions with water molecules. At the same time, the ice volume is the active optical detector volume, creating optical photons by Cherenkov radiation of the charged secondary particles. To detect these optical photons, the ice is interspersed with optical sensors containing PMTs. This setup allows to count neutrinos as well as reconstructing their flight direction.

Obviously, the detector design of both detectors strongly differs from the previously introduced designs, which is caused by the specialisation on atmospheric shower or neutrino detection as well as the enormous dimensions of the detector.

As these examples show, particle detectors often utilise a *variety of optical components*, independent of the actual detector design. The most common and important optical components are introduced in the following section. In this field, a large amount of technological and scientific development has been done in the past years and is still continuing (e.g. [81–89]). These developments make scintillators, optical fibres and optical photodetectors (especially SiPMs) a very good and widely-used choice for particle detection nowadays.

3.2. Optical Detector Elements

After this synopsis of the working principle of modern particle detectors, now, the optical detector elements that are part of these detectors are presented. The following summary is based on [1, 35, 39] for wavelength-shifting and scintillating materials, [90] for optical fibres, and [1, 39, 41, 42] for photodetectors.

3.2.1. Wavelength-Shifting (WLS) Materials

WLS materials absorb optical photons and then re-emit them with a longer wavelength. This effect is referred to as *photoluminescence*, which is one of two subcategories of *fluorescence* (the other subcategory is scintillation). Figure 3.4(a) illustrates the principle of fluorescence. The absorption of the initial photon excites an electron into a vibrational sub-level (1, 2,...) of a higher energy state (S_1). The electron first de-excites non-radiatively to the vibrational ground level of the excited energy state (S_1). Then it emits a photon when de-exciting to the energetic ground state (S_0), usually to a vibrational excited sub-level. This is the reason, why the material is (partially) transparent to its own emitted light.

The main properties characterising a WLS material are the absorption and emission spectrum, the rise and decay time, and the multiplication factor. The *absorption spectrum* specifies the magnitude of the absorption of incident photons, the emitted photon energy/wave-

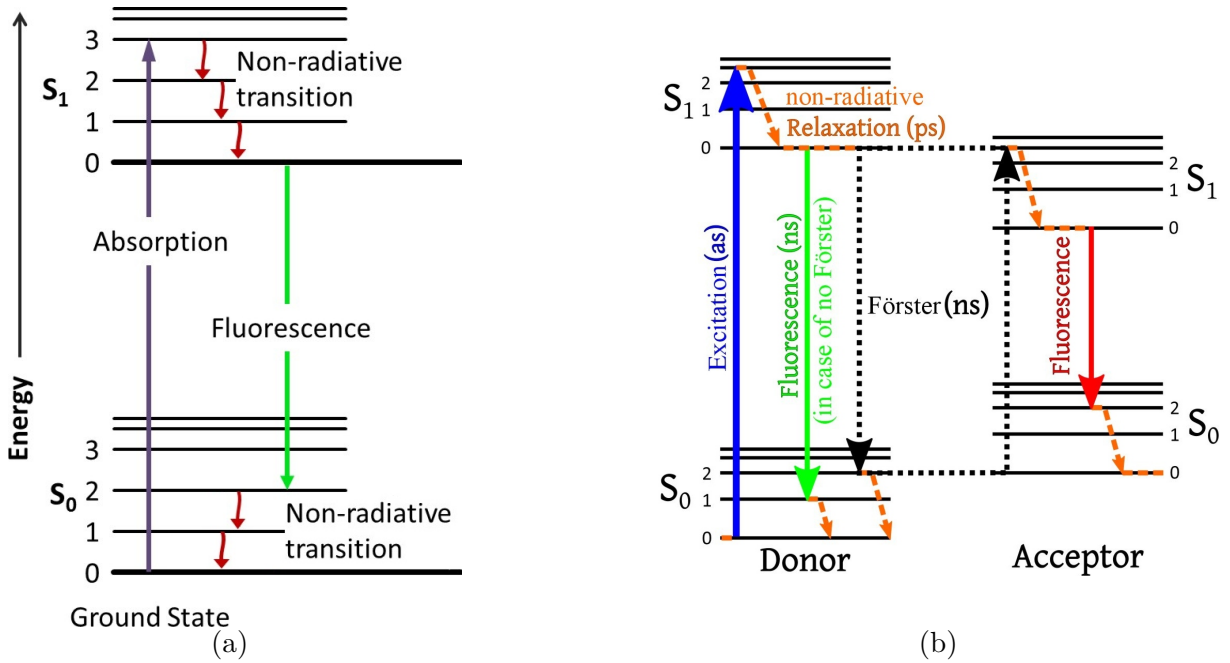

Figure 3.4.: Energy diagrams of the fluorescence process **(a)** and of the Förster resonance energy transfer **(b)** between a scintillator base material (donor) and an included WLS material (acceptor). For all materials, two energy levels (S_0 and S_1) with vibrational sub-levels (0, 1,...) are illustrated. In case of the Förster resonance energy transfer, typical process time scales are stated. The diagrams were adapted from [91] and [92], respectively.

length is distributed according to the *emission spectrum*[20] and the temporal distribution of the photon emission is characterised by a fast rise and the sum of one or more slower exponential decays with different *decay times* (due to different decay paths). The multiplication factor is the number of emitted photons per absorbed photon, which is usually one for the commercial WLS materials.

In particle detectors, WLS materials are used for two different purposes: For one thing, they can be mixed into scintillating materials to improve the scintillator's properties (cf. subsection 3.2.2). Furthermore, they can be used in the form of fibres or bars to collect the scintillation light, shift it to wavelengths more appropriate to the used photodetector, and guide it to the photodetector (cf. subsection 3.2.3).

3.2.2. Scintillating Materials

The energy deposition of charged particles traversing scintillating materials causes excitation of electrons to higher energy states. In the course of the de-excitation, this energy is (partly) emitted in form of optical photons and thus transferred into detectable light. This was detected by eye, until technical devices (which are described later in this chapter) were developed, allowing for their automatised detection. The effect is called *scintillation* and is a subcategory of *fluorescence*.

[20] As the emitted photon cannot possess a higher energy than the corresponding absorbed photon, an overlap of the emission spectrum and the absorption spectrum can result in a shift of the proportions within the emission spectrum. This effect is demonstrated in section 6.1.

The main properties, characterising a scintillating material, are scintillation efficiency, light yield, emission spectrum, and rise and decay time. The *scintillation efficiency* is the ratio between the total energy of the emitted photons and the total energy deposition of the traversing particle in the scintillating material. The *light yield* $\mathscr{L}$, which is stated for scintillation material, is the mean number of emitted photons N_γ per deposited energy ΔE, the actual light yield distribution is following a Gaussian distribution around this mean value. The emitted photons' energy/wavelength is distributed according to the *emission spectrum* and the temporal distribution of the photon emission is characterised by a fast rise and the sum of one or more slower exponential decays with different *decay times*. Additionally to the scintillator properties, the material also has to be transparent to its own scintillation light. As described below, this is usually achieved by the combination of non-radiative and radiative de-excitation processes.

Nowadays, there are several different scintillating materials, which can basically be divided into three classes: *organic*, *inorganic* and *gaseous* scintillators. These are distinguished, as their scintillation processes are caused by different physical mechanisms: electron excitation in molecular bindings (organic scintillators), in a crystal lattice (inorganic scintillators), or in atoms (gaseous scintillators).

Organic scintillators typically possess much shorter decay times than inorganic scintillators, but at the same time the light yield (and thus the energy resolution) is typically significantly higher for inorganic scintillators [78, 93].

Organic Scintillating Materials

In organic scintillators, the scintillation is caused by a **molecular effect**. Special types of organic molecules contain *aromatic rings* (e.g. polystyrene (PS) and polyvinyltoluene (PVT)), which are characterised by the *de-localised electrons* of the π-bond (cf. figure 3.5). Within those, the electrons can be excited to higher energy states by the traversing charged particles. When de-exciting back to the ground state, the energy is partly emitted as a photon and partly non-radiatively via vibrational degradation. The radiative de-excitation happens in general between the non-excited vibrational sub-level of the excited state and the excited vibrational sub-levels of the ground state (cf. figure 3.4(a)). As a consequence, the absorption of the emitted photons by electrons of the non-excited vibrational sub-level of

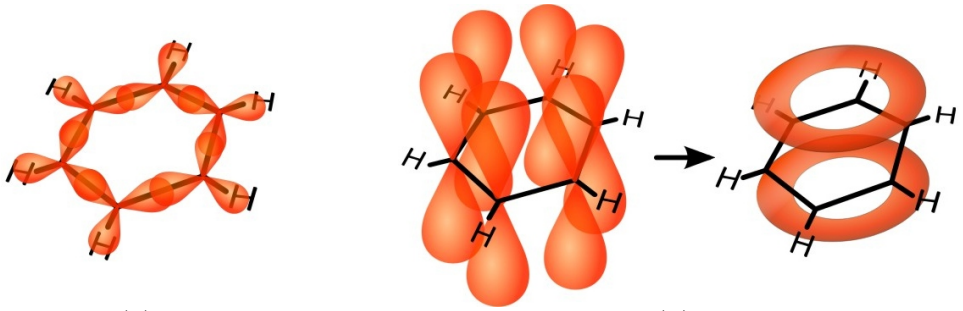

(a) (b)

Figure 3.5.: The electron orbitals contributing to the chemical bond within aromatic rings [94]. The combination of the p-orbitals forming the π-bonds leads to a de-localised orbital containing de-localised electrons **(b)**.

the ground state is highly suppressed, which is the reason for the (partial) transparency of the scintillator base material to its own emitted light. The energy gap between the different states is typically in the range of a few eV, thus the emitted photons of the scintillator base material are in or near the optical range (usually in the near UV-range).

The scintillation decay times of scintillator base materials are in general relatively long (e.g. 16 ns for PS [1]). To reduce the decay time and increase the photon's attenuation length, a secondary material is mixed into the scintillator base material. This secondary material is a WLS material, its absorption spectrum has to overlap with the scintillator base material's emission spectrum and its decay time should be much shorter than the decay time of the scintillator base material. The concentration of the WLS material is chosen as high as necessary (usually around 1 % by weight [1]) so that the average distance between the WLS molecules and the molecules of the scintillator base material is about 100 Å [1]. At this distance, which is much less than the wavelength of the photons that could be emitted, the energy of the scintillator base material's excited state can be transferred very efficiently to the WLS material via *non-radiative dipole-dipole interactions*. This effect is called *Förster resonance energy transfer* [95] and is illustrated in figure 3.4(b). Often, a second WLS material is added with a lower concentration, shifting the light of the first WLS material. For good combinations of the materials, the decay time can be reduced by one order of magnitude and the attenuation length can be increased by a factor of 1000 [1].

According to Birks' widely used *semi-empirical model* [96], the actual light yield of organic scintillators is reduced because of *recombination and quenching effects* between the excited molecules. As these effects have more influence if the density of excited molecules is higher, the response of organic scintillators is not perfectly proportional to the energy deposition of the traversing charged particle. The mean number of photons N_γ per path length x of the charged particle's trajectory within the scintillating material can be approximated with *Birks' equation* [96]

$$\frac{\mathrm{d}N_\gamma}{\mathrm{d}x} = \frac{\mathscr{L} \cdot \left(\frac{\mathrm{d}E}{\mathrm{d}x}\right)_{\text{ion.}}}{1 + C_\mathrm{B} \left(\frac{\mathrm{d}E}{\mathrm{d}x}\right)_{\text{ion.}}} \tag{3.1}$$

$$\Leftrightarrow \quad N_\gamma = \int_{x_\text{in}}^{x_\text{out}} \frac{\mathscr{L} \cdot \left(\frac{\mathrm{d}E}{\mathrm{d}x}\right)_{\text{ion.}}}{1 + C_\mathrm{B} \left(\frac{\mathrm{d}E}{\mathrm{d}x}\right)_{\text{ion.}}} \mathrm{d}x = \int_{E_\text{out}}^{E_\text{in}} \frac{\mathscr{L}}{1 + C_\mathrm{B} \left(\frac{\mathrm{d}E}{\mathrm{d}x}\right)_{\text{ion.}}} \mathrm{d}E.$$

Here, $\mathscr{L}$ is the light yield at a low density of excited molecules[21], $(\mathrm{d}E/\mathrm{d}x)_{\text{ion.}}$ is the particle's mean energy loss due to excitation (cf. equations (2.1) and (2.2)), and C_B is Birks' constant, which has to be determined experimentally for each scintillating material. For the plastic scintillator BC-408 [78] with $C_\mathrm{B} = 0.0115 \, \frac{\mathrm{g}}{\mathrm{MeV cm^2}}$ [97], typical values of $1/\left(1 + C_\mathrm{B} \left(\frac{\mathrm{d}E}{\mathrm{d}x}\right)_{\text{ion.}}\right)$ are 91.7 %, 97.8 %, and 96.7 % for muons with $E_\text{kin} = 10\,\mathrm{MeV}$, $E_\text{kin} = 325\,\mathrm{MeV}$ (MIP), and $E_\text{kin} = 1.19\,\mathrm{TeV}$ (E_crit), respectively.

The decay times of organic scintillators are in the range of a few ns and the rise times are even much shorter. Thus, they provide a good time resolution [1] and are fast enough to be used in applications with high event rates, e.g. at the LHC. The emission spectra are in the optical range, with peak wavelengths between 350 nm and 500 nm [35].

[21] $\mathscr{L}$ is the light yield that is typically specified by the manufacturers.

Organic scintillators can be divided into three subtypes: *crystalline*, *liquid*, and *plastic*. Because of the fact that plastic scintillators can easily be produced in any desired shape, plastic scintillators are the commonly used scintillator type in high-energy physics, whereas organic crystalline scintillators are practically unused. As organic scintillator molecules consist mainly of carbon and hydrogen, they efficiently absorb fast neutrons, the Compton effect dominates for high-energy photons (low Z, cf. figure 2.5), and the energy loss of charged particles is relatively low (low ρ and low A, cf. equations (2.1) and (2.2)). Thus, if used in calorimeters, organic scintillators have to be combined with absorber materials leading to a faster cascade development.

Inorganic Scintillating Materials

In inorganic scintillators, the scintillation is caused by a **lattice effect**. The crystal lattice forms an energetic *valence band*, containing the bound electrons, and an energetic *conduction band*, which allows for quasi-free movement of the electrons through the crystal (cf. figure 3.6). The two energy bands are separated by a gap E_g of a few eV. The electrons of the valence band can be excited to the conduction band by traversing charged particles, leaving a hole in the valence band. Then the electron and the hole either move independently through the crystal or they form a bound state (called exciton), which has slightly less energy and can also move through the crystal. In any case, they transfer the energy to *activation centres* (lattice defects) when reaching them. Thus, these activation centres are transformed into an excited state and de-excite either radiatively or non-radiatively (via lattice vibrations). This causes a certain fraction of the deposited energy to be re-emitted as photons. Whereas some crystals are intrinsic scintillators (e.g. BaF_2, BGO ($Bi_4Ge_3O_{12}$), CeF_3, or PWO), others have to be doped with fluorescent ions acting as activation centres (e.g. CsI(Tl), LiI(Eu), or NaI(Tl)).

In inorganic scintillators, the mean number of scintillation photons per path length of the charged particle's trajectory within the scintillating material can be approximated as proportional to the mean energy loss of the traversing charged particles. However, for very low particle energies ($< 1\,\mathrm{MeV}$ [1]), non-proportionality becomes important and has to be considered.

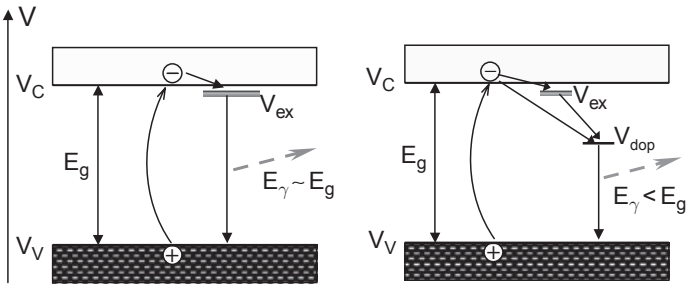

Figure 3.6.: Diagram of the energy bands of inorganic scintillators [39]. V indicates energy levels, V_V is the upper limit of the valence band, V_C is the lower limit of the conduction band, V_ex is the energy level of excitons, V_dop is the energy level of potential doped activation centres, E_G is the energy gap between valence band and conduction band, and E_γ is the energy of emitted photons.

Compared to organic scintillators, inorganic scintillating materials possess high densities ρ, high atomic numbers A, and high proton numbers Z. This results in a higher energy loss per path length for charged particles (cf. equations (2.1) and (2.2)) and a better absorption of high-energy photons (cf. equations (2.20), (2.22), (2.24) and (2.25)). Therefore, they are often used if charged particles or high-energy photons have to be absorbed completely and the energy has be measured precisely at the same time. This is for example the case with the ECAL in particle physics experiments (like e.g. in CMS [36] at LHC) or in other applications (e.g. PET detectors [29]).

The emission spectra of inorganic scintillators are in the optical range, with peak wavelengths between 200 nm and 550 nm [1, 35, 39]. But, in contrast to the organic scintillators, the shape of the light pulses of inorganic scintillating materials is characterised by a very fast rise time and the sum of two exponential decays with different *decay times*. The fast decay time is in the range of ~ 1 ns to ~ 100 ns [1, 39], whereas the slow decay time can be up to ~ 1 ms [1, 39]. Thus, inorganic scintillators can be much slower than organic ones. The fraction of the light emitted with the slow decay time is a property of the material itself.

As the inorganic scintillating materials are crystalline, they suffer from defects in the crystal lattice. Such defects can be induced by radiation, thus the inorganic scintillating materials suffer heavily from *radiation damage*. It results in a reduction of the attenuation length (due to new scattering centres) as well as the reduction of the light yield (due to damage to the activation centres).

Gaseous Scintillating Materials

In gaseous scintillating materials, the scintillation is caused by an **atomic effect**. Traversing charged particles excite the atomic electrons, which de-excite by emitting radiation. The decay times reach values that are comparable to organic scintillators and the intensity of the emitted light is relatively low, because of the low material density. Nevertheless, liquid gases (e.g. liquid Ar[22], Kr, and Xe) can keep up with organic and inorganic scintillators with respect to the density (cf. e.g. [55]) and thus also with respect to the light yield. However, the detection of the scintillation light of gaseous scintillators is difficult, as their emission spectra have peak wavelengths between 130 nm and 175 nm [35].

3.2.3. Optical Fibres

Optical fibres can be used to collect light from optical detector elements (e.g. scintillator volumes) and transport it to a photodetector. They typically consist of a *core* and one or two *claddings*, as well as an absorbing coating if necessary. The materials of these components are chosen in a way that the refractive index decreases from the core to the outer edge. This allows to capture light inside the fibre by *total internal reflection* (cf. section 2.5). Light that is not captured by total internal reflection will lose intensity with every reflection and thus in general does not have a significant effect on the signal at the fibre's ends. Thus, the

[22] Liquid argon is e.g. used in the calorimeters of the ATLAS experiment [98].

fibre's *trapping efficiency*, i.e. its capability to capture light that has been created within the fibre, is defined as the fraction of light that is captured by total internal reflection.

Although it is possible nowadays to produce fibres with *continuous refractive index profiles* (cf. figure 3.7), normally only fibres with *step refractive index profiles* are used in detectors. This is because the advantages of the continuous refractive index profiles (same optical path length (i.e. same propagations times) on all paths directly connecting two points) mainly work for light that is coupled into the fibre at one end to be transported to the other end, e.g. for data transmission or light-guiding of laser light. But if the light is created inside the fibre, the continuous refractive index profile turns into a disadvantage, as also the trapping efficiency decreases towards the fibre edge, which is not the case for step refractive index profiles.

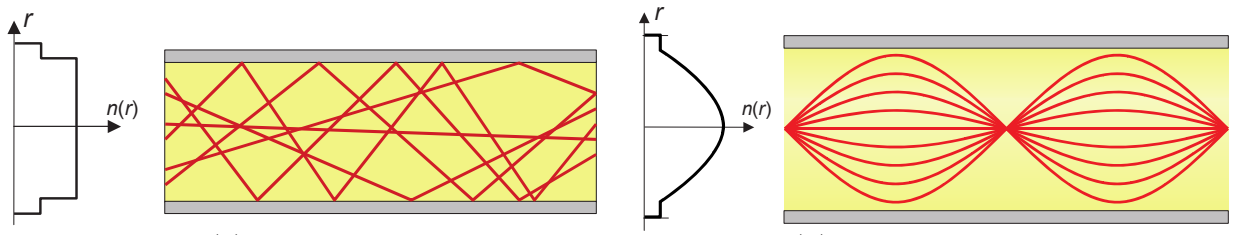

(a) step profile (b) continuous profile

Figure 3.7.: Illustration of different refractive index profiles in optical fibres and their influence on the light rays [90]. The yellow part represents the fibre core and the grey parts are the cladding of the fibre.

In an optical fibre, there are two different types of light rays: *meridional rays*, which cross the fibre axis, and *skew rays*, which do not cross the fibre's axis and whose trajectory therefore has a spiral form. These two types of light rays are illustrated in figure 3.8. Because of the fact that in general skew photons have to traverse longer distances within the fibre material to cover the same fibre distances, their fraction decreases with increasing fibre length.

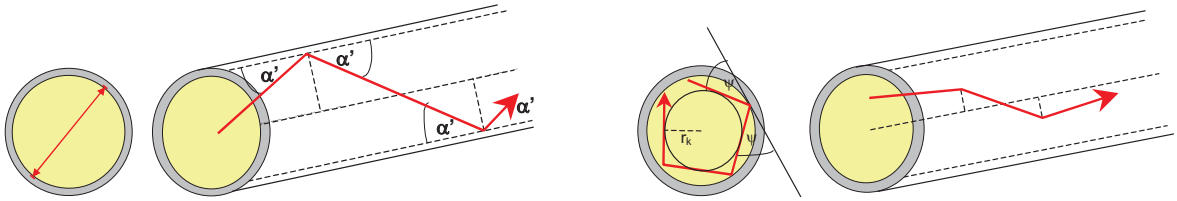

(a) meridional rays (b) skew rays

Figure 3.8.: Illustration of meridional rays (crossing the fibre's axis) and skew rays (not crossing the fibre's axis) in optical fibres [90]. The trajectory of skew rays has a spiral form.

Whereas both types of light rays contribute to the total trapping efficiency, the common calculation of the trapping efficiency **only** considers the **meridional rays**. Furthermore, the surfaces of the fibre are assumed to be perfectly smooth and photons entering the outermost cladding are assumed to be lost. Figure 3.9 illustrates the geometry of the calculation of the trapping efficiency. A detailed description of the trapping efficiency calculation is presented in appendix B. For typical optical fibres, the results vary between $\sim 6.88\,\%$ and $\sim 14.65\,\%$

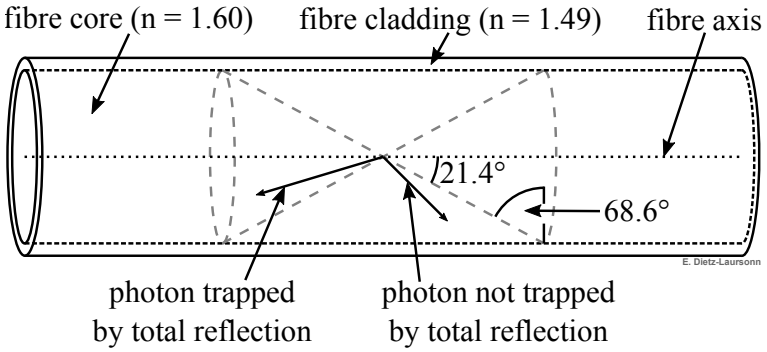

Figure 3.9.: Sketch of a typical optical fibre with one cladding. Light inside the two cones along the fibre axis is captured by total internal reflection and thus contributes to the signal at the fibre's ends.

(for both fibre directions together), depending on the fibre profile (round or square) and the number of claddings. In general, a second cladding increases the trapping efficiency[23] and square fibres have a higher trapping efficiency than round fibres (cf. table B.1). In this context, it should be noted that the calculating the trapping efficiency of square fibres with two claddings results in a too large value, as the cladding geometry is not considered (cf. section 9.1). Apart from that, the constraints of the calculation of the trapping efficiency make the results (which are also stated by the manufacturers) represent the *minimal value* that is achieved. The actual trapping efficiency of an optical fibre depends on several additional factors and can be much higher. These effects are demonstrated in section 9.1. If the trapping efficiency of an optical fibre within a specific setup is to be determined, it should therefore be simulated rather than being calculated or adopted from the manufacturer.

In addition to light losses due to emission of non-trapped light, the effective signal at the fibre's ends is reduced by *absorption* of the photons in the fibre material. The corresponding attenuation lengths are typically in the range of a few metres for scintillating/WLS fibres and up to $\sim 1\,\mathrm{km}$ for special fibres for signal transmission. Thereby, the attenuation length provided by manufacturers is normally the *signal attenuation length*, meaning an effective mean attenuation of the signal containing all possible light paths, rather than the physical attenuation length of a straight light ray in the material. It is also worth mentioning that the light spectrum of traversing light can change in matter because of energy dependent absorption. This applies to all materials but is especially important for long optical fibres. Examples for measurements of the light spectrum change as a function of the fibre length can e.g. be found in [99].

The *numerical aperture* A_N of a fibre is a measure of the maximum angle of the photons leaving the fibre at its ends. It can be important if coupling light into a fibre or if the photodetector is not located directly at the fibre's end, but there is a gap in between. The numerical aperture is defined **for meridional rays only** and can be determined from the fibre's critical angle for total internal reflection [90]:

$$A_N = \sin \alpha_{\mathrm{max}} = \frac{\sqrt{n_{\mathrm{core}}^2 - n_{\mathrm{cladding}}^2}}{n_{\mathrm{ambient}}}, \tag{3.2}$$

[23] This improvement of the trapping efficiency could also be achieved by exchanging the cladding material of a single-clad fibre with the material of the outer cladding of a double-clad fibre. But this would result in a higher total reflectivity (Fresnel equations (2.40)) at the surfaces for light coming from outside the fibre than when using two claddings. Therefore, two claddings are a better choice, especially for WLS fibres.

where the n_x are the refractive indices of the corresponding materials and α_{max} is the maximum exit angle of photons with respect to the fibre axis, i.e. the half opening angle of the cone formed by the exiting photons. As trapped **skew rays** can have much larger angles with respect to the fibre axis than meridional rays, they can lead to photons that are leaving the fibre with angles exceeding the numerical aperture.

There are three types of optical fibres, fulfilling different tasks: the standard light-guides as well as fibres containing WLS or scintillating core material. *Light-guiding fibres* just transport the light that is coupled in at one end to the other end. *Scintillating fibres* can be used instead of scintillator tiles, e.g. for particle tracking (like e.g. in the MICE [13] or the LHCb [38] experiment.). *WLS fibres* are mainly used for light collection in other optical detector parts like scintillator tiles. The scintillation light is absorbed in the WLS fibre, re-emitted isotropically (with a longer wavelength), and captured inside the fibre according to its trapping efficiency. The light that is captured inside the scintillating or WLS fibre can then directly be transported to a photodetector or coupled into a light-guiding fibre (which in general has a much longer attenuation length) to be transported over longer distances.

3.2.4. Photodetectors

The task of photodetectors is the generation of a detectable electrical signal if the detector is hit by a photon.[24] To achieve this goal, the detector has to carry out three independent steps:

1. Generation of a primary charge carrier by an incident photon.
2. Amplification by creation of secondary charge carriers.
3. Forming a measurable electrical signal from the secondary charge carriers.

The important characteristic quantities of photodetectors are:

- *Photon Detection Efficiency* (PDE): The fraction of incident photons that creates a measurable signal. This is heavily depending on the wavelength of the incident photons.
- *Gain*: The number of photoelectrons created for each photon, i.e. the electrical signal amplitude is proportional to it.
- *Dark count rate* or *dark current*: The electrical signal rate or amplitude due to thermal excitation, which is measured without any incident photon.
- *Dynamic range*: The maximum signal achievable from the detector, i.e. how many single photons can be detected and distinguished within a certain time window.
- *Time dependence* of the signal: There is a delay between the creation of the photoelectron and the electrical signal as the steps 2 and 3 of the signal creation take some time and the electrons have to travel through the detector. Fluctuations in the time needed for these processes contribute to the rise time and width of the electrical signal.

Nowadays, there are three basic types of photodetectors existing, which differ in the way how the secondary electrons are created.

[24] In fact, photodetectors are not solely sensitive to photons, but every ionising particle can create a signal.

Semiconductor Photodetectors

Semiconductors[25] are materials that possess a *conduction band* that is energetically separated from the *valence band*, but only with a relatively *small energy gap* in the order of 1 eV. As a result, electrons from the valence band can be excited to the conduction band thermally, i.e. the conductivity increases with increasing temperatures. To improve the electrical properties and adapt them to the needs, semiconductors can be doped with atoms of different materials. Therefore, a small amount of the desired material is introduced into the crystal lattice of the semiconductor material. By introducing an element of the 3rd main group into the lattice of a 4th-group semiconducting element, impurities are created that are able to accept electrons[26]. Thus, an *acceptor energy level* appears slightly above the valence band (cf. figure 3.10) and the semiconductor is called "*p-type*" (it is "positively doped", as the dopant itself offers less valence electrons than the semi-conductive element). If a 5th-group dopant is used for a 4th-group semiconductor, a *donor energy level* appears slightly below the conduction band and the semiconductor is called "*n-type*".

If a p-type and an n-type semiconductor are connected, the electrons of the donor levels in the n-region diffuse into the p-region because of the *electron concentration gradient* (assuming temperatures high enough to bridge the gap between the donor levels and the conducting band). There, the electrons can be bound by the acceptor atoms, creating a region with negatively charged ions on the p-side of the contact and leaving a region with positively charged ions on the n-side. In the thermal equilibrium, this charge separation in the *recombination region* leads to a *constant intrinsic potential difference* (the "built-in voltage") and electric field, cf. figure 3.11. Inside the recombination region, no free charge carriers are left over (they are bound by the atoms), therefore it is also called *depletion zone*.

Such a pn-junction can be used to detect charged particles and photons. If they transfer energy to the semiconducting material (photons by being absorbed), *electron-hole pairs* are created by exciting an electron from the valence band to the conduction band, leaving a

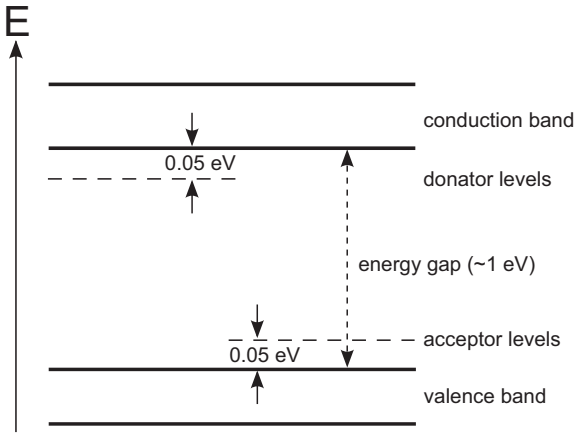

Figure 3.10.: The schematic energy band structure of semiconductors [100]. The left side of the sketch shows n-type doping with donor levels, on the right side illustrated p-type doping with acceptor levels. In realistic materials, the band structure is much more complex (cf. e.g. [42]).

[25] A detailed description of semiconductors and their properties can e.g. be found in [42].

[26] This is because the dopant possesses insufficient valence electrons for the atomic bindings it has to form in the crystal lattice.

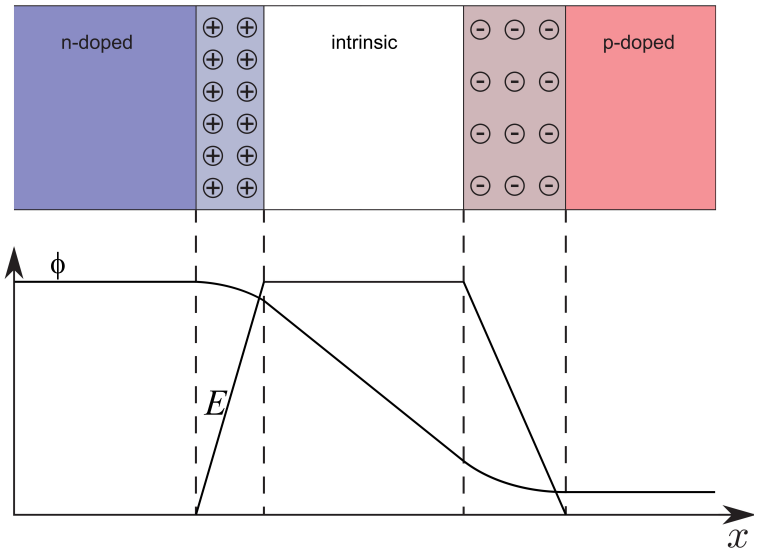

Figure 3.11.: The p-i-n junction in thermal equilibrium (adapted from [100]). The red and blue regions symbolise the n- and p-doped regions, respectively. The lighter regions form the recombination region with its ions ($\oplus$ and $\ominus$). The white region is the intrinsic region. The graph shows the electric field E and potential ϕ in the different regions of the junction. The picture for a p-n junction can be obtained by just "cutting out" the intrinsic region and reducing the potential difference until the potential curves of the recombination regions meet.

hole[27] in the valence band. If being created inside the depletion zone, the charge carriers are separated by the intrinsic field. This leads to an electric field opposing the intrinsic field and thus reducing the total electric field between the charge carriers. As a result, the total potential difference over the depletion zone (and thus over the whole pn-junction) is reduced. While performing a directed movement inside the intrinsic field and thus increasing the distance in between them, the charge carriers constantly further reduce the total potential difference over the depletion zone. This voltage pulse (as well as the corresponding photo-current) can theoretically be measured, but it is far too low for practical measurement in case of a single electron-hole pair.

To solve the problem of the very small sensitive volume of pn-junctions, there are two ways to increase the depletion zone (which also leads to an increase in the gain):

- Introduction of an undoped[28] *(intrinsic) region* between the p- and n-type region. This structure is illustrated in figure 3.11. Devices using it are referred to as *PIN-diodes*.
- Applying a *reverse voltage*[29] to the junction, meaning that a positive voltage is applied

[27] A "hole" is a missing electron in the valence band (i.e. in the atomic bindings of the lattice). Because of an electron from a neighbouring binding "jumping" into the hole and leaving a new hole in its origin binding, the holes can traverse the material. Thus, it is possible to describe the holes as positive charge carriers with a higher effective mass than that of electrons.

[28] Often, the "intrinsic" region does not consist of undoped, intrinsic semiconductor material, but is slightly doped. The heavily doped regions are then referred to as p^+- and n^+-type, whereas the "intrinsic" region is called p-type / n-type or p^--type / n^--type.

[29] For "reverse voltage", the voltage is applied in such a way that (for not too high voltages) no current can flow through the diode. Actually, in this case, there is a small constant dark current flowing through the diode. In contrast to this, "forward voltage" leads to a current that is increasing with increasing voltage (after overcoming the built-in voltage).

to the n-type region with respect to the p-type region. This external voltage and the built-in voltage of the junction add up to a larger total potential difference over the junction and thus the depletion zone has to widen. Its width can be estimated by [42]

$$d(U) = \sqrt{\frac{2\epsilon}{e}\left(\frac{1}{n_\mathrm{A}} + \frac{1}{n_\mathrm{D}}\right)(U_\mathrm{in} - U)}, \tag{3.3}$$

where ϵ is the absolute permittivity of the material, e is the electron's charge, n_A and n_D are the densities of the acceptor and donor dopants, U_in (> 0) is the intrinsic voltage of the junction, and U is the external voltage (< 0 for reverse voltage). This equation does not consider a possible intrinsic region between the doped regions.

The application of a reverse voltage has also another effect: Because of the higher potential difference and thus stronger electric field, the conduction electrons gain more kinetic energy on their way through the diode. If the external voltage is high enough, the conduction electrons[30] gain enough energy to create further *secondary electron-hole pairs* by interacting with the valence electrons. This leads to an *avalanche of electrons* (cf. figure 3.12(a)) and results in a higher gain (10 to 1000 [1, 39]) and a signal amplification inside of an *Avalanche Photodiode* (APD). Because of its internal signal amplification, an APD is able to detect much lower light intensities than normal pn-diodes/PIN-diodes.

If single photon detection with semiconductor detectors is desired, even the gain of APDs is not sufficient. In order to increase the gain, the external voltage has to be increased further. When exceeding a critical external reverse voltage, the *breakdown voltage*, and reaching the diode's so-called *Geiger-mode* (in analogy to the ionisation discharge observed in a Geiger-Müller tube), not only the conduction electrons but also the holes are able to create new electron-hole pairs and thus contribute to the avalanche breakdown. As a result, the avalanche diverges (cf. figure 3.12(b)) and the whole diode breaks down. Without external intervention, the avalanche would not stop and the diode would be destroyed. Therefore, a high-ohmic quenching resistor is placed into series with the *Geiger-mode Avalanche Photo-*

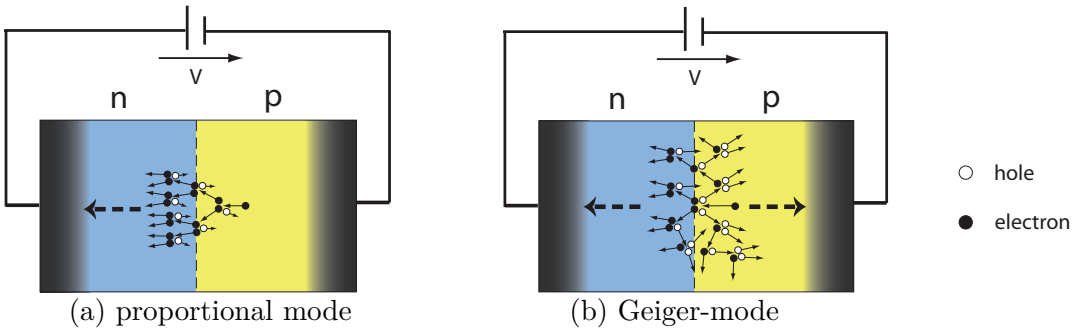

(a) proportional mode (b) Geiger-mode

Figure 3.12.: Illustration of the avalanche mechanism in APDs **(a)** and GAPDs **(b)** [101]. In APDs, the electric field is not strong enough to enable the holes to create new electron-hole pairs. Thus, only the electrons contribute to the avalanche. In GAPDs, the electric field is strong enough and the avalanche diverges (as electrons and holes).

[30] The holes need higher external voltages than electrons to be able to create new electron-hole pairs. This is due to their higher effective mass, or (more physically) because the valence electrons (which are "jumping" between neighbouring bindings and effectively making the holes move) have to gain the necessary energy on a shorter distance (the binding distance) than the conduction electrons.

diode (GAPD). The photo current induced by the avalanche leads to a voltage increase over this resistor and thus reduces the effective external voltage of the diode, until the effective external voltage falls below the breakdown voltage and the creation of new electron-hole pairs stops. Operating in Geiger-mode, GAPDs can reach a gain up to 10^8 [1], allowing for the detection of single photons.

(G)APDs cover a wavelength range from 300 nm to 1700 nm [1] and reach a PDE of up to $\sim 70\,\%$ [1]. The available products typically cover sensitive areas of $10\,\mathrm{mm}^2$ to $1000\,\mathrm{mm}^2$ [1] and work with bias voltages of 400 V to 1400 V [1].

One major disadvantage of GAPDs is that the signal amplitudes do not correspond to the number of primary electron-hole pairs (i.e. number of simultaneously detected photons) any more, but is constant and thus only allows for the detection but not the counting of photons. To solve this problem and increase the dynamic range, the *Silicon PhotoMultiplier* (SiPM)[31] was developed. Here, many (typically in the order of 100 to 1000 per mm^2 [102]) small GAPDs (the "cells") are connected in parallel, cf. figure 3.13. Then, the total signal depends on the number of cells that break down simultaneously (as well as on the recharge characteristics of the cells). Figure 3.14 shows exemplary signals of an SiPM. For short pulses of equally distributed photons, the relation to the number of photons that hit the SiPM can be approximated by [102, 104, 105]

$$N_{\mathrm{fired}}(N_\gamma, N_{\mathrm{total}}, U, \lambda) = N_{\mathrm{total}} \left(1 - \exp\left(-\frac{PDE(U,\lambda)\cdot N_\gamma}{N_{\mathrm{total}}}\right)\right), \tag{3.4}$$

where U is the external voltage, λ is the wavelength of the photons, and N_{fired}, N_{total}, and N_γ are the number of fired cells, the total number of cells, and the number of incident photons, respectively. For $PDE \cdot N_\gamma \ll N_{\mathrm{total}}$, the relation is approximately linear. For larger numbers of detected photons ($PDE \cdot N_\gamma$), the relation is not linear any more and it comes to *saturation*, because individual cells are hit by multiple photons. This shows that the dynamic range of an SiPM heavily depends on the number of cells[32] and the correlated noise rate (i.e. the probability of an avalanche in one cell to trigger another avalanche in a neighbouring cell or delayed in the same cell).

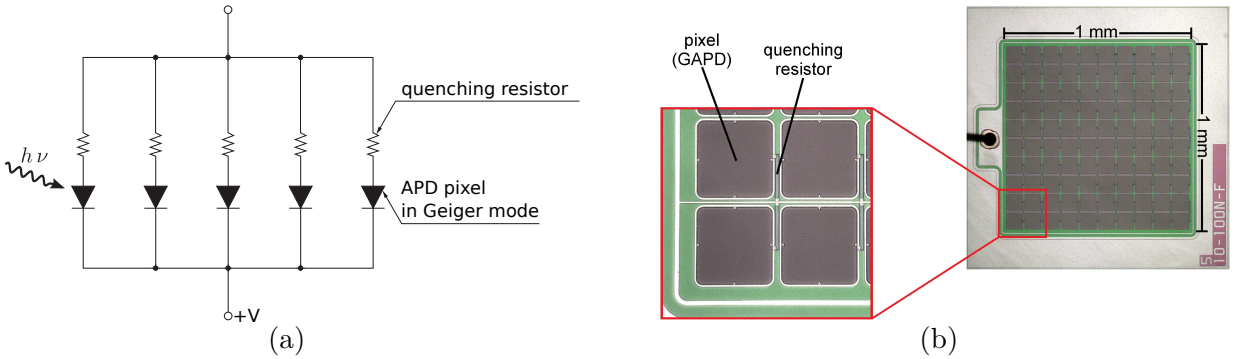

Figure 3.13.: The SiPM: schematic circuit diagram (**(a)**, adapted from [100]) and microscopic picture (**(b)**, adapted from [103]).

[31] In the literature and depending on the manufacturer, there are several different names for SiPMs, which are all describing the same type of device: SiPM (**Si**licon **P**hoto**M**ultiplier), MPPC (**M**ulti-**P**ixel **P**hoton **C**ounter), PPD (**P**ixelated **P**hoton **D**etectors).

[32] To be more precise, the dynamic range of an SiPM depends on the number of cells that can be hit by photons. If e.g. an SiPM is directly plugged to a round optical fibre with a diameter that equals the SiPM's sensitive area's edge length, only $\approx 78.5\,\%$ of its cells can be illuminated.

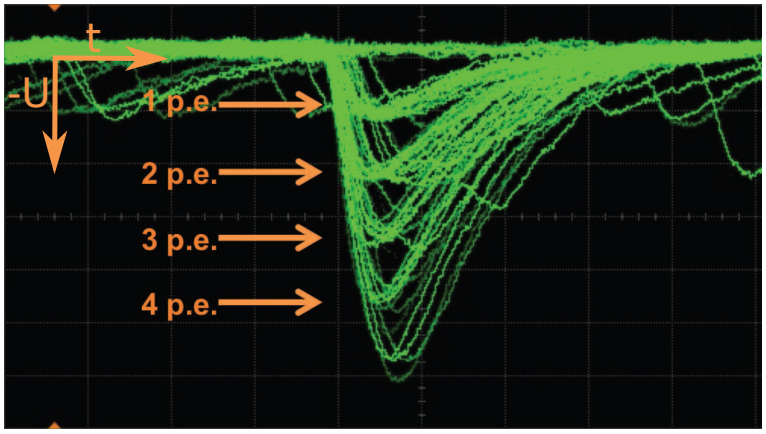

Figure 3.14.: Oscilloscope reading of SiPM output [102]. Discrete pulse heights can be distinguished, which correspond to different photon equivalents (p.e.), i.e. different numbers of photons that would create a signal of this height (assuming that no cell is hit by multiple photons simultaneously).

In comparison to vacuum- and gaseous photodetectors, SiPMs have many advantages. They are more compact (which can also be a disadvantage if large areas have to be covered), lightweight, robust, tolerant to magnetic fields, and often less expensive. Additionally, they operate with low voltages ($< 30\,\mathrm{V}$ [1] to $\approx 110\,\mathrm{V}$ [106]) and allow for fine pixelisation. As they are also matching or exceeding most performance criteria of the other photodetectors types, SiPMs are often chosen, except if the coverage of very large areas (SiPM sensitive areas of typically $1\,\mathrm{mm}^2$ to $10\,\mathrm{mm}^2$) is required.

The available SiPMs typically cover a wavelength range from 320 nm to 900 nm [1] and reach a gain of $\sim 10^6$ [1, 39]. Because of the (insensitive) space needed for the quenching resistors and the geometrical separation of the cells (cf. figure 3.13(b)), the actual sensitive area can be much smaller than the nominal sensitive area, depending on the number of cells. This is expressed by the *geometric fill factor*, which is the fraction of the nominal sensitive area that remains after subtracting the insensitive regions. The geometric fill factor also affects the SiPMs' maximum PDE, which is in the range of 15 % to 30 % [1] and thus much lower than for (G)APDs.

A major disadvantage of previous APD and SiPM series was their high noise rate ($\sim 1\,\mathrm{MHz/mm}^2$ [1]), which is strongly depending on the applied bias voltage and the temperature. With the current series, the noise effects have been reduced significantly (cf. [81]).

Vacuum Photodetectors

In vacuum photodetectors, the incident photon hits a photocathode that consists of a material with a low work function. A primary photoelectron is emitted (photoelectric effect, cf. subsection 2.2.1) and accelerated by an electric field towards an anode, which is used to collect electrons and generate an electrical signal. The creation of secondary electrons for signal amplification can be done in different ways:

- In a *PhotoMultiplier Tube* (PMT) the electrons are accelerated towards several secondary-emission electrodes (or dynodes) on the way to the anode. Figure 3.15 schematically illustrates the working principle of PMTs. For each accelerated electron hitting a dynode, a small number (typically in the order of 5) of new secondary electrons is emitted and accelerated towards the next dynode. By repeating this process with about 10 consecutive dynodes, the signal amplification is high enough to create a measurable pulse with a total gain of around 10^5 to 10^6 [1]. PMTs possess a PDE of typically 15 % to 25 % [1].

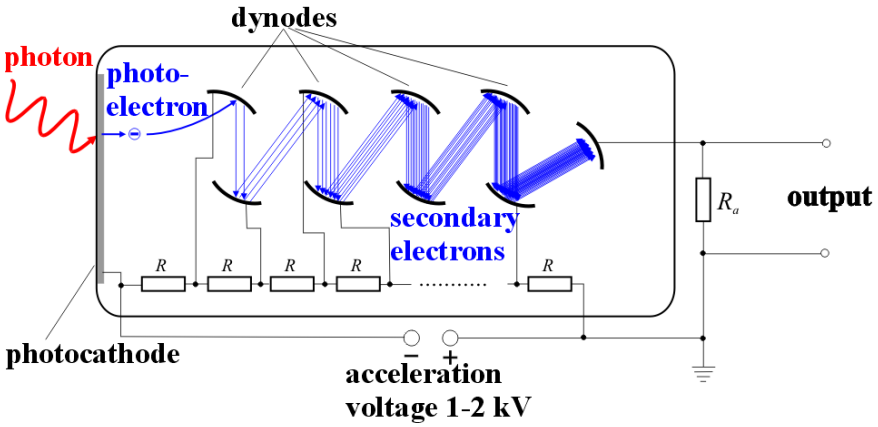

Figure 3.15.: Schematic illustration of the working principle of PMTs (adapted from [107]).

- In a *MicroChannel Plate* (MCP), there are no discrete dynodes. Instead, between the photocathode and the anode, there are one or more $\sim$ 2 mm thick glass plates with a high density of inclined cylindrical holes with $\sim$ 10 µm diameter (cf. figure 3.16). The inner surfaces of these holes serve as continuous dynodes within which the full multiplication process takes place. The PDE of MCPs is very low with typical values of 1 % to 10 % [1] and the gain is in the range of 10^3 to 10^7 [1].

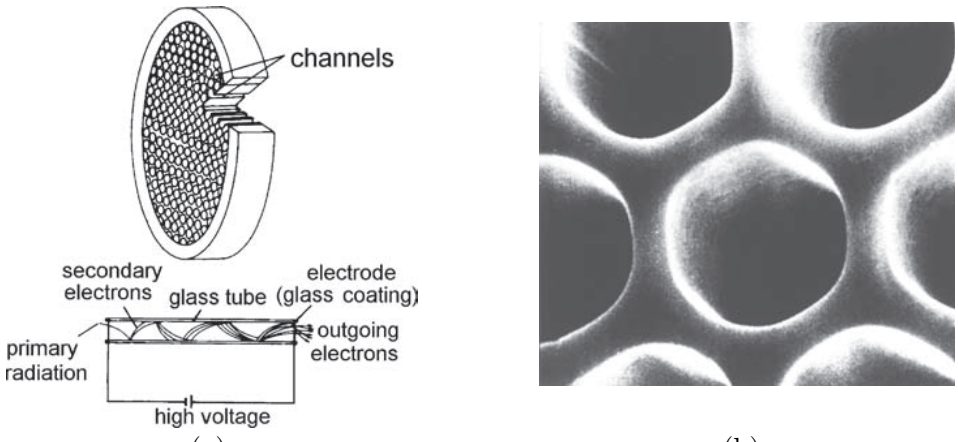

(a) (b)

Figure 3.16.: **(a):** Schematic illustration of the working principle of MCPs. **(b):** Picture of the holes in the MCP, the diameters are in the order of 10 µm. Taken from [39].

- In *Hybrid Photon Detectors* (HPD), the primary photoelectrons are accelerated to energies E_e up to 20 keV, before they hit a silicon PIN-diode[33], where they create

[33] The principle of particle detection with semiconducting devices is introduced in paragraph "Semiconductor Photodetectors"

many electron-hole pairs with a gain of $G \approx E_e/E_{gap} \approx E_e/3.7\,\text{eV}$ [1]. HPDs typically reach a PDE of 10 % to 30 % [1].

Depending on the photocathode material, the vacuum photodetectors cover a wavelength range from infrared to extreme ultraviolet and the available products can cover large sensitive areas, typically $10^2\,\text{mm}^2$ to $10^5\,\text{mm}^2$ [1]. As the photoelectrons and secondary electrons have to cover comparatively long distances to reach the dynodes and anodes, the usage is problematic in magnetic fields. Additionally, a relatively high bias voltage is needed, typically several kV, and especially classical PMTs have a high space requirement, as the amplification volume containing the dynodes is very large.

Gaseous Photodetectors

In gaseous photodetectors, the signal amplification is achieved by an avalanche process in a high-voltage region within the gas volume. The photoelectrons[34] are accelerated and ionise other gas molecules. Thus, an avalanche of secondary impact-ionisation electrons is created and the signal is amplified to measurable values. The primary photoelectrons are created by the incident photons by hitting either a solid photocathode (similar to vacuum photodetectors) or suitable molecules mixed into the gas.

Gaseous photodetectors typically have a PDE of 15 % to 30 % [1] and the gain is in the range of 10^3 to 10^6 [1]. They can cope with high magnetic fields and can be produced in thin panels. The necessary bias voltage is slightly lower than for vacuum photodetectors but still in the kV range.

[34] In fact, also the ions can ionise other gas molecules for high voltages (Geiger-mode).

4. Simulations in Physics and Detector Construction

The previous chapters illustrated that detailed physics simulations are mandatory because of the complexity of state-of-the-art detector systems. Because of the potentially low light yield of modern optical detector components, a detailed simulation of optical physics processes is necessary (in combination with a detailed particle-physics simulation). In this chapter, the topic of computational simulation in physics will be addressed. Furthermore, the particle physics simulation framework Geant4 [3], which has been used in the scope of this thesis, will be presented in detail.

4.1. Physics Simulations

In general, simulations are useful, if the boundary conditions of a basically mathematical problem are known, while at the same time an analytical determination of the solution to this problem is very complex or not possible (with reasonable effort). Typical examples for the application of such Monte Carlo (MC) simulations are the numerical determination of integrals or the analysis/prediction of fluid dynamics (e.g. sea currents or air currents), thermodynamic reactions, interactions of high-energy particles within complex materials (e.g. in particle detectors or human tissue), or the performance of complex optical systems (e.g. scintillator volumes with readout via WLS fibres).

In the field of particle physics, MC simulations are generally used for two purposes. One purpose is the **analysis of measured data** of an experiment. Here, MC simulations can serve as a *precise prediction of background events*. This is necessary to define variables that separate signal events from background events and thus to *interpret the results of the experiment*.[35] For example, the data analyses that led to the recent discovery of the Higgs boson (e.g. [24, 25]) included billions of simulated proton-proton collisions and their signature in the different detectors. This allowed to determine the significance of the deviation between the measurement and the prediction of the standard model (represented by MC simulations). In contrast to this, no evidence for the existence of the Higgs boson had been found in previous experiments and thus limits on its mass have been set (using MC). The other purpose for the application of MC simulations is the **detector design**. In the scope of designing or optimising a particle detector, simulations are an indispensable tool. They allow for the *detailed understanding* of how the *individual detector elements* (e.g. optical components) re-

[35] Actually, for some particle-physics processes that contribute to the background events, it is also possible to estimate their contribution directly from the measured data (cf. e.g. [28]).

spond to different particles with different energies etc. as well as of the *resulting response of the complete detector*. Otherwise, designing a well working particle detector or correctly analysing the data of a detector would be extremely difficult, if not impossible.

This shows that simulation frameworks that correctly simulate the interactions of particles with matter are needed. Several dedicated and multi-purpose simulation tools are available. Whereas only Geant4 has been used in the scope of this thesis, a few important examples should briefly be introduced, roughly sorted by the degree of their specialisation:

- Garfield [108] / Garfield++ [109]:
  detailed simulation of ionisation and transport in gas mixtures for drift chambers, an important feature is the generation of electric fields from user-specified charge distributions

- PENELOPE (**P**enetration and **ENE**rgy **LO**ss of **P**ositrons and **E**lectrons) [110]:
  simulation of electron and photon transport in matter, specialisation on (ToF-)PET scanners with the extension PeneloPET [111]

- EGS (**E**lectron **G**amma **S**hower) [112]:
  simulation of high-energy electrons and photons interacting with matter

- SRIM (**S**topping and **R**ange of **I**ons in **M**atter) [113]:
  simulation of ion transport in matter

- MCNP (a **M**onte **C**arlo **N**-**P**article transport system) [114]:
  simulation of neutron, electron and photon transport in matter (other particles possible with the multi-purpose extension MCNPX [115])

- PGS (**P**retty **G**ood **S**imulation of high energy collisions) [116]:
  fast but rough simulation of generic detectors of collider experiments to produce semi-realistic reconstructed physics objects from events of particle-physics event generators

- FLUKA (**FLU**ktuierende **KA**skade) [117]:
  multi-purpose simulation of particle interactions with matter with a special focus on nuclear interactions

- Geant4 (**Ge**ometry **an**d **t**racking) [3]:
  multi-purpose simulation of particle interactions with matter

As stated before, modern optical detector components, e.g. WLS and scintillating fibres or small components (due to high segmentation), might have to work with very low quantities of light (down to few photons). Thus, the optical properties of the materials and the surfaces can have a significant impact on the measurement and a flexible and detailed simulation of these properties is very important. In the above list of simulation tools, only the multi-purpose simulation framework Geant4 contains a very extensive and flexible optical physics simulation. Therefore, it has been used in the scope of this thesis (Geant4, version 10.00.p02).

4.2. Geant4

In this section, the Geant4[36] [3, 118, 119] framework will be presented, focusing on the simulation of optical detector components and optical properties that influence their response. Hence, the following is not to be considered as a complete introduction to Geant4. More complete and detailed descriptions can be found in the Geant4 User Documentation [120], which, among other things, contains the user's guides [121–123] as well as the Physics Reference Manual [52]. Help in form of instructions, frequently asked questions, various examples, and an active users forum (including the Geant4 collaborators) is available in [124, 125].

Geant4 has been developed at CERN and is the basis for the detector simulation frameworks of the LHC experiments and other high-energy physics experiments. It is by far the most widely-used and most-cited simulation tool for particle interactions with matter [126]. Its wide range of physics in combination with its object-oriented design and the modular and hierarchical structure make Geant4 a very flexible tool. Therefore, the usage of Geant4 is not restricted to particle physics in the narrow sense, but its field of application extends over various disciplines and topics [3, 126], e.g. (astro-)particle physics, medical physics, radiation damage studies of materials/electronics/detectors, plasma physics, and radiation studies for space flight. This flexibility makes Geant4 a good choice for simulations of particle interactions with matter. Additionally, its extensive and flexible optical physics capabilities also allow for the detailed simulation of optical detector components.

4.2.1. Basic Principles

Geant4 is a C++-based software toolkit for the simulation of the passage of particles through matter and the interactions they undergo. For this purpose, several aspects are considered, namely:

- the geometry
- the materials and their properties
- external electromagnetic fields
- physics processes that cause the interactions
- the traversing particles and their properties
- particle tracking through matter and electromagnetic fields
- sensitive detector components performing user-defined actions
- access to the simulation data at several levels
- visualisation of geometries and particle trajectories

Thereby, Geant4 can cover many physics processes for electromagnetic and hadronic physics (including decay- and optical physics as well as atomic excitation and de-excitation) for a large energy range from the eV to the TeV scale and for a spatial range from the cosmic down to the DNA scale.

Geant4 is not an out-of-the-box simulation program itself, but it provides additional C++

[36] Geant stands for "**Ge**ometry **an**d **t**racking".

classes that are necessary for creating a simulation. To do so, the user has to extend several Geant4 classes to provide the necessary information about particles, matter, and physics processes as well as to define actions and to access the simulation data. Additionally, an executable main program has to be created, which combines the (extended) Geant4 classes and controls the simulation.

To create a working simulation, the user has to define at least its basic features, namely the physics models and particle types to be considered (cf. subsection 4.2.2), the matter and its geometry (cf. subsection 4.2.3), and the primary particles whose interactions with the matter are to be simulated (cf. subsection 4.2.5). This is done by extending the corresponding basic Geant4 classes. Further basic Geant4 classes can be extended to implement user-defined actions or to access the desired simulation data (cf. subsection 4.2.6).

In Geant4, each `G4Run` (representing a full simulation run) is divided into several levels. A `G4Run` consists of one or more events (`G4Event`), which combine one or more primary particles, which are handled one after the other. Each primary particle is created at the position and with the properties that have been specified by the user. The primary particles and potential secondary particles from interactions are tracked through space and time on their way through the simulated volume. The tracking of a particle stops, if it leaves the simulated volume or if it is stopped by either the total loss of its kinetic energy, decaying, or a user-defined action. The track (`G4Track`) of each particle is divided into `G4Steps`. In general, one `G4Step` is the distance between two successive, discrete interactions. Two exceptions from this rule are that traversing the boundary between two different geometric volumes always defines the starting/end point of a `G4Step` and that some physics processes are simulated continuously rather than discretely (cf. next section) and thus one `G4Step` might contain several of such continuous interactions. In each case, the `G4Steps` and the processes defining them depend on the considered physics models as well as on the material and particle properties. Additionally, this subdivision allows the user to access the simulation at each level (cf. subsection 4.2.6).

4.2.2. Physics and Particle Types

The physics processes and particles that are to be considered during the simulation are defined by registering them in a `PhysicsList`. Additionally, the parameters of some processes can be adjusted, e.g. activating the synchrotron radiation process, allowing for finite rise times of the scintillation process, or setting the decay time spectrum of the WLS process to exponential rather than delta-like.

In Geant4, the *optical physics* has an exceptional position among the physics processes, as it adds special particles (optical photons) and new properties for materials and optical surfaces. Being the only particle that can be reflected or refracted at optical surfaces[37], as well as being only created in optical processes like scintillation, Cherenkov radiation, and WLS (cf. sections 2.1 and 3.2) makes the `G4OpticalPhoton` differing from the "usual" high-energy particle-physics photon (`G4Gamma`) in Geant4.

[37] In Geant4, optical photons are particles, i.e. single photons can only be either reflected or refracted (or absorbed in case of a surface between a dielectric and a metal, cf. paragraph "Optical Physics Peculiarities" of subsection 4.2.7). To obtain the splitting of a light beam according to the reflectivity/transmittance of the optical surface, several optical photons have to be simulated.

4.2.3. Geometry and Materials

Creating the setup of a Geant4 simulation requires several steps, as the geometry and the materials have to be specified.

First of all, the *geometric shape* of a component, the so-called "solid", has to be defined. Therefore, the user can choose from simple geometric objects like boxes or cylinders to complex ones like polygons or rotational solids. All available basic solids can be found in [122]. Additionally, solids can be combined by boolean operations to create more sophisticated geometric objects.

The next step is to assign a *material* to the solid. There are two ways to implement materials into the simulation. The Geant4 framework supports the automated extraction of predefined material data from the databases of the National Institute of Standards and Technology (NIST) [127], which contain a large number of elements, isotopes, and chemical compounds. Alternatively, the users can create materials themselves, specifying its exact composition of elements or isotopes, its density, and if required its state, pressure, or temperature. This allows for maximum flexibility on the chemical composition of the materials.

Additionally, whenever optical physics processes are to be considered in the simulation, *optical properties* need to be assigned to the materials. This is necessary for user-defined materials as well as for predefined materials. Every material needs at least a refractive index spectrum (which corresponds to the dispersion relation) and an attenuation length spectrum, though the attenuation length is set to infinity if it is not defined. Special optical materials, i.e. scintillating and WLS materials, additionally require the specification of the emission spectra as well as of the rise and decay times. The spectra have to be defined as a function of the particle energy and have to be sorted by rising energy values. Whereas refractive index values and attenuation length values are interpolated by a straight line between two given points of the spectrum, the values of emission spectra are not. For energy values between two given points, the values of an emission spectrum are "interpolated" by applying the mean of the energy-dependent quantity values of those points. This is shown in section 6.1.

In the next step, the volumes have to be *positioned*. For this purpose, their mother volume (the volume they are to be placed into), their position inside and their rotation relative to the mother volume have to be specified by the user. Thereby, it is important that the volume may not protrude from its mother volume or overlap with other volumes. If this requirement is not fulfilled, the simulation will probably yield incorrect results, e.g. by ignoring affected volumes. Therefore, if a volume has to protrude from its mother volume like e.g. a WLS fibre from a scintillator tile or optical glue volume (cf. figure 4.3), this volume has to be divided and distributed to the different mother volumes. As it is often not easy to detect such overlaps by eye, e.g. for complex geometries with many volumes or for small overlaps, Geant4 provides functions to search for overlaps automatically.

In the last step, `G4OpticalSurfaces` or *sensitive detectors* can be assigned to the volumes, in order to simulate various different surface conditions (cf. subsection 4.2.4) or to specify user-defined actions that are to be performed if a particle reaches a certain volume (cf. subsection 4.2.6), respectively.

4.2.4. Optical Surfaces

The properties of the optical surfaces can be used to simulate various different surface conditions. By default, the optical surface processes (reflection and refraction, cf. section 2.5) are exclusively determined from the refractive indices of the two materials forming the surface (Fresnel equation, Snell's law, cf. section 2.5). This corresponds to the simulation of a perfectly smooth surface between two dielectrics. If other configurations have to be simulated, `G4OpticalSurfaces` and their properties have to be defined by the user. Thereby, several surface models, surface types, and surface finishes can be used.

The current standard surface model in Geant4 is the *Unified Model for optical physics*. It is described in detail in [122] and an overview can be found in figure 4.2. Because of various possible combinations of several surface types, surface finishes, and variables, this model is very flexible. It is e.g. possible to simulate painted or wrapped surfaces with or without air gap, without having to create additional volumes for the wrapping material. Or it is possible to simulate a surface between a dielectric and a metal (with the complex refractive index that is necessary for the Fresnel equations) by defining the `G4OpticalSurface` in the corresponding way. Additionally, more properties can be specified, namely the surface's reflectivity spectrum[38] (bypassing the Fresnel equations), its roughness, and reflection models that are to be applied to a surface.

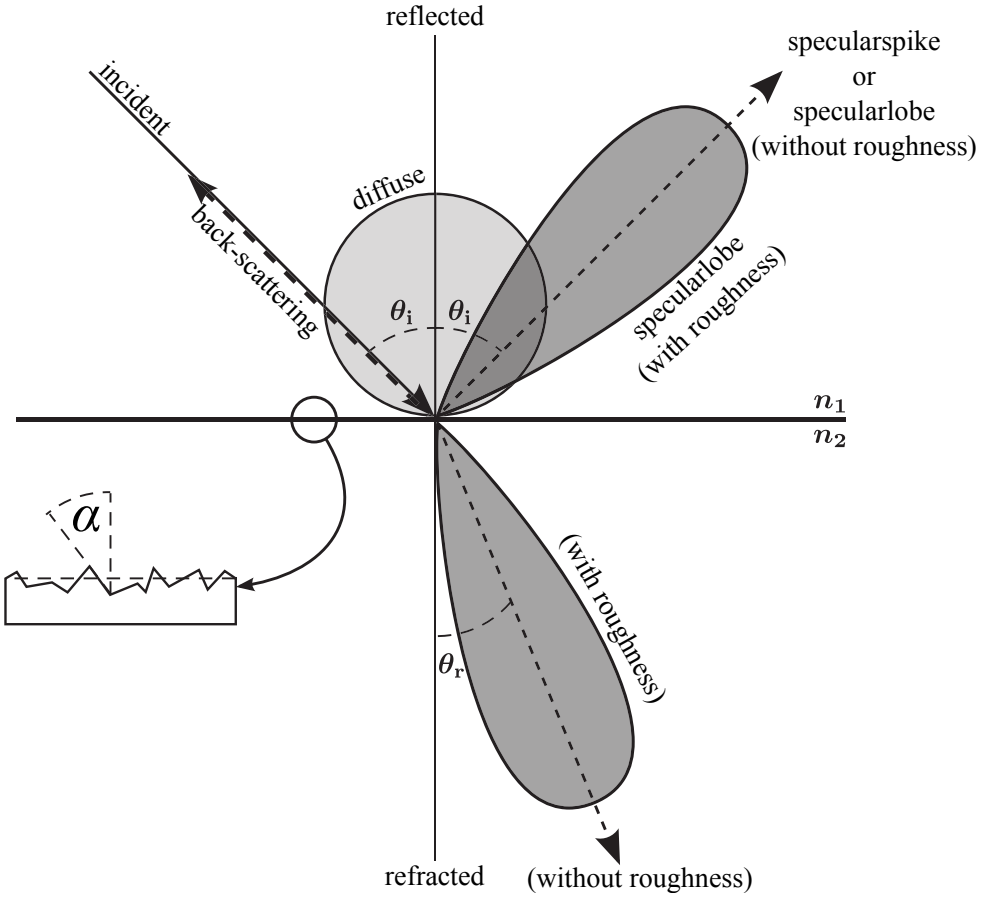

Figure 4.1.: Overview of the reflection models in the Unified Model for `G4OpticalSurfaces` in Geant4 (adapted from [100]).

[38] Reflectivity values are interpolated by a straight line between two given points of the spectrum.

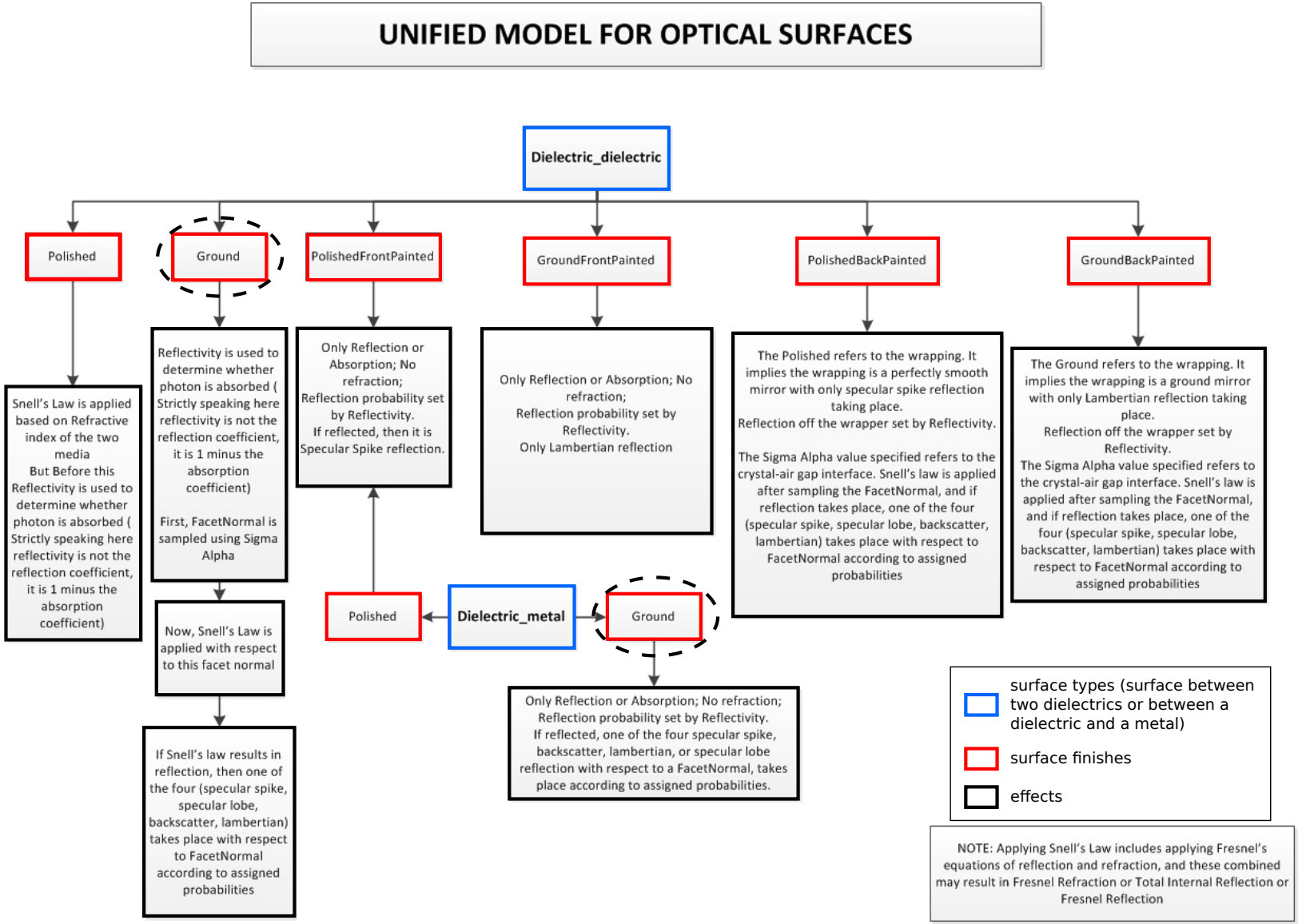

Figure 4.2.: Overview of the effects of the different options in the Unified Model for `G4OpticalSurfaces` in Geant4 [122]. The two marked options (dashed ellipses) have been used in the scope of this thesis.

The *surface's roughness* is specified in terms of σ_α, which is the standard deviation of the Gaussian distribution (around zero) of the angle α between the local, microscopic surface and the overall mean surface (cf. figure 4.1). The roughness affects the angular distribution of refracted photons as well as of reflected photons in the `specularlobe` reflection model (geometric reflection at the microscopic surface). The other reflection models (`backscattering` (exact backscattering due to multiple reflections), diffuse reflection (Lambertian), and `specularspike` reflection (geometric reflection at the overall mean surface)) are independent of the roughness. This is illustrated in figure 4.1. The specific impact of the different reflection models can be defined by the user.

Another method is to use surfaces with predefined properties from *Look-Up Tables* (LUT). This method allows for a very easy definition of surfaces, without having to define their properties manually.

4.2.5. Primary Particles

The `G4ParticleGun` is responsible for starting single `G4Events` of a `G4Run`. Here, the user has to specify the *number of primary particles* and their *properties*: particle type, initial position, initial kinetic energy or momentum, and momentum direction. Besides the particle type, the properties can be provided as fixed values or as probability distributions. Additionally, a polarisation has to be specified for optical photons.

4.2.6. User-defined Actions

Besides the mandatory Geant4 classes, which the user has to extend in order to define the necessary properties of the simulation, there are further classes that can be extended to access the simulation at `G4Run`, `G4Event`, `G4Track`, or `G4Step` level. Thereby, the user has the possibility to *gather the desired simulation data* and/or to *specify user-defined actions*. For example, particles can be "killed" (i.e. stopping the simulation of their track) when reaching specific volumes or number of steps, the number of Cherenkov or scintillation photons per run/event/primary particle can be determined, etc..

In case that such user-defined actions are to be executed for particles reaching specific volumes, this can be simplified by using the concept of *sensitive detectors* in Geant4. Every volume can be declared as a `G4SensitiveDetector`. As a result, the user-defined action that has been assigned to a certain `G4SensitiveDetector` is executed if a particle reaches the corresponding volume. Using sensitive detectors avoids the necessity of a user-defined check of the current volume for each `G4Step` and simplifies the definition of different actions for different volumes. Additionally, the sensitive detector can create a `G4Hit` for each particle reaching the volume. These `G4Hits` contain user-defined data of the particles (e.g. particle type, four-momentum, deposited energy,...) and can be collected throughout an event. At the end of the event, the `G4Hits` can be digitised by applying user-defined criteria. Thus, the simulation of a realistic detector response is possible.

4.2.7. Peculiarities

As described before, Geant4 is very flexible and contains a very extensive optical physics simulation, including optical surface properties. On the one hand, this makes Geant4 a very powerful tool concerning particle-physics simulations. On the other hand, the large flexibility leads to the fact that building a correctly working simulation (that should be easily modifiable in the best case) is very laborious and requires significant user-effort and advanced understanding of the internal workflow of Geant4 as well as of its optics model. Some examples of potential challenges will be presented in the following, especially focusing on optical physics and the simulation of optical detector elements. These issues have to be considered and resolved by the user when setting up a simulation with Geant4. These peculiarities were concerned in the scope of this thesis, in order to reduce the required user-effort. As the specific challenges for the simulation of optical detector components were not addressed by any Geant4 extension up to now (cf. subsection 4.2.8), a new extension was created (cf. chapter 5).

Geometrical Challenges

There are two issues in Geant4 that can make the creation or modification of complex geometric setups challenging and laborious. One is the fact that the *positions and rotations* for placing the volumes have to be specified *relative to the mother volume*. This can require complex calculations by the user, if the desired position and rotation are only known relative to another volume (e.g. if a SiPM is to be positioned relative to an optical fibre).

The other issue is the fact that there may be *no overlaps* in the geometry (cf. subsection 4.2.3). The rather simple example of a scintillator tile with a WLS fibre illustrates that this may be problematic. As long as the end faces of the fibre are parallel to the faces of the scintillator tile, there is no problem: If the fibre protrudes from the tile on one or both ends, the fibre can be assembled by two or three cylinders instead of one. This case is shown in figure 4.3(a). However, if the fibre is tilted against the tile (cf. figure 4.3(b)), this simple solution is not possible any more. Instead, the fibre has to be cut into two or three parts via boolean operations now, if it protrudes from the scintillator tile. If additionally the

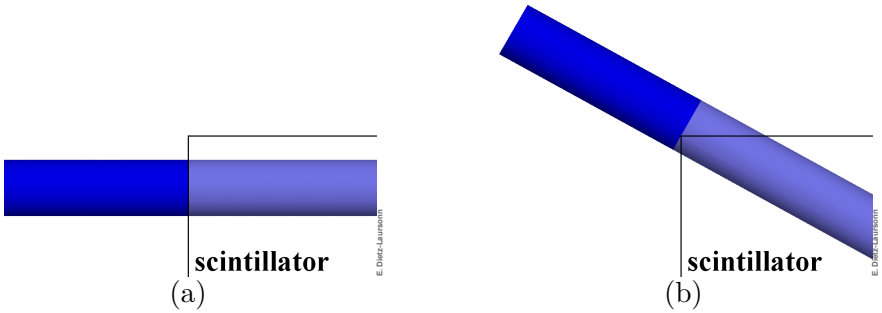

(a) (b)

Figure 4.3.: Simulated optical fibre in a scintillator tile (or optical glue volume): with its end faces parallel to the faces of the scintillator tile **(a)** and for being tilted against the tile **(b)**. In the first case, the complete fibre can simply be assembled by several fibre parts (represented by the different colours) to avoid overlaps. Obviously, this is not possible in the second case.

scintillator is to be be wrapped and the fibre has one or two claddings, setup is again more complicated. If the user furthermore wants to keep the geometric setup flexible, in order to be able to quickly change e.g. the fibre position or any other specification, this is not a trivial task and results in a significant effort, even before starting with the first simulation.

Visualisation Restrictions

The visualisation within Geant4 is restricted by the fact that most visualisation tools use *approximated volumes* [128], which is especially imprecise for round contours. As the particle tracking uses the exact volumes, the resulting picture may look strange, e.g. when simulating a bent optical fibre. In this case, the envelope of the optical photons' tracks describes a perfectly round shape, whereas the fibre is illustrated with edges. As a result the optical photons seem to leave the fibre (cf. upper fibre in figure 4.4), which is not the case. This issue can be dealt with by increasing the number of visualised line segments per circle (cf. lower fibre in figure 4.4 and appendix C.1).

Another visualisation restriction is connected to the usage of *boolean volumes*. Boolean volumes are used if volumes have to be separated (e.g. because of the prohibition of overlaps between volumes, cf. "Geometrical Challenges") or if non-standard geometric shapes are necessary (e.g. to create the cladding volumes of optical fibres with a square profile). When using boolean volumes, the visualisation might show wrong volumes, which is illustrated for two examples in figures 4.5 and 4.6. The latter also shows how to verify whether an incorrect volume is restricted to the visualisation only or whether it is also incorrect with respect to particle tracking.

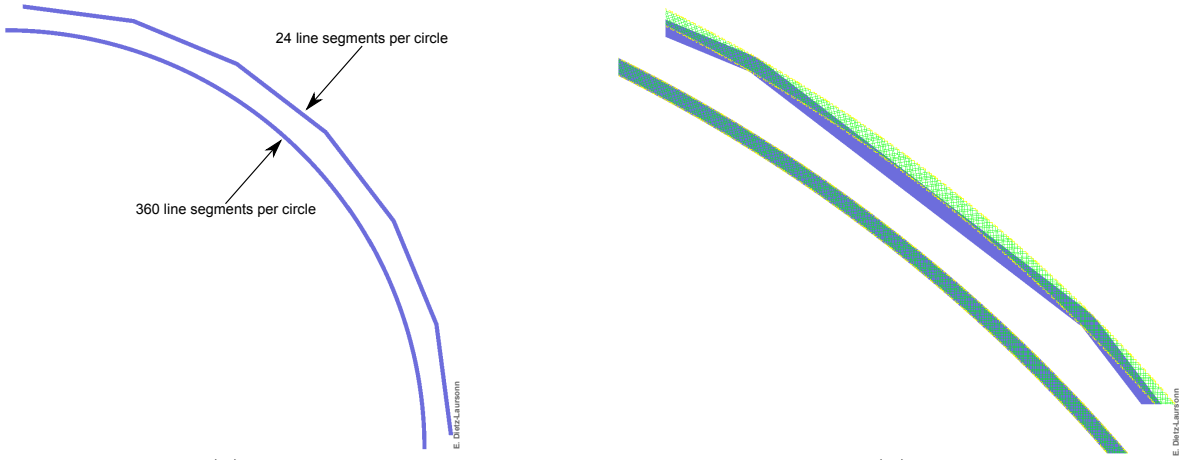

(a) (b)

Figure 4.4.: Example of *visualisation problems* in Geant4 simulations (overview **(a)** and close-up **(b)** with optical photons (green)): With the default configuration of Geant4 (24 line segments per circle), the fibres (blue) are visualised with edges and the optical photons seem to leave the fibre (upper fibre). The reason is that the fibre visualisation is approximative, whereas the photons are tracked and visualised using the exact fibre volumes. Using a higher number of line segments per circle (360), the fibre seems to be visualised without edges and the optical photons do not seem to leave the fibre any more (lower fibre).

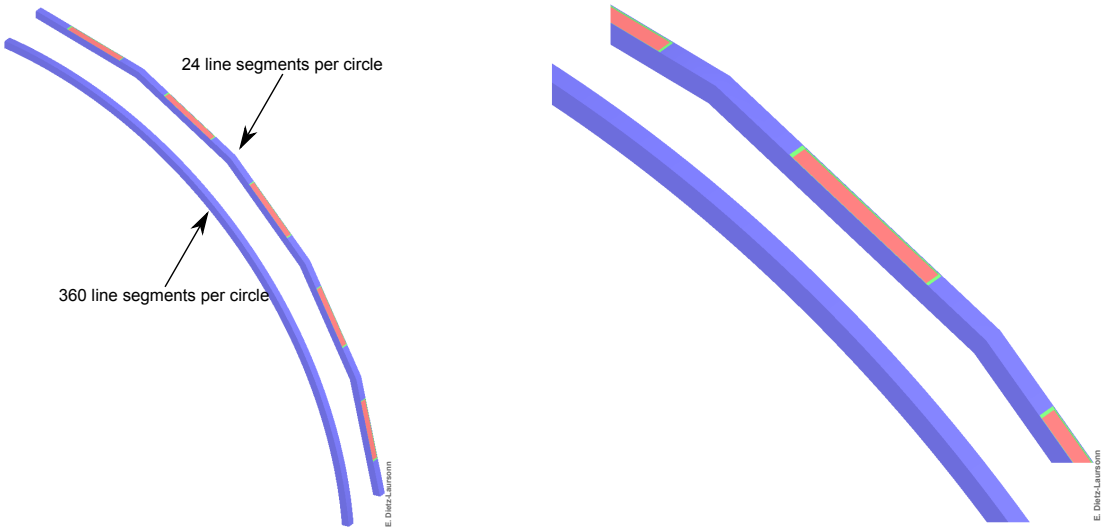

(a) (b)

Figure 4.5.: Example of *visualisation problems* in Geant4 simulations (overview **(a)** and close-up **(b)**): With the default configuration of Geant4 (24 line segments per circle), the bent optical fibre seems to have holes, where the inner cladding (green) and the core (red) can be seen (upper fibre). Using a higher number of line segments per circle (360), the "holes" disappear along with the edges of the visualised fibre (lower fibre).

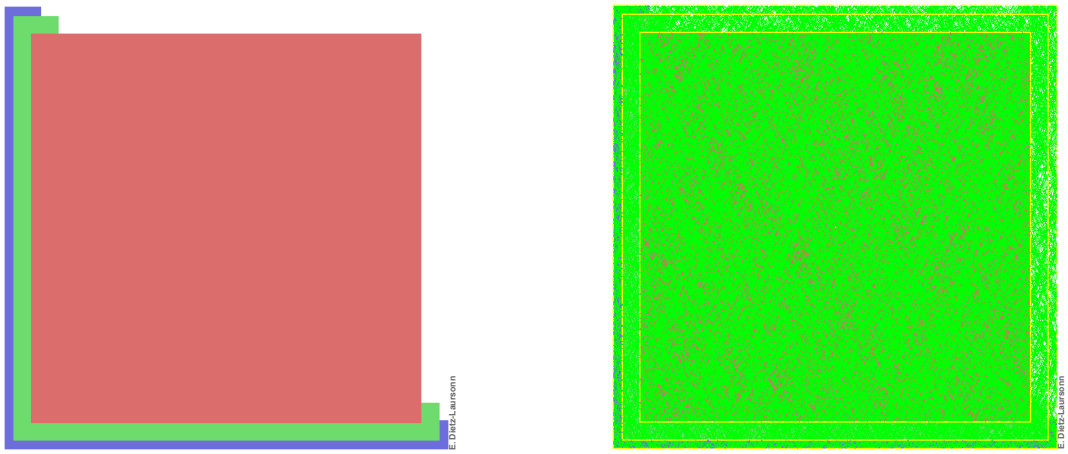

(a) (b)

Figure 4.6.: Example of *visualisation problems* in Geant4 simulations: The figures show the cross section of a square optical fibre with its core (red) and two claddings (dark-green and blue, respectively). Parts of the claddings seem to be missing **(a)**. The test with optical photons (light-green) which are captured within the fibre shows **(b)** that the claddings are actually complete and this is only a visualisation issue. Otherwise the photons would not be restricted to the intended fibre volume and there would be no reflections or refractions (yellow dots represent step end points) at the intended fibre volume boundaries at the left and top edge. As no circular geometry is used here, this visualisation problem cannot be solved by increasing the number of line segments per circle.

The presented restrictions are issues of the visualisation only. Thus, they can indeed lead to restrictions in visual debugging of the simulated setup, but the simulation results are not affected. Additionally, these issues do not apply for all visualisation tools, which can be used in Geant4. The RayTracer visualisation tool does not suffer from the described problems [128, 129]. However, tracks cannot be visualised with RayTracer and the navigation of its (virtual) camera is not trivial.

Optical Physics Peculiarities

The optical physics in Geant4 is designed to be very flexible and extensive. Therefore, a variety of properties can be set for the physics itself and for `G4OpticalSurfaces`. At the same time, this leads to some issues the user has to be aware of:

- *All optical properties* are specified as a function of the photon energy within Geant4, i.e. if a property spectrum is available as a function of the photon wavelength, it has to be converted by the user. In this context, the user has to be aware that the spectra are also processed as a function of the photon energy, e.g. when interpolating between two points of the spectrum. Additionally, all optical properties have to be specified on the same energy range. Otherwise errors will occur, e.g. if a scintillation photon is created with an energy for which no refractive index is specified in the material.

- The *rise time variables* of the scintillation process are deactivated by default, i.e. the simulated rise times are always zero, independent of the user-specified rise time values of the materials. If finite rise times are to be used, the rise time variables have to be activated when registering the optical physics process in the `PhysicsList` (cf. appendix C.1).

- The *WLS decay time spectrum* is by default a δ-function rather than an exponential spectrum. If an exponential spectrum is to be used, this has to be activated when registering the optical physics process in the `PhysicsList` (cf. appendix C.1).

- *Birks' constant* (cf. subsection 3.2.2) is the only optical material property that cannot be specified via a property variable. Instead, it has to be defined directly for the ionisation process of the material (cf. appendix C.1).

- The *default reflection model* of `G4OpticalSurfaces` differs from the case without `G4OpticalSurfaces`: If no `G4OpticalSurface` is defined, the reflection is simulated as geometric reflection at a perfectly smooth optical surface, i.e. applying Snell's law (cf. section 2.5). When introducing a `G4OpticalSurface` without specifying the reflection model, the default reflection model is diffuse reflection. An example how to specify the desired reflection model can be found in appendix C.1.

- The *spectra* of the reflectivity, the refractive index, and the absorption are interpolated by a straight line between two given points of the spectrum, emission spectra are not (cf. subsections 4.2.3 and 4.2.4 and section 6.1). In order to avoid unexpected behaviour, the latter should therefore be specified with a high density of data points.

- Even though the *refractive index spectra* are usually interpolated by a straight line between two given points of the spectrum, they should be specified with a high density of data points, as long as they are not constant. Otherwise, unexpected deviations for the number of created Cherenkov photons may occur, as in this context, $1/n^2$ is calculated for each point and this value is interpolated by a straight line, in contrast to the usual procedure (cf. subsection 6.10).

- The generation of Cherenkov photons in Geant4 is designed for normally-dispersive materials only (cf. section 6.10 and [130]).

- Geant4 itself does not limit the emission spectrum of the *Cherenkov process* to reasonable energy ranges. Limiting the Cherenkov process is necessary as otherwise simulated Cherenkov radiation can occur in non-physical energy regions (cf. section 6.10). Therefore, the refractive index and all other optical properties[39] should be restricted to the necessary optical energy range or the physical Cherenkov energy range, respectively.[40]

- Using surfaces with predefined properties (*LUT surfaces*) can lead to unexpected results, at least when using them for the simulation of wrappings or paints. This is a known problem [131] and it is demonstrated in section 6.11.

- By default, the processing of the (mother) particle is postponed in Geant4 at the point of time when it creates new `G4OpticalPhotons` (e.g. via scintillation) [132]. After the processing of the `G4OpticalPhotons` (together with all their potential child particles) has been completed, the mother particle's processing will continue. Therefore, it may appear to the user, as if the mother particle's trajectory consist of multiple `G4Tracks`. This can lead to *double counting* and *wrong data acquisition*[41], when not considering the track identification number, which is unique to all particles and thus the same for "all `G4Tracks`" of the mother particle's trajectory. Whereas also the practice of preponing `G4OpticalPhotons` can be changed when registering the optical physics process in the `PhysicsList` (cf. appendix C.1), this approach is not recommended as it can lead to problems with memory allocation for large numbers of `G4OpticalPhotons` [132].

- `SensitiveDetectors` are not only activated by optical photons that enter the corresponding volume, but also by optical photons that are reflected at the surface of this volume. This is simply due to the way how sensitive detectors and optical reflections are treated internally by Geant4 and has to be considered by the user (cf. appendix C.2.2).

- `G4OpticalSurfaces` can be defined via two ways: Between two specific volumes (`G4LogicalBorderSurface`) or around one volume (`G4LogicalSkinSurface`). Using **`G4LogicalBorderSurfaces`**, the two volumes forming the surface have to be specified as well as its properties and the photon direction of flight for which the properties are to be applied. If a **`G4LogicalSkinSurface`** is specified, its properties are ap-

[39] Defining individual optical properties on different energy ranges can cause problems as photons could be created with energies for which e.g. no refractive index is defined.

[40] If not stated differently, it is limited to the energy rang between 1 eV and 7 eV in the scope of this thesis (cf. appendix D).

[41] In this context, "wrong data acquisition" means that incorrect data is acquired, e.g. by only considering one of the apparently multiple `G4Tracks` belonging to the trajectory of a particle.

plied to every surface of the corresponding volume for both directions of flight of the photons. If the properties are not to apply for one of the surfaces, additional G4LogicalBorderSurfaces have to be specified for the corresponding volumes.

The following table summarises the effective G4OpticalSurfaces, which are responsible for the surface properties, for all possible combinations of G4OpticalSurfaces. Thereby, the photons cross the surface from volume 1 to volume 2, "skin" stands for a G4LogicalSkinSurface around the corresponding volume, "border" represents a G4LogicalBorderSurface between both volumes (where the properties are specified for photons that approach the border from the volume corresponding to the column), and "a" or "b" distinguish different surfaces of the same type.

volume 1	volume 2	eff. surface	volume 1	volume 2	eff. surface
skin	/	skin	/	skin	skin
skin_a	skin_b	skin_a*	skin_b	skin_a	skin_b*
border	/	border	/	border	/
border	skin	border	skin	border	skin
border_a	border_b	border_a	border_b	border_a	border_b

* If one of the volumes is the mother volume of the other volume, the effective surface is always the G4LogicalBorderSurface of the daughter volume, disregarding from which volume the photons are approaching the surface.

The effect of these combinations has to be considered when creating G4OpticalSurfaces. It is e.g. a bad idea to use G4LogicalBorderSurfaces to define the optical properties of the surface between outer cladding of an optical fibre and its surroundings. If the fibre is positioned in such a way that its cladding touches the outer surface of its mother volume (e.g. for fibres directly at the surface of a scintillator tile or optical glue volume), a surface is formed between the fibre cladding and a volume different from the mother volume. This surface only possesses the desired properties, if a G4LogicalSkinSurface is used instead.

- The *optical property variables* can have different meanings, depending on the object they are referred to:

  – The *refractive index* is not a surface property but a material property. Therefore, assigning it to an G4OpticalSurface has no effect. However, exceptions are G4OpticalSurfaces with the "backpainted" surface finish. Here, a refractive index has to be defined, which is interpreted as the refractive index of the medium in the gap between the painted volume and the paint (cf. figure 4.2).

  – In contrast, the *complex refractive index* is not treated as a material property but as a surface property. Therefore, it only has an effect when being specified for G4OpticalSurfaces.[42] In particular, assigning a complex refractive index to a material does not result in an implicit specification of the attenuation length spectrum.

[42] This is physically reasonable, as all optical processes besides reflection probability and absorption (which is directly specified for materials) only depend on the real part of the refractive index (cf. section 2.5).

– Specifying the *complex refractive index* of a `G4OpticalSurface` leads to the use of a *modified Fresnel equation*. This equation only considers the complex refractive index of the surface, rather than the refractive indices of both materials that form the surface (cf. [133] and section 6.8). Besides the fact that only considering one refractive index is physically not absolutely correct [77], this does not make any sense for surfaces between two dielectrics. The complex refractive index should therefore only be used for `G4OpticalSurfaces` between a dielectric and a metal, where in the best case the refractive index of the dielectric is close to 1. Another possibility is to pass an effective complex refractive index (considering the refractive indices of both materials forming the surface) to the `G4OpticalSurface`.

– For direct specification of the *reflectivity* of `G4OpticalSurfaces`, two optical property variables can be set and have to be distinguished. One is the `REFLECTIVITY` variable. In case of a surface between a **dielectric** and a **metal**, it does exactly what its name suggests: The optical photons are reflected with the probability that has been set via the `REFLECTIVITY` variable (i.e. bypassing the Fresnel equations). Not reflected photons are absorbed.[43] However, in case of a surface between **two dielectrics**, the result is not as the variable name suggests: The photons are absorbed with a probability of $100\,\% - r$, where r is the specified "reflectivity" value. The remaining photons are then reflected/refracted according to the Fresnel equation. Thus, in this case, the `REFLECTIVITY` variable simulates something like absorbing dirt on the surface.[44] To specify the reflectivity of a surface between two dielectrics, the `TRANSMITTANCE` variable has to be used, where the reflectivity R derives from the transmittance T by $R = 100\,\% - T$.

4.2.8. Geant4 Extensions

Several extensions to the Geant4 software toolkit have been created by the community of Geant4 users over time. Their purpose is either to extend Geant4's potential or to simplify its usage for special applications. Thus, for one thing, the extensions increase the flexibility of Geant4 and allow for considering more effects of radiation interacting with matter, e.g. at the DNA scale. Furthermore, for frequently used applications like e.g. medical imaging, they help to minimise the necessary experience of the users, to reduce potential sources of errors, and to minimise the needed effort by the users. In order to demonstrate this and at the same time to show the necessity of a new extension focusing on the simulation of optical detector elements, some prominent examples are presented below:

- **G4beamline** [134, 135] is a simulation program optimised for simulating *particle-physics beamlines* and the interactions within. It extends Geant4 by a software framework that allows for performing simulations without the need of `C++`-skills. For this purpose, the available Geant4 features are limited to the needs of simulating "beam-

[43] Strictly speaking, this is a discrepancy with respect to the behaviour of "realistic" surfaces, which do not absorb photons. Photons that are not reflected at such a surface enter the next volume and undergo absorption corresponding to the attenuation length of the material, which is typically very short for optical photons in metals.

[44] One should note that Geant4 does not perform any optical process at a surface between two dielectrics that consist of the same material. In this case, it is **not** possible to simulate an absorbing dirt layer.

lines" in the broadest sense and common beamline elements are predefined. The setup description including the detector, the particles, and the physics (i.e. accessing the Geant4 framework) is done by a simple text file with user-friendly language.

- **GATE** (**G**eant4 **A**pplication for **T**omographic **E**mission) [136, 137] was created to simplify the application of Geant4 in the field of *medical imaging* (CT, SPECT, and (ToF-)PET). Nowadays, it also includes an extension regarding radiation therapy applications (GateRT). The purpose of **GAMOS** (**G**eant4-based **A**rchitecture for **M**edicine-**O**riented **S**imulations) [138, 139] is to simplify Geant4 simulations for nuclear medicine. Besides additional medical-specific commands, both extensions possess two major features in comparison to basic Geant4. The first is the additional software layer that allows to control GATE / GAMOS via macro files, thus the user does not need to have `C++`- or comprehensive Geant4-skills. Despite the possibly easier access to the creation of new simulations, using macro files in a standardised simulation program simplifies the exchange of existing simulations between the users. The second feature is the ability to read in clinical data (e.g. from a CT scan) and to convert it into physical volumes for simulations (e.g. for planning radiation therapies).

- **G4DNA** [140–142] is an extension that is fully included in the Geant4 public distribution. It extends Geant4 to the field of biological damage at the *DNA scale* that is caused by ionising radiation, especially by low-energy secondary particles, e.g. from interactions of high-energy particles with the tissue.

- **MEGAlib** (**M**edium **E**nergy **G**amma-ray **A**stronomy **lib**rary) [143, 144] is a set of software tools optimised for the simulation of *Compton telescopes* and the analysis of resulting simulation data. These tools are operated via ASCII files and thus can be used without `C++`-skills.

- In the field of *space flight*, several highly specialised Geant4-based simulation tools have been created. Some of them can be found on **ESA's Geant4 Space Users** webpage [145]. It includes GRAS (**G**eant4 **R**adiation **A**nalysis for **S**pace), MULASSIS (**MU**lti-**LA**yered **S**hielding **SI**mulation **S**oftware), and PLANETOCOSMICS (a tool for the simulation the interaction of cosmic rays with the electromagnetic field, the atmosphere and the matter of planets).

The specific challenges for the simulation of optical detector components (cf. subsection 4.2.7) were not addressed by any Geant4 extension up to now. Therefore, a new extension has been created in the scope of this thesis.

5. The GODDeSS[45] package

In the previous chapter, the particle-physics simulation tool Geant4, which has been used in the scope of this thesis, was introduced. This chapter will present the GODDeSS software tool, which the author has developed during the work on this thesis. The development of GODDeSS has been performed in collaboration with the other members of the research group of the Physics Institute III at RWTH Aachen University. The aim was to address and solve the main problems that limit Geant4's flexibility regarding the simulation of optical detector components and to lower the Geant4 skill level that is necessary for creating or modifying such a simulation.

5.1. The GODDeSS Framework

The GODDeSS framework is an extension of Geant4 (version 10.00.p02), which focusses on the simulation of optical detector components and adds new C++ object classes. It is publicly available [4][46], including its source code, the source code of a simple example simulation, and the documentation of the package as well as of the GODDeSS object classes and their functions. The example simulation demonstrates the basic application of GODDeSS, but can also be used as a basis for a new user-specific simulation. Additionally, since the GODDeSS framework is C++/Geant4-based, it is possible to adapt the single parts of GODDeSS to the user's needs.

Figure 5.1 illustrates how GODDeSS integrates into the Geant4 framework.[47] The diagram shows that the user only has to create basic GODDeSS objects and to provide some parameters (e.g. the property files to be used), whereas the rest (e.g. processing the property files or creating the volumes and calculating their translation and rotation) is done by GODDeSS automatically. As a result, it is easy to implement GODDeSS into an existing Geant4 simulation.[48] Of course, the user can always modify the GODDeSS code and change the actions that are taken internally, if necessary.

GODDeSS allows for a simple and fast creation or modification of complex optical detector setups, including their geometry and material properties. Thus, everyone, particularly also

[45] GODDeSS stands for "**G**eant4 **O**bjects for **D**etailed **De**tectors with **S**cintillators and **S**iPMs".
[46] For the future, there are also plans to include GODDeSS directly into the Geant4 software package as an extended example of usage.
[47] The Geant4 framework has to be set up by the user as described in section 4.2.
[48] A description how to implement the GODDeSS package into an existing Geant4 simulation can be found in [4] or in appendix C.2.1.

less experienced users, can quickly perform detailed Geant4 simulations of optical detector components. The main features are:

- *New object classes* that allow for an easy creation of *scintillator tiles*, *optical fibres*, *wrappings* and *paints*, and *photodetectors*. These object classes take care of the correct usage of Geant4's optical property variables. Additionally, they solve potential geometrical problems and provide an easier and more intuitive way of positioning objects.

- All *material properties* of the optical detector components are specified via *easy text files*. An example of such a property file can be found in appendix C.2.2. This method makes it easy to define the various properties without changing the Geant4 source code. Consequently, it also allows for the modification of properties without recompiling the simulation source code and thus easy batch processing.

- The object classes feature the *automatic registration of the physics processes* they need. This is done by extending the user-defined `PhysicsList`, if necessary. Thus, to a certain extent, the user does not have to pay attention to the registration of the physics processes. If necessary, the physics of the GODDeSS objects can be adapted by the user.

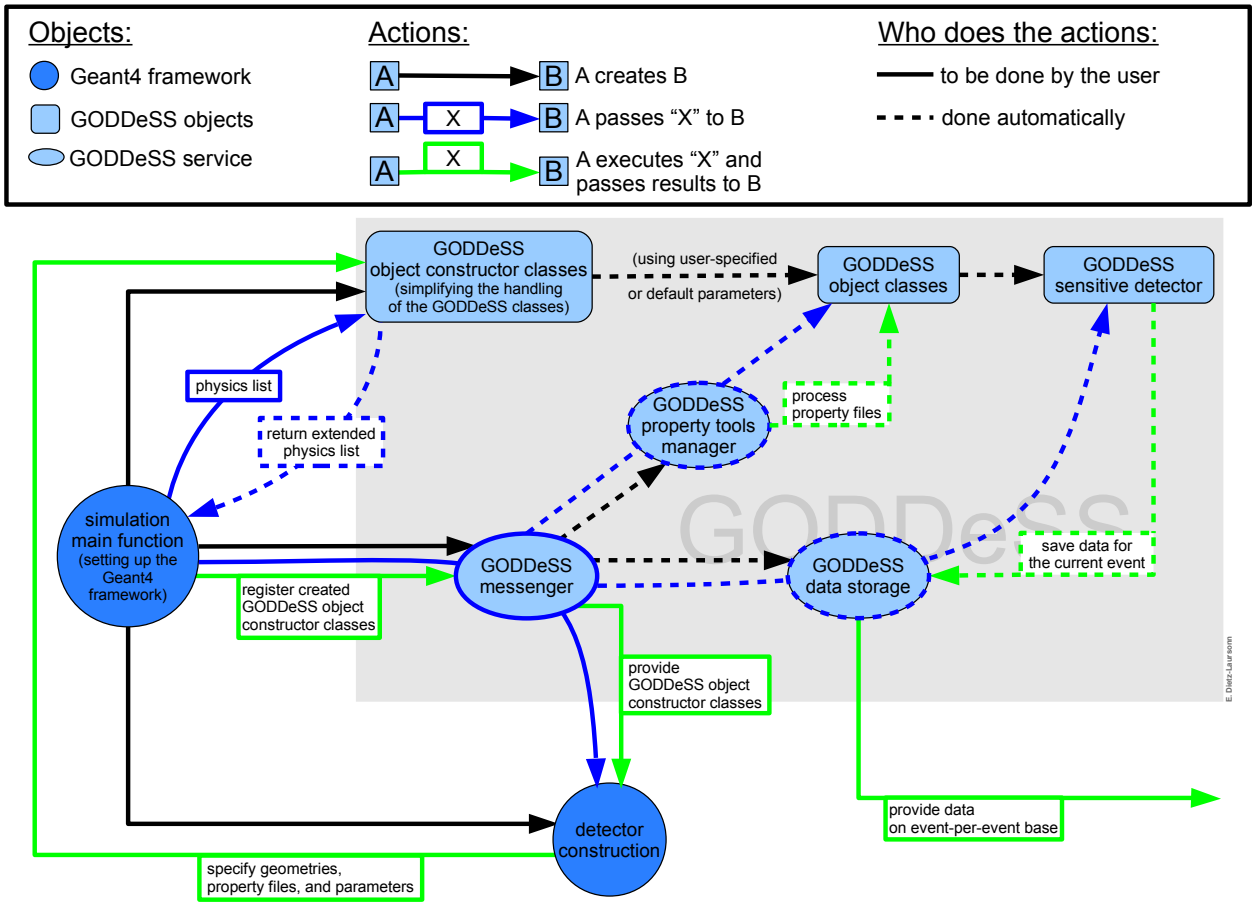

Figure 5.1.: Workflow of a Geant4 simulation using GODDeSS. The "Geant4 framework objects" (blue circles) are classes that are used to set up the Geant4 framework and to define the simulation parameters (cf. section 4.2). All other objects belong to the GODDeSS package.

- The object classes follow a totally *modular design*. Therefore, it is possible to include GODDeSS into existing detector simulations. Besides that, the simple example simulation, which is included in the public GODDeSS package, can serve as a basis for a new simulation.
- The internal data storage takes care of the *bookkeeping of particle tracks*, preventing multiple-counting of particles that created optical photons (cf. subsection 4.2.7).
- The internal management of the GODDeSS framework is designed for as much *automation* as possible. Thus, the user only has to deal with few upper-level-classes.

The parts that GODDeSS consists of will be described in detail below. They will be introduced in the order in which they need to be constructed in a simulation: scintillator tile → optical fibre → photodetector → wrapping. After introducing the object classes of GODDeSS, the remaining Geant4 problems will be examined.

5.1.1. Object Classes

The GODDeSS object classes create the corresponding objects (including geometry, materials, properties, placement,...) and allow to access them.

Scintillator Tile (`G4ScintillatorTile`)

A `G4ScintillatorTile` can be constructed by specifying its geometric dimensions[49], its material property file, and a reference to the mother volume. In the case of scintillators, a property file contains the scintillator's material properties (chemical composition, refractive index spectrum, absorption spectrum), surface properties (roughness, impact of the different reflection models), and scintillation properties (light yield, emission spectrum, rise and decay time). The `G4ScintillatorTile` can be placed by specifying its position and orientation relative to any volume. This *reference volume* does not necessarily have to be the mother volume, but can e.g. be another `G4ScintillatorTile`, belonging to the setup. Additionally, a parametrised placement is possible, i.e. a certain number of `G4ScintillatorTiles` with the same properties are positioned with a specified translation and rotation between two consecutive tiles. A graphical illustration of a `G4ScintillatorTile` with an optical fibre can be found in figure 5.2(a).

If desired, a *sensitive detector* is created automatically for each tile. By default, it collects the data of each primary particle entering the specific `G4ScintillatorTile`, as well as the (ionising) energy deposition of each particle within the tile. The data is stored in a data storage class and can be obtained for analysis purpose after each event.

All *physics processes*, which are required for a correct simulation of the tiles, are registered to Geant4 automatically.

[49] Currently, only cuboids are available.

Optical Fibre (`G4Fibre`)

Similar to `G4ScintillatorTiles`, `G4Fibres` are constructed by providing material properties and a reference to the mother volume. The material property file contains the fibre's material properties (chemical composition, refractive index spectrum, absorption spectrum), profile and edge length or radius, and the number and thickness of claddings. Additionally, the corresponding emission spectrum and decay time constant have to be included for WLS fibres, whereas for scintillating fibres the scintillation properties have to be defined. If desired, also the properties of an absorbing/reflecting coating can be specified, which is placed around the fibre like an additional, opaque cladding.

The `G4Fibre` can be placed by specifying its *length, position and orientation* or by providing *a starting and an end point*. In both cases, the values can be specified relative to an arbitrary reference volume. Like for `G4ScintillatorTiles`, parametrised placement is possible. Additionally, *round or square* fibres, *straight or bent* fibres, and *cut, mirrored, or roughened* fibre ends can be chosen and the fibre can be wrapped with an absorbing or reflecting *coating* with modifiable gap in between. Figure 5.2 illustrates a rather complex fibre setup within a scintillator tile (a) and the profile of a simulated round multi-cladding-fibre (b).

Furthermore, a *sensitive detector* can record the particles reaching the `G4Fibre`. This detector can be extended to record more information.

The `PhysicsList` that is registered to Geant4 is extended by the *optical physics processes*, if required.

In comparison to other optical detector components, the simulation of optical fibres often poses an *extraordinary challenge*: Optical fibres are likely to protrude from their mother

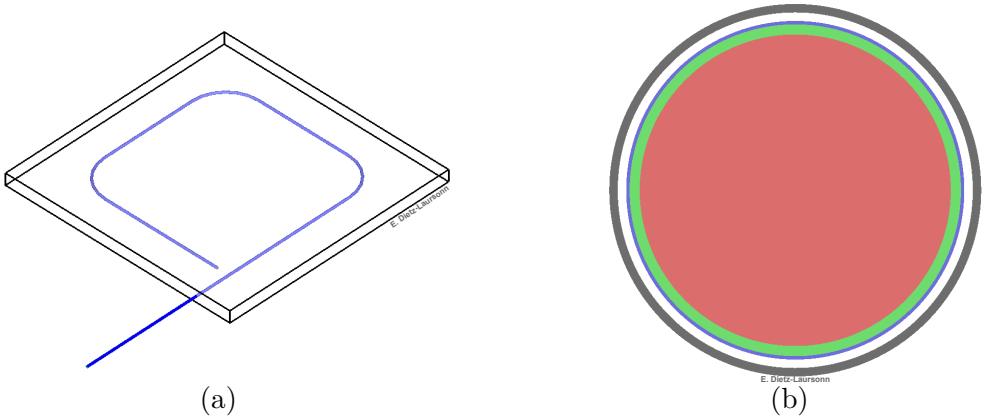

(a) (b)

Figure 5.2.: **(a):** Relatively complex fibre setup within and protruding from a scintillator tile. If GODDeSS is used for the simulation, this setup can be generated by the user with 8 lines of code (one for the scintillator tile and one for each of the three bent and four straight fibre parts). **(b):** Profile of a simulated round multi-cladding-fibre. The big red part represents the fibre core (which may be light-guiding, scintillating, or wavelength-shifting), whereas the two claddings are illustrated in green and blue. The outer grey part represents the optional absorbing/reflecting coating.

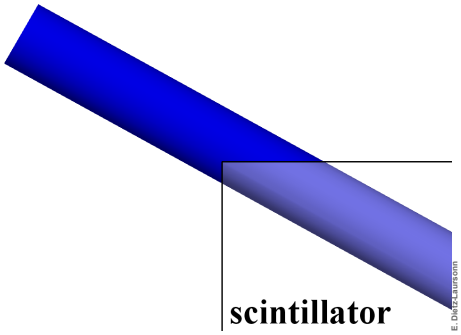

Figure 5.3.: An optical fibre protruding from the edge of a scintillator tile, which is its mother volume. This requires a complex separation of the fibre into parts inside (light-blue) and outside (dark-blue) the scintillator tile. When using GODDeSS, this is performed automatically.

volume, e.g. if they are combined with scintillators (cf. figures 5.2 and 5.3). This might result in geometrical problems (cf. subsection 4.2.7) and makes the handling of optical fibres challenging, when using the basic Geant4 classes. Depending on how complicated the fibre setup is (e.g. a fibre protruding from a scintillator tile in one of its edges), dividing the optical fibre is not trivial. As a major improvement of the GODDeSS extension of Geant4, the user does not have to pay attention to this any more. The `G4Fibres` are automatically divided into single pieces and distributed to the different mother volumes. More precisely, `G4Fibres` are only distributed to their mother volume, their "grandmother" volume (the mother volume of their mother volume), and their "aunt" volumes (all volume having the "grandmother" volume as mother volume). This restriction is due to the fact that it is not possible in Geant4 to obtain the translation and rotation between two arbitrary volumes.

Photodetector (`G4PhotonDetector`)

To *detect optical photons* that have been produced in the optical detector components and to record their properties, GODDeSS provides a `G4PhotonDetector` object class, which can be understood as a pseudo-photodetector, as it detects photons with 100 % efficiency and does not suffer from any noise or saturation effects. Therefore, it can be used to determine the number and properties of the optical photons, reaching a photon detection device at some position in a simulated setup. This is very useful when comparing different setups, e.g. in order to optimise the detector design for maximum signals or for fast signals. Of course, the results cannot be compared to measured data directly. If this is needed, a more sophisticated photodetector has to be simulated, e.g. like the SiPM described in the next paragraph. The structure of the `G4PhotonDetector` is illustrated in figure 5.4.

A `G4PhotonDetector` can be constructed by specifying its edge length and mother volume. It can be placed via its position and viewing direction relative to any volume (e.g. a scintillator tile or optical fibre).

For every `G4PhotonDetector` that is constructed, a *sensitive detector* is created automatically. It collects the data of each optical photon hitting the sensitive area of a `G4Photon-`

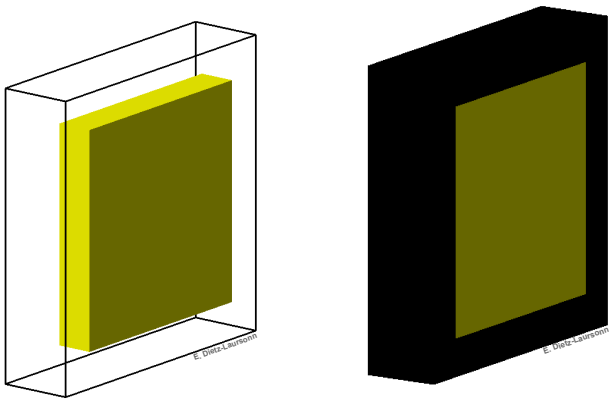

Figure 5.4.: The GODDeSS's photodetector with its sensitive volume (yellow) and an absorbing cover (black). For visibility purpose, the thickness of the absorbing cover is increased by a factor of 100 and additionally shown transparent in the left picture.

`Detector`, saves the data to the data storage class, and "kills" the optical photons. Afterwards, the data can be passed to a dedicated simulation, to study or optimise the photon detection itself. For example, different types of photodetectors or SiPM models with different cell configurations can be simulated (cf. next paragraph) and exposed to the photons recorded by a `G4PhotonDetector`, in order to choose a suitable photodetector for the previously simulated detector geometry.

Silicon Photomultiplier (`G4SiPM`)

The full-scale SiPM simulation can be performed with the external `G4SiPM` software package [147, 148], which is another Geant4 extension that has been developed at the Physics Institute III at RWTH Aachen University. It allows for the *realistic simulation* of the SiPM's behaviour concerning geometry and housing as well as temperature and over-voltage depen-

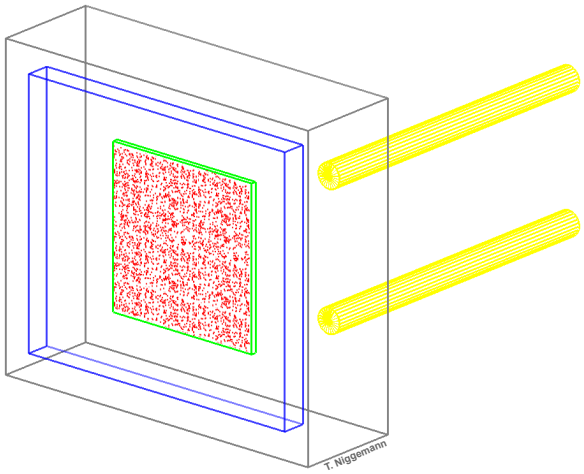

Figure 5.5.: Illustration of a `G4Sipm` with its housing (grey), window (blue), and sensitive area (green). The red dots show the positions of photon hits that have been registered by the SiPM (taking its PDE and fill factor into account).

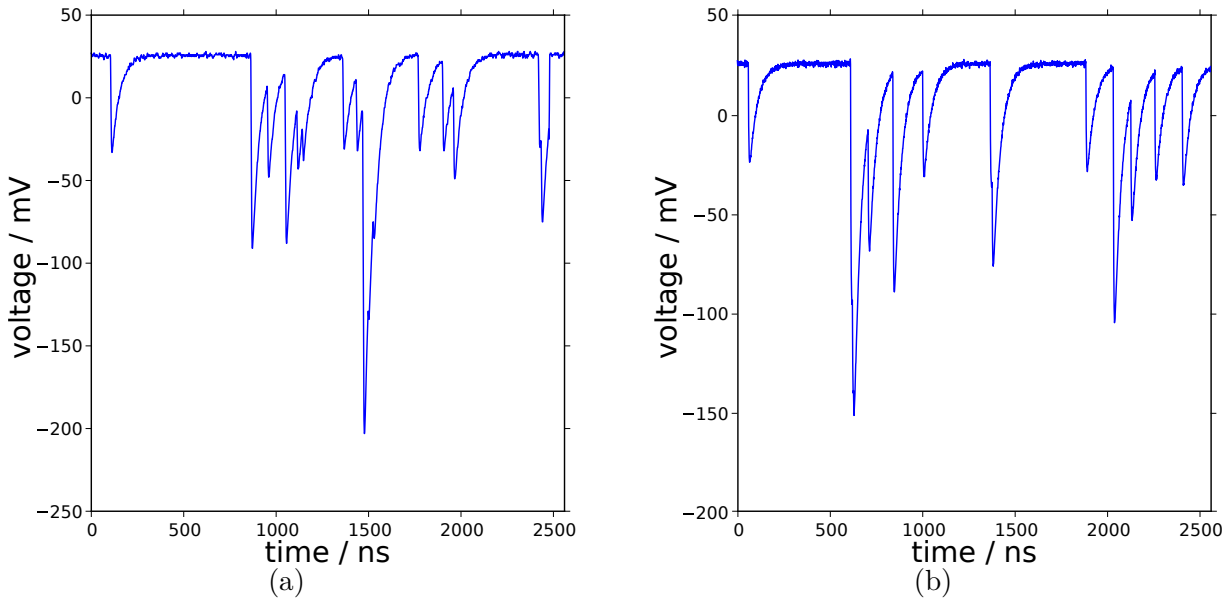

Figure 5.6.: Typical oscilloscope reading of an amplified SiPM signal **(a)** and a voltage trace simulated with G4Sipm **(b)**. The simulated voltage trace is well reproducing the characteristics of measured SiPM signals. Adapted from [146].

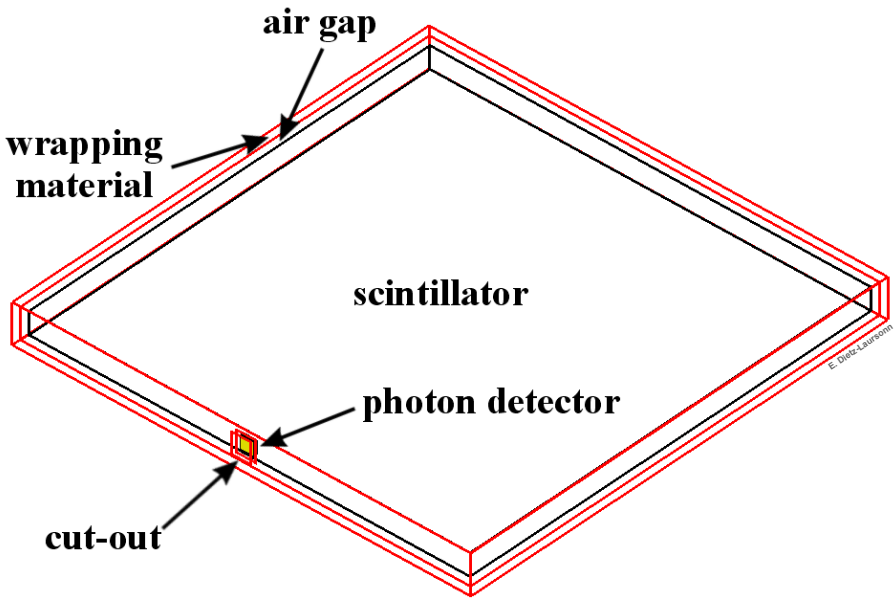

Figure 5.7.: Setup consisting of a wrapped scintillator tile with a photodetector. To make them visible, the dimensions of the wrapping as well as the gaps between wrapping and scintillator or photodetector have been enlarged when generating the picture.

dency (PDE, thermal and correlated noise, recovery time). This is illustrated in figure 5.5. As a result, the user can either obtain a list of cell triggers for further processing in his own electronics simulation or a voltage trace similarly to an oscilloscope reading (cf. figure 5.6). The properties of the SiPM can be provided by a text file.

Wrapping (`G4Wrapping`)

The `G4Wrapping` plays an exceptional role in the GODDeSS framework. It can only be applied to a `G4ScintillatorTile`. To construct a wrapping volume, its property file and a reference to the corresponding `G4ScintillatorTile` have to be specified. A wrapping property file contains the number and thickness of wrapping layers, their material properties (chemical composition, refractive index spectrum, absorption spectrum) and surface properties (roughness, impact of different reflection models), as well as the thickness of a potential air gap. If a `G4ScintillatorTile` is to be wrapped, the wrapping layers are automatically placed around it. All other volumes, which have been created at this stage and are overlapping with the wrapping, are automatically cut out of the wrapping volume(s). This is illustrated for a wrapped scintillator tile with a photodetector in figure 5.7.

If desired, a sensitive detector is created, by default saving the data of traversing primary particles.

Other object classes of GODDeSS

There are several other object classes of GODDeSS that do not represent parts of a detector:

- *GODDeSS messenger*: This class is used internally to handle classes and settings and to allow for user access to the GODDeSS framework.
- *Property tools*: A class for parsing the properties files.
- *Data storage class*: The purpose of this class is to internally save the data recorded by the sensitive detectors. The data is sorted according to the `TrackID` of the `G4Tracks`, which is unique to each particle of a `G4Event`. Thus, this class also deals with the fact that the particle trajectories may appear to consist of several `G4Tracks` instead of only one (cf. subsection 4.2.7). If not taken into account, this could lead to wrong data acquisition. The data can be retrieved by the user after each event.
- *General particle source*: The user is free to choose the particle type, the position and dimensions of the source, as well as the direction and energy distribution of the particles. This input can also be supplied by a text file.
- *Photon source*: This source re-emits the photons recorded beforehand by a `G4PhotonDetector`, e.g. to study diverse photodetectors and optical couplings.

5.1.2. Solved Challenges and Remaining Issues

As described above, most of the challenges of using the basic Geant4 classes to simulate optical detector components are solved by GODDeSS. Many issues the user normally has to pay attention to, are automatised within its framework. Consequently, a setup like the one shown in figure 5.2 can be created with a few lines of code, including material and surface definition.

However, some problems are not eliminated. Using LUT surfaces may still lead to unexpected results like described in paragraph "Optical Physics Peculiarities" of subsection 4.2.7 and in section 6.11. Likewise, the visualisation restrictions due to boolean volumes like illustrated in figure 4.6 are still existing.

6. Consistency Check of Material Property Input and Physics Processes

After the GODDeSS framework has been introduced in the previous chapter, the following chapters will describe the efforts, which have been made to validate the proper functioning of the GODDeSS framework. The next chapters will present adjustments that had to be implemented to resolve severe deviations between simulations and measurements or manufacturer data as well as the validation against measurements with complete optical detectors, consisting of several elements. Beforehand, the correct operation of Geant4/GODDeSS on source code level will be tested in this chapter. This includes three topics:

For one thing, the correct processing of the material property input. This means, it has to be verified that the simulated results of the material properties are in agreement with the values that have been provided as input for the corresponding simulations. This has been investigated for the material properties, which are important in case of optical detector components:

- the emission spectra and decay times of light-creating processes (scintillation and WLS) as well as the scintillation light yield
- the reflectivity spectra of wrapping materials
- the bulk attenuation lengths of optical photons for scintillating and WLS materials as well as the gamma ray attenuation length of the scintillators

For another thing, the correct implementation of important physics processes in Geant4[50] has to be verified. This applies to:

- the influence of surface roughness
- the reflectivity as a function of refractive indices (Fresnel equation)
- the energy change during the WLS process
- the Cherenkov spectrum
- the application of LUT surfaces

Furthermore, the correct modelling of the optical fibres, which are the most complex optical components in GODDeSS, has to be tested with respect to available manufacturer data concerning:

- the trapping efficiency
- the bending loss

The setups have been created using the GODDeSS object classes. The material properties, which have been used for modelling the optical detector components, their references, and a description of their implementation in the simulation can be found in appendix D.

[50] Of course, also Geant4 has to be validated. The user should not just rely on its correct functionality.

6.1. Emission Spectra

To validate the correct processing of the emission spectrum input in simulations with Geant4/GODDeSS, the simulated scintillating materials (BC-404, BC-408, and BC-452) were excited with traversing muons. The emitted scintillation light was used for exciting the embedded WLS fibres (BCF-92 and Y-11). The initial energy of each optical photon that was created by scintillation or WLS was then filled into histograms.

When using only a small number of additional data points to linearly extrapolate the original emission spectra provided by the manufacturers (cf. figures D.2 and D.9), step-structures appeared in regions where the original spectrum had been extended. Therefore, a simple test emission spectrum was simulated, in order to find the reason for this unexpected behaviour. The result is shown in figure 6.1(a). It shows that in Geant4, the simulated emission spectrum is not interpolated by a straight line between two points of the spectrum, but the mean of the values of two neighbouring points is applied as constant value between these points.

As consequence of this *interpolation by average determination* of emission spectra in Geant4, parts of emission spectra that are not constant, which is usually the case for realistic refractive indices, have to be specified with a high density of data points. Thus, the linear extensions of the emission spectrum input with respect to the manufacturer data were improved by adding more data points. The resulting emission spectra of the simulated scintillators and WLS fibres is illustrated in figure 6.1(b). *Poisson statistics* has been used to determine the

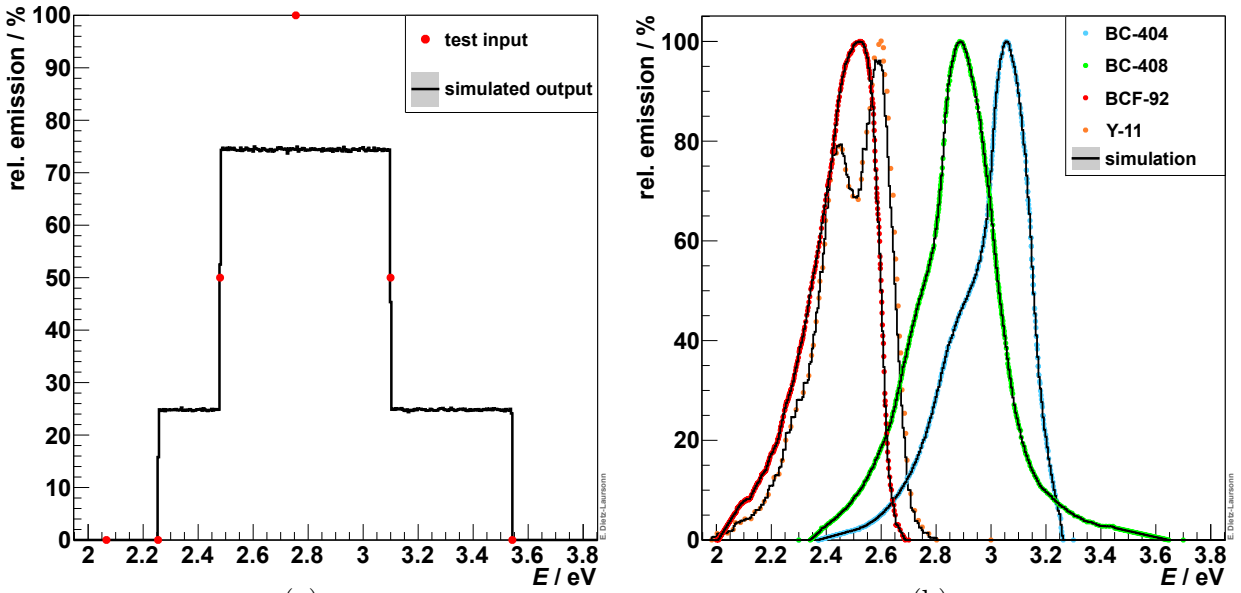

(a) (b)

Figure 6.1.: **(a):** Test of the processing of (relative) emission spectra in Geant4, showing that simulated emission spectra are not interpolated by a straight line between two points of the spectrum. **(b):** Simulated emission spectra of the scintillators (BC-404, BC-408, and BC-452 (its emission spectrum equals BC-408)) and WLS fibres (BCF-92 and Y-11). The dots represent the input used for the simulations, the lines illustrate the corresponding output. The deviation between input and simulation output for Y-11 is caused by a significant overlap of the emission spectrum of Y-11 with its WLS absorption spectrum.

statistical uncertainty of the simulation output. All spectra have been normalised by their maximum emission value, with the exception of the spectrum of Y-11. The output of the simulated emission spectra precisely fits to the input, with the exception of the spectrum of the WLS fibre Y-11. The Y-11-spectrum has therefore been normalised to match the peak around 2.45 eV

However, this deviation between the input spectrum and the simulated output is not an error but a result of the overlap between the emission spectrum and the WLS absorption spectrum of Y-11 (cf. figure D.8): As the photons cannot gain energy during the WLS process (also cf. section 6.9), it is only possible to emit photons on the energy ranges of the emission spectrum that are below the energy of the initial photon. Thus, an overlap of the emission spectrum with the WLS absorption spectrum results in a shift of the proportions of the former, if the initial energies of the exciting photons include the overlap region. Accordingly, the deviations disappear when restricting the initial photon energies to values above the emission spectrum (or likewise, restricting the WLS absorption spectrum to this energy range). Therefore, this is also done by the manufacturer when measuring emission spectra [99]. In contrast, the consideration of this effect is of course important and desired when simulating WLS fibres as parts of optical detector components.

All together it can be summarised that the emission spectra behave as expected, as long as their non-constant ranges are specified with a high density of data points.

6.2. Decay Times

The de-excitation of the excited states during the scintillation or the WLS process can be described as decay processes with specific decay times. This leads to the fact that the difference of the creation time t_{creation} of scintillation or WLS photons to the corresponding excitation time $t_{\text{excitation}}$ follows an exponential distribution. To validate this and the correct processing of the input decay times in Geant4/GODDeSS, the simulated scintillating materials (BC-404, BC-408, and BC-452, which has the same decay time as BC-408) were excited with traversing muons and the emitted light was used for exciting the embedded WLS fibres (BCF-92 and Y-11, which have the same decay time). For each scintillation or WLS photon, the excitation time was determined from the properties of the corresponding mother particle (which was identified via its `TrackID`). For **WLS photons** by

$$t_{\text{excitation}} = t_{\text{absorption}}$$

and for **scintillation photons** by

$$t_{\text{excitation}} = t_{\text{starting point}} + \frac{\left|\vec{r}_{\gamma\text{ creation}} - \vec{r}_{\text{starting point}}\right|}{\bar{v}_{\text{mother (last step)}}}.$$

$\bar{v}_{\text{mother}}$ is the mother particle's mean velocity during the current step, the other variables are illustrated in figure 6.2.

The resulting time $t = t_{\text{creation}} - t_{\text{excitation}}$ of each optical photon that was created by scintillation or WLS was then filled into cumulative histograms. The resulting distributions,

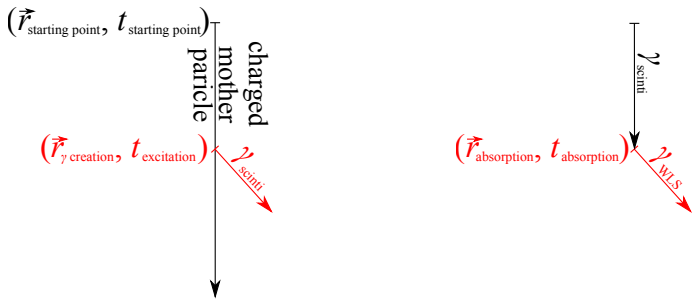

(a) scintillation (b) WLS

Figure 6.2.: Geometry for excitation time determination for the scintillation process **(a)** and the WLS process **(b)**. The arrows represent `G4Steps` of the corresponding particle.

which are presented in figure 6.3, were normalised to the entry of their first bin. Thus, the distributions represent the fraction of the remaining excited states as a function of the time elapsed since the excitation. *Poisson statistics* has been used to determine the statistical uncertainty of the simulation output.

To determine the decay times, an exponential fit was performed to the distributions. Whereas the fit was performed over the whole t-range for the WLS process, the fits for the scintillation process were restricted to values with $t \geq 5\,\text{ns}$. This restriction was imposed because of the deviation of the simulated results from an exponential distribution for small values of t. The reason for this deviation is the contribution of a rise time to the scintillation time spectrum, in addition to the decay time. In contrast, the WLS process does not have a finite rise time. The fit results ($(1.8004 \pm 0.0002)\,\text{ns}$, $(2.1007 \pm 0.0002)\,\text{ns}$, and $(2.70050 \pm 0.00006)\,\text{ns}$) match the input values (1.8 ns, 2.1 ns, and 2.7 ns) for BC-404, BC-408/BC-452, and BCF-92/Y-11, respectively.

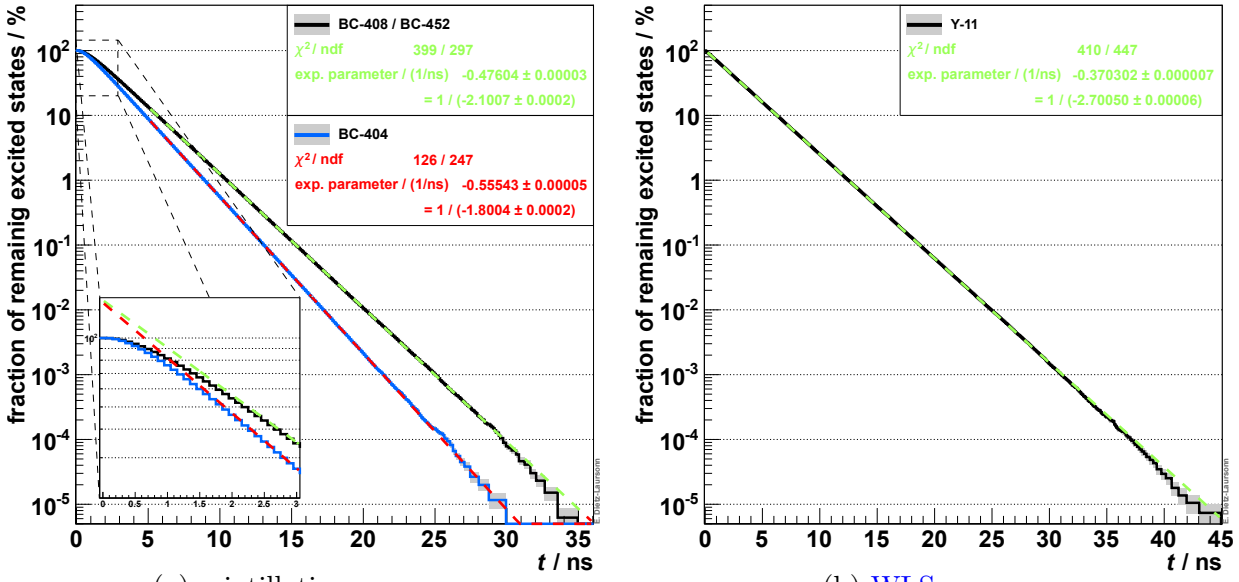

(a) scintillation process (b) WLS process

Figure 6.3.: Remaining excited states of the scintillation process **(a)** and the WLS process **(b)** (simulated with GODDeSS) as a function of the elapsed time t since the excitation. The corresponding decay times have been determined by exponential fits to the distributions.

6.3. Scintillation Light Yield

The light yield of scintillating materials (i.e. the number of scintillation photons per energy deposition of the individual traversing charged particle) is expected to be Gaussian distributed around the specific mean light yield of the material (cf. subsection 3.2.2). In order to validate this for Geant4, the simulated scintillating materials (BC-404 and BC-408) were excited with traversing muons ($\beta\gamma = 3.5$, i.e. $E_\mu = 278.9\,\text{MeV}$). The simulations were performed twice, with and without taking saturation according to Birks' equation (equation (3.1)) into account. This was done to validate the correct simulation of the saturation. For each muon, the scintillation photons were counted, their number was normalised to the energy deposition of the muon and filled into a histogram. The result is presented in figure 6.4. The statistical uncertainty of the simulation output has been determined via *Poisson statistics*.

Gaussian functions have been fitted to the simulated distributions in order to validate their Gaussian behaviour and to determine their mean values. **Without** considering the **saturation effects**, the resulting mean light yield is (13599 ± 2) photons/MeV and (12800 ± 2) photons/MeV for BC-404 and BC-408, respectively. These values perfectly match the input values of 13600 photons/MeV and 12800 photons/MeV (cf. table D.3). Additionally, the χ^2/ndf-values show the good agreement between the Gaussian function and the light yield distributions.

When taking the **saturation effects** into account, the results of the fits are reduced to (13301 ± 3) photons/MeV and (12519 ± 4) photons/MeV for BC-404 and BC-408, respectively.

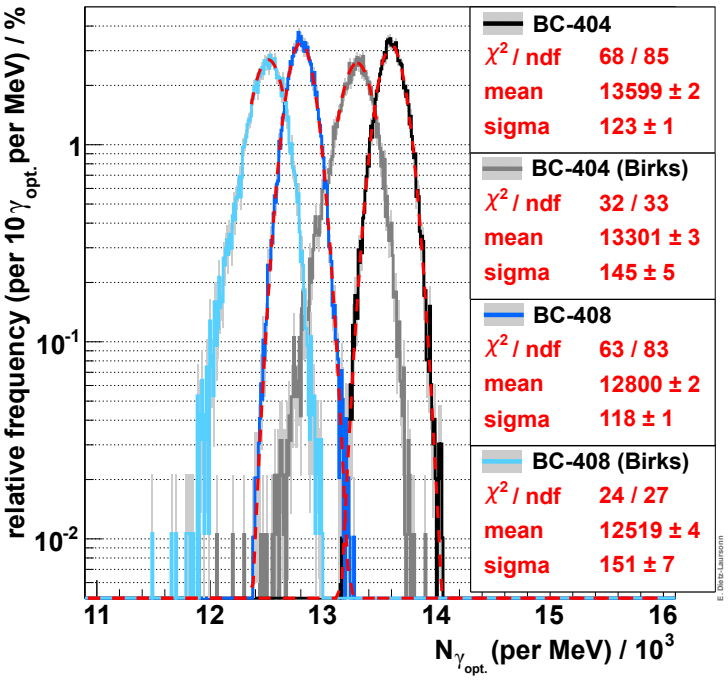

Figure 6.4.: Light yield distribution of the simulated scintillating materials (BC-404 and BC-408) for simulations with (light-blue/grey lines) or without (dark-blue/black lines) considering saturation effects. The dashed red lines represent the Gaussian fits to the simulated distributions, the corresponding fit results are given in the legends.

This corresponds to a reduction to $\approx (97.80 \pm 0.03)\,\%$. As the MPV of the simulated energy deposition is $\approx 1.64\,\mathrm{MeV/cm}$, only a reduction to $\approx 98.22\,\%$ would be expected ($C_\mathrm{B} = 0.0115\,\frac{\mathrm{g}}{\mathrm{MeVcm^2}}/\rho = 0.111\,\frac{\mathrm{mm}}{\mathrm{MeV}}$, cf. table D.3). Thus, the correction obtained from the simulation results is significantly larger than expected.

The reason for this is the non-linearity of Birks' equation with respect to the energy deposition: higher energy depositions per path length undergo larger reductions. As a consequence, the resulting correction is larger[51] when calculating it for several path segments than for calculating it for the full path, or mathematically:

$$\sum_{j=1}^{N>1}\left[N_\gamma\big(\Delta E_j, \Delta x_j\big)\right] \leq N_\gamma\left(\sum_{j=1}^{N>1}\left[\Delta E_j\right], \sum_{j=1}^{N>1}\left[\Delta x_j\right]\right) \tag{6.1}$$

with the integrated Birks equation (cf. equation (3.1)):

$$N_\gamma(\Delta E, \Delta x) = \mathscr{L} \cdot \frac{\frac{\Delta E}{\Delta x} \cdot \Delta x}{1 + C_\mathrm{B}\frac{\Delta E}{\Delta x}} = \mathscr{L} \cdot \frac{\Delta E}{1 + C_\mathrm{B}\frac{\Delta E}{\Delta x}},$$

where ΔE_j is the energy deposition on the jth path segment with a length of Δx_j. The equality sign in equation (6.1) is only valid for the case that all $\frac{\Delta E_j}{\Delta x_j}$-values are the same or for $C_\mathrm{B} = 0$. The validity of relation (6.1) was demonstrated by some easy mathematical simulations, which are presented in appendix E. In Geant4, the number of scintillation photons is calculated for every `G4Step` from its length and from the corresponding energy deposition. As this corresponds to the left part of relation (6.1), the resulting correction is larger than expected from the MPV of the total energy deposition distribution, as mentioned above.

Additionally, the energy dependence of Birks' equation leads to another effect: **Theoretically**, Birks' constant C_B is a material constant, i.e. does not depend on the geometry, the way of its determination, etc.. **In contrast**, the measured values of C_B do depend on the way they were determined. This becomes clear using the example of the measurements in the original work of Birks [96]. There, the number of scintillation photons of particles that were absorbed within the scintillating material was plotted against $\left(\frac{\mathrm{d}E}{\mathrm{d}x}\right)_\mathrm{ion.}$-values that were calculated from the initial particle energies via the Bethe-Bloch equation. Obviously, a C_B-value determined from these data would probably not be applicable to particles that are not absorbed, as $\left(\frac{\mathrm{d}E}{\mathrm{d}x}\right)_\mathrm{ion.}$ is higher shortly before the absorption than at the beginning of the path. Consequently, the implementation of saturation effects according to Birks' equation into simulations as well as the verification of the correctness of the simulation results is much more complex than it seems to be at first glance. Purely formal, Birks' equation is correctly implemented in Geant4 on `G4Step` level. This corresponds to values of C_B that were measured for MIPs (far from being absorbed during the measurement) and have been corrected for the difference between the step length in Geant4 and the effective path length during the measurement (smaller saturation effect over the same distance for a higher number of segments, cf. equation 6.1).

In addition to the shift of the MPV of the light yield distributions in figure 6.4, the shape of the distributions changes significantly. The reason for this effect is the Landau distribution

[51] This means, the resulting total number of photons is smaller.

of the energy deposition of the muons (cf. paragraph "Fluctuation of the Energy Loss" of subsection 2.1.1). For the high-energy tail, the Birks corrections are larger. Therefore, it forms a tail to small numbers of photons/MeV after normalising the number of scintillation photons to the energy deposition of the muons. For this reason, the Gaussian fits have only been performed on a small region around the MPV of the corrected light yield distributions.

Drawing a conclusion, the results from this section can be summarised as follows: Without considering saturation effects, the scintillation light yield meets the expectations when being simulated with GODDeSS/Geant4. When considering saturation effects, the scintillation light yield is reduced, as it is qualitative expected. Nevertheless, the energy dependence of the correction according to Birks' equation leads to the fact that measured values of C_B depend on the way they were determined. This makes the quantitatively correct simulation as well as the quantitative comparison of simulation results and measurements rather complex. The implementation in Geant4 corresponds to using values of C_B that were measured for particles far from being absorbed during the measurement. Additionally, they have to be corrected for the difference between the step length in Geant4 and the effective path length during the measurement (smaller saturation effect over the same distance for higher number of segments, cf. equation 6.1). It is the responsibility of the users to decide carefully for their specific application, whether this is the correct way of simulating it or whether the possible deviations are negligible.

6.4. Reflectivity Spectra

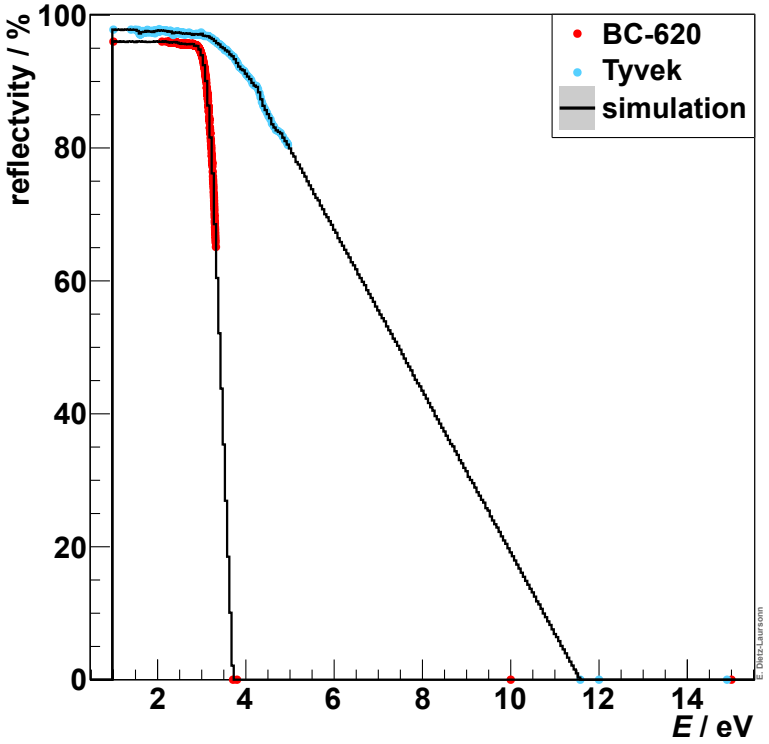

Figure 6.5.: Reflectivity spectra of the simulated wrapping materials (BC-620 and Tyvek). The dots represent the input used for the simulations, the lines illustrate the corresponding output.

For validating the correct processing of the input reflectivity spectrum in Geant4/GODDeSS, optical photons with varying energies were shot vertically onto the surface of the simulated wrapping materials (BC-620 and Tyvek). The reflected photons were detected using the `G4PhotonDetector` and their energy was filled into a histogram. Afterwards, the reflectivity was determined by normalising each energy bin to the corresponding number of initial photons and the statistical uncertainty was estimated via *Clopper-Pearson confidence intervals*[52] with a confidence level of 68.3 %[53]. Figure 6.5 shows the resulting distributions together with the digitised manufacturer data. The simulated reflectivity spectra perfectly describe the digitised manufacturer data. In contrast to emission spectra (cf. section 6.1), this is also true for the regions where the original spectra had been extended linearly with only a small number of additional data points.

6.5. Bulk Attenuation Length for Optical Photons

The **bulk attenuation length** is the pure attenuation length of the *material*, i.e. it describes the attenuation of a photon beam that is traversing the material following a straight line. In contrast to this, the **signal attenuation length** additionally considers the *geometry* and *optical surface properties* of the material, i.e. losses at optical surfaces as well as longer effective path lengths due to reflections and indirect propagation are taken into account.

To validate the correct processing of the bulk attenuation lengths, long volumes of material have been simulated and optical photons were shot straight through these volumes. For each optical photon, the maximum path length inside the volume was filled into a cumulative histogram. In case of the energy-dependent bulk attenuation lengths (for the WLS materials), the path length of optical photons with different energies were filled into separate histograms. The statistical uncertainty of the simulation output has been determined using *Poisson statistics*. All distributions were normalised to the entry of their respective first bin. Thus, they represent the fraction of the remaining photons in the beam as a function of the covered path length inside the material. The bulk attenuation lengths were determined by fitting exponential functions to the distributions.

Figure 6.6 shows the resulting distributions for the **scintillating materials** (BC-404 as well as BC-408 and BC-452, which possess the same bulk attenuation length). The fits return bulk attenuation lengths of (1599.72 ± 0.02) mm and (3801.26 ± 0.05) mm for BC-404 and BC-408/BC-452, respectively. These values are in a good agreement with the input values of 1600 mm and 3800 mm, respectively.

For **WLS materials** (i.e. the materials that the core of the WLS fibres consist of) in Geant4, the bulk attenuation length consists of two energy-dependent parts: the "normal" attenuation length of the base material (cf. figure D.7) and the attenuation length of the additives (cf. figure D.8), which contributes to the WLS process. In contrast to the former,

[52] In contrast to binomial errors $\sigma_\epsilon^{\text{bin}} = \sqrt{\frac{\epsilon(1-\epsilon)}{N}}$, which are often chosen to calculate the errors of efficiencies ϵ or efficiency-like parameters, Clopper-Pearson confidence intervals [149] determine asymmetric errors, which are non-vanishing in case of $\epsilon = 0\,\%$ or $\epsilon = 100\,\%$.

[53] In the scope of this thesis, the Clopper-Pearson confidence intervals have always been determined with a confidence level of 68.3 %.

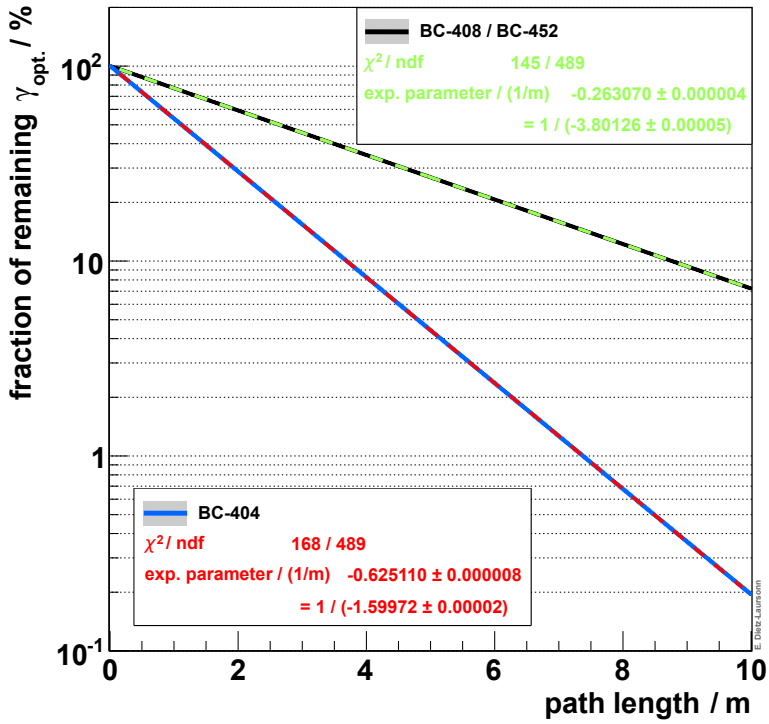

Figure 6.6.: Remaining photons in the simulated photon beam as a function of the covered path length inside the scintillating materials (BC-404, BC-408, BC-452). The corresponding bulk attenuation lengths have been determined by exponential fits to the distributions.

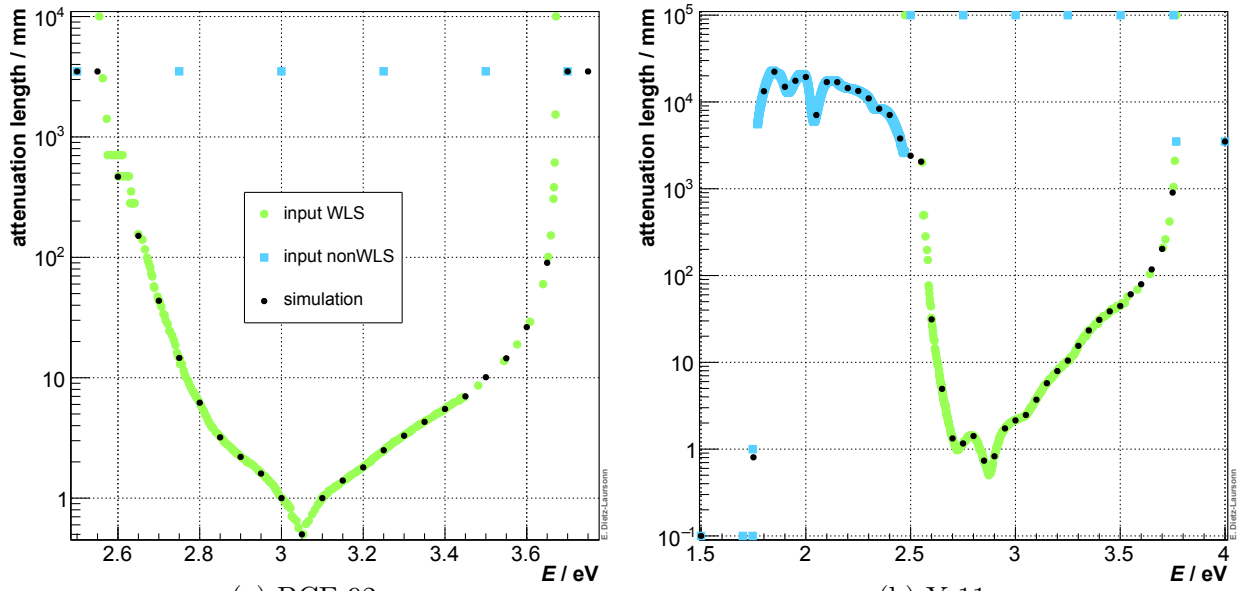

(a) BCF-92 (b) Y-11

Figure 6.7.: Bulk attenuation length spectrum of the WLS materials of the optical fibres BCF-92 **(a)** and Y-11 **(b)**. The green dots and blue squares represent the input used for the simulations (WLS and "normal" attenuation, respectively), the black dots illustrate the simulation output, i.e. the effective attenuation length. For each point of the output distribution, the bulk attenuation length has been determined by exponential fits to a distribution like shown in figure 6.6. The statistical uncertainties (from the fits) are below 0.1 ‰.

the latter triggers the emission of a WLS photon after an optical photon has been absorbed. The effective bulk attenuation length, which should be found in the simulation output, is the superposition of these two parts. Figure 6.7 summarises the two input spectra together with the simulation output. The statistical uncertainties (from the fits) are below 0.1 ‰. The simulation output perfectly reproduces the input spectra and the effective attenuation length is correctly determined from the superposition in Geant4.

This means in summary that the bulk attenuation length of materials is processed within GODDeSS/Geant4 as expected.

6.6. Scintillator Gamma Ray Attenuation Length

The manufacturer Saint-Gobain states values of the gamma ray attenuation length (i.e. the attenuation length of high-energy photons) for its scintillating materials [78, 150]. In Geant4 or GODDeSS, this property cannot be specified explicitly, but the composition of the simulated material implies its values. Thus, strong deviations between the manufacturer data and the gamma ray attenuation length of the simulation might indicate incorrect simulated material compositions.

To determine the gamma ray attenuation length, high-energy photons (`G4Gamma`s with energies corresponding to those of the manufacturer data) were shot into $350 \times 350 \times 4000\,\mathrm{mm}^3$-volumes of the simulated scintillating materials (BC-404, BC-408, and BC-452 with 5 % lead). For each photon, the path length inside the scintillating material was determined and filled into a cumulative histogram. Thus, the distributions represent the fraction of the remaining photons as a function of the path length. The statistical uncertainty of the simulation output was determined via *Poisson statistics*. All distributions were normalised to the entry of their first bin. Examples are presented in figure 6.8.

For each photon, three different path lengths were determined:

- the full path length of the photon inside the scintillating material,
- the maximum depth (i.e. the maximum distance in terms of the z-coordinate of the scintillator volume) that was reached by the photon inside the scintillating material,
- the path length of the photon inside the scintillating material before the first interaction of the photon.

Because of the *photon absorption law* (cf. equation (2.18)), an exponential behaviour of the path length distributions is expected. The **"first interaction"**-distributions fulfil this expectation for each of the simulated energies (cf. the bottom plots of figure 6.8). In contrast, the distributions for **full path length** and for **maximum depth** deviate from an exponential behaviour for high photon energies and low path lengths (cf. the top and middle plots of figure 6.8(b)). This is due to the fact that the photon absorption law strictly speaking does not describe the absorption of photons but the *intensity loss* of photon beams *by absorption or scattering*. This corresponds to the path length of the photons to the first interaction, rather than to the maximal depth or the full path length in the material. As a result, the

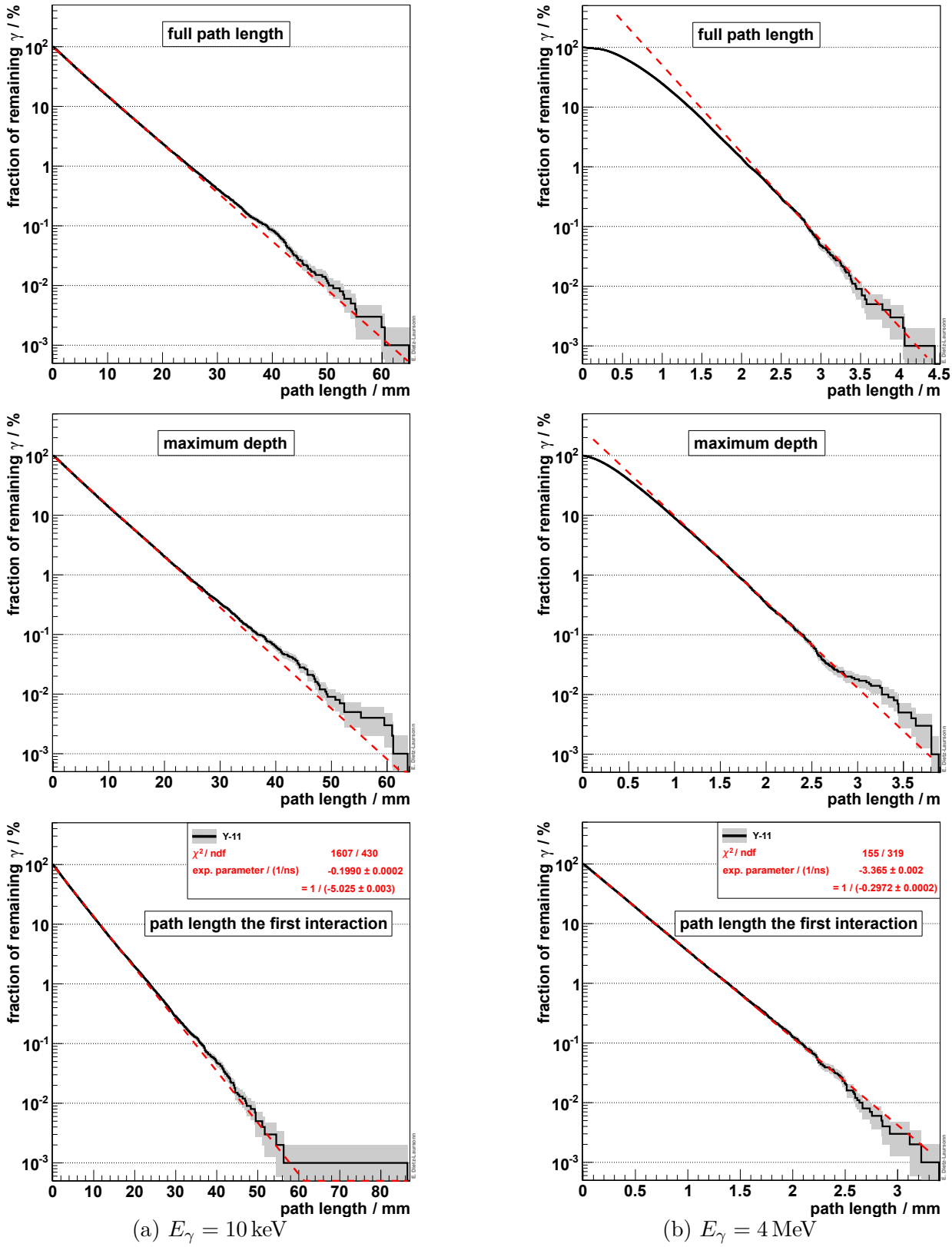

(a) $E_\gamma = 10\,\mathrm{keV}$ (b) $E_\gamma = 4\,\mathrm{MeV}$

Figure 6.8.: Example distributions of the fraction of remaining photons as a function of the full path length **(top)**, maximum depth **(middle)**, and the path length to the first interaction **(bottom)**. The simulated scintillating material is BC-408 and the photon energy is 10 keV **(a)** or 4 MeV **(b)**, respectively. The dashed red line illustrates an exponential behaviour, as it is expected qualitatively because of the photon absorption law.

latter path length distributions deviate from the photon absorption law if the Compton effect (scattering) dominates. For lower photon energies, the influence of the Compton effect decreases and the influence of the photoelectric effect increases. Therefore, the deviations vanish (cf. figure 6.8(a)).

An exponential function was fitted to the **"first interaction"**-distributions to determine the corresponding gamma ray attenuation length. Performing an exponential fit to the high path length regions of the distributions for full path length or maximum depth might result in comparable attenuation length values as for the "first interaction"-distribution. Nevertheless, an offset due to the non-exponential regions would have to be considered. Thus, for high photon energies, only the exponential fits to the "first interaction"-distributions lead to attenuation length values that are comparable to the manufacturer data. This also means that the manufacturer data have to be calculated values (for the path length to the first interaction of the photons) rather than measured gamma ray attenuation lengths, as the measured path length to the absorption of the photons would behave like the "maximum depth"-distributions. Consequently, realistic gamma ray attenuation lengths of the scintillating materials can be much longer than the attenuation lengths specified by the manufacturer.

The results of the fits to the **"first interaction"**-distributions are summarised in figure 6.9. The statistical uncertainties (from the fits) are below 1 ‰. The results of the simulations are in a good overall agreement with the manufacturer data. For either low or very high photon energies, the simulation leads to slightly higher or lower values than given by the manufacturer. Reasons for this could e.g. be rounding errors in the calculations or a difference of the exact material composition used for the calculations and the simulations. The simulation of BC-452 also features the characteristic absorption edges of lead well, especially the K-edges between 85 keV and 90 keV as well as the L-edges between 12 keV and 16 keV (cf. figure 2.6 and [151, 152]).

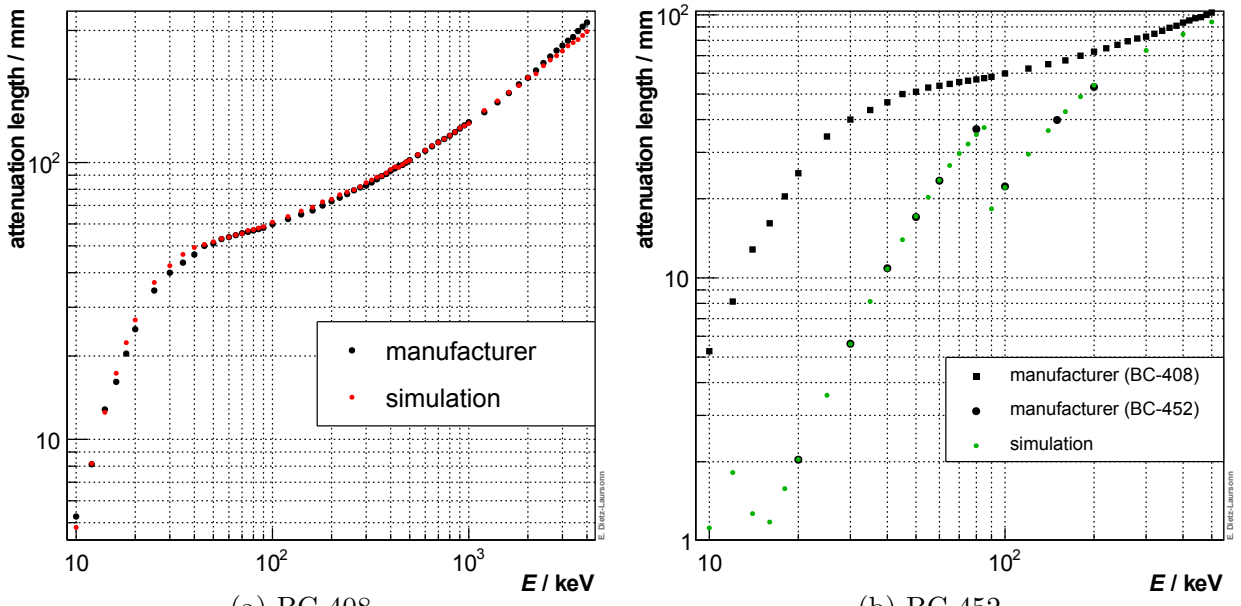

(a) BC-408 (b) BC-452

Figure 6.9.: Gamma ray attenuation length spectrum of scintillating materials (BC-404, BC-408 **(a)**, and BC-452 with 5 % lead **(b)**). The statistical uncertainties (from the fits) are below 1 ‰. As BC-404 and BC-408 have almost the same gamma ray attenuation lengths, only the simulation results of BC-408 are illustrated in **(a)**.

Due to the fact that the manufacturer data only covers the K absorption edge (but does not describe them very exactly) and that the manufacturer data does not consider photon scattering (i.e. longer path lengths are actually necessary for the absorption of the photons), the gamma ray attenuation lengths should be simulated for the necessary energy regions rather than using the manufacturer data.

6.7. Influence of Surface Roughness

In Geant4, the roughness of optical surfaces is specified in terms of σ_α, which is the standard deviation of the Gaussian distribution (around zero) of the angle α between the local, microscopic surface and the overall mean surface (cf. subsection 4.2.4). This affects the refraction and the reflection of optical photons, depending on the used reflection model. In order to validate the correct implementation of the different reflection models as well as of the influence of σ_α, a beam of optical photons has been shot onto a `G4OpticalSurface` between a volume with a refractive index of $n_1 = 1$ and a volume with a refractive index of $n_2 = 10$. The simulation was performed for all reflection models, for incidence angles of the photon beam with respect to the surface normal of 0 ° and 45 °, and for σ_α-values of 0 ° (no roughness), 5 °, and 10 °. Examples of event displays of the simulations are presented in figure 6.10. At first glance, the reflection models as well as the roughness affects the photon beam as expected: Without roughness, the photon beam remains thin after being refracted whereas it significantly diverges after refraction at a rough surface. The same applies to the reflected photon beam in case of the `specularlobe` reflection model[54]. Regardless of the surface roughness, the reflected beam is never diverging for the `specularspike` and `backscattering` reflection models whereas it always completely diverges in case of diffuse reflection.

For a more detailed investigation of the influence of σ_α, the reflected as well as the refracted photons were detected by `G4PhotonDetectors` (parallel to the surface) and the reflection angle α' or the refraction angle β between their trajectory and the surface normal was determined. The angles were filled into histograms and the statistical uncertainty was determined via *Poisson statistics*. The resulting distributions for `specularlobe` reflection can be found in figure 6.11(a). It can clearly be seen that the most probable values of the distributions with roughness do not match the expected reflection angle, especially in case of vertical incidence. This phenomenon is caused by the combination of two effects:

The first is the fact that the determination of α' mathematically represents the projection of a solid angle onto a one-dimensional angle. As the *phase space of solid angles* with the same α' increases with increasing α'-values, the α'-distributions have to be corrected for the solid angle phase space. This can be done by dividing the entries of each bin by $(\cos\alpha_{\text{low}} - \cos\alpha_{\text{high}})$, where α_{low} and α_{high} are the lower and the upper bin edge, respectively.

The second effect is that α' is determined with respect to the mean surface normal (black cone in figure 6.12(a)), whereas the roughness (σ_α) leads to small variations $\Delta\alpha$ of the incidence angle, which result in deviations $\delta(\Delta\alpha)$ of the reflected photon directions around

[54] The reflection models are described in subsection 4.2.4.

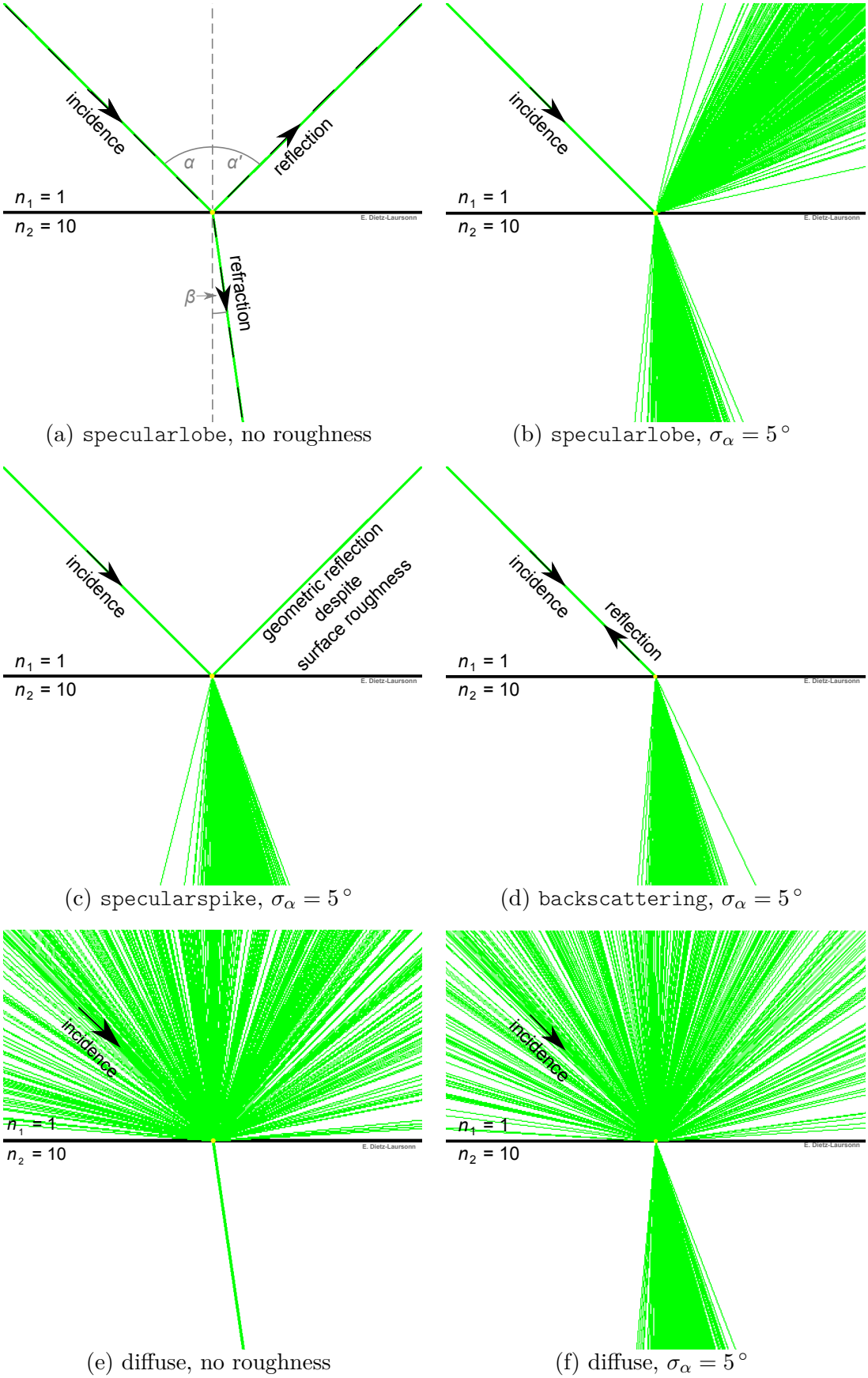

(a) `specularlobe`, no roughness

(b) `specularlobe`, $\sigma_\alpha = 5\,^\circ$

(c) `specularspike`, $\sigma_\alpha = 5\,^\circ$

(d) `backscattering`, $\sigma_\alpha = 5\,^\circ$

(e) diffuse, no roughness

(f) diffuse, $\sigma_\alpha = 5\,^\circ$

Figure 6.10.: Characteristics of the Geant4 reflection models. The black arrows indicate the mean direction of flight of the photons for incidence, reflection, and refraction.

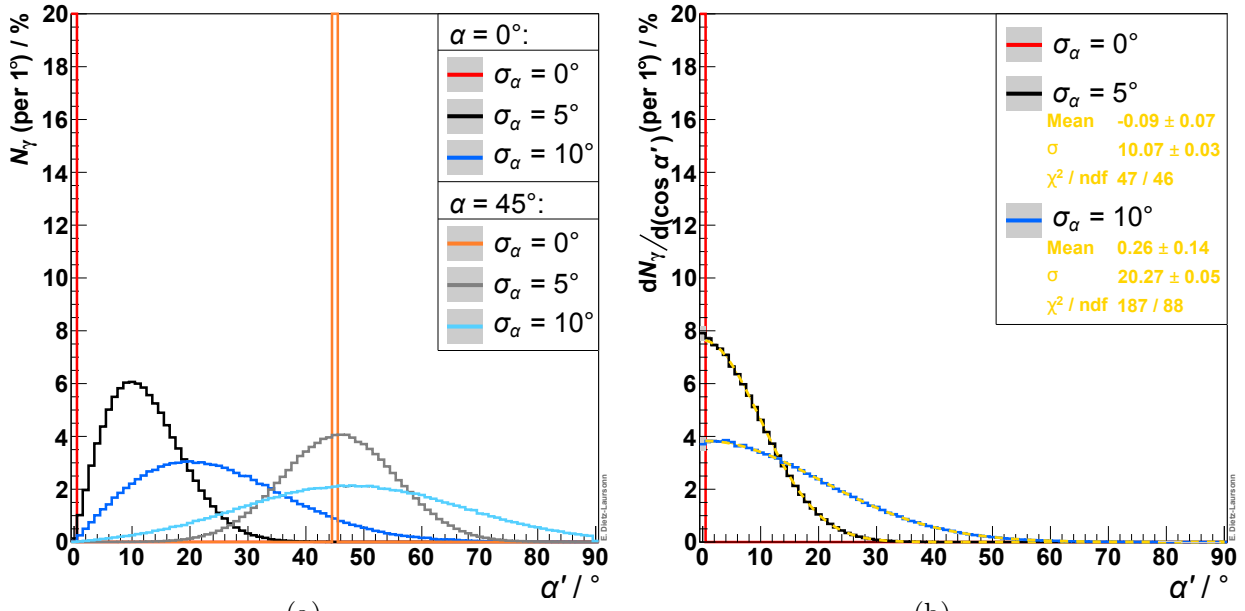

(a) (b)

Figure 6.11.: Distribution of the refraction angles $\sigma_{\alpha'}$ in case of `specularlobe` reflection in Geant4. **(a):** Raw simulation data (without corrections) for several values of surface roughness (σ_α, indicated by the colour) and incidence angles α. **(b):** Solid-angle-corrected distributions for vertical incidence with Gaussian fits for the determination of the resulting values for $\sigma_{\alpha'}$ and the mean values of α'. N_γ represents the relative number of photons with respect to the total number within each distribution. The ordinates have been limited to 20 %, although the distributions for $\sigma_\alpha = 0\,^\circ$ of course reach 100 %.

the expected direction (grey cone in figure 6.12(a)). If the photon incidence direction does not match the mean surface normal, a specific reflection angle α' does not correspond to one specific $\Delta\alpha$-value, but combines several different $\Delta\alpha$-values. This can be understood by the fact that in figure 6.12(a) the two exemplary cones (for α' and for $\delta(\Delta\alpha)$) are not equal but only overlap, i.e. the same $\delta(\Delta\alpha)$ results in very different α'-values and vice versa. Therefore, it is not trivial to draw conclusions about the value of σ_α from the α'-distribution for incidence angles of 45 ° in figure 6.11(a). These distributions are only presented to show the behaviour of α' for non-vertical photon incidence in contrast to vertical photon incidence.

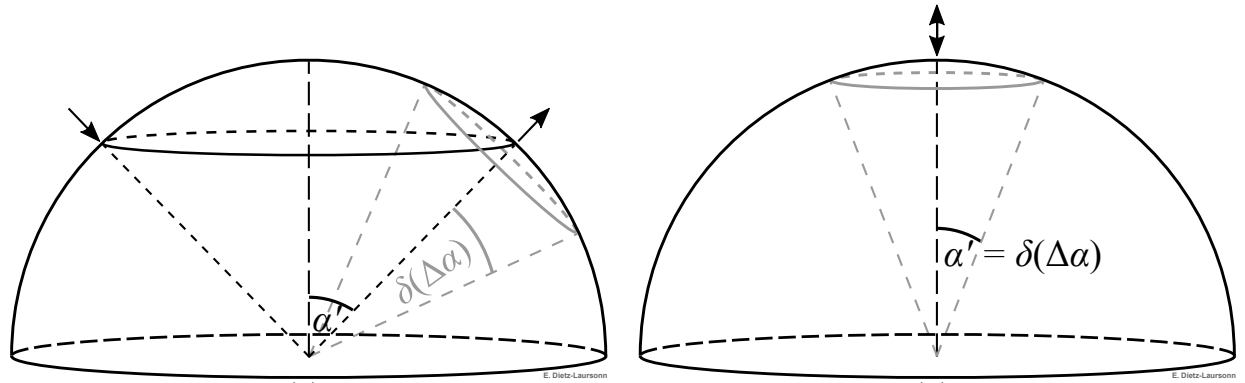

(a) (b)

Figure 6.12.: Relation between the measured refraction/reflection angle α' and the deviations $\delta(\Delta\alpha)$ due to surface roughness for an incidence angle of 45 ° **(a)** and for vertical incidence **(b)**, symbolised by the arrows.

In case of vertical incidence, both cones are the same (cf. figure 6.12(b)) and each specific α'-value corresponds to one specific $\Delta\alpha$-value. Thus, the correct most probable values as well as $\sigma_{\alpha'}$-values can be determined from the α'-distributions, after the solid-angle correction.

The results of the Gaussian fits to the solid-angle-corrected distributions of `specularlobe` reflection (cf. figure 6.11(b)) are in a good agreement with the expected mean values of 0 ° and the expected[55]

$$\sigma_{\alpha'} = 2 \cdot \sigma_\alpha. \tag{6.2}$$

As the `specularspike` reflection model and the `backscattering` reflection model are independent of the surface roughness, their distributions equal the distributions of `specularlobe` reflection with $\sigma_\alpha = 0\,°$. Figure 6.13 presents the same distributions for the refraction angle β. The mean values of the Gaussian fits match the expected 0 ° and the corresponding σ-values are in good agreement with the expected values of 4.5 ° and 9.0 °, respectively. The expected σ-values have been calculated via

$$\sigma_\beta(\alpha, \sigma_\alpha) = |\beta(\alpha, \sigma_\alpha) - \beta(\alpha, 0)| \tag{6.3}$$

with the refractive angle

$$\beta(\alpha, \Delta\alpha) = \arcsin\left(\frac{n_1}{n_2}\sin(\alpha + \Delta\alpha)\right) - \Delta\alpha \tag{6.4}$$

with respect to the mean surface.

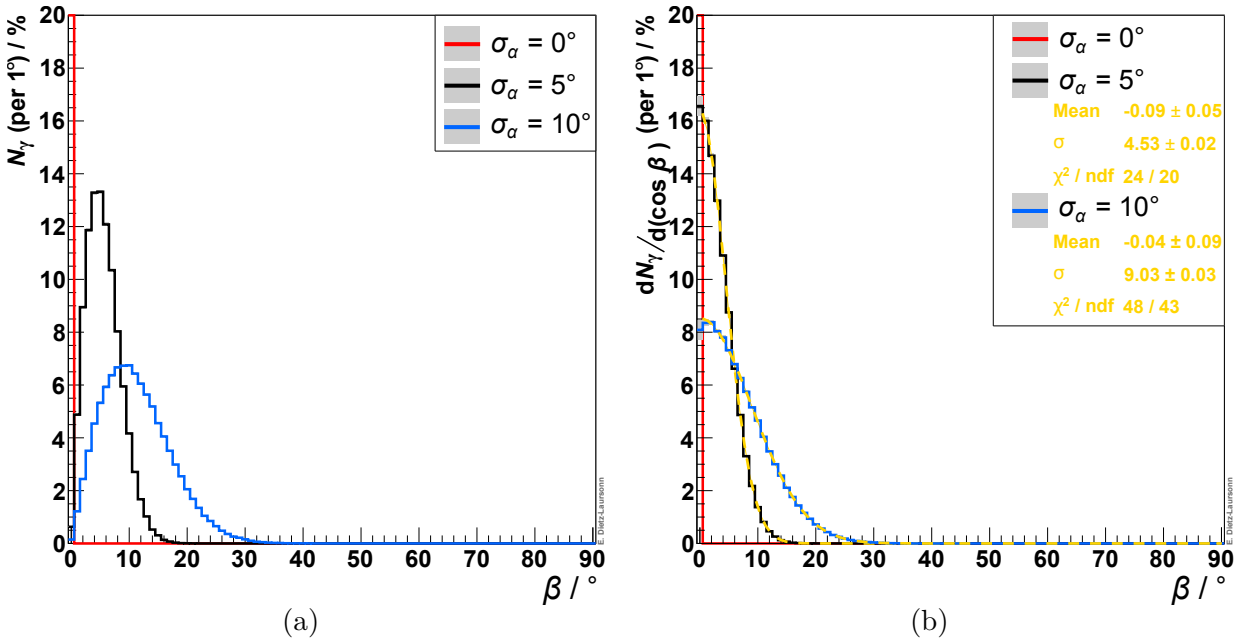

(a) (b)

Figure 6.13.: Distribution of the refraction angles β for vertical incidence in Geant4. **(a):** Raw simulation data (without corrections) for several values of surface roughness (σ_α). **(b):** Solid-angle-corrected distributions for vertical incidence with Gaussian fits for the determination of the resulting values for $\sigma_{\alpha'}$ and the mean values of α'. N_γ represents the relative number of photons with respect to the total number within each distribution. The ordinates have been limited to 20 %, although the distributions for $\sigma_\alpha = 0\,°$ of course reach 100 %.

[55] This expectation can be determined via simple geometrical considerations.

In case of diffuse/Lambertian reflection, the distribution of the reflection angles α' is expected not to depend on the incidence angle α nor the surface roughness σ_α and to fulfil Lambert's cosine law:

$$\mathrm{d}I(\alpha') = I_{\max} \cdot \cos(\alpha') \cdot \mathrm{d}\Omega = -I_{\max} \cdot \cos(\alpha') \cdot \mathrm{d}(\cos(\alpha'))\,\mathrm{d}\phi. \tag{6.5}$$

$\mathrm{d}\Omega$ is the differential solid-angle and I is the intensity of the emitted/reflected light, i.e. it is proportional to the number of photons. The distributions are illustrated in figure 6.14. It shows that the cosine-fit describes the simulated data very well after the solid-angle correction.

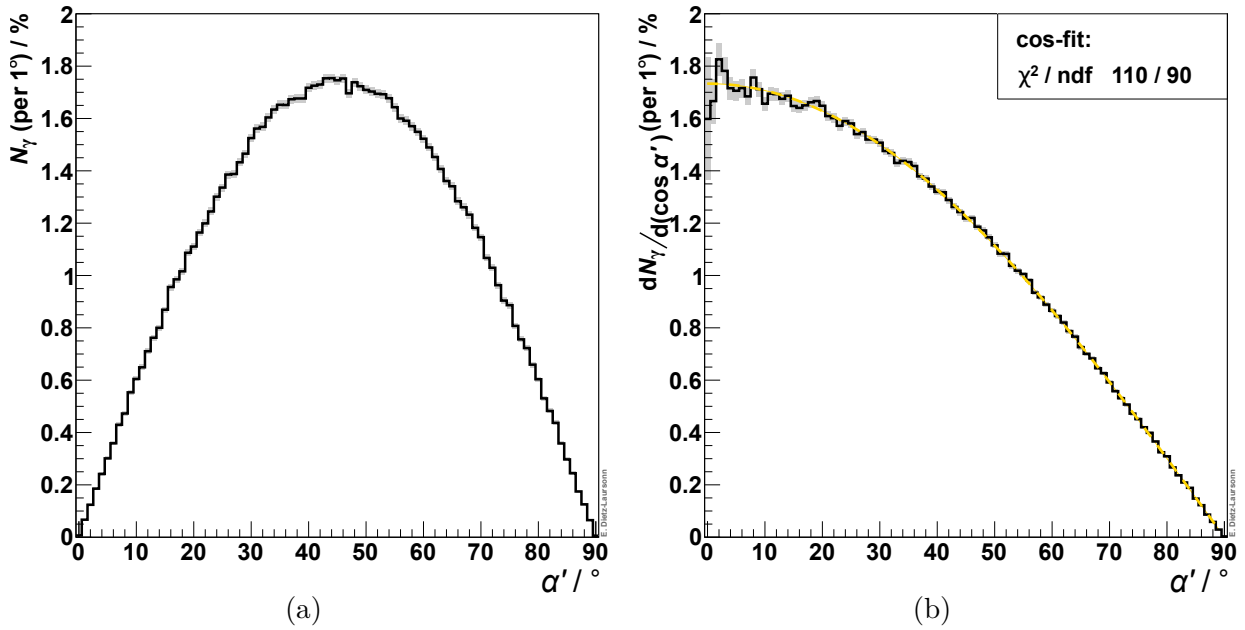

Figure 6.14.: Distribution of the refraction angles α' in case of diffuse reflection in Geant4. Raw simulation data **(a)** and solid-angle-corrected distributions **(b)** with cosine-fit. N_γ represents the relative number of photons with respect to the total number within each distribution. The results are the same regardless of the surface roughness and the incidence angle.

As a summary it can be concluded that the reflection models as well as the surface roughness behave as expected.

6.8. Reflectivity (Fresnel Equation)

In order to check the calculation of the reflectivity of optical surfaces from the refractive indices of the corresponding volumes in Geant4, a volume V with constant refractive index[56] $n_2 = 5$ was simulated inside the mother volume. For varying values of the refractive index n_1 of the mother volume, optical photons were shot vertically onto the surface from outside

[56] The refractive indices, which have been used in this section, are arbitrary values. They have been chosen to investigate the results of the Fresnel equations in Geant4 for several different pairs of refractive indices and do not possess any physical meaning with respect to existing materials.

V. The reflected photons were counted using the G4PhotonDetector and the reflectivity for each value of n_1 was determined by dividing the number of reflected photons by the corresponding number of initial photons. The statistical uncertainty of the simulated reflectivity was estimated via *Clopper-Pearson confidence intervals*. The simulations were repeated for several surface types: no `G4OpticalSurface`, "dielectric-dielectric", "dielectric-metal", and "dielectric-metal" with complex refractive index (cf. subsection 4.2.4). The results are summarised in table 6.1.

		$n_1 = 1$	$n_1 = 3$	$n_1 = 5$	$n_1 = 7$
Fresnel equation		44.44 %	6.25 %	0.00 %	2.78 %
`G4Optical-Surface:`	none	(44.48 ± 0.05) %	(6.23 ± 0.03) %	$(0\,^{+\,0.0002}_{-\,0})$ %	(2.79 ± 0.02) %
	di-di	(44.42 ± 0.05) %	(6.24 ± 0.03) %	$(0\,^{+\,0.0002}_{-\,0})$ %	(2.76 ± 0.02) %
	di-met (no n)	$(100\,^{+\,0}_{-\,0.0002})$ %	$(100\,^{+\,0}_{-\,0.0002})$ %	$(100\,^{+\,0}_{-\,0.0002})$ %	$(100\,^{+\,0}_{-\,0.0002})$ %
	di-met ($n = n_2$)	(44.43 ± 0.05) %	(44.46 ± 0.05) %	(44.56 ± 0.05) %	(44.50 ± 0.05) %

Table 6.1.: Reflectivity values of an optical surface between two volumes with n_1 and $n_2 = 5$: theoretical expectation calculated via the Fresnel equations (equation (2.40)) and simulated values for varying values of n_1 and several versions of `G4OpticalSurfaces`. Here, "di-di" and "di-met" stand for the "dielectric-dielectric" and "dielectric-metal" surface type, respectively, and n is the complex refractive index that can be specified for `G4OpticalSurfaces` between a dielectric and a metal.

The theoretical expectation is well reproduced by the simulation, with the exception of "dielectric-metal" `G4OpticalSurfaces`, for which the reflectivity does not depend on the refractive indices of the volumes forming the surface any more. In this case, if neither a complex refractive index nor the reflectivity is specified, the reflectivity is 100 % by default. If a complex refractive index is specified for a "dielectric-metal" `G4OpticalSurfaces`, the reflectivity only depends on this refractive index. This is a known issue in Geant4 [133]. The reason for this effect is that specifying the complex refractive index of a `G4OpticalSurface` leads to the use of a modified Fresnel equation. This has to be considered when using "dielectric-metal" `G4OpticalSurfaces` with complex refractive indices. There is no possibility to change this behaviour (besides changing the source code of Geant4 itself), but the user has to be aware of this. A solution could be to pass an effective complex refractive index to the `G4OpticalSurface`, which includes the refractive indices of both materials forming the surface. This is not yet done in the GODDeSS framework, as the automation is not trivial, e.g. when using `G4LogicalSkinSurfaces` (cf. paragraph "Optical Physics Peculiarities" of subsection 4.2.7).

6.9. Energy Change during the WLS Process

Because of the physical aspects of the WLS process (cf. subsection 3.2.1), an emitted WLS photon cannot possess a higher energy than its corresponding absorbed photon. As a result, the energy difference between the energy of the photons that have been emitted or absorbed by the WLS material must not assume positive values, not even if the emission spectrum and the absorption spectrum overlap.

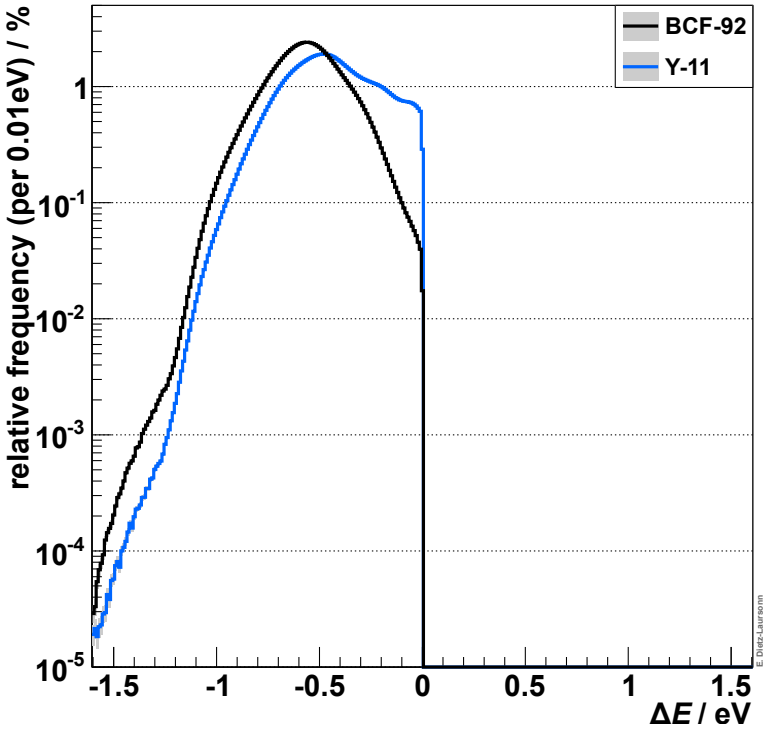

Figure 6.15.: Energy change during the WLS process in Geant4.

To validate the correct implementation of this fact in Geant4, the simulated scintillating material was excited with traversing muons and the emitted scintillation light was used for exciting the embedded WLS fibres (BCF-92 and Y-11). The mother particle of every WLS photon was determined via the `TrackID` of the corresponding `G4Tracks` and the energy difference $\Delta E = E_{\text{wls}} - E_{\text{mother}}$ was filled into a histogram. The statistical uncertainty of the simulation output has been determined via *Poisson statistics*. The resulting distributions are illustrated in figure 6.15. They have been convoluted with the absorption spectrum and the emission spectrum and their actual shape is not important. But they show that ΔE is indeed always negative.

6.10. Cherenkov Spectrum

The total number of Cherenkov photons as well as the energy or wavelength distribution of the Cherenkov photons depends on the β-value of the traversing particle and on the refractive index spectrum of the material (cf. equation (2.9)).[57] To validate the correct simulation of the Cherenkov radiation in Geant4, muons with $\beta\gamma = 1$ and with[58] $\beta\gamma = 3$ have been simulated traversing a 2 cm thick material layer with several different refractive index spectra. The energies/wavelengths of the resulting Cherenkov photons have been filled into histograms and the statistical uncertainty of the simulation output has been determined via *Poisson statistics*. The results are presented in figures 6.16 and 6.17.

[57] The refractive index spectrum has been specified for an energy range between 0.5 eV and 15 eV. This fact also reflects in figures 6.16 and 6.17. The spectra themselves have been chosen to investigate the behaviour of Cherenkov radiation in Geant4 for different shapes of refractive indices spectra and do not possess any physical meaning with respect to existing materials.

[58] Due to $\beta\gamma = \frac{\beta}{\sqrt{1-\beta^2}} \Leftrightarrow \beta = \sqrt{\frac{(\beta\gamma)^2}{(\beta\gamma)^2+1}}$, $\beta\gamma$-values of 1 and 3 equal β-values of $\sqrt{0.5}$ and $\sqrt{0.9}$, respectively.

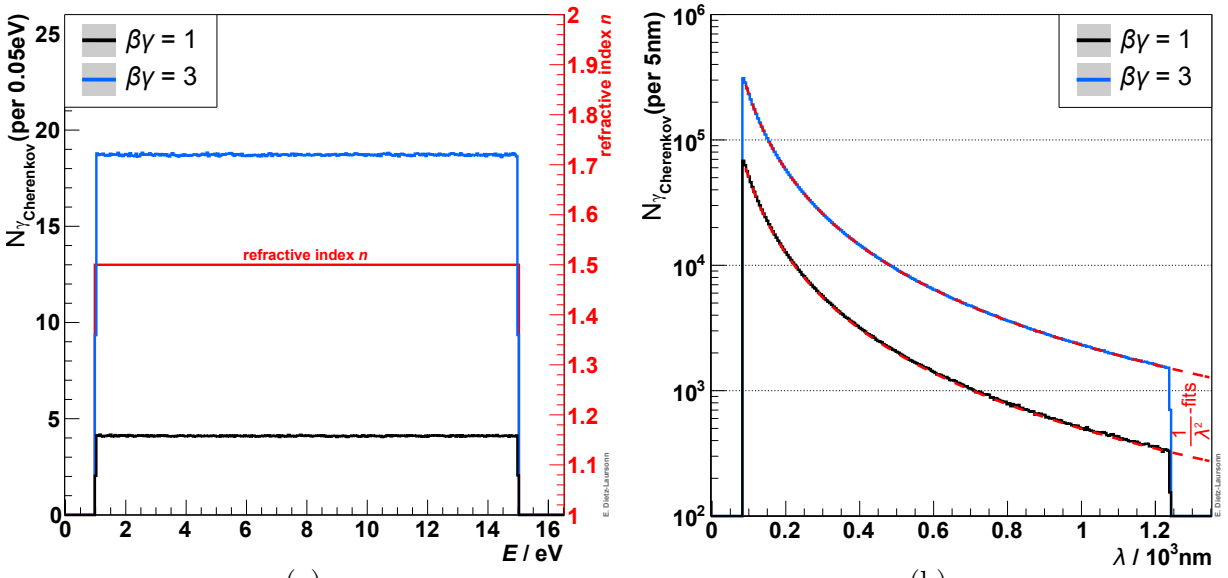

(a) (b)

Figure 6.16.: Simulated Cherenkov spectra in case of constant refractive indices: Refractive index spectrum (red axis and distribution) and energy spectra of Cherenkov photons **(a)**, wavelength spectra of Cherenkov photons **(b)**. The simulated material layer was 2 cm thick.

In case of **constant refractive indices** (figure 6.16), the energy and wavelength distributions possess the expected shape (cf. equation (2.9)): the energy spectra of the Cherenkov photons are uniformly distributed and the wavelength spectra follow a $1/\lambda^2$-distribution, which was verified by fitting quadratic functions to the simulation results. Besides the shape of the distributions, the total number of Cherenkov photons ((1150 ± 34) photons for $\beta\gamma = 1$ and (5241 ± 73) photons for $\beta\gamma = 3$) perfectly matches the expected values (1151 photons and 5241 photons, respectively), which have been calculated via equation (2.9).

In figure 6.17, the results for energy-dependent refractive indices are summarised. The upper histogram always shows the refractive index spectra and the histograms below present the corresponding simulated Cherenkov photon spectra. For the **linearly rising refractive index** (represented by the light lines in the left histograms), the total number of Cherenkov photons is (1914 ± 44) photons for $\beta\gamma = 1$ and (5384 ± 74) photons for $\beta\gamma = 3$. Whereas the latter value matches the expectation of 5428 photons, the former value is significantly below the expectation of 2074 photons. The same applies to the entries, which have been calculated for selected bins via[59]

$$N_{\text{bin}} = \frac{\alpha z^2}{\hbar c}\left(1 - \frac{1}{\beta^2 n^2(E_\gamma)}\right) \cdot d_{\text{bin}} \cdot d_{\text{material}}.$$

Here, d_{bin} and $d_{\text{material}} = 2\,\text{cm}$ are the bin width and the thickness of the material layer, respectively. This phenomenon is caused by a peculiarity of the refractive index processing in Geant4 with respect to the generation of Cherenkov radiation: in this context, instead of interpolating n by a straight line between two points of the refractive index spectrum (as it is done in Geant4 in every other case, cf. paragraph "Optical Physics Peculiarities" of subsection 4.2.7), $1/n^2$ is calculated for each point and this value is interpolated by a straight

[59] This equation can be determined by integrating equation 2.9 over one bin and the full thickness of the material layer.

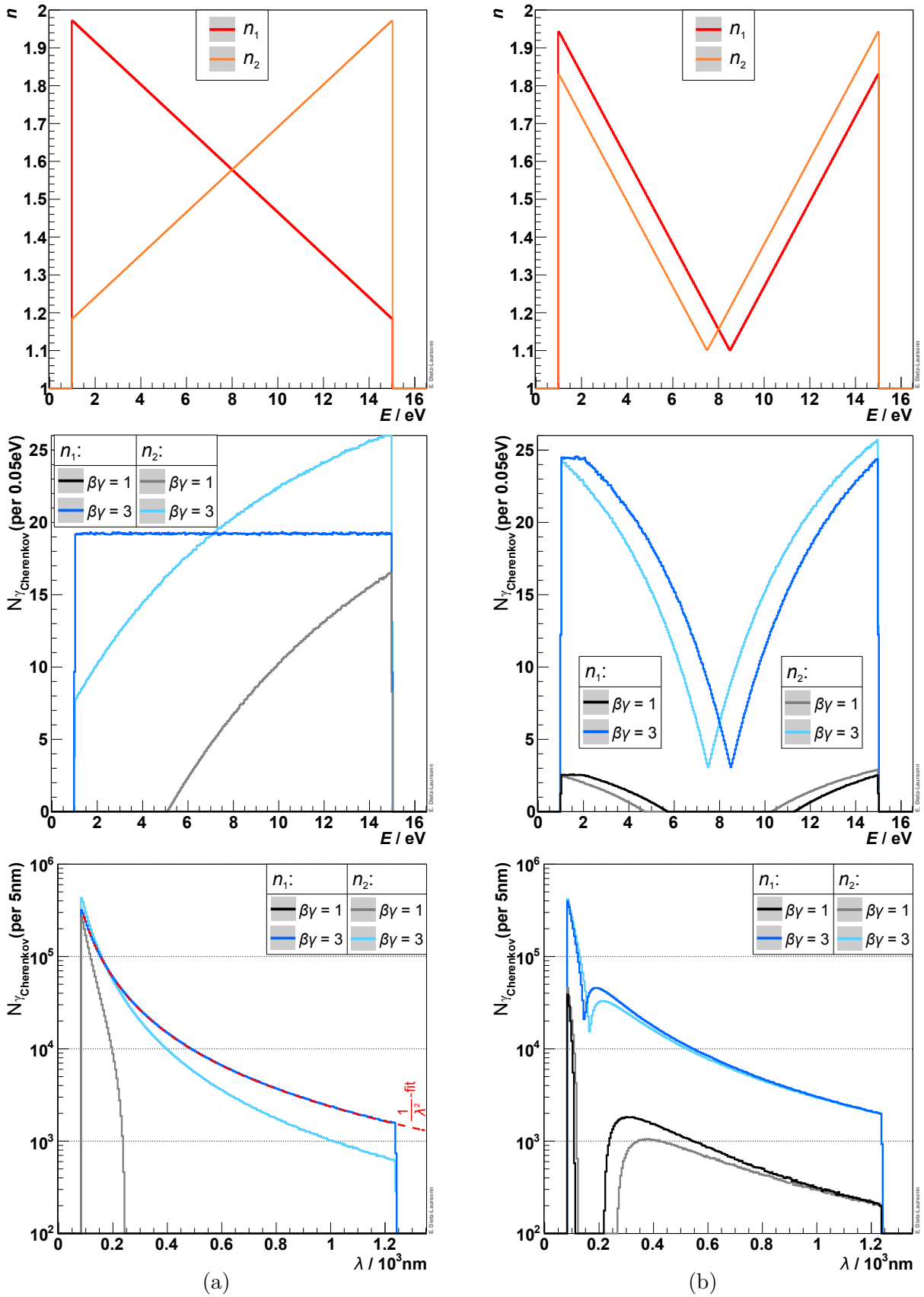

Figure 6.17.: Simulated Cherenkov spectra in case of linear refractive index spectra without **(a)** and with **(b)** dip: refractive index spectra **(top)**, energy spectra of Cherenkov photons **(middle)**, and wavelength spectra of Cherenkov photons **(bottom)**. The simulated material layer was 2 cm thick.

line. In order to avoid deviations from the expected behaviour due to this peculiarity, the refractive index spectrum has to be specified with high resolution. When repeating the previous simulations with highly resolved refractive indices (100 values per 1 eV instead of 10 values for the full spectrum), the resulting total numbers of Cherenkov photons is changed to (2074 ± 46) photons and (5428 ± 74) photons, respectively. This again perfectly fits to the expected values.

For $\beta\gamma = 1$, the Cherenkov spectrum does not cover the full energy range. This is because the refractive index is below the critical value of $n_{\text{crit}} = 1/\beta = \sqrt{2}$ for low energies. As expected, the energy value at which the Cherenkov spectrum starts matches this critical refractive index value. Likewise expected is the deviation of the Cherenkov wavelength spectra from the $1/\lambda^2$-distribution, which is represented by the red line.

Unexpected results are obtained when simulating a **linearly falling refractive index** (the dark lines in the left histograms): For $\beta\gamma = 1$, the muons do not create a single Cherenkov photon and for $\beta\gamma = 3$, the correct number of photons is created ((5384 ± 74) photons ((5428 ± 74) photons for highly resolved refractive index) when expecting 5428 photons), but they are distributed uniformly on the whole energy range. This strongly deviates from the expectation that inverting the refractive index spectrum should lead to an inversion of the energy spectrum of the Cherenkov photons. The reason for this behaviour is that, instead of the full refractive index spectrum, only the value $n(E_{\text{max}})$ corresponding to the highest energy of the spectrum is used within Geant4 to examine whether Cherenkov photons are created at all. This is done to reduce the computing time and is usually no problem, as transparent materials typically possess refractive index spectra that rise with increasing energy. More problematic is the fact that $n(E_{\text{max}})$ also seems to serve as an upper limit on the refractive index spectrum when it is used to determine the energy distribution of the Cherenkov photon. Therefore, the simulated spectrum for $\beta\gamma = 3$ is constant.

The expected inversion of the Cherenkov energy spectra can almost be found in the results of the simulations with **linear refractive indices with a dip**. They are illustrated in the histograms at the right-hand side of figure 6.17. Also here, the limitation to $n(E_{\text{max}})$, which has been found in the simulations with a linearly falling refractive index, can be observed. It is expressed in the constant regions of the "dark-line" spectra for low energies. As expected, the Cherenkov spectra do not cover the full energy range for $\beta\gamma = 1$ and the energy ranges without Cherenkov photons match the parts of the refractive index spectra that are below the critical value of $n_{\text{crit}} = 1/\beta = \sqrt{2}$. As a consequence of the more complex refractive index spectra, also the wavelength spectra of the Cherenkov photons have a more complex shape, deviating from a $1/\lambda^2$-distribution.

Additionally, for $\beta\gamma = 3$, the simulated number of Cherenkov photons ((4748 ± 69) photons ((4821 ± 70) photons for highly resolved refractive index)) agrees with the expected value of 4820 photons, whereas this does not apply for $\beta\gamma = 1$. In this case, only (263 ± 17) photons have been created in the simulations ((392 ± 20) photons for highly resolved refractive index), but 1573 photons were expected. This deviation is caused by the fact that the number of Cherenkov photons is calculated on the full energy range in Geant4 instead of on the energy ranges with $n \geq 1/\beta$ only.[60] If doing so for the calculation of the expected number

[60] In Geant4, the energy range for the calculation of the total number of Cherenkov photons is only limited, if the refractive index is below the critical value of $1/\beta$ at the low energy edge of the refractive index spectrum.

of Cherenkov photons as well, the exception decreases to 393 photons, which matches the simulation result for highly resolved refractive index. This shows that this problem is actually caused by using the incorrect energy range for the calculation of the number of Cherenkov photons in Geant4.

Another thing to be noticed in all simulated Cherenkov spectra is that the Cherenkov spectra are not limited to the optical range, but spread over the full energy range that has been covered with the specified refractive index spectrum. This is caused by the fact that Geant4 itself does not limit the emission spectrum of the Cherenkov process to reasonable energy ranges (cf. paragraph "Cherenkov Radiation" of subsection 2.1.3).

To summarise this section, non-constant parts of refractive index spectra should be specified with a *high density of data points* and a correct simulation of the Cherenkov radiation (with respect to the number of photons and the emission energy spectrum) is implemented for *normally dispersive materials only* [130]. As transparent materials are usually characterised by normal dispersion, this should be no problem for optical detector components like e.g. scintillators or optical fibres. In case of (partial) anomalous dispersion, unexpected emission spectra might occur and the number of Cherenkov photons might be underestimated (cf. section 2.5). Furthermore, Geant4 itself does not limit the emission spectrum of the Cherenkov process to reasonable energy ranges. Thus, refractive index spectra and all other optical properties[61] should be restricted to the necessary optical energy range or the physical Cherenkov energy range, respectively.[62]

6.11. Application of LUT Surfaces

In Geant4, predefined properties from Look-Up Tables (LUT) can be used as alternative to manually defining the properties of a `G4OpticalSurface`. However, this method leads to unexpected results when using the surfaces to simulate wrappings. This is a known problem [131] and can e.g. be shown using the example of a wrapped $100\times100\times10\,\mathrm{mm}^3$ `G4ScintillatorTile` with a $3\times3\,\mathrm{mm}^2$ `G4PhotonDetector` at the centre of one of the lateral surfaces. The setup has been simulated three times: with a `G4Wrapping` with the material properties of Teflon (with and without a 10 µm air gap between scintillator and wrapping) and with a LUT `groundteflonair` `G4LogicalBorderSurface` (representing the wrapping) between the scintillator and its mother volume. The scintillator was excited with traversing muons.

Figure 6.18 shows the angular distribution of the resulting optical photons on the `G4PhotonDetector`. It is obvious that the shape of the distribution completely differs for both wrapping types.[63] Furthermore, for "LUT-wrapping", the distribution features many sharp spikes.

[61] Defining individual optical properties on different energy ranges can cause problems as photons could be created with energies for which e.g. no refractive index is defined.

[62] If not stated differently, it is limited to the energy rang between 1 eV and 7 eV in the scope of this thesis (cf. appendix D).

[63] The deviations between the two distributions in figure 6.18(b) (`G4Wrapping` with and without air gap) are expected. They are a result of the different combinations of reflection types: Without air gap, there is only diffuse reflection at the Teflon surface. With air gap, there is also geometric reflection at the surface between scintillator and air.

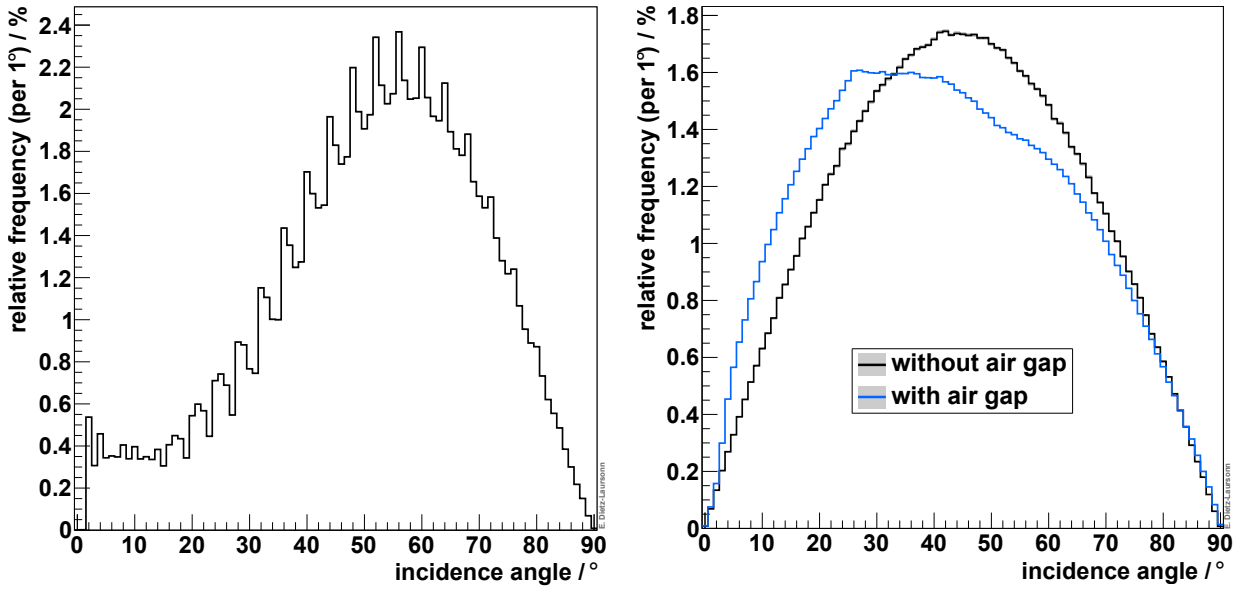

(a) (b)

Figure 6.18.: Simulated angular distribution of optical photons on the `G4PhotonDetector` for Teflon "LUT-wrapping" **(a)** and for `G4Wrapping` with Teflon properties **(b)**. The distributions have been normalised to the number of entries.

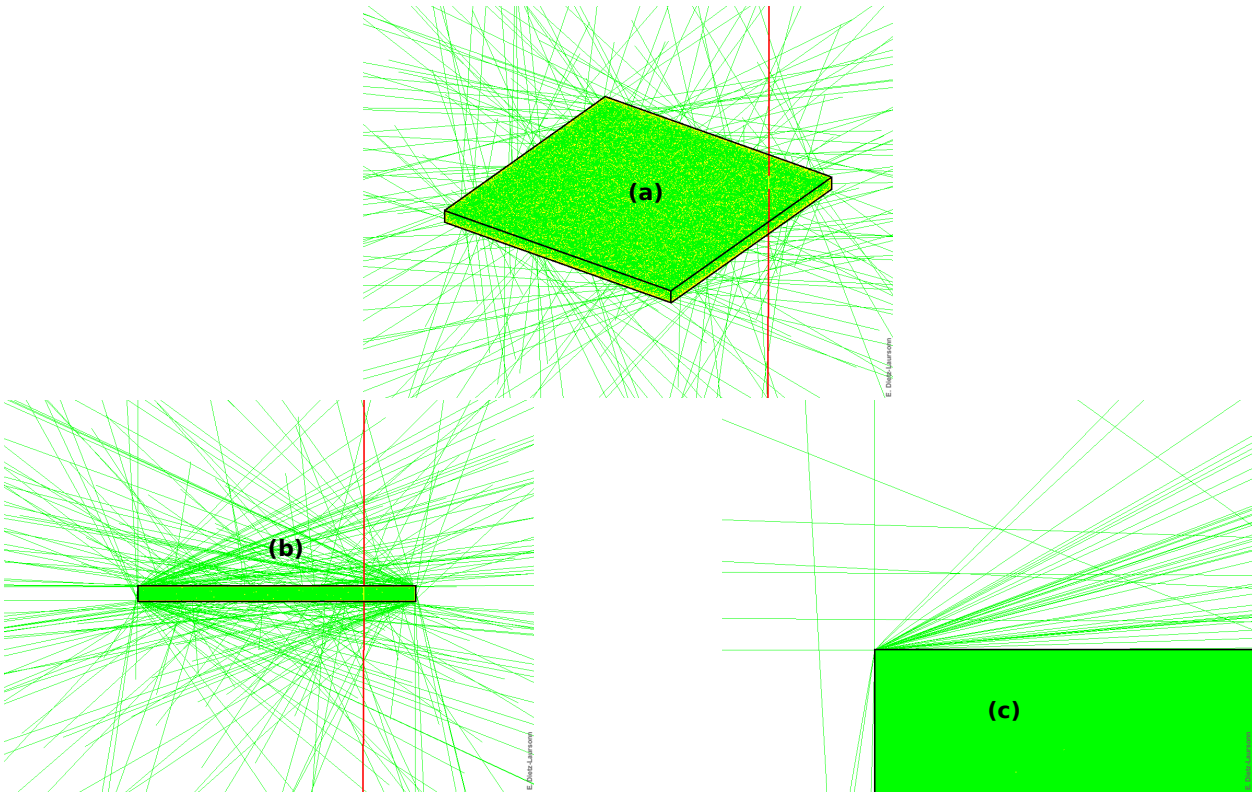

Figure 6.19.: Escaping photons from a simulated scintillator tile with "LUT-wrapping": The scintillator tile is displayed in a slanted view from above **(a)**, in a side view **(b)**, and zoomed into the side view **(c)**. The muon is displayed in red and the photons are green. The scintillator tile seems to be homogeneously filled with green because of the large number of photons and reflections. If the wrapping was opaque, no green lines should be outside the scintillator volume. Obviously, some photons leave this volume, preferentially at the edges **(c)**. In total, 326 of 12539 photons escaped in this event.

The reason for the deviation of the shape of the angular distribution is unknown. It is possible that the "LUT-Teflon" simply simulates different properties than the properties that have been used for the `G4Wrapping`. Unfortunately, it is not possible to verify this assumption, as it is not or not easily possible to determine the properties used by "LUT-Teflon".

Additionally, when inspecting the visualisation of single events of the simulation, it becomes clear that there is another problem. The "LUT-wrapping" is not fully opaque, but some photons escape from the edges of the scintillator volume. This is illustrated in figure 6.19.

Apart from the deviations in the angular distribution, the spikes in the angular distribution of the "LUT-wrapping" as well as the "escaping" photons are definitely unexpected and non-physical. Altogether, using LUT surfaces is therefore not recommended, at least for the simulation of wrappings.

6.12. Fibre Trapping Efficiency

The fibre trapping efficiency has been introduced in subsection 3.2.3 and its value has been calculated for several fibre geometries in appendix B. In order to check if it is correctly reproduced by the `G4Fibres` of GODDeSS, the corresponding fibres have been simulated with the following settings, which reflect the constraints of the definition of the fibre trapping efficiency:

- constant refractive indices (taken from [153]);
- perfectly smooth surfaces;
- very low absorption;
- optical photons are emitted isotropically from one point on the fibre axis (→ only meridional rays);
- the surrounding volume has the same refractive index as the outer cladding of the fibre (→ photons entering the outer cladding leave the fibre and are lost);
- fibre length of 1 m between the emission point and both fibre ends (→ avoid contributions of photons that were captured by non-total reflection (Fresnel equations, cf. section 2.5)).

The photons reaching the fibre ends were counted and their number was compared to the number of emitted photons. The resulting trapping efficiencies are summarised in table 6.2. The statistical uncertainty has been estimated via *Clopper-Pearson confidence intervals*.

	simulation (GODDeSS)		calculation (manufacturer)	
	single-clad	double-clad	single-clad	double-clad
round	$(6.878 \pm 0.003)\,\%$	$(11.249 \pm 0.004)\,\%$	$6.875\,\%$	$11.250\,\%$
square	$(8.865 \pm 0.003)\,\%$	$(12.740 \pm 0.004)\,\%$	$8.866\,\%$	$14.654\,\%$

Table 6.2.: Fibre trapping efficiency values for "standard" fibres with $d = 1\,\text{mm}$, $n_{\text{core}} = 1.6$, $n_{\text{inner cladding}} = 1.49$, and $n_{\text{outer cladding}} = 1.42$ [153], considering both fibre directions and only meridional rays.

The comparison with the calculated values (cf. appendix B) shows that the results of the simulation are consistent with the calculation within the uncertainties for all but the square fibre with two claddings. The simulated trapping efficiency of this fibre is significantly lower than the expectation from the calculation. This effect is caused by the fact that the trapping efficiency calculation (as it is used by the manufacturers and is described in appendix B) does not take the real geometry of the fibre and its claddings into account. Instead (and in contrast to Geant4, which of course uses the unsimplified geometry), the two surfaces between the core, the inner cladding, and the outer cladding are mathematically simplified to one virtual surface between the core and the outer cladding (cf. figure 6.20).[64] In contrast to square fibres, this is not a problem in case of round fibres. For square fibres, in the real geometry, some photons are refracted at the surface between the core and the inner cladding and then hit a surface between the inner cladding and the outer cladding, which is vertical to the previously traversed surface instead of being parallel. Thus, they hit the outer cladding with a smaller incidence angle than expected in the calculation and leave the fibre instead of undergoing total reflection. This is illustrated in figure 6.20. As the mathematically

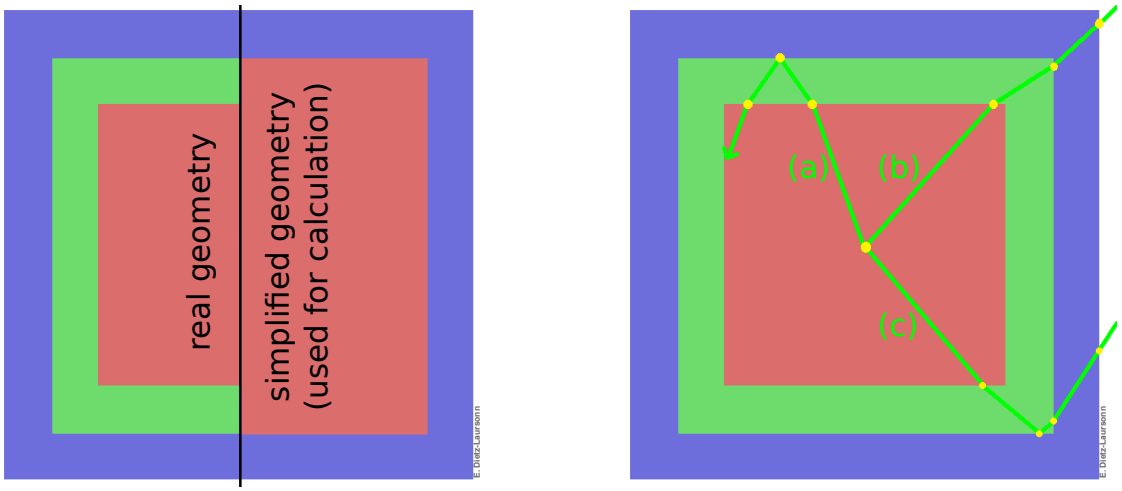

Figure 6.20.: Geometrical reason for deviations between the calculation and the simulation (or measurement) of the trapping efficiency of square fibres: A simulated square fibre is positioned vertically to the image plane and its cross section is illustrated. The thickness of the claddings has been increased for better visibility. The **left** picture shows the difference between the geometry of the fibre, as it is considered in the simulation and in the calculation, respectively. The **right** pictures presents the effect of the different geometries on the trapping efficiency. Being emitted in the centre of the core (red), three optical photon are traversing the fibre. According to the **calculation**, each of them is expected to undergo total reflection at the surface between the inner cladding (green) and the outer cladding (blue) and, thus, to contribute to the trapping efficiency. But in contrast to case **(a)**, the photons **(b)** and **(c)** hit a surface between the inner cladding and the outer cladding, which is vertical to the previously traversed surface between the core and the inner cladding instead of being parallel. This is possible in the **simulation** because of the finite distance between the two surfaces, which is neglected in the calculation.

[64] A more complex calculation of the trapping efficiency, which considers the real geometry of the claddings is probably possible. But as the manufacturers state the results of the simplified calculation method, this method is also used as reference method in the scope of this thesis. This allows for the explanation of the deviations between the simulated trapping efficiency values and the manufacturer data.

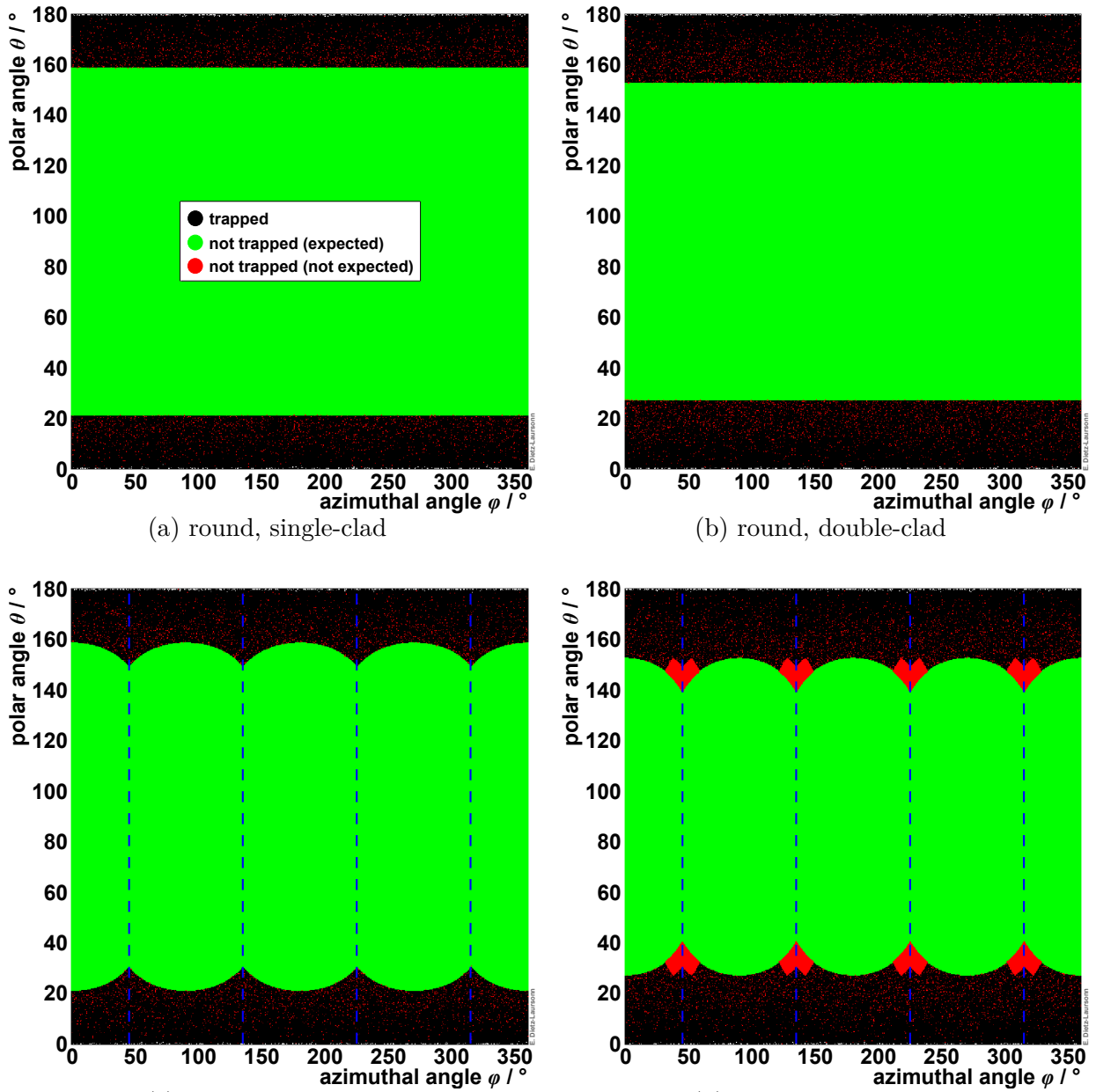

(a) round, single-clad

(b) round, double-clad

(c) square, single-clad

(d) square, double-clad

Figure 6.21.: Geometry dependence of the trapping efficiency for round fibres with one **(a)** or two **(b)** claddings and for square fibres with one **(c)** or two **(d)** claddings, simulated with GODDeSS: The position inside the scatter plots represents the initial direction of the photons in spherical coordinates (the fibres are parallel to the ordinate) and the colour indicates whether the photons were trapped and thus have contributed to the simulated trapping efficiency. "(Expected)" and "(not expected)" refer to the question whether not being trapped is expected (according to the simplified geometry for trapping efficiency calculation) for the photons that were not trapped in the simulation. Thus, the red regions depict inadequacies of the method for calculating the trapping efficiency of optical fibres, which is typically used, also by the manufacturers. The edges of the square fibres are marked with dashed lines.

simplification of the geometry is not allowed in such cases, these photons are mistakenly expected to contribute to the calculated trapping efficiency, whereas they do not contribute to the simulated trapping efficiency when considering the real geometry of the fibre. This leads to the deviation that is found in table 6.2.

Figure 6.21 shows the geometry dependence of the trapping efficiency. The position inside the scatter plots represents the initial direction of the photons in spherical coordinates and the colour indicates whether the photons were trapped and thus have contributed to the simulated trapping efficiency. As expected (cf. appendix B), the plots show no ϕ-dependence for the round fibres. For total reflection in the square fibres, the necessary deviation of θ from 90 ° is smaller in the edges of the square fibres than straight along the fibre. This is because the incidence angle on the surfaces is a combination of θ and ϕ. In case of square fibres with two claddings, sharply separated regions in the fibre edges can be found (illustrated in red). For these regions, total reflection is expected according to the simplified geometry for trapping efficiency calculation, but they do not contribute to the simulated trapping efficiency. These regions depict inadequacies of the method for calculating the trapping efficiency of optical fibres, which is typically used, also by the manufacturers.

The conclusion of the results of this section is that the simulated fibre layout behaves as expected and leads to trapping efficiencies, which match the (calculated) manufacturer data or even correct it (in case of square double-clad fibres). Nevertheless, the trapping efficiency values, which have been determined in this section, do not necessarily agree with its values for realistic conditions (meridional as well as skew rays, realistic refractive indices, possible reflection at the boundary between the outer cladding and the surroundings, surface roughness). The influence of these parameters will be investigated in section 9.1.

6.13. Fibre Bending Loss

Optical fibres can cope with bending as long as the bending radius is not too small. If the bending radius falls below a critical value, the fibre starts to break and the transportation of light becomes very inefficient. But even for bending radii above this critical value, the light transportation capabilities decline with decreasing bending radius. This is a result of the *changing incidence angles* between the light and the fibre surfaces. The manufacturer Kuraray states measured values of the bending loss (i.e. the signal loss of the fibre due to bending) of its optical fibres [99] and derives minimal bending radii from these data.

In order to validate whether the `G4Fibres` of GODDeSS correctly reproduce the bending losses, a round, double-clad, light-guiding fibre (BCF-98) with an increased optical attenuation length (10^{12} m) has been simulated. The full fibre consisted of a straight part (varying lengths) and a bent part (135 ° bending angle, varying bending radii r) to simulate fibres with different bending radii but the same total length. Optical photons are emitted isotropically from the end face of the straight fibre. The photons reaching the other fibre end were counted with a `G4Photondetector`. The resulting numbers have been normalised to the result with $r = 100$ mm. The simulation was performed for a refractive index of the surroundings that was equal to the refractive index of the outer cladding ($n_{\text{ambient}} = n_{\text{clad}}$,

meaning that photons entering the outer cladding are lost) as well as for $n_{\text{ambient}} = 1$ with a smooth or rough ($\sigma_\alpha = 5\,°$, cf. subsection 4.2.4) surface of the outer cladding. This was necessary, as the exact fibre setup, which was used by the manufacturer during the measurements, is not known. The results of the simulations are summarised in figure 6.22, together with the manufacturer data. As manufacturer data, the values for the "S-type" fibres of Kuraray have been taken, because they have mechanical properties that make them break at smaller critical bending angles [99]. The data of this fibre type was chosen, because the simulation does not consider the breaking of fibres at small bending angles. The statistical uncertainty has been estimated via *Clopper-Pearson confidence intervals* and are below 1 ‰ (with respect to the bending loss values).

It is obvious that the simulation with smooth fibre surface does not reproduce the manufacturer data correctly, but is underestimating the signal loss due to fibre bending. This is anyhow no surprise, as a rough fibre surface is necessary to reproduce other measurement results and thus the smooth surface is not the correct description of real fibres (cf. section 7.1). The simulation with rough fibre surface reproduces the manufacturer data relatively well down to $r \approx 20\,\text{mm}$. Below that, it results in too low bending losses. The simulation with $n_{\text{ambient}} = n_{\text{clad}}$ is best matching the manufacturer data over the whole measurement range.

A full quantitative comparison between simulation and manufacturer data is not possible, as the uncertainties of the manufacturer data as well as their reproducibility is unknown. Additionally, cracks in the fibre due to bending are not considered in the simulation and it is not known, whether the measurement has been performed for fibres with or without

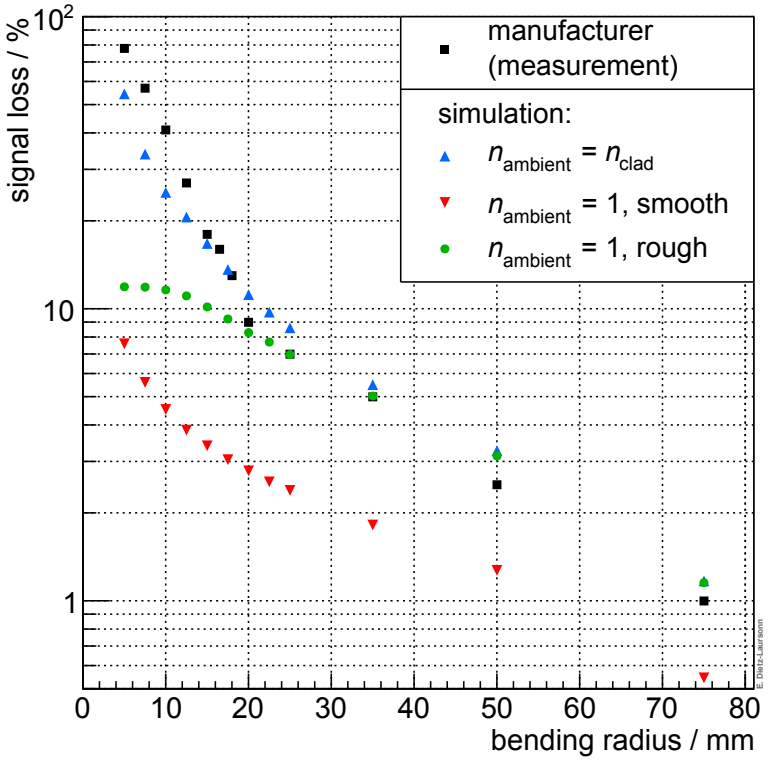

Figure 6.22.: Signal loss of optical fibres as a function of the bending radius, manufacturer data ("S-type", from [99]) and simulation results. The statistical uncertainty of the simulation has been estimated via Clopper-Pearson confidence intervals and are below 1 ‰ (with respect to the bending loss values)

absorbing coating. The usage of such a coating could lead to the loss of every photon entering the outer cladding. Thus, due to the similarities between the manufacturer data and the simulation with $n_{\text{ambient}} = n_{\text{clad}}$, it seems to be likely that a coating was used for the measurements. Under this assumption, together with assuming high uncertainties for the measurement (due to cracks and reproducibility), the simulation (with $n_{\text{ambient}} = n_{\text{clad}}$) can be assumed to reproduce the manufacturer data. Nevertheless, for real applications of optical fibres, the recommended minimal bending radius, which is between 50 and 100 times the fibre diameter [99], should be adhered to. Thus a perfect simulation of the bending losses is not necessary.

As a conclusion of chapter 6, the main results can be summarised as follows:

- The behaviour of most of the investigated subjects meets the expectation completely or predominantly. An exception are *LUT surfaces*. They are not recommended to be used, due to unexpected behaviour.

- *Emission spectra* behave as expected, as long as their energy dependent parts are specified with a high density of data points.

- The *scintillation light yield* qualitatively meets the expectations (reduction) when being simulated with considering saturation effects according to *Birks' equation*. Nevertheless, the energy dependence of the correction makes the quantitatively correct simulation as well as the quantitative comparison of simulation results and measurements rather complex. The implementation of Birks' equation in Geant4 corresponds to the application of values of C_{B} that were measured for particles far from being absorbed during the measurement. Additionally, they have to be corrected for the difference between the step length in Geant4 and the effective path length during the measurement (smaller saturation effect over the same distance for higher number of segments, cf. equation 6.1).

- The *Cherenkov spectrum* meets the expectation as long as the material is normal-dispersive and the non-constant parts of refractive index spectra are specified with a high density of data points. Furthermore, all optical properties should be restricted to the necessary optical energy range or the physical Cherenkov energy range, as this is not done by Geant4 itself.[65]

- In case of "dielectric-metal" `G4OpticalSurfaces`, a *modified Fresnel equation* is used to calculate the reflectivity of the surface. This modified Fresnel equation does not depend on the refractive indices of the volumes forming the surface but only on the complex refractive index of the "dielectric-metal" `G4OpticalSurface`. This can be solved by passing an effective complex refractive index (considering the refractive indices of both materials forming the surface) to the `G4OpticalSurface`.

[65] If not stated differently, it is limited to the energy rang between 1 eV and 7 eV in the scope of this thesis (cf. appendix D).

- The simulation of the *trapping efficiency* matches the expectations and additionally reveals an insufficient accuracy in the calculated trapping efficiency of square double-clad fibres. This inaccurate value is also stated in the manufacturer data, e.g. [153]. Furthermore, the trapping efficiency that has been determined in this section, does not necessarily agree with the trapping efficiency for realistic conditions (meridional as well as skew rays, realistic refractive indices, possible reflection at the boundary between the outer cladding and the surroundings, surface roughness). Therefore, the influence of these parameters will be investigated in section 9.1.

- The *gamma ray attenuation length* of the scintillators shows a good overall agreement with the manufacturer data, if only the first interaction of the photons is taken into account (i.e. no photon scattering). This means that the manufacturer data underestimates the path length that is actually necessary for the absorption of the photons and simulations should be performed to estimate this path length.

The next chapter will describe some adjustments that had to be implemented to resolve severe deviations between simulations and measurements or manufacturer data. Thereafter, the validation against measurements with complete optical detectors, consisting of several elements, will be presented.

7. Adapting GODDeSS to Reality

In the previous chapter, the correct operation of the GODDeSS framework on source code level was tested. The next chapters will present the validation against measurements with complete optical detectors, consisting of several elements. Beforehand, this chapter will summarise comparisons between those simulations and manufacturer data or own measurements, respectively, which showed severe deviations. As a result, adjustments had to be made to the way optical fibres are modelled in the GODDeSS framework in order to adapt the results of the simulations to the measurements and manufacturer data. The material properties, which have been used for modelling the optical detector components, can be found in appendix D.

7.1. Exit Characteristics of Light from Optical Fibres

The GODDeSS framework, in particular the `G4Fibre` and the `G4PhotonDetector` have been used in the scope of a master thesis at the Physics Institute III of RWTH Aachen University [154]. The goal of that thesis was to measure the exit characteristics of light from optical fibres as well as to use the measurements to validate the simulation results of GODDeSS. The intermediate results are summarised in figure 7.1. It is easy to see that the simulation results differ severely from the measurements.

Up to this point, no possibility of simulating surface roughness was provided for the `G4Fibre`. Following the measured surface roughness of scintillator tiles (cf. appendix D), an approach for the solution of this problem was to repeat the simulations with various roughness values for the surface of the outer cladding of the fibre. The results for the angular distribution are presented in figure 7.2. The simulation results approach the measurement results with increasing roughness (specified in terms of σ_α, cf. subsection 4.2.4). For values of σ_α above $5\,^\circ$, the results do not improve much more. Therefore, $\sigma_\alpha = 5\,^\circ$ has been found to be the roughness that is necessary for the optical surface of the outer cladding of optical fibres, in order to achieve an appropriate simulation of their exit characteristics.

Figure 7.3 shows the comparison of the resulting simulations with the measurements for three different fibre types. It is clearly visible the matching is much better than without considering roughness in the simulation of optical fibres. However, they do not match perfectly and there is still room for further improvements.

As a consequence of these results, the possibility to simulate rough surfaces was implemented for the `G4Fibres` and $\sigma_\alpha = 5\,^\circ$ has been chosen as the standard value for the roughness of the fibre's outer surface (with the exception of the fibre's end faces). If not stated differently, this standard value was used in every simulation in the scope of this thesis.

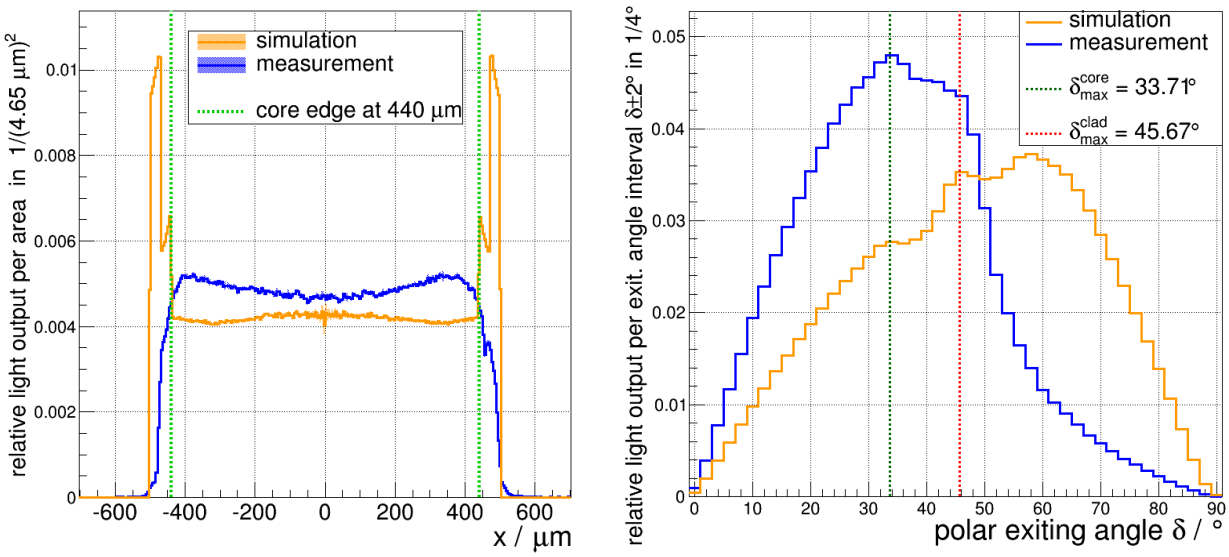

(a) (b)

Figure 7.1.: Measurement and simulation (without simulated roughness for the surface of the outer cladding) results of the photon distribution at the end of a round, double-clad, optical fibre with a diameter of 1 mm [154]. **(a):** Radial spatial distribution with the dotted lines marking the edge of the fibre core. The edge of the inner cladding is located at a radius of 470 µm, where the simulated distribution sharply increases. **(b):** Angular distribution with the dotted lines marking the maximum possible exit angle (when only considering meridional rays, cf. subsection 3.2.3) of the core and the inner cladding, respectively.

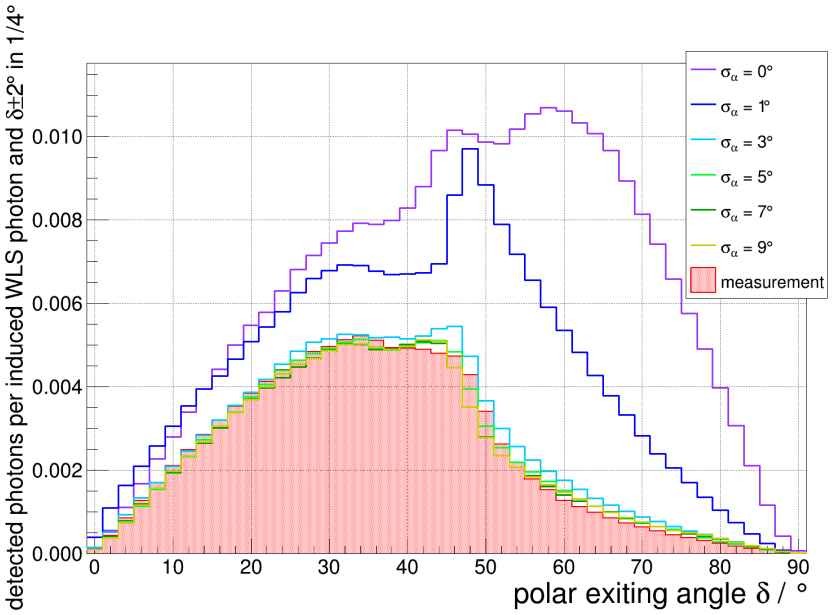

Figure 7.2.: Comparison of the measured angular distribution at the end of an optical fibre with the corresponding distribution resulting from simulations with several different roughness values (σ_α) for the surface of the outer cladding [154]. A round, double-clad, optical fibre with a diameter of 1 mm was used for the measurement and the simulations.

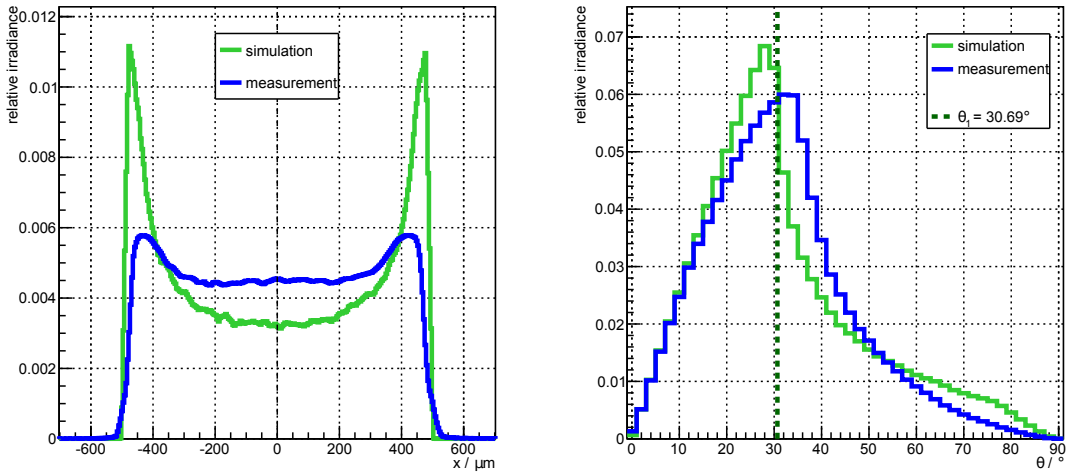

(a) round, single-clad

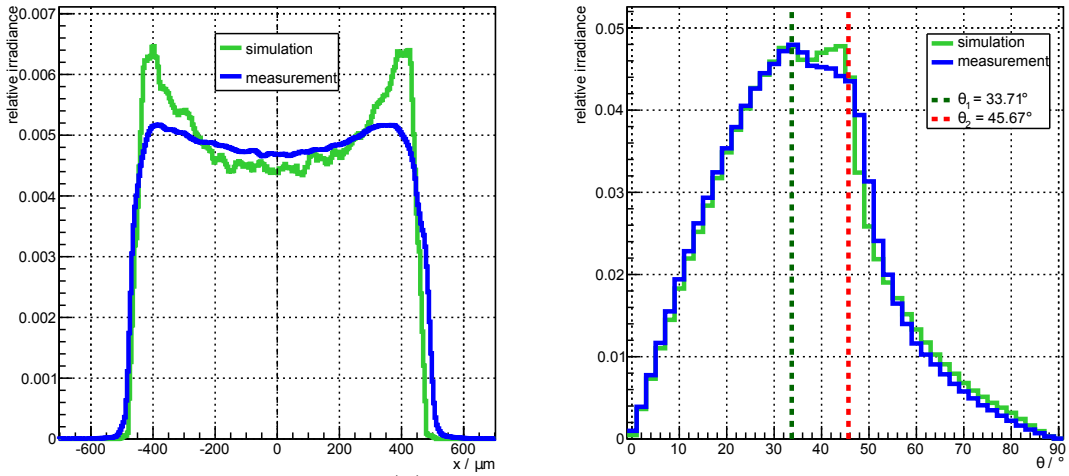

(b) round, double-clad

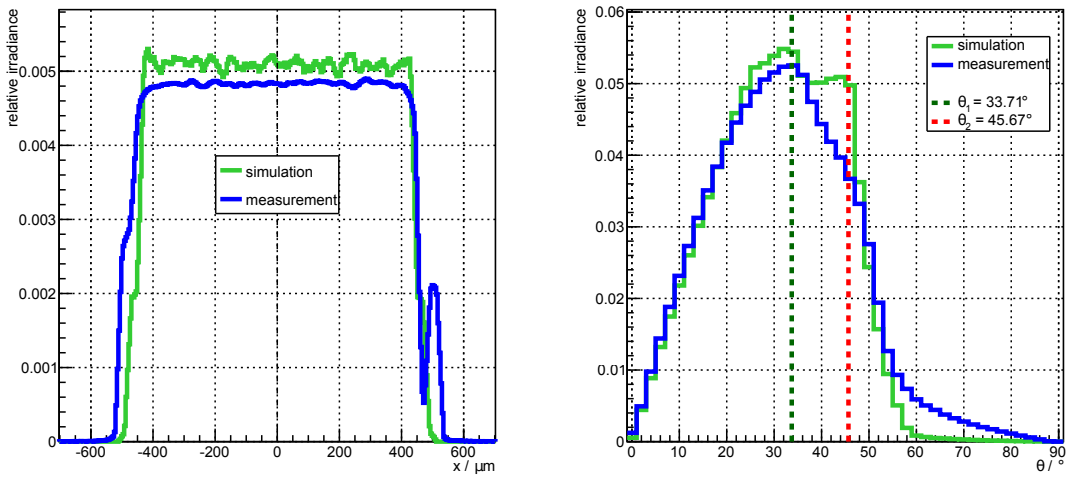

(c) square, double-clad

Figure 7.3.: Measurement and simulation results of the spatial and angular distribution of photons at the end of optical fibres [154]. The dotted lines are marking the maximum possible exit angle (when only considering meridional rays) of the core and the inner cladding, respectively. A round, single-clad fibre **(a)**, a round, double-clad fibre **(b)**, and a square, double-clad fibre **(c)** with a diameter/edge length of 1 mm were used and a roughness of $\sigma_\alpha = 5\,^\circ$ was simulated for the surface of the outer cladding.

7.2. Fibre Signal Attenuation Length

In contrast to the bulk attenuation length (which is the pure *material attenuation length*), the signal attenuation length additionally considers the *geometry* and *optical surface properties* of the material. This means, losses at optical surfaces as well as longer effective path lengths due to reflections and indirect propagation are taken into account. The bulk attenuation lengths have been validated in section 6.5. In this section, the validation and adjustment of the signal attenuation length of optical fibres (`G4Fibres` of GODDeSS) will be described. The adjustment is necessary, because using the measured signal attenuation length as bulk attenuation length for the simulation of the fibres is expected to lead to much shorter simulated signal attenuation lengths.

The signal attenuation length $\mu_{\text{att., sig.}}$ of the optical fibres was determined similarly to the determination of the gamma ray attenuation length of the scintillating materials (cf. section 6.6): 10 m long fibres were simulated with a rough surface ($\sigma_\alpha = 5\,^\circ$) and a surrounding refractive index of $n = 1$. In case of the WLS fibre BCF-92, for which only a constant signal attenuation length value was given by the manufacturer, the simulated fibre was excited with optical photons from outside the fibre. The photons were created close to one of the fibre ends in the cross-section plane of the fibre in a distance to its centre of 1.02 times its radius (round fibres) or 0.71 times its edge length (square fibres), respectively. From there, the photons were isotropically emitted into the cross-section plane of the fibre.[66] For the other fibres, for which signal attenuation length spectra are available, the optical photons were emitted isotropically from one end face of the fibre. For each photon (WLS for BCF-92, primary photon for the other fibres), the maximum covered fibre length[67] was determined and filled into a cumulative histogram. Thus, the distributions represent the fraction of the remaining photons as a function of the covered fibre length. All distributions were normalised to the entry of their first bin and the statistical uncertainty of the simulation output was determined via *Poisson statistics*. An example is presented in figure 7.4. It is striking that the distribution deviates from a pure exponential behaviour, which is represented by the two straight lines in the figure. Instead, the signal attenuation length of the remaining photons increases with increasing distance to the light emission position, e.g. from $\mu_{\text{att., sig.}} = (1.4560 \pm 0.0011)\,\text{m}$ for distances between 1 m and 3 m to $\mu_{\text{att., sig.}} = (1.6858 \pm 0.0020)\,\text{m}$ for distances between 5 m and 10 m in the example distribution. This means that the signal consists of fractions with different signal attenuation lengths, due to the energy or the trajectory of the photons. The influence of fractions with the shorter signal attenuation lengths decreases with increasing distance, the corresponding photons are simply absorbed on shorter fibre length scales. This has to be taken into account, when using the term "signal attenuation length" in case of optical fibres.

[66] This procedure is necessary, as the signal attenuation length depends on the refractive indices of the fibre material, which were specified as a function of the photon energy. Consequently, though being given as a constant value by the manufacturer, the signal attenuation length is depending on the energy spectrum of the investigated photons. Therefore, the emission spectrum of the fibre should be applied in order to reproduce the manufacturer data.

[67] The covered fibre length of a photon was defined as the distance of the photon position (inside the fibre) to the end face of the fibre, which was the origin of the photon. The maximum covered fibre length of a photon is the maximum value of the covered fibre length that has been assumed by the corresponding photon. As the photons can be scattered back or be reflected at the end of the fibre, this maximum value does not necessarily need to be the value of the position where the photons are absorbed or leave the fibre.

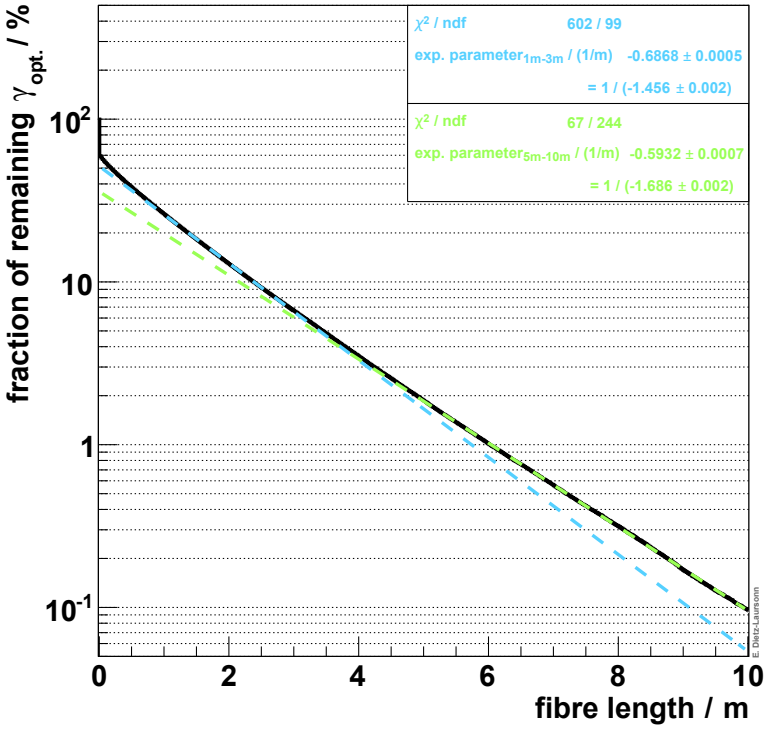

Figure 7.4.: Example distribution for the determination of the simulated signal attenuation length of `G4Fibres`. The distribution shows the fraction of remaining photons as a function of the fibre length. Exponential fits have been performed to the fibre length range of 1 m to 3 m (blue) and of 5 m to 10 m (green).

For the further determination of the signal attenuation lengths in this section, the exponential fit was performed for distances between 1 m and 3 m, as this corresponds to the range that was used by the manufacturer when determining the signal attenuation length from measurements [99, 153]. The resulting signal attenuation spectra for several fibre geometries of the light-guiding fibre BCF-98 and the WLS fibre Y-11 can be found in figure 7.5, together with the digitised manufacturer data (cf. figure D.7). The plots illustrate that using the signal attenuation length as simulation input (i.e. as bulk attenuation length of the the simulated material) leads to a simulated signal attenuation length that is too small, as expected. Therefore, the input has to be adjusted in order to allow for a correctly simulated signal attenuation length. Another thing to notice is the fact that the signal attenuation length varies with the fibre geometry: for the same bulk attenuation length, square fibres possess much higher signal attenuation lengths than round fibres (up to several metres, cf. figure 7.5) and different numbers of claddings as well as different fibre diameters lead to additional small variations.

The manufacturers do not specify which fibre geometry was used for measuring the signal attenuation lengths, but only state that the measurements were performed for fibres with a diameter of 1 mm [99, 153]. Therefore, a fibre geometry had to be chosen, whose simulated signal attenuation length is to match the manufacturer data after adjusting the simulation input. As the manufacturer data of the signal attenuation length is stated to be the minimum value [99, 153], the fibre geometry was chosen, which lead to the lowest signal attenuation length in the simulations without adjustment. Namely, these are round, single-clad fibres for BCF-98, and round, double-clad fibres for BCF-92 and Y-11.

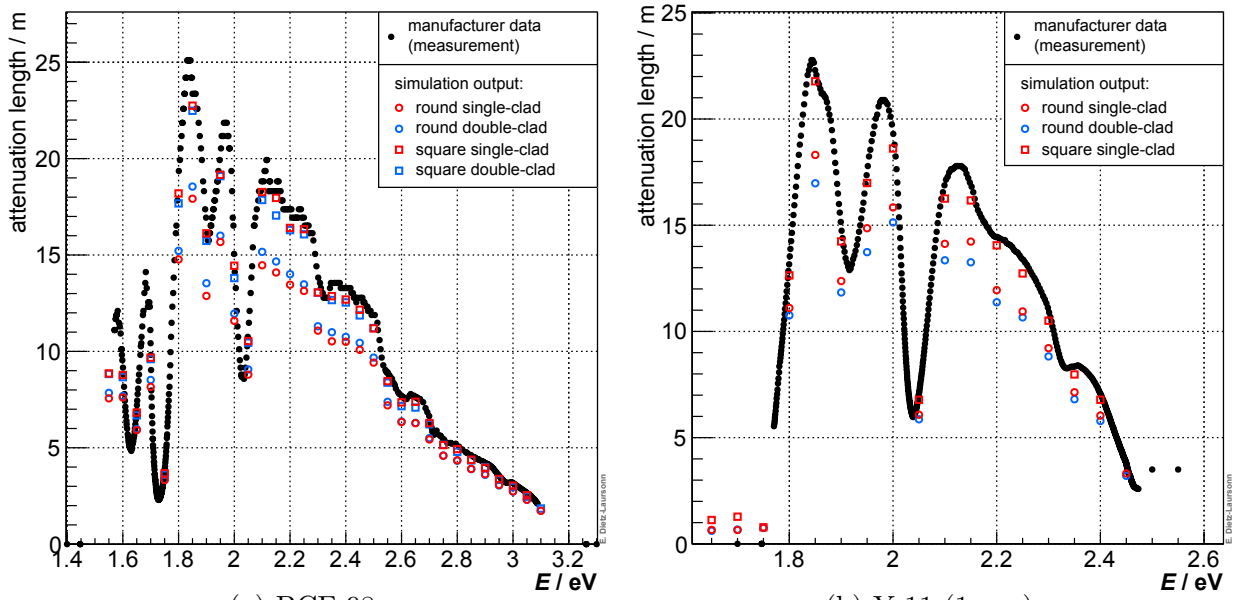

(a) BCF-98 (b) Y-11 (1 mm)

Figure 7.5.: Simulated signal attenuation length spectra (**before the adjustment**) of the light-guiding fibre BCF-98 **(a)** and the WLS fibre Y-11 (1 mm diameter, **(b)**). The statistical uncertainties (from the fits) are below 1 %. Although the simulation results for the square fibres match the manufacturer data better than the results for round fibres, this does not indicate that the measurements were performed with square fibres, as large deviations are expected. Instead, this indicates that square fibres have longer signal attenuation lengths due to their geometry.

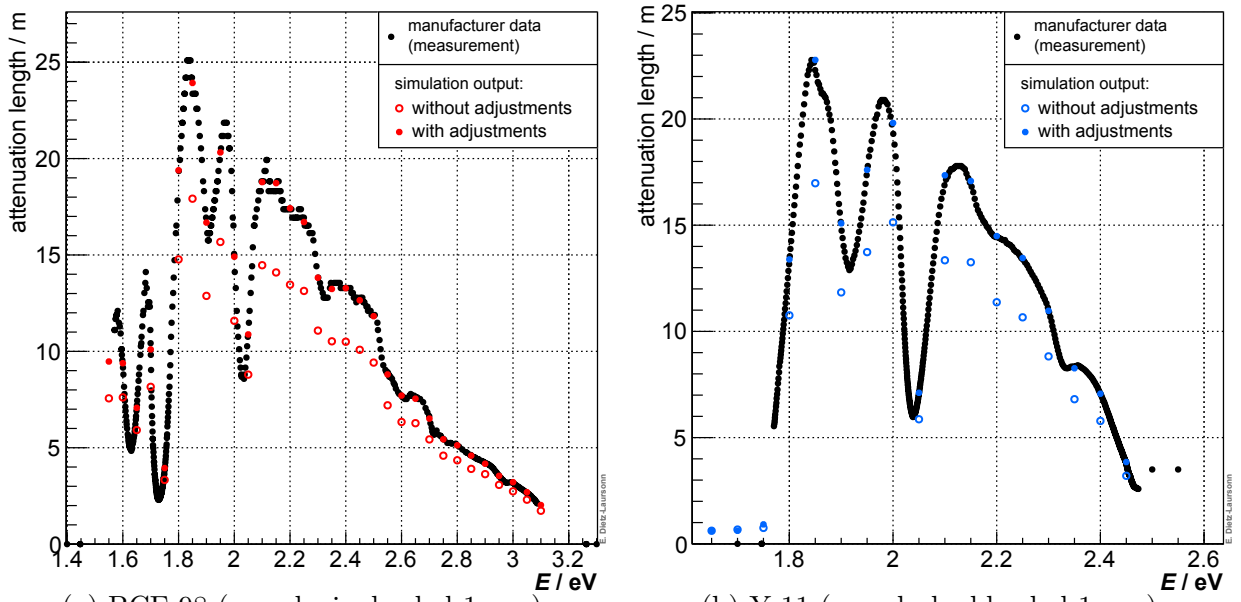

(a) BCF-98 (round, single-clad 1 mm) (b) Y-11 (round, double-clad 1 mm)

Figure 7.6.: Simulated signal attenuation length spectra (**after the adjustment**) of the light-guiding fibre BCF-98 (round, single-clad with 1 mm diameter, **(a)**) and the WLS fibre Y-11 (round, double-clad with 1 mm diameter, **(b)**). The statistical uncertainties (from the fits) are below 1 %.

Due to the fact that only a constant signal attenuation length is given for BCF-92 by the manufacturer, the adjustment can simply be done by specifying a suitable linear multiplication factor. The factor 1.31 was chosen, which leads to an adjustment of the signal attenuation length from $(2786 \pm 6)\,\mathrm{mm}$ to $(3501 \pm 8)\,\mathrm{mm}$, whereas a value of $> 3500\,\mathrm{mm}$ is stated by the manufacturer. In case of the other two fibres, a simple linear factor allows for a correct adjustment of the full energy-dependent signal attenuation length spectrum. Thus, a combination of a linear and a quadratic adjustment factor (f_l and f_q, respectively) was chosen: $\mu_{\mathrm{att,\,adjusted}} = f_\mathrm{l} \cdot \mu_\mathrm{att} + f_\mathrm{q} \cdot \mu_\mathrm{att}^2$.[68] The adjustment factors that have been determined are $f_\mathrm{l} = 1.15$ and $f_\mathrm{q} = 0.00001$ for BCF-98 and $f_\mathrm{l} = 1.175$ and $f_\mathrm{q} = 0.0000075$ for Y-11, respectively. The resulting adjusted signal attenuation length spectra are illustrated in figure 7.6.

As a consequence of these results, the option was implemented for the `G4Fibres`, to specify linear and quadratic adjustment factors for the bulk attenuation length inside the material property files. The adjustment factors, which have been determined in this section, have been chosen as the standard values. They were used in every simulation that is described in the following chapters.

[68] Another possibility would be to determine a distinct linear adjustment factor for every point of input spectrum. This might lead to an even better matching of the simulated signal attenuation length and the manufacturer data. However, this requires much more computational effort, which is not justified by the slight achievable improvement.

8. Validation against Measurements with Prototype Modules

In the previous chapters, the correct operation of the GODDeSS framework on source code level was tested and some necessary adjustments were presented. In this chapter, the results of simulations with GODDeSS will be compared to measurements with prototype modules. Thus, the GODDeSS framework can be validated with respect to complete optical detectors consisting of several optical detector elements. The prototype modules have been exposed to cosmic muons or a high-energy proton beam, respectively. The material properties, which have been used for modelling the optical detector components in the simulations, can be found in appendix D.

8.1. Hodoscope Measurements of Prototype Modules

The Physics Institute III of RWTH Aachen University possesses a hodoscope, which is able to trigger on traversing cosmic muons and to determine their trajectory. In the scope of this thesis, this allowed for performing measurements of the response of scintillator-based detector prototype modules as a function of the particle incidence position. These measurements have then been compared to the results of simulations of the corresponding modules with GODDeSS, in order to validate the performance of the GODDeSS framework with respect to the results of simulations of complete optical detector parts.

The hodoscope consists of two trigger detectors, which are scintillator tiles with PMT read-out, as well as of four silicon strip detectors, each two of them combined perpendicularly to a detector layer of the hodoscope. The latter allow for the reconstruction of the particle trajectory by determining two of its points. Detailed information about the setup and of the working principle of the hodoscope can be found in [155–160], it will be omitted at this point.

Whereas the simulations and final measurements, their analysis, as well as the comparison of the results have been performed by the author of this thesis, the initiation and troubleshooting of the hodoscope (the resulting adjustments to the hodoscope software are summarised in appendix F for documentation purpose) were substantially supported by other scientists of the Physics Institute III of RWTH Aachen University.

8.1.1. Experimental Procedure

The prototype modules, which have been used in the scope of this thesis, were already introduced as modules 3 and 7 in [158–160]. **Module 3** consists of a $100\times100\times3\,\mathrm{mm}^3$ scintillator tile (BC-404) with Teflon wrapping. The scintillation light is collected via straight WLS fibres (BCF-92, round, 1 mm diameter, double-clad) at two opposite lateral surfaces of the scintillator tile and guided to $1\times1\,\mathrm{mm}^2$-SiPMs (Hamamatsu S10362-11-100C) at one end of each fibre. The other fibre ends, which are not connected to an SiPM, are mirrored with aluminium paint. The fibres are optically coupled to the scintillating material via optical cement (BC-630) and have a total length of 230 mm. In contrast, **module 7** consists of a $100\times100\times5\,\mathrm{mm}^3$ scintillator tile (BC-404) with Teflon wrapping. It is readout directly via two $3\times3\,\mathrm{mm}^2$-SiPMs (Hamamatsu S10362-33-100C), which are centred on one of the lateral surfaces with a distance of 4 cm between each other. The layout of the modules is presented in figure 8.1.

During the QDC measurements, a gate of 1 µs was used for the readout of the SiPM signals in each triggered event, in order to detect all photons belonging to the event. The

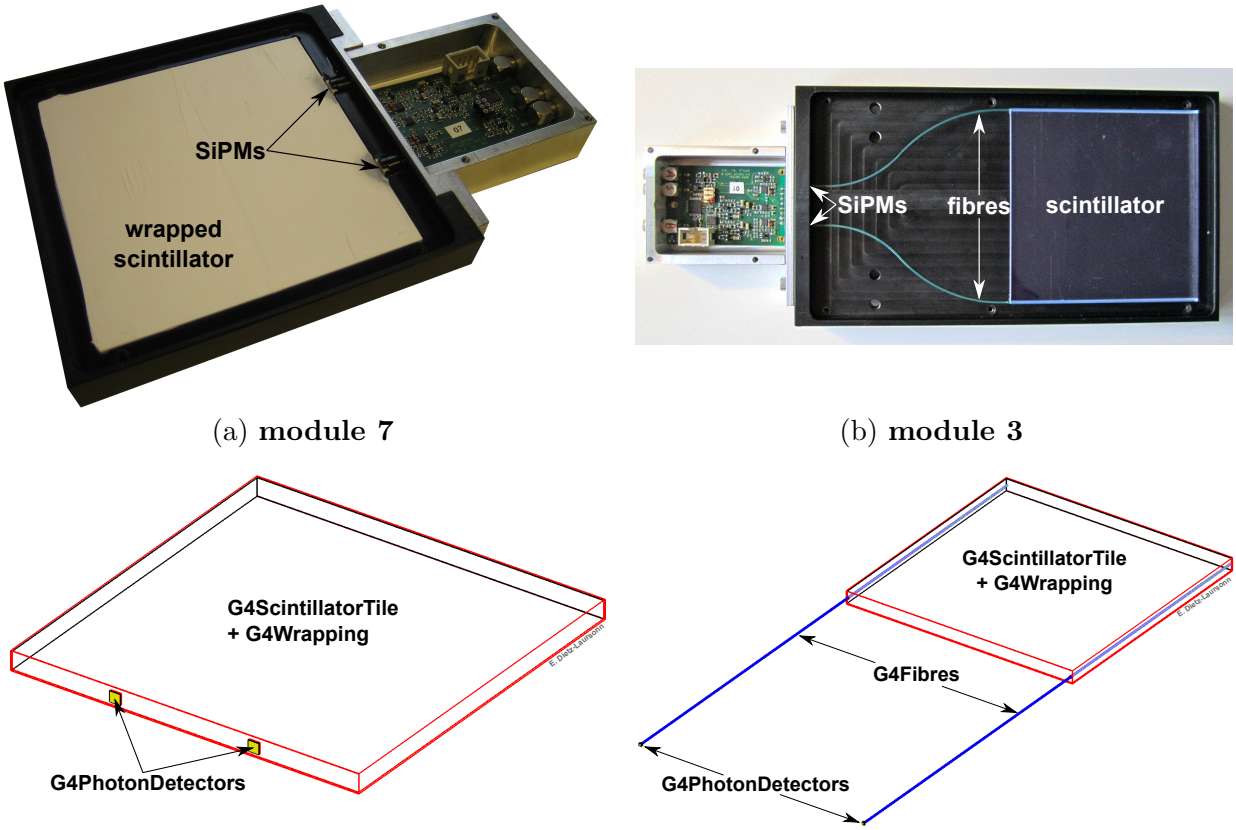

(a) **module 7** (b) **module 3**

Figure 8.1.: Pictures of the prototype modules that have been used for the measurements **(top)** and the corresponding setups for the simulations **(bottom)**: **(a)** presents module 7, **(b)** shows module 3. In the pictures, the scintillator tile of module 7 is wrapped (like they were during the measurements), whereas the scintillator tile of module module 3 is shown without wrapping. The pictures have been adapted from [159] (module 3) and [161] (module 7). For simplicity reasons, the bending of the fibres outside the scintillator tile of module 3 has been neglected in the corresponding simulation.

full configuration that has been used for the hodoscope measurements with the prototype modules is summarised in appendix G, for the sake of completeness.

The sensitive area of the hodoscope is smaller than the scintillator tile within the used prototype modules ($\sim 8{\times}9\,\mathrm{cm}^2$ versus $10{\times}10\,\mathrm{cm}^2$). Therefore, four measurements of each module had to be performed with different positions of the modules relative to the sensitive area of the hodoscope, in order to scan the full scintillator tiles. The positions are sketched in figure 8.2 and the resulting raw data of the corresponding measurements are presented in figure 8.3, using the example of one of the SiPMs of module 7. The positions were chosen in such a way that in each case a strip of the sensitive area was not covered with scintillating material at two of its edges. This allows for a determination of the edges of the scintillator tile from the measurement data and thus for a combination of the results of the individual measurements at different positions during the data analysis. For each measurement position and module, 200,000 cosmic muon events were recorded within ~ 10 days of measurement.

In the simulations, the mirroring of the WLS fibres was realised by applying a reflectivity of 90 % and the wrapping was simulated with an air gap between scintillator and wrapping material. 100,000 MIP muons (with a $\beta\gamma$ of 3.5) were shot perpendicularly and homogeneously distributed onto the top surfaces of the prototype modules. For each muon, the incidence position on the scintillator tile as well as the optical photons that reached the `G4PhotonDetectors` were recorded.

8.1.2. Analysis and Comparison

Adding up the individual measurements, 800,000 cosmic muon events were recorded for each prototype module. In order to guarantee a high purity of the events that are contributing to the final results, the criteria of containing an unambiguously reconstructible muon trajectory, i.e. exactly one hit in each of the four silicon strip modules, was applied. This was done by using the configuration from appendix G, especially with respect to the signal over noise threshold for hits in the silicon strip modules. As a result, $\sim 70,000$ of the recorded events fulfilled the requested criteria.

Before the results of the individual measurements of the same prototype module at different positions could be combined, they had to be transformed from the coordinates of the hodoscope to the coordinates of the module. For that purpose, the edges of the scintillator tile were visually determined in the data and their coordinates were redefined in a way that the centre of the tile is the origin of the coordinate system. An example is shown in figure 8.4. Figure 8.5 illustrates the combined measurement results for one of the two SiPMs of module 7, i.e. the combined data of the plots that have been presented in figure 8.3.

After coordinate transformation and combination of the results, the data was filled into a histogram with a binning that guarantees a reasonable minimal number of entries in the bins (in the area of the scintillator material, more than 250 events in each bin). Additionally, the range of the histograms was restricted to the area of the scintillator tile, as the events

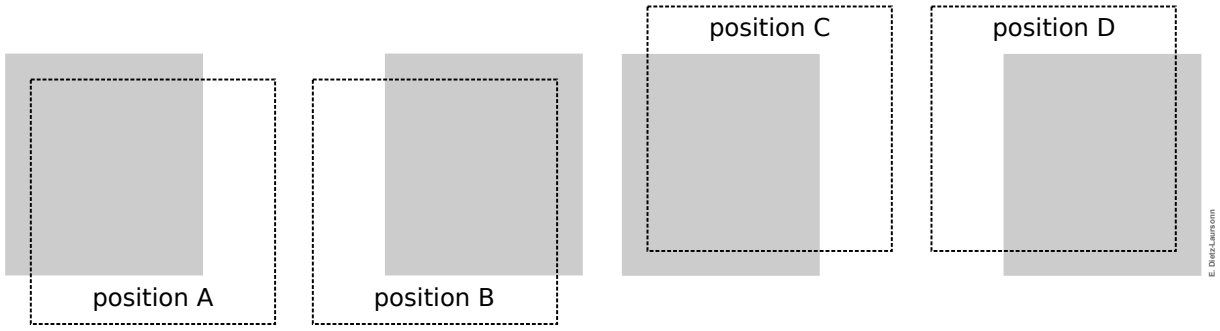

Figure 8.2.: Measurement positions of the prototype modules (represented by the black-framed squares) with respect to the sensitive area of the hodoscope (grey rectangles).

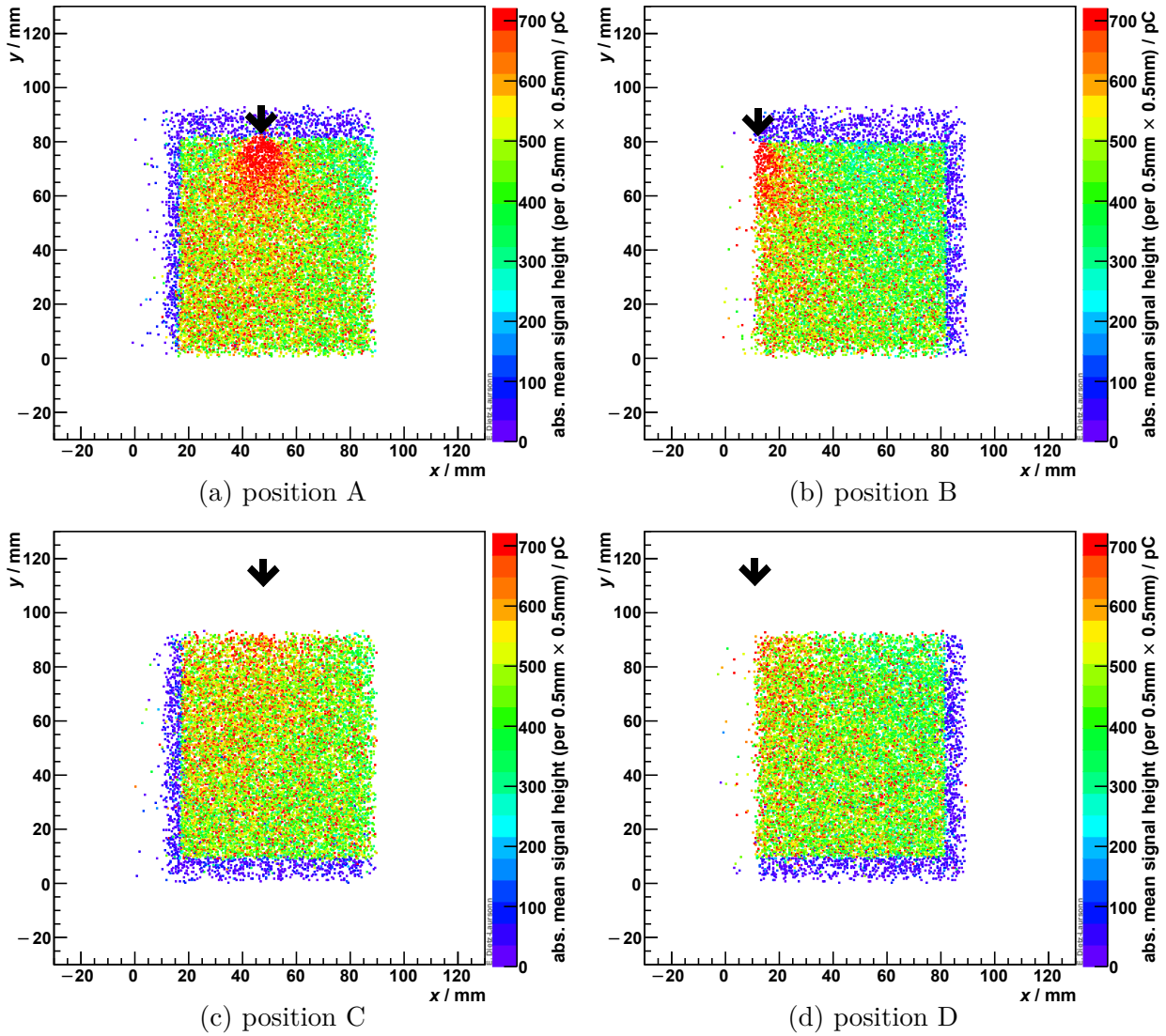

(a) position A

(b) position B

(c) position C

(d) position D

Figure 8.3.: Raw results of the QDC measurements for one of the two SiPMs of module 7 at the individual measurement positions. The data of the second SiPM is not illustrated. The x-y-plane represents the incidence position of the comic muons on the prototype module as determined by the hodoscope. The colour of the bins symbolises the mean measured signal height. The position of the SiPM is indicated by the black arrows.

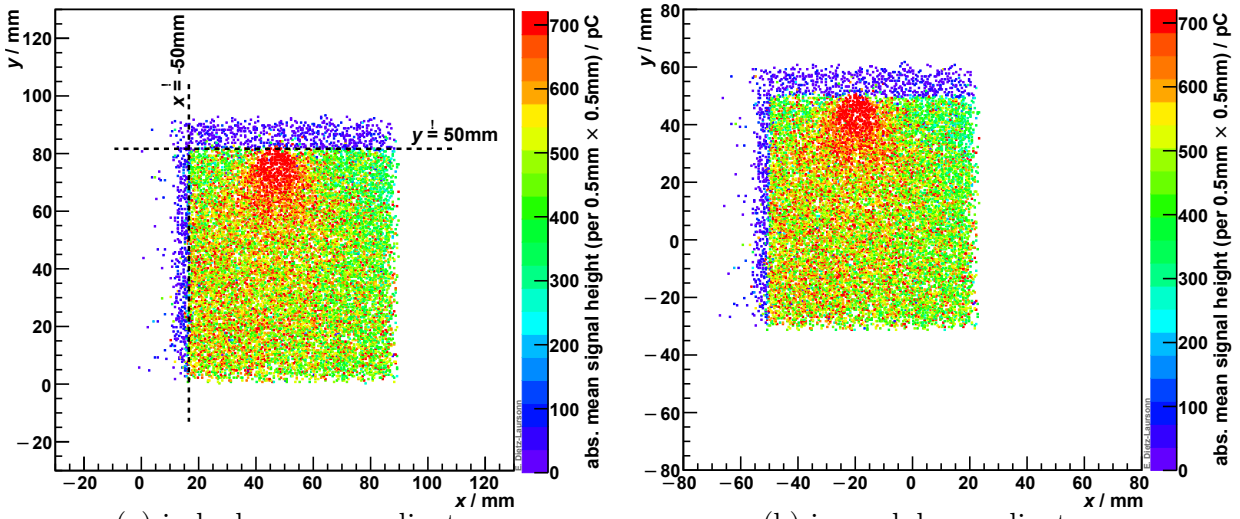

(a) in hodoscope coordinates (b) in module coordinates

Figure 8.4.: Coordinate transformation from hodoscope coordinates to coordinates of the prototype modules: **(a)** shows the signal height distribution (of module 7 at position A, in this case) in the coordinates of the hodoscope. The visually determined edges of the scintillator tile of the prototype module are marked with dashed lines and labelled with the coordinates they are to correspond to after the coordinate transformation. **(b)** presents the same distribution after the coordinate transformation (in coordinates of the prototype modules).

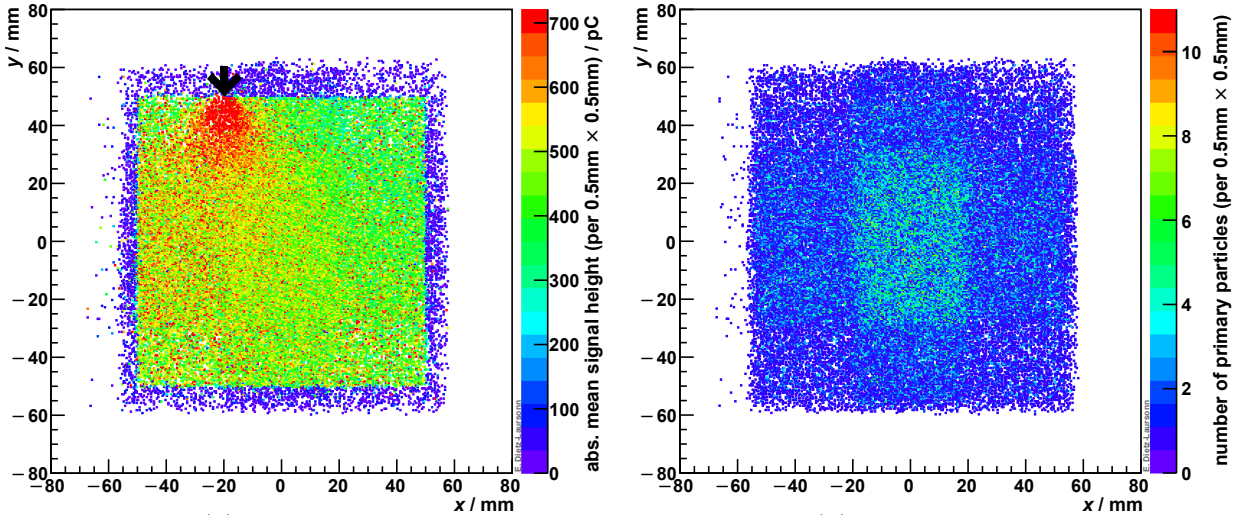

(a) mean signal (b) muon position

Figure 8.5.: Combined results of the measurements at the individual module positions. **(a)** shows the spatial distribution of the mean measured signal height. The black arrow indicates the position of the SiPM. **(b)** presents the spatial distribution of the number of events per bin, with the clearly visible areas of higher statistics due to overlaps of the individual measurements.

of muons missing the scintillator material do not provide any meaningful information for the comparison between measurement and simulation. Exemplary results are presented in figure 8.6.

Before filling the histograms, a pedestal correction has been performed for the SiPM signals of the prototype modules. For every bin, the mean value of the SiPM signal of all corresponding events was calculated and the statistical uncertainty was determined via

$$u_{\bar{s}} = \frac{\sigma_s}{\sqrt{N}} = \frac{1}{\sqrt{N}} \sqrt{\frac{1}{N-1} \cdot \sum_{j=1}^{N} (s_j - \bar{s})^2} = \frac{1}{\sqrt{N}} \sqrt{\frac{1}{N-1} \cdot \left(\sum_{j=1}^{N} s_j^2 - \frac{1}{N} \left(\sum_{j=1}^{N} s_j \right)^2 \right)}, \quad (8.1)$$

where N is the number of events in the bin, s_j are the N individual signal values, $\bar{s}$ is their mean value, and σ_s is their standard deviation.[69] The same procedure was performed for the simulation data.

Whereas the signal of the prototype modules was measured in units of the total charge of the fired cells of the SiPMs, the simulations return the signal in units of photons. Thus, an *absolute comparison* of measurement and simulation requires a conversion of the measured total charge of the fired cells to the corresponding number of fired cells. The latter is equal to the number of photon equivalents (p.e.), i.e. the number of photons that were detected by the SiPMs. The corresponding scaling function depends on the gate length, which was used in the measurement, as well as on the gain of the SiPMs, which is a function of e.g. the temperature and the external voltage. Therefore, it has to be determined for each SiPM for each measurement. Nevertheless, the gain is stabilised in means of temperature and external voltage by the readout electronics of the prototype modules. As a result, a scaling function that has been determined once can be applied to all measurement results of the corresponding module/SiPM, provided that the same gate length is used. Although scaling functions were determined for module 3 and 7 before [160], it is not possible to apply them to the current measurements due to two reasons:

- The measurements presented in [160] were performed with different gates than the current measurements.
- After the measurements presented in [160], the readout electronics of the prototype modules was changed to obtain smaller gain factors and thus less saturation of the pre-amplifier (cf. e.g. [161]).

Therefore, new scaling functions would have to be determined for the current measurements in order to allow for absolute comparisons between measurement and simulation. To obtain a scaling function from the recorded data, a finger spectrum is needed (cf. [160]), i.e. the distribution of the measured signal heights has to contain several separable peaks[70]. Unfortunately, such finger spectra could not be obtained from the recorded data of the cur-

[69] In contrast to equation (8.1), the ROOT data analysis framework [162] (which has been used in the scope of this thesis) uses a modified equation for calculating the standard deviation: $\sigma_s = \sqrt{\frac{1}{N} \cdot \sum_{j=1}^{N} (s_j - \bar{s})^2}$. As a result, ROOT returns a standard deviation value that is smaller than the correct value, by the factor $\sqrt{N/(N-1)}$. This corresponds to a deviation of $< 5\,\%$ for $N > 10$, $< 1\,\%$ for $N > 50$, and $< 0.2\,\%$ for $N > 250$.

[70] These peaks correspond to the lowest photon equivalents.

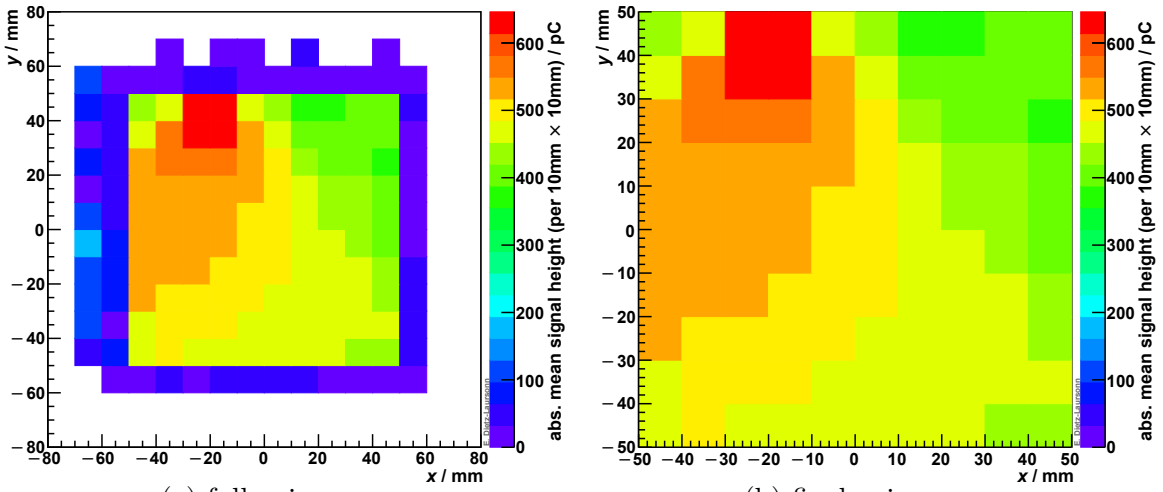

(a) full axis ranges (b) final axis ranges

Figure 8.6.: The combined measurement results with the final binning.

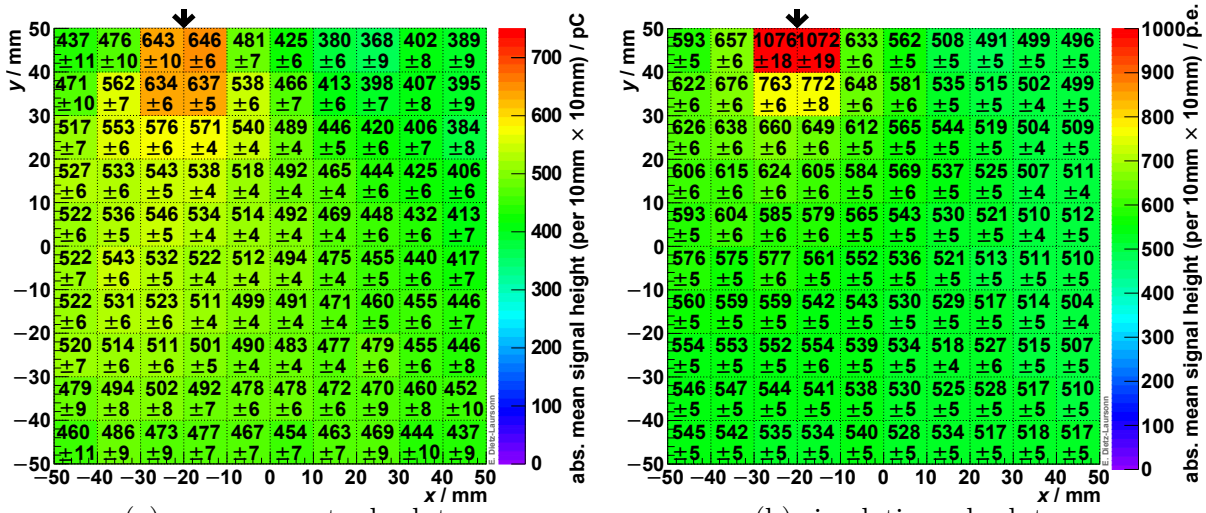

(a) measurement, absolute (b) simulation, absolute

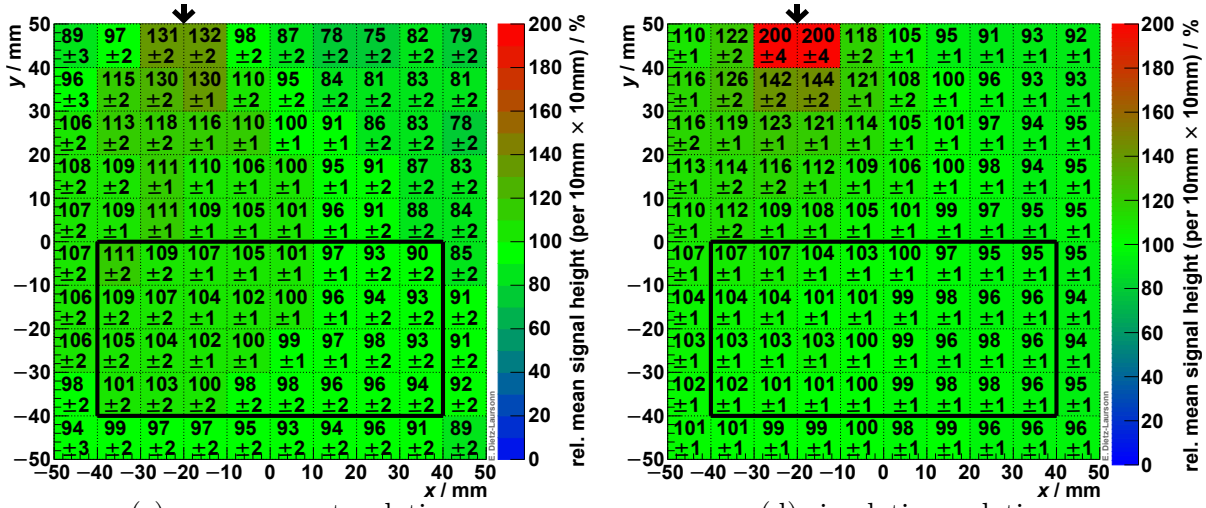

(c) measurement, relative (d) simulation, relative

Figure 8.7.: Normalisation of the signal distributions (for module 7): The **top** plots show the absolute signal distributions for one SiPM of module 7 for measurement and simulation. The **bottom** plots present the corresponding distributions after normalising them to the average signal height of the reference bin-region (marked by the black rectangle). The black arrows indicate the position of the SiPM.

rent measurements. This is probably a result of the lower gain. Consequently, no absolute comparisons but only *relative comparisons* are possible. For this purpose, the absolute distributions that were obtained from the measurements and simulations have to be transformed into relative distributions by normalising them. Suitable bin-regions were defined as a basis for the normalisation and their average bin entry was used as value to normalise the distributions to. These bin-regions were chosen in a way to avoid extreme cases. This means that no bins from the edge of the scintillator tile were chosen as well as no bins next to the SiPMs or fibres were used. In the plots within this chapter, the chosen bin-regions are always marked by a black rectangle. The results of the normalisation are exemplarily presented in figure 8.7.

For comparing the results of measurement and simulation, the relative distribution of the measurement results was subtracted from the relative distribution of the corresponding simulation. Thus, a space-resolved distribution of the *relative deviation* between measurement and simulation is obtained. This means, bins significantly differing from zero represent deviations between the relative results of measurement and simulation. Positive deviations represent too large signals in the simulation (with respect to the reference bin-region), negative deviations stand for too low signals in the simulation. Figure 8.8(a) presents the result for one SiPM[71] of module 7.

The agreement is good in the reference bin-region but there are significant deviations in triangular regions left and right of the SiPM (marked by white dashed lines) and in the

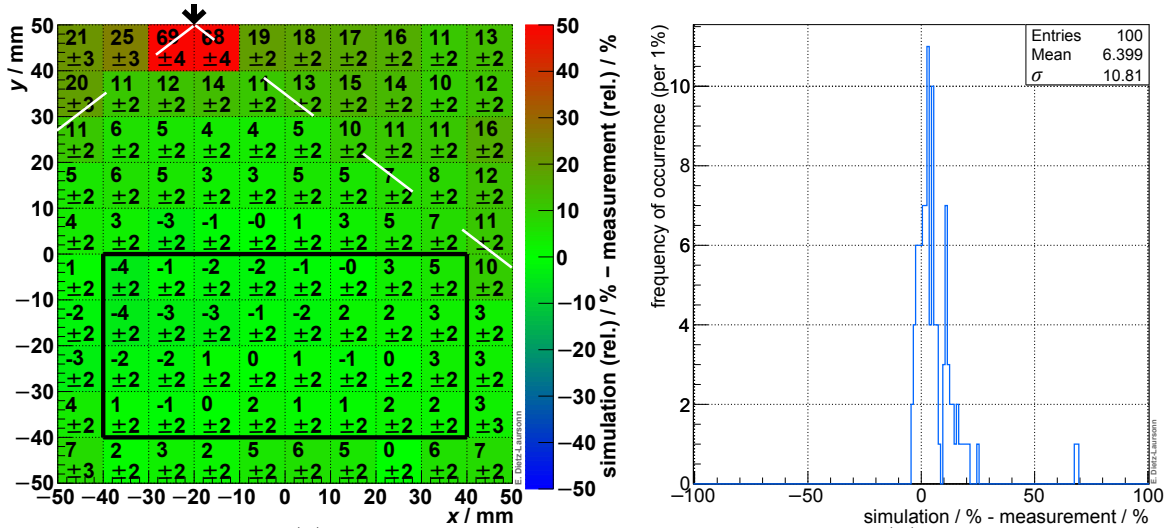

(a) (b)

Figure 8.8.: Deviations between measurement and simulation for one SiPM of module 7: **(a)** presents the space-resolved deviation distribution, i.e. the relative measurement distribution (figure 8.7(c)) subtracted from the relative simulation distribution (figure 8.7(d)). The black arrow indicates the position of the SiPM, the black rectangle marks the reference bin-region. **(b)** illustrates the frequency distribution of the deviation values of the bins of (a). In case of perfect agreement of measurement and simulation, only the zero-bin would have entries. This means, the better the agreement, the lower the mean value and standard deviation σ of the distribution.

[71] The results for the second SiPM are qualitatively mirror-symmetric to the presented results.

bins next to the SiPM position, especially the two bins directly in front. The reason for these significant deviations is the usage of the G4PhotonDetector in the simulation of the prototype module. As described in subsection 5.1.1, the G4PhotonDetector detects every photon that reaches its sensitive surface. This especially means that neither the geometry of the SiPM (fill factor, window[72]) and its PDE are considered, nor the effects of pulse form, gate length, noise, saturation (in case of multiple photons hitting the same cell), and optical coupling of the SiPM.

In order to verify the impact of geometry of the SiPM and its PDE, the photons, which had been detected by the G4PhotonDetector during the simulation, were shot onto a G4SiPM (with the configurations of the SiPM model that was used in the prototype modules) in another simulation step. In an additional analysis step, the influence of SiPM saturation effects was considered by applying equation (3.4). The resulting deviation distributions can be found in figure 8.9. As expected, the number of detected photons dramatically decreases when *considering the geometry of the SiPM and its PDE* and the agreement in the triangular regions as well as the overall deviation distribution improve significantly. This is also expressed by the significant decrease of the mean value and the standard deviation of the frequency distribution of the deviation values. When additionally *considering saturation effects of the SiPM*, the number of detected photons again decreases slightly, the overall deviation distribution improves slightly, and the agreement improves especially next to the SiPM. Nevertheless, there are still significant deviations next to the SiPM, especially in the two bins directly in front of it.

These remaining deviations are caused by the fact that high signals reach the *saturation of the pre-amplifier* in the readout electronics of module 7. This is especially the case for events next to the SiPM, as they tend to cause the highest signals. These deviations disappear when the signal height is restricted in order to simulate this saturation effect. The resulting distributions are presented in figure 8.10, together with the original distributions without any corrections (G4SiPM, SiPM saturation, pre-amplifier saturation) for comparison.

The GODDeSS simulation of **module 7** shows a very good agreement with the measurements when taking the geometry and the PDE of the SiPM into account as well as the saturation effects of the SiPM and the pre-amplifier. Maybe even better results could be achieved when also considering the effects of the pulse form of the SiPM and the gate length, noise effects of the SiPM, and especially the correct optical coupling of the SiPM to the scintillator material. This would be possible with GODDeSS and G4SiPM, but would go beyond the (time) frame of this thesis. As also an absolute comparison would be interesting, a new measurement (allowing for determining finger spectra) in combination with a more detailed simulation (taking the previously mentioned factors into account) could be performed in the scope of a subsequent bachelor or master thesis.

A thing that can be noticed in all space-resolved deviation distributions is that there seems to be a tendency to higher (positive) deviations at the edges and especially in the corners of the scintillator tile. This means that the simulation tends to result in higher (relative) signals for particle transitions at the edges and in the corners than the measurement does.

[72] The optical surface between the scintillator material and the window of the SiPM and the resulting total reflection for large incidence angles causes the triangular structures in the deviation distributions.

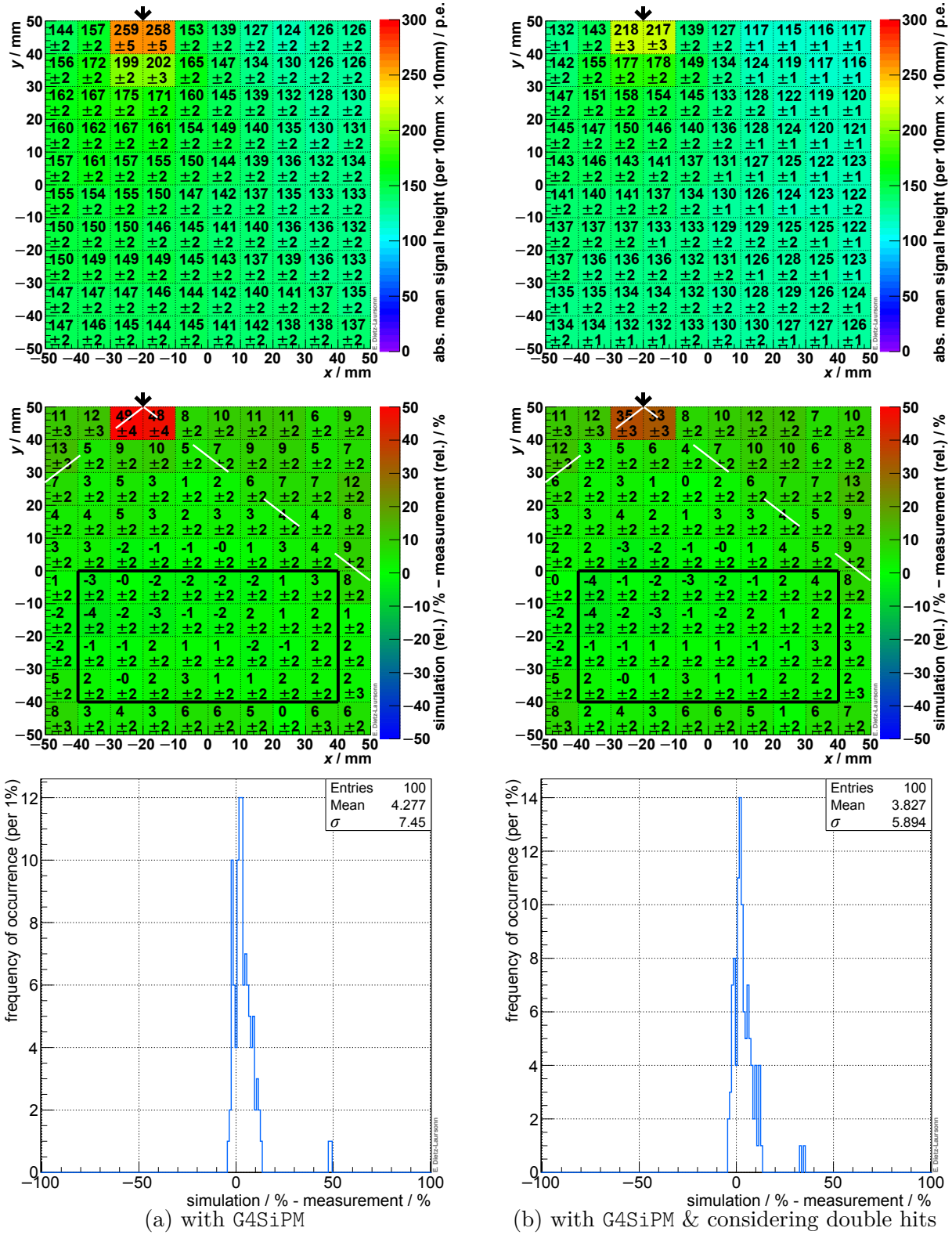

(a) with G4SiPM (b) with G4SiPM & considering double hits

Figure 8.9.: Results for one SiPM of module 7 when considering the geometry and the PDE of the SiPM **(left)** and when additionally taking the saturation effect of SiPMs into account **(right)**: Absolute simulated signal height distribution **(top)**, space-resolved deviation distribution **(middle)**, and frequency distribution of the deviation values **(bottom)**. The black arrows indicate the position of the SiPM, the black rectangles mark the reference bin-regions.

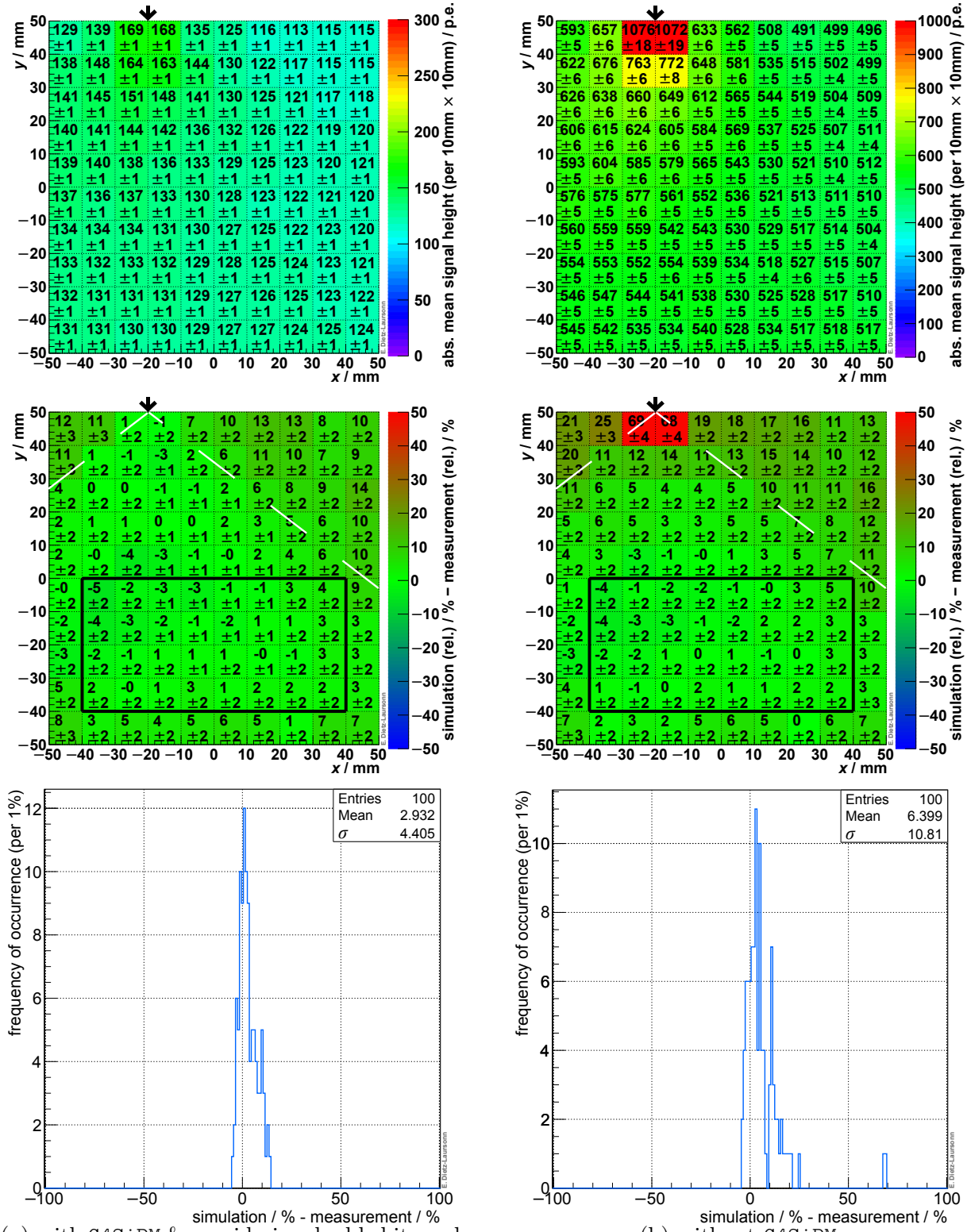

(a) with G4SiPM & considering double hits and saturation

(b) without G4SiPM

Figure 8.10.: Results for one SiPM of module 7 with **(left)** and without **(right)** considering the geometry, the PDE, and the saturation effect of the SiPM, as well as the saturation of the pre-amplifier: Absolute simulated signal height distribution **(top)**, space-resolved deviation distribution **(middle)**, and frequency distribution of the deviation values **(bottom)**. The black arrows indicate the position of the SiPM, the black rectangles mark the reference bin-regions.

Reasons for this effect might be a larger probability of the photons to hit a surface of the scintillator with a small incidence angle[73] (i.e. no total reflection) as well as a not perfectly uniform wrapping, especially at the edges of the real scintillator tile.

The same analysis procedure as described above for module 7, was also applied to the results of **module 3** (besides the pre-amplifier saturation, which did not occur in this case). In contrast to module 7, the consideration of the `G4SiPM` only had a minor influence (large incidence angles are suppressed for photons reaching the fibre end), whereas saturation effects of the SiPM had a large influence (the SiPMs used in module 3 have only 100 cells instead of 900). Figure 8.11 illustrates the resulting distributions. It can clearly be seen that there is a large deviation next to the fibre, which decreases with increasing distance to the fibre. This means that the simulation results in a less steep (relative) increase of the mean signal height towards the fibre position than the measurement does. This could possibly indicate a lower (overall) reflectivity of the wrapping in the measurements than assumed in the simulation: Neglecting absorption, every photon would reach one of the fibres after some time in a perfect module without any light losses. A decreasing reflectivity would lead to increasing light losses and thus the probability of the photons to reach the fibre decreases. The influence of this effect depends on the path length the photons have to cover before reaching a fibre. Thus, signals from muons that traverse the scintillator tile in a larger distance are more effectively suppressed by a lower reflectivity.

To check the assumption of a deviating reflectivity, the simulation was repeated for a reduced reflectivity value of 90 % and analysed with the same procedure as the original simulation. The results are summarised in figure 8.12. They show a much better agreement between the simulation and the measurement. Reasons for the low effective reflectivity could be an

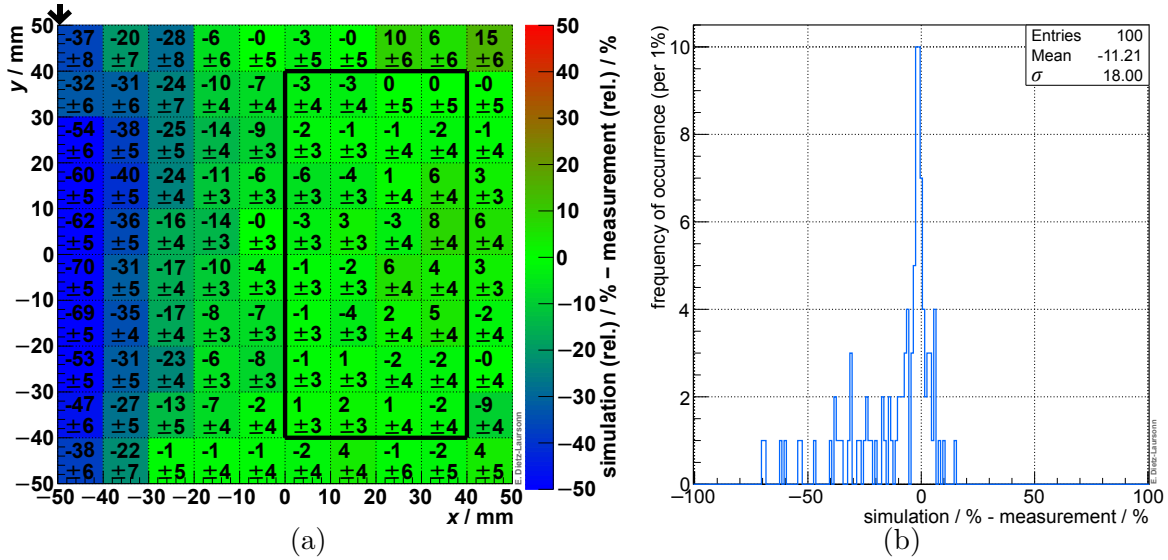

(a) (b)

Figure 8.11.: Results for one SiPM of module 3 (considering the geometry, the PDE, and the saturation effect of the SiPM): **(a)** shows the space-resolved deviation distribution. **(b)** presents the frequency distribution of the deviation values. The black arrow indicates the position of the WLS fibre that guided the photons to the SiPM, the black rectangle marks the reference bin-region.

[73] The probability is larger, just because there are additional surfaces next to the initial position of the photons.

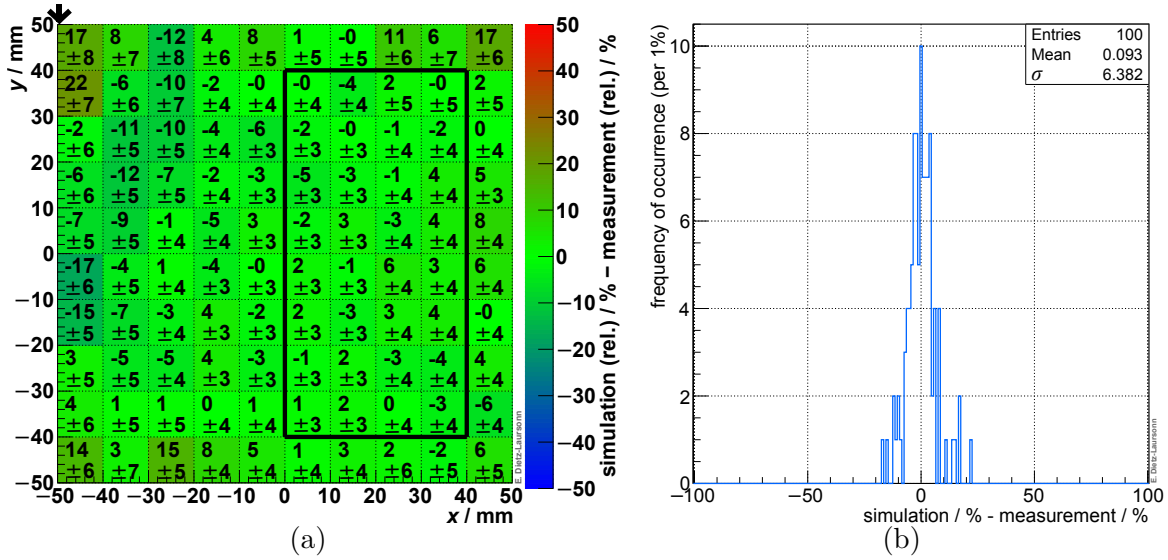

(a) (b)

Figure 8.12.: Results for one SiPM of **module 3** (considering the geometry, the PDE, and the saturation effect of the SiPM) for a **reduced reflectivity value (90 %)** of the simulated wrapping: Illustrated are the space-resolved deviation distribution **(a)** and the frequency distribution of the deviation values **(b)**. The black arrows indicate the position of the WLS fibre that guided the photons to the SiPM, the black rectangles mark the reference bin-regions.

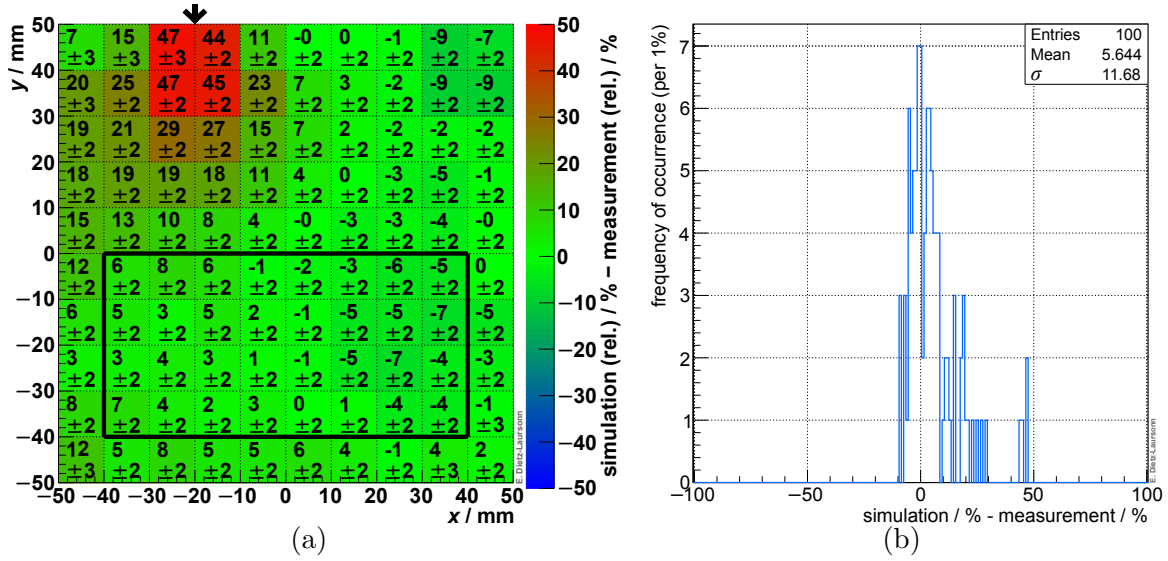

(a) (b)

Figure 8.13.: Results for one SiPM of **module 7** (considering the geometry, the PDE, and the saturation effect of the SiPM, as well as the saturation of the pre-amplifier) for **90 % reflectivity** of the simulated wrapping: **(a)** shows the space-resolved deviation distribution. **(b)** presents the frequency distribution of the deviation values. The black arrow indicates the position of the SiPM, the black rectangle marks the reference bin-region.

inhomogeneous or damaged wrapping of the prototype module.[74] In order to find the reason for this seemingly reduced overall reflectivity of module 3, it would be interesting to examine the scintillator tile and its wrapping. Additionally, the wrapping could be renewed and the measurement could be repeated for the new wrapping. As it would go beyond the (time) frame of this thesis, this could be performed in the scope of a subsequent bachelor or master thesis.

In contrast, a reduction of the simulated reflectivity of module 7 does not improve the agreement between simulation and measurement but leads to increasing deviations (cf. figure 8.13). Seemingly, the reflectivity is correctly simulated with a value of 99 %.

8.2. Test-Beam Measurements of Prototype Modules

In addition to the hodoscope measurements with cosmic muons, space-resolved measurements have been performed with a high-energy proton beam ($E_{\text{kin.}} = 2.95\,\text{GeV}$) at the COSY particle accelerator [164] at Forschungszentrum Jülich by other scientists. The measurements and their results are presented in [165]. The reason for performing these measurements was to gain high statistics within a short period of time ($\sim$ 1,000,000 events per prototype module within a few hours of measurement). The disadvantage of these test-beam measurements is a restriction of the spatial resolution, due to the radial extent of the proton beam of $\approx 1\,\text{cm}$ (σ of the two-dimensional Gaussian distribution). Like for the hodoscope measurements, simulations of the corresponding modules have been performed with GODDeSS. Their results were compared to the measurements, in order to validate the correct performance of the GODDeSS framework with respect to the results of simulations of complete optical detectors.

8.2.1. Experimental Procedure

The prototype modules, which have been investigated during the test-beam measurements, are a newer development in the scope of the studies on the MTT-upgrade [2, 15] for CMS. A description of the module layout can be found in [165]. They consist of larger ($300\times300\times5\,\text{mm}^3$) scintillator tiles (BC-404) and are wrapped with Tyvek. **Module mtt1** is readout directly via two $3\times3\,\text{mm}^2$-SiPMs (Hamamatsu S10362-33-100C), which are centred on one of the lateral surfaces with a distance of 4 cm between each other. This module is basically a larger version of module 7 from section 8.1. In case of **module mtt2**, the scintillation light is collected via two WLS fibres (BCF-92, round, 1 mm diameter, double-clad) and guided to a single SiPM (Hamamatsu S10362-33-100C). The fibres are optically coupled to the scintillating material via optical cement (BC-630). The exact fibre layout is illustrated in figure 8.14. Both fibres are arranged in the same way, one fibre at the top and one fibre at the bottom surfaces. Next to the SiPM, the fibres are brought together at the central plane of the scintillator tile, where they are coupled to the SiPM. For simplicity reasons, this has been neglected in the simulation and the fibres were coupled to a `G4PhotonDetector`

[74] It was already demonstrated before that the signal height of the prototype modules could significantly change when re-wrapping them [161, 163].

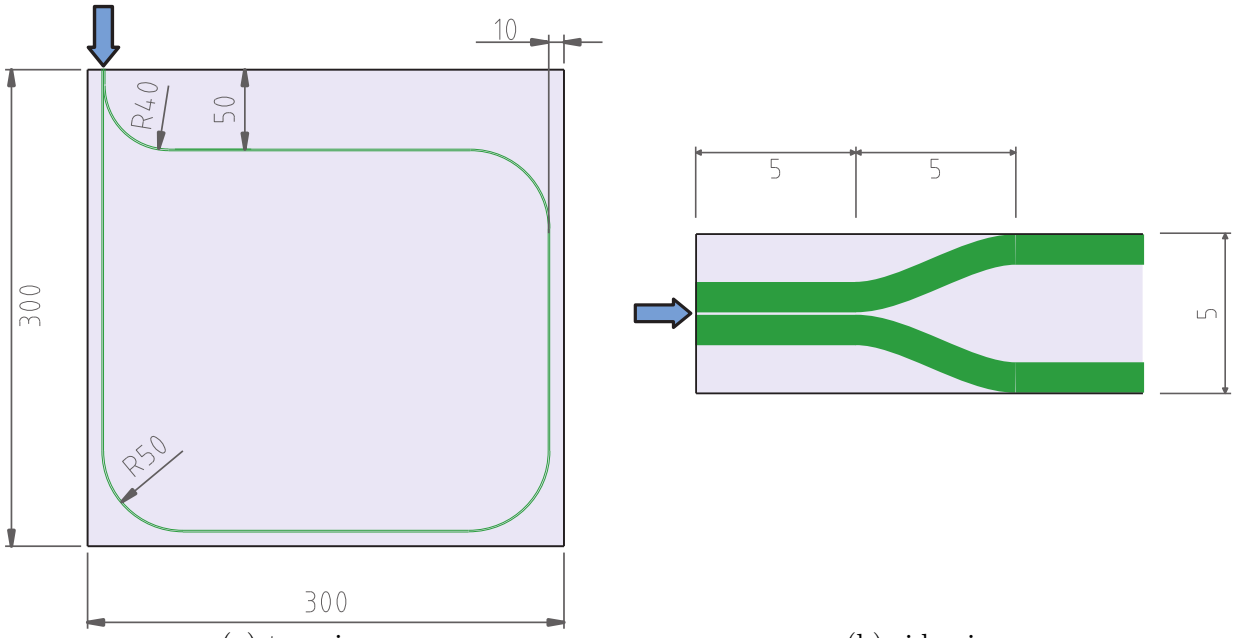

(a) top view (b) side view

Figure 8.14.: Mechanical drawing of module mtt2. The top view **(a)** shows the full scintillator tile and the top fibre, the side view **(b)** presents a zoom into the area where the fibres meet the SiPM. The arrows indicate the SiPM position.

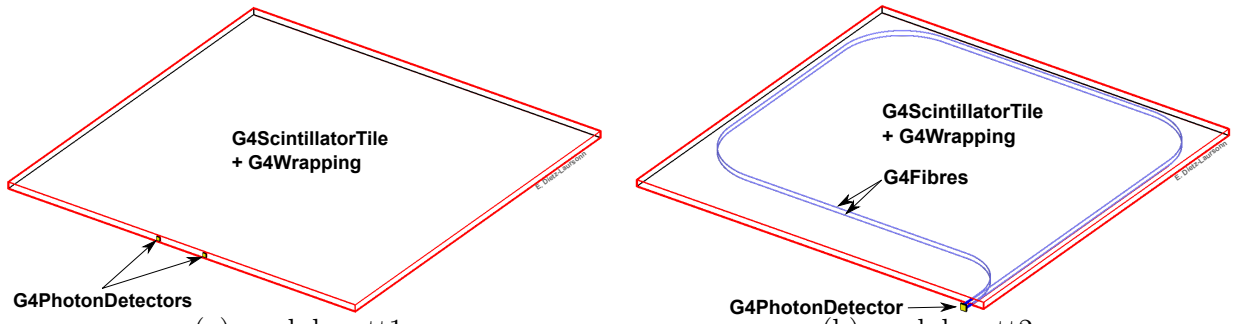

(a) module mtt1 (b) module mtt2

Figure 8.15.: Setups of the prototype modules, which have been used for the simulations.

with a sensitive area of $5\times5\,\mathrm{mm}^2$.[75] The simulated layout of both modules is presented in figure 8.15.

During the measurements, the proton beam was directed perpendicularly onto one of the top surfaces of the prototype modules. The surface was divided into 100 equal squares (bins) and the proton beam (with its radial extent of $\sigma \approx 1\,\mathrm{cm}$) was successively directed onto the centre of each bin. A combination of trigger detectors and veto detectors was used to identify events with exactly one proton traversing the prototype modules at the desired position. For each of these events, the signal of the prototype module and the bin, which the proton beam was aiming at, were recorded. A detailed description of the measurement procedure as well as of the experimental setup can be found in [165].

[75] For considering the geometry, the PDE, and the saturation effect of the SiPM, the hit position of the photons on the SiPM was corrected for the fibre position when shooting the photons onto a $3\times3\,\mathrm{mm}^2$-`G4SiPM`.

In the simulations, the wrapping was simulated with an air gap between scintillator and wrapping material. 1,000,000 protons with a (kinetic) energy of 2.95 GeV were shot perpendicularly onto the top surface of the prototype modules. In contrast to the measurements, the protons were not bundled to a beam and directed at the bin centres as described before. Instead, they were homogeneously distributed over the whole surface. This was done for simplicity reasons and is not expected to lead to large deviations between the results of the simulation and of the measurement, as they are both binned in the same way in the course of the analysis. For each proton, the incidence position on the scintillator tile as well as the optical photons that reached the `G4PhotonDetectors` were recorded.

8.2.2. Analysis and Comparison

Like in the case of the hodoscope measurements, which were presented in the previous section, no absolute comparison is possible between the test-beam measurement and the simulation. The reason is that the conversion of the measured signal heights from voltage to photon equivalents was not necessary for analysing the measurements and, thus, no scaling function was determined. Therefore, only relative comparisons can be performed. For this purpose, the same analysis procedure as in case of the hodoscope measurements was applied, with two differences:

- The bins of the spatial signal height distributions were not filled with the mean signal height of the corresponding events and its uncertainty. Instead, the MPV of the signal height was used. It was determined by fitting a *Landau-Gauss convolution* to the signal height distribution for each bin and determining its maximum (cf. [165]). This was possible because of the higher statistics of the test-beam measurements. The fit only returned the uncertainty of the MPV of the included Landau function rather than the uncertainty of the MPV of the Landau-Gauss convolution. For the **simulation results**, the latter was therefore estimated by applying the same relative uncertainty as obtained for the former. Taking the results into account (relative uncertainties of $\approx 1\,\%$ on average), the relative uncertainties for the **measurement results** were retroactively estimated to $1\,\%$ in the scope of the comparison.
- Like in the hodoscope measurements with module 7, pre-amplifier saturation occurred in the measurements with module mtt1. However, as the fit is not influenced by this, no pre-amplifier saturation was applied to the simulation results.

The results for **module mtt1** are presented in figure 8.16. In contrast to the hodoscope measurements, there are large deviations, especially next to the SiPM position. Similar to the case of the hodoscope measurement with module 3, this could possibly indicate a higher (overall) reflectivity of the wrapping in the measurements than assumed in the simulation. Furthermore, the influence of the distribution of the protons (homogeneously in the simulations, bundled to a beam in the measurements) might be larger than expected, which could be an additional reason for the deviations. As it would go beyond the time frame, it was unfortunately not possible to verify these assumption in the scope of this thesis. Thus, this could be done in a subsequent study. Another thing to notice is that the spatial distribution is not mirror-symmetric for the two SiPMs of module mtt1. This effect stems from the measurement results, whereas the simulation results are mirror-symmetric. The reasons

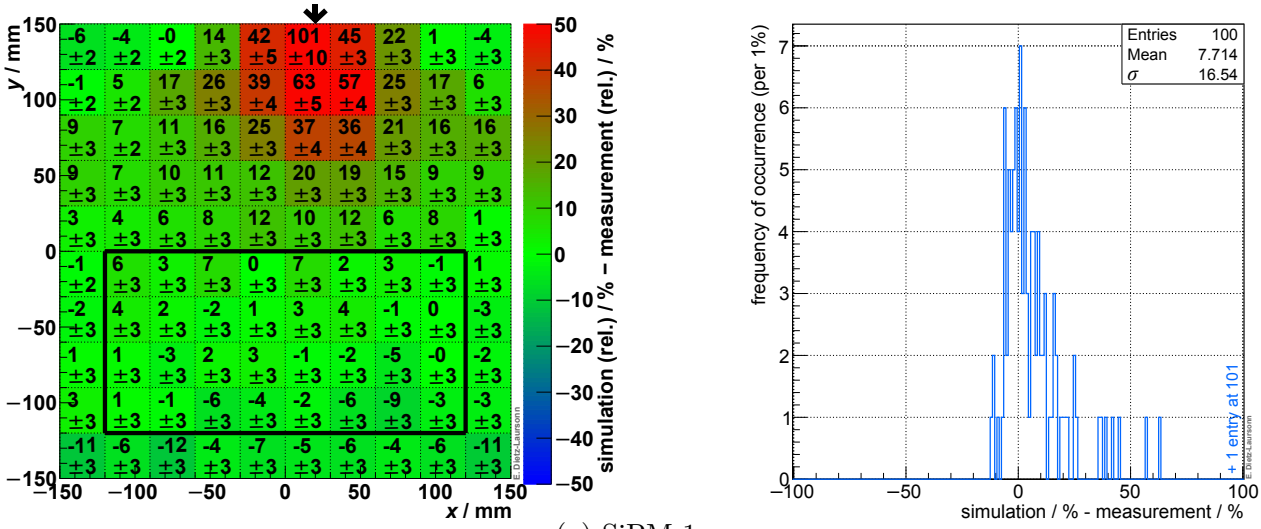

(a) SiPM 1

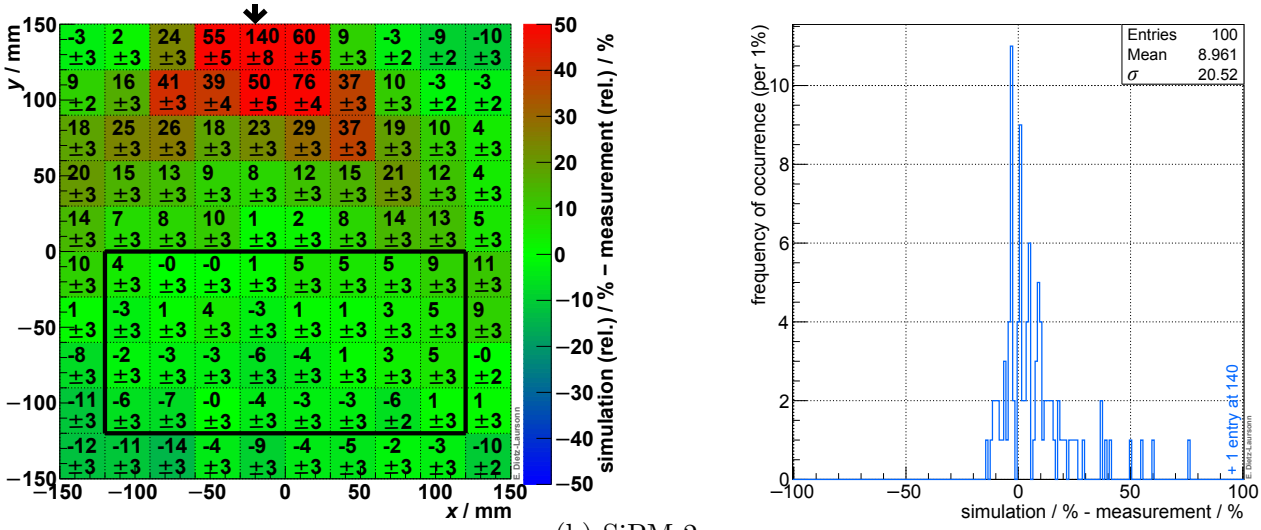

(b) SiPM 2

Figure 8.16.: Results for both SiPMs of module mtt1 (considering the geometry, the PDE, and the saturation effect of the SiPM): The plots on the **left** show the space-resolved deviation distribution. The plots on the **right** present the frequency distribution of the deviation values. The black arrows indicate the position of the SiPM, the black rectangles mark the reference bin-regions.

for this effect are unknown. Possible explanations could be a gain difference between the two SiPMs in the measurement and a deviation of the optical coupling of SiPM 2 from the optical coupling of SiPM 1 (and from the expectations) during the measurement. This could also explain the different structures next to the SiPM in the distribution for SiPM 2.

The results for **module mtt2** are illustrated in figure 8.17. The overall agreement between simulation and measurement is acceptable and much better than for module mtt1. Nevertheless, there are two things to be noticed: There seems to be a slight trend for decreasing deviation values with increasing x-values and there are large deviations next to and especially directly in front of the SiPM. A possible reason for the deviations could again be a deviating reflectivity between the prototype module in the measurement and in the simulation. Additionally, there might be scintillation photons directly hitting the SiPM. This

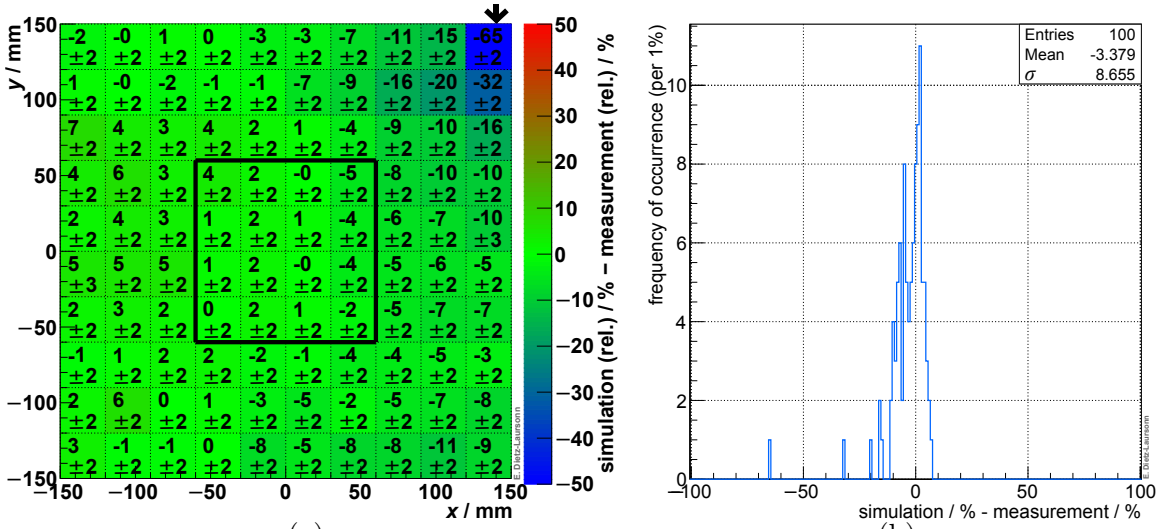

(a) (b)

Figure 8.17.: Results for module mtt2 (considering the geometry, the PDE, and the saturation effect of the SiPM): **(a)** shows the space-resolved deviation distribution. **(b)** presents the frequency distribution of the deviation values. The black arrow indicates the position of the SiPM, the black rectangle marks the reference bin-region.

could be possible, as the wrapping material is not perfectly enclosing the scintillator where the fibres protrude from the scintillator tile and the SiPM is located next to this position (unlike for module 3, cf. figure 8.1). As this case is excluded in the simulations, it would result in too high measured signals, especially in the bins next to the SiPM position and thus lead to deviations like the observed. Both assumptions could not be investigated in the time frame of this thesis. Thus, subsequent studies, e.g. in the scope of a bachelor or master thesis, would be interesting.

In addition to the signal height, the *time delay* between the proton transition (represented by the trigger signal) and the corresponding signal was determined for the measurements [165]. This can also be done for the simulation results, by determining the time after which a specified number of photons was detected (relative to the transition time of the proton). In contrast to the delay from the simulation, the measured delay does not only include the transit time of the optical photons inside the prototype module, but does additionally take the delays of the readout electronics into account. Additionally, the thresholds to define a signal are probably not the same for measurement and simulation, as they are defined in different units (mV and p.e., respectively). Therefore, the resulting absolute values cannot be compared. However, a rough comparison of the behaviour of the signal delay can be performed.

The spatial distributions of the signal delay of both modules for measurement and simulation are presented in the figures 8.18 and 8.19. In case of **module mtt1**, the characteristics of the distributions obviously deviate for simulation and measurement. This could e.g. be caused by a "wrong" choice of the threshold for the simulation (with respect to the threshold of the measurement) or by the optical coupling of SiPM 2 (cf. deviations of the signal height for module mtt1). In contrast, the qualitative characteristics of the distributions are similar for measurement and simulation of **module mtt2** and also the absolute values seem to be compatible. Nevertheless, more detailed studies are desirable also for this topic.

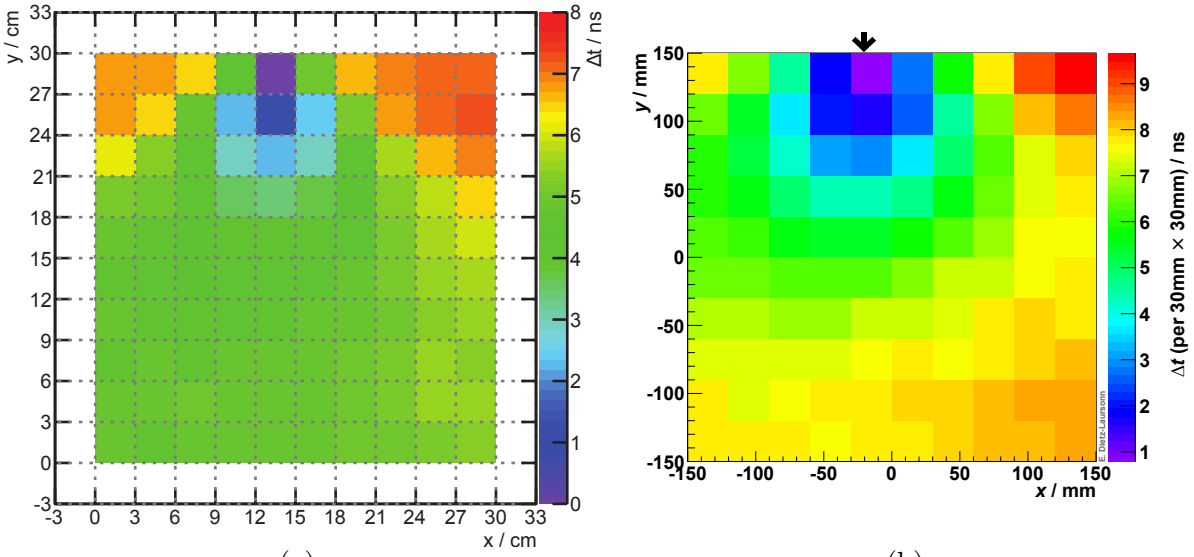

(a) (b)

Figure 8.18.: Time delay between proton transition and the corresponding signal for module mtt1. **(a)** shows the results of the measurement (100 mV threshold, adapted from [165]). In the simulation **(b)**, the geometry, the PDE, and the saturation effect of the SiPM were **not** taken into account and thus a threshold of 25 p.e.[76] was used to define the beginning of the signal. The black arrow indicates the position of the SiPM.

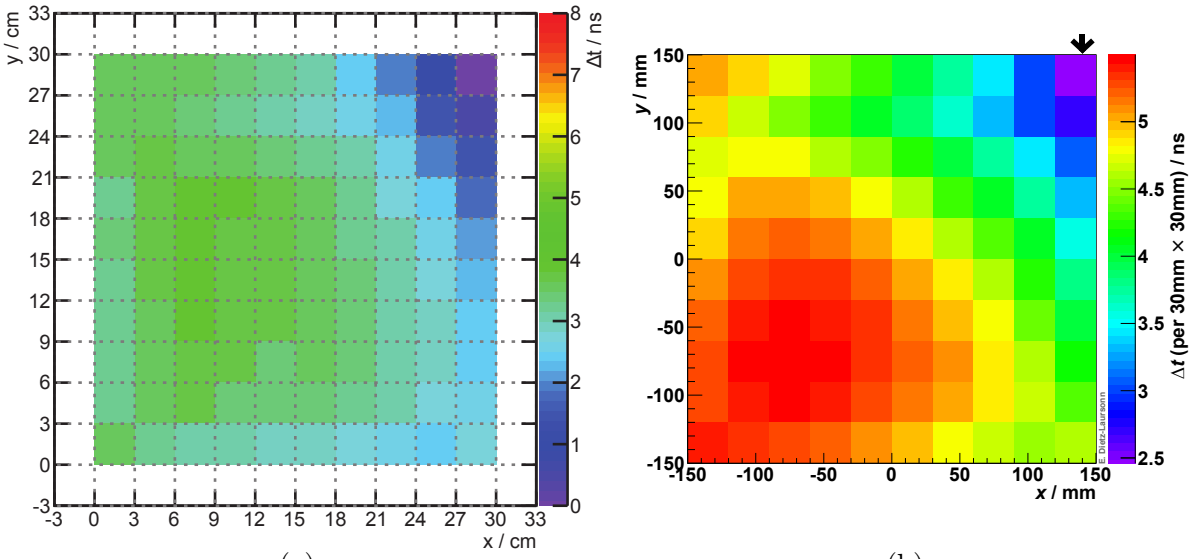

(a) (b)

Figure 8.19.: Time delay between proton transition and the corresponding signal for module mtt2. **(a)** shows the results of the measurement (100 mV threshold, adapted from [165]). In the simulation **(b)**, the geometry, the PDE, and the saturation effect of the SiPM were **not** taken into account and thus a threshold of 25 p.e. was used to define the beginning of the signal. The black arrow indicates the position of the SiPM.

[76] In the simulations of module 3 (cf. section 8.1), the signal reduction due to SiPM effects was a factor of approximately 5.

All together, the comparison between the test-beam measurements and the simulations, which have been performed in the scope of this thesis, results in reasonable agreements for module mtt1 and very good agreements for module mtt2. Nevertheless, the existing deviations should be further investigated in order to determine their origins.

9. Detailed Studies

In the previous chapters, the validation of the GODDeSS framework has been presented. In this chapter, further detailed simulations will be described. They have been performed to investigate the optical properties of optical fibres in more detail (trapping efficiency, signal attenuation length, and photon distribution at the fibre end as well as their dependence on several parameters). Additionally, the characteristics of the detector response of various benchmark detector setups will be studied with regard to the average value and the fluctuation of the number of photons (signal height), the time delay of the signal, and the pulse length. The material properties, which have been used for modelling the optical detector components, can be found in appendix D.

9.1. Trapping Efficiency of Optical Fibres

The trapping efficiency of optical fibres, i.e. its capability to capture light that has been created within the fibre, has already been studied in section 6.12 and in appendix B. This was done to validate the resulting values from the simulation against the calculated values. For this purpose, the constraints of the definition of the fibre trapping efficiency (cf. subsection 3.2.3) were applied and only the geometry of the fibre was varied. Nevertheless, these trapping efficiency values do not necessarily agree with the values for realistic conditions. Therefore, the influence of several parameters will be investigated with GODDeSS simulations in this section. These are namely:

- fibre length
  (trapping efficiencies of short fibres can have contributions of photons that were not captured by total reflection)
- meridional rays as well as skew rays
  (realistic trapping efficiencies for scintillating and WLS fibres)
- possibility of reflection at the surface between the outer cladding and the surroundings
  (photons entering the outer cladding do not automatically leave the fibre)
- surface roughness of the outer cladding
- realistic refractive indices

The simulations were performed and analysed like described in section 6.12, with the difference that the above-mentioned parameters were modified. As example of a *short fibre*, a fibre

length of 100 mm between the emission point and both fibre ends was used. For considering *skew rays*, the optical photons were emitted isotropically from the cross-sectional area of the fibre (→ meridional and skew rays). A refractive index of the surrounding volume of $n_{\text{ambient}} = 1$ was used to allow for reflections at the boundary between the *outer cladding* of the fibre and the surroundings. The *roughness* of the rough outer cladding was set to $\sigma_\alpha = 5\,°$. Considering realistic refractive indices requires more changes to the simulation than replacing the specified refractive indices. Therefore, this will be described separately at the end of this section. The results are summarised in table 9.1, including the results of table 6.2 (highlighted with a grey background).

					$n_{\text{ambient}} = n_{\text{clad}}$	$n_{\text{ambient}} = 1$	
						smooth	rough
short fibre (100 mm)	round	single clad		meridional	$(6.877 \pm 0.003)\,\%$	$(37.502 \pm 0.005)\,\%$	$(9.715 \pm 0.003)\,\%$
				all	$(13.266 \pm 0.004)\,\%$	$(58.783\,^{+\,0.006}_{-\,0.005})\,\%$	$(15.347 \pm 0.004)\,\%$
		double clad		meridional	$(11.252 \pm 0.004)\,\%$	$(37.505 \pm 0.005)\,\%$	$(12.612 \pm 0.004)\,\%$
				all	$(18.463 \pm 0.004)\,\%$	$(58.023\,^{+\,0.006}_{-\,0.005})\,\%$	$(19.444 \pm 0.004)\,\%$
	square	single clad		meridional	$(8.867 \pm 0.003)\,\%$	$(41.920 \pm 0.005)\,\%$	$(12.757 \pm 0.004)\,\%$
				all	$(8.868 \pm 0.003)\,\%$	$(41.653 \pm 0.005)\,\%$	$(12.741 \pm 0.004)\,\%$
		double clad		meridional	$(12.742 \pm 0.004)\,\%$	$(39.542 \pm 0.005)\,\%$	$(15.845 \pm 0.004)\,\%$
				all	$(12.749 \pm 0.004)\,\%$	$(39.566 \pm 0.005)\,\%$	$(15.879 \pm 0.004)\,\%$
long fibre (1000 mm)	round	single clad		meridional	$(6.878 \pm 0.003)\,\%$	$(37.495 \pm 0.005)\,\%$	$(6.880 \pm 0.003)\,\%$
				all	$(13.274 \pm 0.004)\,\%$	$(58.778\,^{+\,0.007}_{-\,0.005})\,\%$	$(13.271 \pm 0.004)\,\%$
		double clad		meridional	$(11.249 \pm 0.004)\,\%$	$(37.499 \pm 0.005)\,\%$	$(11.257 \pm 0.004)\,\%$
				all	$(18.471\,^{+\,0.005}_{-\,0.004})\,\%$	$(58.017\,^{+\,0.007}_{-\,0.005})\,\%$	$(18.467\,^{+\,0.005}_{-\,0.004})\,\%$
	square	single clad		meridional	$(8.865 \pm 0.003)\,\%$	$(40.182 \pm 0.005)\,\%$	$(8.865 \pm 0.004)\,\%$
				all	$(8.868 \pm 0.003)\,\%$	$(40.137 \pm 0.005)\,\%$	$(8.868 \pm 0.003)\,\%$
		double clad		meridional	$(12.740 \pm 0.004)\,\%$	$(38.428 \pm 0.005)\,\%$	$(12.735 \pm 0.004)\,\%$
				all	$(12.737 \pm 0.004)\,\%$	$(38.435 \pm 0.005)\,\%$	$(12.735 \pm 0.004)\,\%$

Table 9.1.: Simulated fibre trapping efficiency for constant refractive indices of the fibre materials ($n_{\text{core}} = 1.6$, $n_{\text{inner cladding}} = 1.49$, $n_{\text{outer cladding}} = 1.42$). "Rough" refers to the roughness of the outer cladding of the fibre and stands for a σ_α of 5 °, whereas "smooth" means 0 °. n_{ambient} is the refractive index of the material surrounding the fibre and "$n_{\text{ambient}} = n_{\text{clad}}$" indicates that the surrounding material has the same refractive index as the outer cladding of the fibre. This means, photons entering the outer cladding automatically leave the fibre and are lost. "Meridional" and "all" refer to the rays that are considered: For "all", the optical photons were emitted isotropically from the cross-sectional area of the fibre (→ meridional and skew rays). For "meridional", the optical photons were emitted isotropically from the centre of the cross-sectional area of the fibre (→ meridional rays). The values highlighted with a grey background are the values from table 6.2.

There are several effects to be noted when looking at the results:

- For **round fibres**, the trapping efficiency is higher when taking all rays into account, which is due to the skew rays. For the same initial angle with respect to the fibre axis, these photons possess higher incidence angles on the claddings, the larger the distance between the fibre axis and their initial position is. Thus, a higher fraction of skew rays can be trapped by total reflection, which results in a higher trapping efficiency. For **square fibres**, it does not make a difference whether only meridional or all rays are considered. This is due to the fact that the fraction of skew rays is very small, as the trajectory of most photons will cross the fibre axis due to geometrical reasons.

- For the same reason, the trapping efficiency of square fibres is higher than of round fibres when considering only **meridional rays**. If **all rays** are taken into account, the situation is reversed.

- Allowing for reflections at the boundary between the perfectly **smooth outer cladding**[77] and the surroundings ($n_{\text{ambient}} = 1$) leads to much higher trapping efficiency values (factor 3 to 4). This is caused by the smaller effective critical angle for total reflection and can also be seen in the dependence of the trapping efficiency from the photon emission angle. For round fibres (figure 9.1), the "trapped"-regions just expand. For square fibres (figure 9.3) this is also the case, but additionally large regions form, for which total reflection is expected according to the simplified geometry for trapping efficiency calculation, but which do not contribute to the simulated trapping efficiency (cf. also section 6.12 and appendix B). The oval shape of the regions that are expected not to contribute to the trapping efficiency is caused by the fact that the effective critical angle for total reflection is $\approx 38\,^\circ < 45\,^\circ$. Thus, photons being emitted into the direction of an edge of the fibre would be trapped, if the real geometry of the fibre and its claddings is neglected (cf. also section 6.12 and appendix B).

- In case of a **rough surface**, the increase of the trapping efficiency is less distinct than for smooth surfaces and only appears for short fibres. This is due to the fact that rough surfaces lead to deviations from the geometrical trajectory of the reflected/refracted photons as well as to local deviations of the critical angle with respect to the average surface. As a result, photons that would be trapped in the outer cladding in case of a smooth surface are lost with a significant probability each time when reaching the rough surface between the outer cladding and the surroundings. This also shows in the emission angle dependence of the trapping efficiency, which is illustrated in figure 9.2. Here, the regions that expectedly do not contribute to the trapping efficiency equal the corresponding region of the case of perfectly smooth surfaces, whereas the regions that contribute equal the corresponding region for the case when not taking this surface between the outer cladding and the surroundings into account ($n_{\text{ambient}} = n_{\text{clad}}$). The large remaining region in between represents the photons that are lost from the outer cladding due to the roughness of its surface.

[77] This is the least realistic of the three cases, as the surfaces of realistic fibres are not *perfectly* smooth. The case of reflections at the boundary between a rough outer cladding and the surroundings with $n_{\text{ambient}} = 1$ corresponds to the extreme case of an optical fibre without coating and fully surrounded by air. The case of $n_{\text{ambient}} = n_{\text{clad}}$ is another extreme case, which can be approximated by an optical fibre in scintillation material or optical cement.

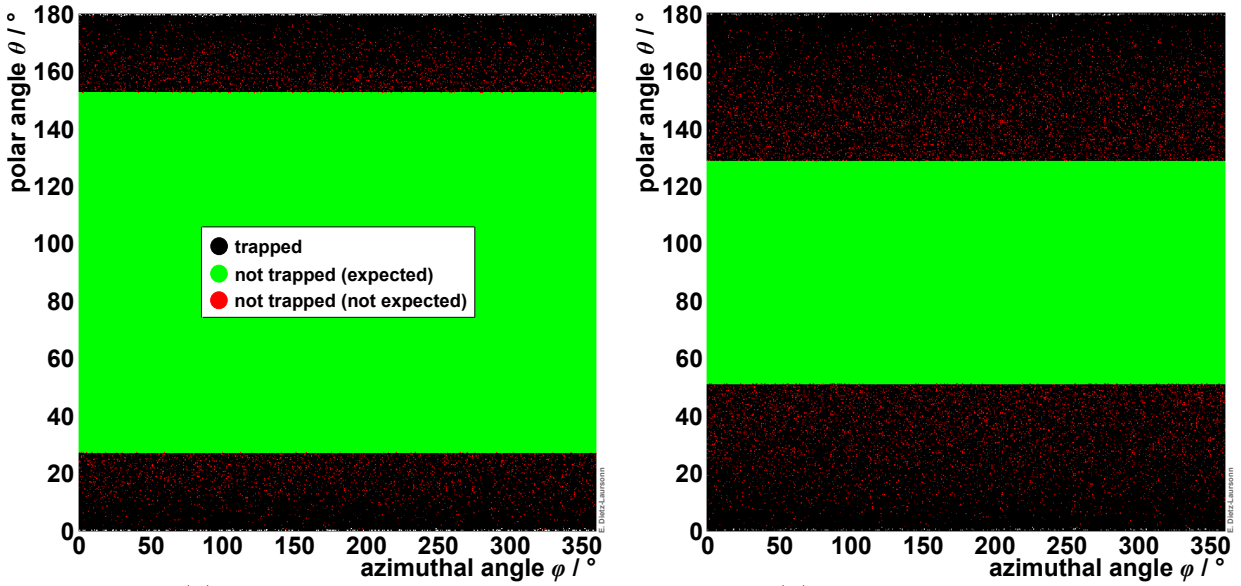

(a) $n_{\text{ambient}} = n_{\text{clad}}$ (b) $n_{\text{ambient}} = 1$, smooth

Figure 9.1.: Simulated photon emission angle dependence of the trapping efficiency of **round** fibres without **(a)** or with **(b)** taking the surface between the outer cladding and the surroundings into account. The position inside the scatter plots represents the initial direction of the photons in spherical coordinates (the fibres are parallel to the ordinate) and the colour indicates whether the photons were trapped and thus have contributed to the simulated trapping efficiency. "(Expected)" and "(not expected)" refer to the question whether not being trapped is expected (according to the simplified geometry for trapping efficiency calculation, cf. section 6.12) for the photons that were not trapped in the simulation (which considers the real geometry of the fibre).

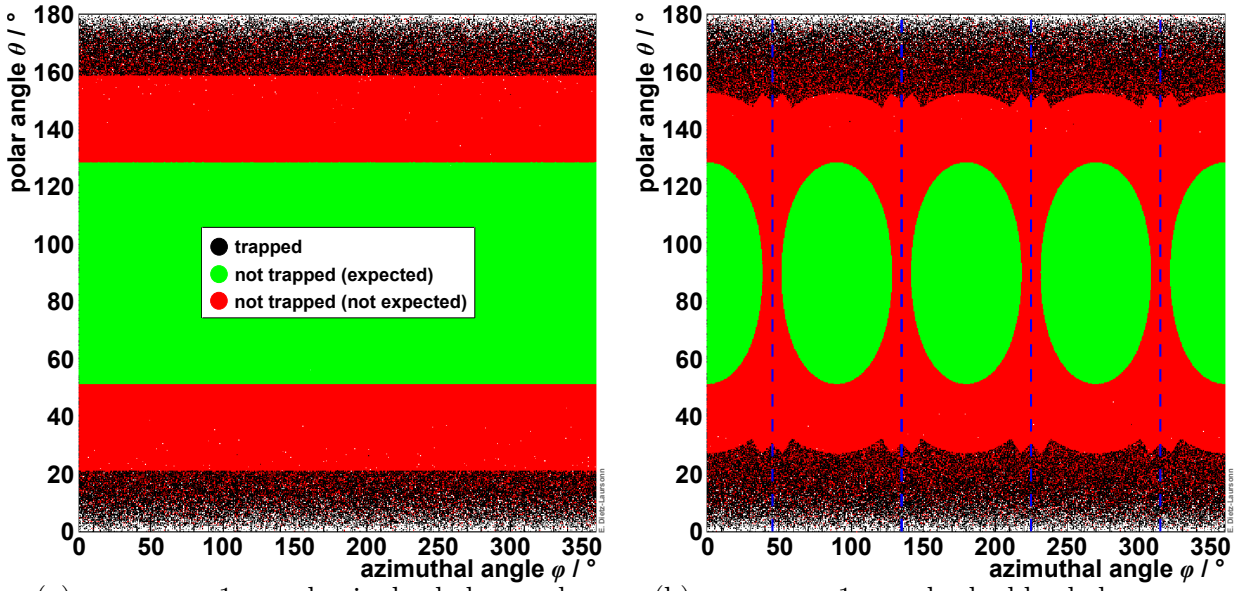

(a) $n_{\text{ambient}} = 1$, rough, single-clad, round (b) $n_{\text{ambient}} = 1$, rough, double-clad, square

Figure 9.2.: Simulated photon emission angle dependence of the trapping efficiency when taking the **rough surface** between the outer cladding and the surroundings into account. A roughness of $\sigma_\alpha = 5\,^\circ$ has been used. The dashed lines mark the edges of the square fibre.

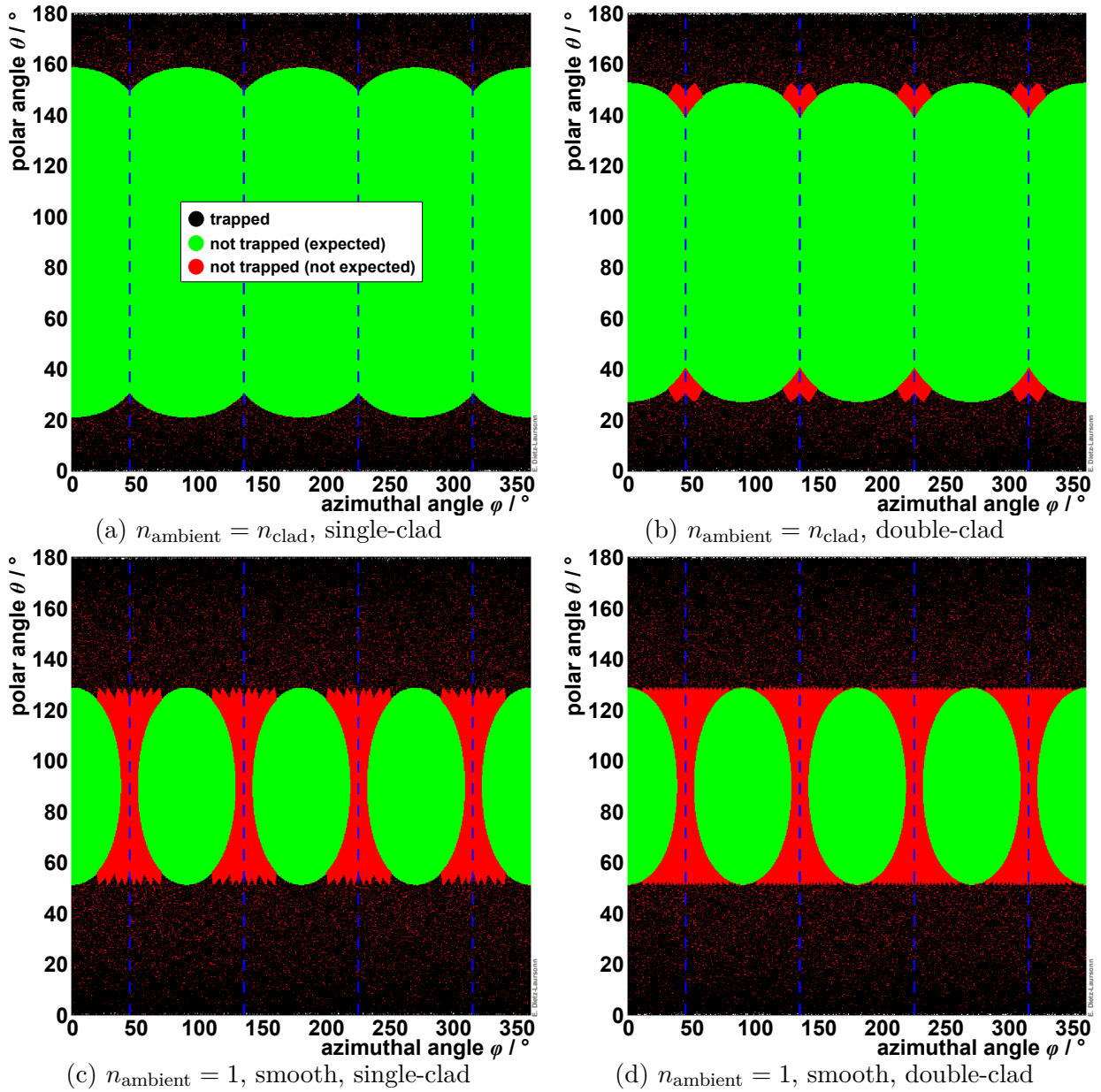

(a) $n_{\text{ambient}} = n_{\text{clad}}$, single-clad

(b) $n_{\text{ambient}} = n_{\text{clad}}$, double-clad

(c) $n_{\text{ambient}} = 1$, smooth, single-clad

(d) $n_{\text{ambient}} = 1$, smooth, double-clad

Figure 9.3.: Simulated photon emission angle dependence of the trapping efficiency of **square** fibres without **(top)** or with **(bottom)** taking the surface between the outer cladding and the surroundings into account. The edges of the fibres are located at $\phi = 45\,°$, $135\,°$, $225\,°$, $315\,°$, marked with dashed lines. "(Expected)" and "(not expected)" refer to the question whether not being trapped is expected (according to the simplified geometry for trapping efficiency calculation, cf. section 6.12) for the photons that were not trapped in the simulation (which considers the real geometry of the fibre). Thus, the red regions depict inadequacies of the method for calculating the trapping efficiency of optical fibres, which is typically used, also by the manufacturers.

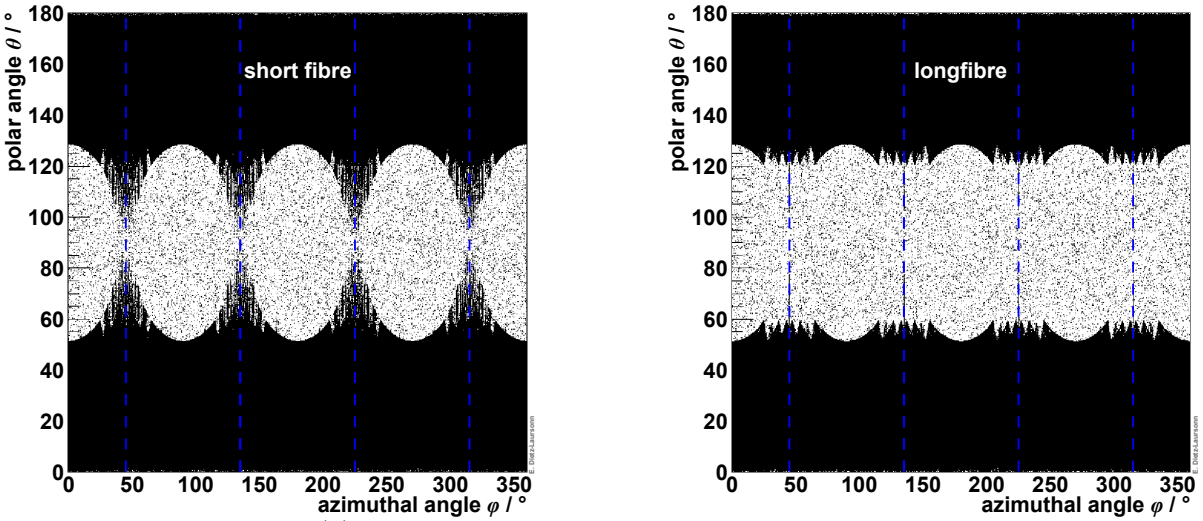

(a) $n_{\text{ambient}} = 1$, smooth, square, single-clad

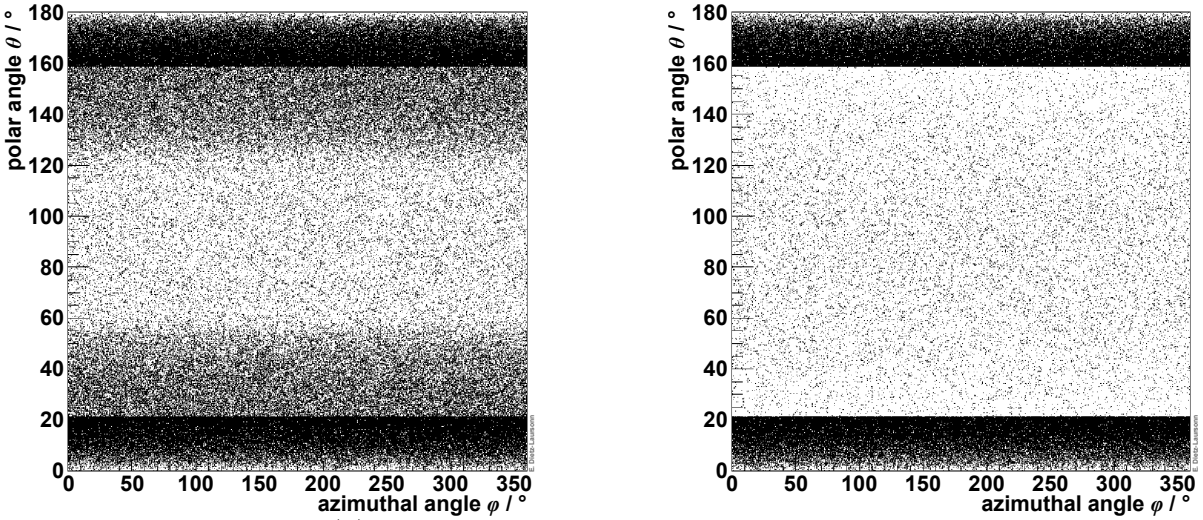

(b) $n_{\text{ambient}} = 1$, rough, round, single-clad

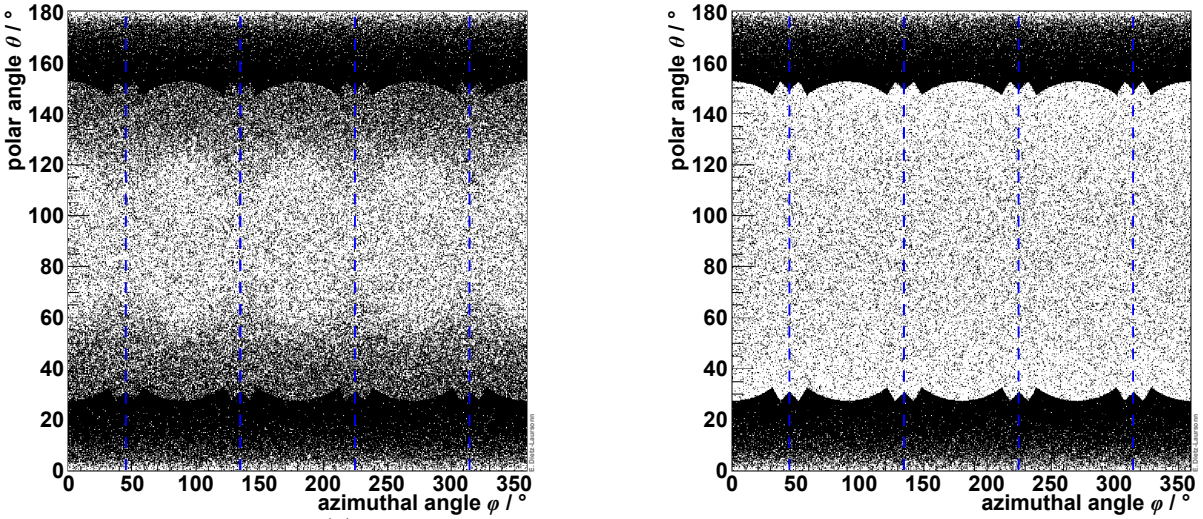

(c) $n_{\text{ambient}} = 1$, rough, square, double-clad

Figure 9.4.: Simulated emission angle distribution of the **trapped photons** of short fibres (100 mm, **left**) or long fibres (1000 mm, **right**) when taking the surface between the outer cladding and the surroundings into account. A roughness of $\sigma_\alpha = 5\,^\circ$ has been used. The dashed lines mark the edges of the square fibre.

- In general, **short fibres** have a higher trapping efficiency for all fibres types with a rough surface as well as for square fibres with a perfectly smooth surface (much less distinct). This is caused by a significant number of photons, which are not trapped by total reflection but do anyhow contribute to the trapping efficiency. This is possible, as there is a certain probability for reflection for each contact with the optical surfaces (Fresnel equations, equation (2.40)).[78] The fraction of these "additional" photons inside the fibre decreases with the fibre length as the probability of leaving the fibre increases with the number of these (non-total) reflections. Thus these photons contribute to the trapping efficiency in short fibres but do not contribute in long fibres. Figure 9.4 shows the emission angle distribution of the trapped photons for long and short fibres. This illustrates that the "additional" photons appear in certain regions, which vanish for long fibres.

- When considering **all rays** for fibres with a **rough surface**, which is the most realistic combination, the trapping efficiency is up to 50 % higher for round fibres than for square fibres.

Realistic Refractive Indices

Like in case of a constant overall signal attenuation length (cf. section 7.2), the trapping efficiency of the fibre depends on the energy spectrum of the photons when considering realistic refractive indices. Consequently, a meaningful trapping efficiency can only be obtained when simulating the appropriate signal, i.e. the WLS photons for WLS fibres, the scintillation photons for scintillating fibres, or light that is coupled into a light-guiding fibre at one of its ends. As WLS fibres have been used in the scope of this thesis, their trapping efficiency will be studied here.

To obtain the signal, the simulated fibre was *excited with optical photons* from outside the fibre. The photon energy was randomly distributed between 2.555 eV and 3.671 eV to cover the full WLS absorption spectrum of the fibre. The photons were created in the cross-section plane of the fibre in a distance to its centre of 1.02 times its radius (round fibres) or 0.71 times its edge length (square fibres), respectively.[79] From there, the photons were isotropically emitted into the cross-section plane of the fibre. As realistic refractive indices (in contrast to the constant refractive indices used in section 6.12), the energy-dependent values have been used, which can be found in figure D.6. The results of the determination of the trapping efficiency by this method are summarised in table 9.2. They present the results for the full signal, i.e. all rays are considered as well as WLS photons that were created because of the absorption of another WLS photon.

The comparison of the results for constant refractive indices with the results presented in table 9.1 shows significant differences[80], mostly a reduction of the trapping efficiency. This indicates that the initial position of the emitted photons is not homogeneously distributed. Otherwise, there should be no differences between the values of the tables 9.1 and 9.2. In order to verify this assumption, the initial positions of the WLS photons were determined

[78] Additionally, rough surfaces lead to the same effects as described above.
[79] These distances were chosen to make sure that all photons started from outside the fibre.
[80] In terms of photons, the difference can be small. Nevertheless, it is significant with respect to the uncertainties.

			$n_{\text{ambient}} = n_{\text{clad}}$	$n_{\text{ambient}} = 1$	
				smooth	rough
short fibre (100 mm)	round	single clad	$(13.602 \pm 0.003)\,\%$	$(56.224 \pm 0.004)\,\%$	$(14.665 \pm 0.003)\,\%$
		double clad	$(18.919 \pm 0.004)\,\%$	$(55.710 \pm 0.004)\,\%$	$(18.828 \pm 0.003)\,\%$
	square	single clad	$(8.692 \pm 0.003)\,\%$	$(41.147 \pm 0.004)\,\%$	$(12.555 \pm 0.003)\,\%$
		double clad	$(12.544 \pm 0.003)\,\%$	$(39.150 \pm 0.004)\,\%$	$(15.683 \pm 0.003)\,\%$
long fibre (1000 mm)	round	single clad	$(12.657 \pm 0.003)\,\%$	$(54.285 \pm 0.006)\,\%$	$(11.713 \pm 0.003)\,\%$
		double clad	$(17.686 \pm 0.004)\,\%$	$(53.769 \pm 0.007)\,\%$	$(16.686 \pm 0.003)\,\%$
	square	single clad	$(8.047 \pm 0.003)\,\%$	$(37.672 \pm 0.004)\,\%$	$(8.076 \pm 0.002)\,\%$
		double clad	$(11.635 \pm 0.003)\,\%$	$(36.067 \pm 0.004)\,\%$	$(11.661 \pm 0.003)\,\%$

Table 9.2.: Simulated trapping efficiency of the signal of externally excited WLS fibres with **constant refractive indices**. "Rough" refers to the roughness of the outer fibre cladding and stands for a σ_α of $5\,^\circ$, whereas "smooth" means $0\,^\circ$. n_{ambient} is the refractive index of the material surrounding the fibre and "$n_{\text{ambient}} = n_{\text{clad}}$" indicates that the surrounding material has the same refractive index as the outer cladding of the fibre. This means, photons entering the outer cladding leave the fibre and are lost.

and filled into histograms. These are presented in figure 9.5. They show structures deviating from homogeneous distributions. In square fibres, the probability of creating WLS photons is increasing towards the edge of the core. In case of round fibres, the creation of WLS photons is most probable for a certain radius. These are about the same when considering the surface of the outer cladding and are much larger when not taking the surface of the outer cladding into account ($n_{\text{ambient}} = n_{\text{clad}}$). This is the reason why the reduction is much less distinct in the latter case and there is even an increase of the trapping efficiency for short round fibres (higher trapping efficiency of skew rays).

Using **realistic refractive indices** (cf. table 9.3), generally again leads to slightly lower trapping efficiency values. This is caused by the fact that the realistic refractive index values are higher than the given constant refractive index values, when looking at the emission energy range of the fibres (cf. appendix B and D). Thus, the critical angle for total reflection is larger at the surfaces between the claddings and smaller at the surfaces between the outer cladding and the surroundings, respectively. As a result, more photons are trapped in case of $n_{\text{ambient}} = 1$ with perfectly smooth surfaces. In the other two cases, total reflection at the surfaces between the outer cladding and the surroundings does not play a role: this is trivial for $n_{\text{ambient}} = n_{\text{clad}}$ and in case of $n_{\text{ambient}} = 1$ with rough surfaces, the roughness leads to the loss of the the photons in the outer cladding. Thus less photons are trapped. The emission angle dependence is illustrated in figure 9.6, using the example of $n_{\text{ambient}} = n_{\text{clad}}$. For realistic refractive indices, a thin band develops around the regions that do not contribute to the trapping efficiency in case of constant refractive indices. In this band, the photons partly do or do not contribute and the overall trapping efficiency is reduced.

As a conclusion of the studies of the trapping efficiency it can be stated that the (calculated) values given by the manufacturers (cf. appendix B) are always too low for round fibres. In contrast, the trapping efficiency is lower than given by the manufacturers for square fibres.

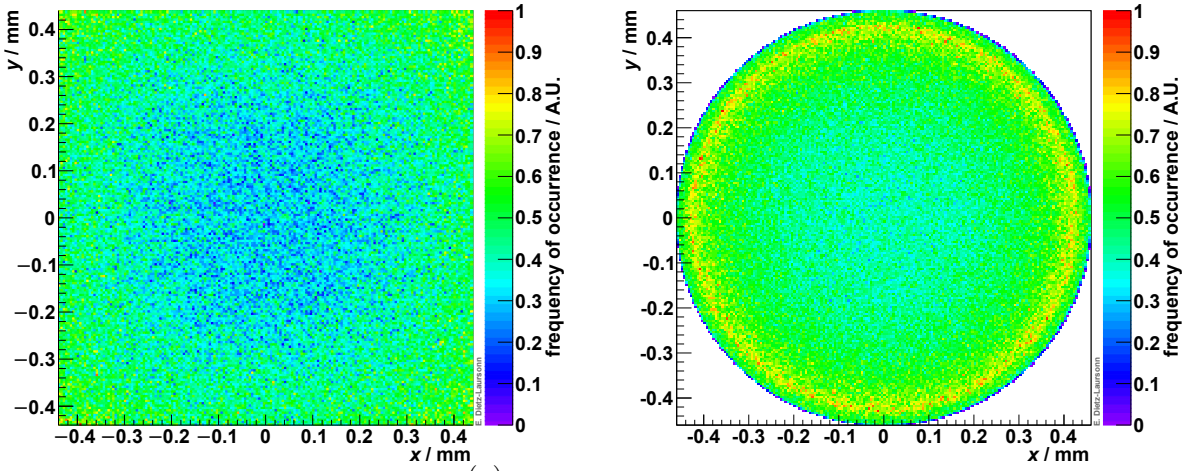

(a) $n_{\text{ambient}} = n_{\text{clad}}$

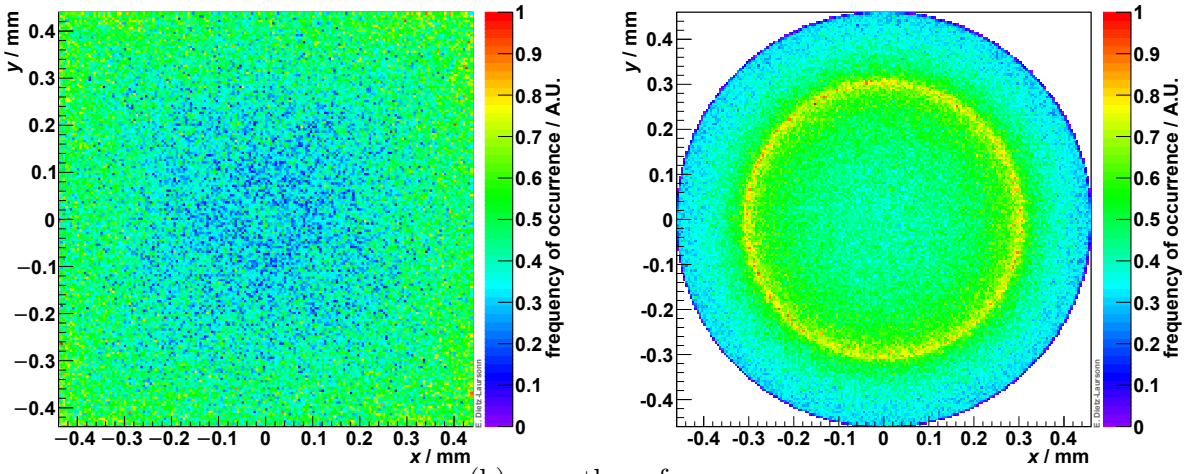

(b) smooth surface

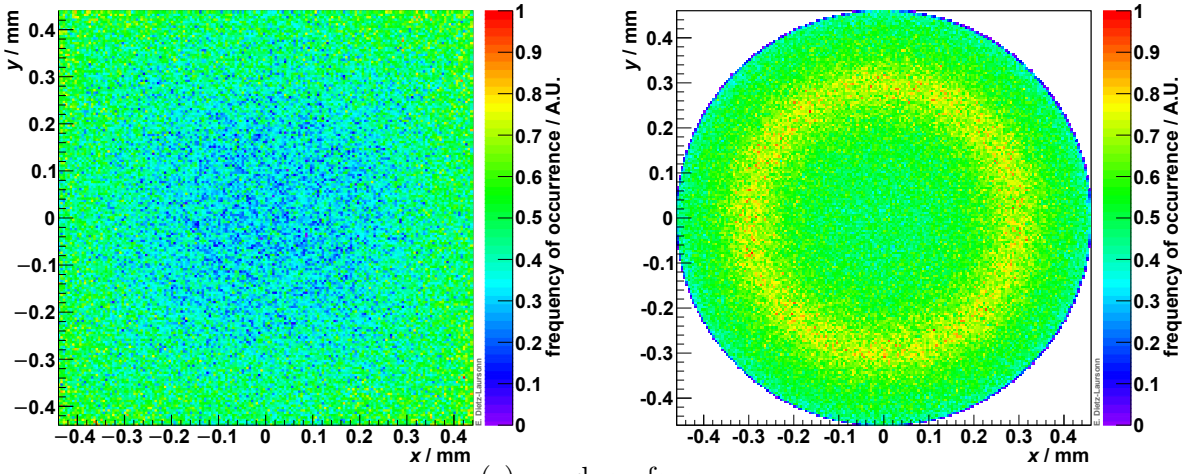

(c) rough surface

Figure 9.5.: Spatial distribution of the initial position of WLS photon in square **(left)** and round **(right)** fibres, simulated with GODDeSS. The x-y-plane represents the cross-section plane of the fibre.

			$n_{\text{ambient}} = n_{\text{clad}}$	$n_{\text{ambient}} = 1$	
				smooth	rough
short fibre (100 mm)	round	single clad	$(13.100 \pm 0.003)\,\%$	$(55.937 \pm 0.004)\,\%$	$(14.234 \pm 0.003)\,\%$
		double clad	$(18.440 \pm 0.003)\,\%$	$(55.409 \pm 0.004)\,\%$	$(18.366 \pm 0.003)\,\%$
	square	single clad	$(8.377 \pm 0.003)\,\%$	$(41.312 \pm 0.004)\,\%$	$(12.364 \pm 0.003)\,\%$
		double clad	$(12.261 \pm 0.003)\,\%$	$(39.142 \pm 0.004)\,\%$	$(15.492 \pm 0.003)\,\%$
long fibre (1000 mm)	round	single clad	$(12.163 \pm 0.003)\,\%$	$(54.002 \pm 0.006)\,\%$	$(11.192 \pm 0.003)\,\%$
		double clad	$(17.215 \pm 0.004)\,\%$	$(53.472 \pm 0.007)\,\%$	$(16.172 \pm 0.003)\,\%$
	square	single clad	$(7.717 \pm 0.003)\,\%$	$(38.162 \pm 0.004)\,\%$	$(7.746 \pm 0.002)\,\%$
		double clad	$(11.363 \pm 0.003)\,\%$	$(35.834 \pm 0.004)\,\%$	$(11.392 \pm 0.003)\,\%$

Table 9.3.: Simulated trapping efficiency of the signal of externally excited WLS fibres with **realistic refractive indices**. "Rough" refers to the roughness of the outer fibre cladding and stands for a σ_α of 5°, whereas "smooth" means 0°. n_{ambient} is the refractive index of the material surrounding the fibre and "$n_{\text{ambient}} = n_{\text{clad}}$" indicates that the surrounding material has the same refractive index as the outer cladding of the fibre. This means, photons entering the outer cladding leave the fibre and are lost.

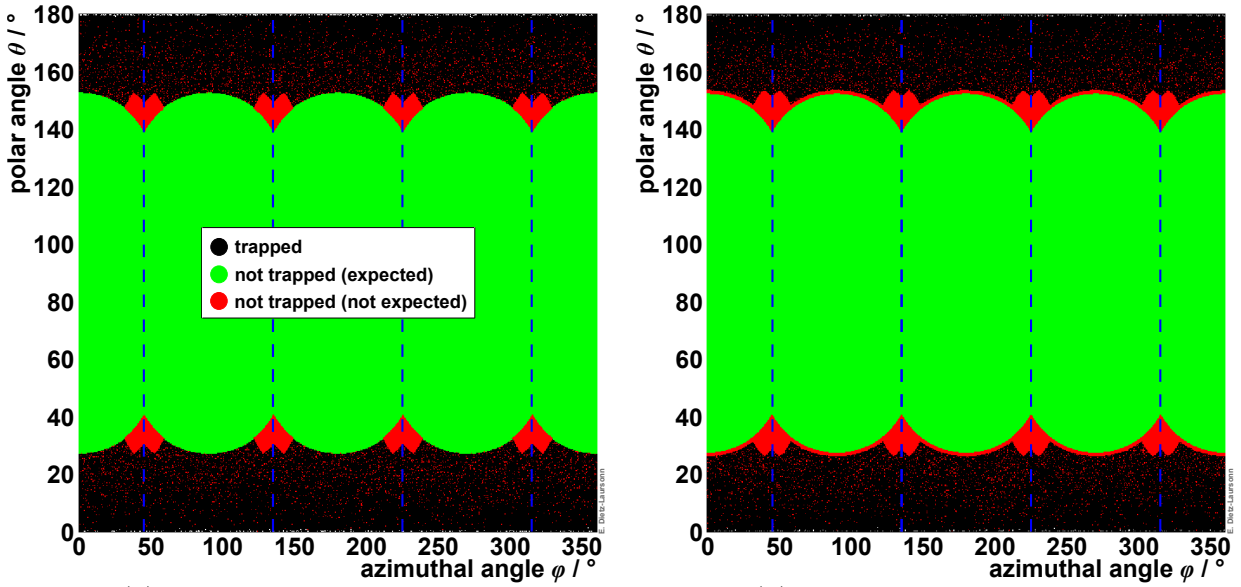

(a) constant refractive index (b) realistic refractive index

Figure 9.6.: Simulated photon emission angle dependence of the trapping efficiency using constant **(a)** or realistic **(b)** refractive indices (using the example of square, double-clad fibres). The surface between the outer cladding and the surroundings has not been taken into account. The dashed lines mark the edges of the square fibre.

However, this does only apply to light that is created inside the fibres. If light is coupled into the fibres at one of its ends (e.g. when coupling a scintillating or WLS fibre to a light-guiding fibre), the results might be very different. Furthermore, the edges of available square fibres are not sharp but rounded [154]. This has not yet been implemented into the GODDeSS framework and has thus not been considered in the presented studies.

9.2. Signal Attenuation Length of Optical Fibres

The signal attenuation length of optical fibres is an effective mean attenuation of the signal considering all possible light paths as well as losses at optical surfaces. The signal attenuation length of realistic optical fibres (with rough surface), their determination from simulation data, as well as their adjustment to the manufacturer data has been presented in section 7.2. In this section, the influence of the *fibre type* (profile and number of claddings), the *diameter* of the fibre, and the properties of the *surface* between the outer cladding and the surroundings will be studied with GODDeSS simulations. They were performed and analysed as described in section 7.2 with the difference that the above-mentioned parameters were varied. The results for the WLS fibre BCF-92 are summarised in table 9.4. Comparing the values, several things can be noted:

- There are no significant deviations of the signal attenuation length values between the two cases $n_{\text{ambient}} = n_{\text{clad}}$ (neglecting the surface between the outer cladding and the surroundings) and $n_{\text{ambient}} = 1$ (allowing for reflections at the surface between the rough ($\sigma_\alpha = 5\,^\circ$) outer cladding and the surroundings). In case of a **smooth cladding**, the signal attenuation length is much shorter. This is probably caused by the higher trapping efficiency of smooth fibres (cf. section 9.1). The additional photons, which are trapped by total reflection, mainly possess large angles with respect to the fibre axis, i.e. with small incidence angles with respect to the fibre surfaces. These additional photons therefore have to traverse longer distances in the material to cover the same distance along the fibre. Thus, their probability to be absorbed is higher. However, because smaller initial losses, the signal of fibres with smooth surface is higher than of fibres with rough surface.[81] This is illustrated in figure 9.7(a).

				$n_{\text{ambient}} = n_{\text{clad}}$	$n_{\text{ambient}} = 1$	
					smooth	rough
round fibre	single clad		1 mm	(3467 ± 10) mm	(2911 ± 4) mm	(3508 ± 9) mm
			2 mm	(3464 ± 8) mm	(2906 ± 3) mm	(3512 ± 8) mm
	double clad		1 mm	(3471 ± 8) mm	(2912 ± 4) mm	(3501 ± 8) mm
			2 mm	(3451 ± 7) mm	(2919 ± 3) mm	(3524 ± 7) mm
square fibre	single clad		1 mm	(3792 ± 16) mm	(3284 ± 5) mm	(3795 ± 14) mm
			2 mm	(3784 ± 13) mm	(3276 ± 4) mm	(3836 ± 11) mm
	double clad		1 mm	(3768 ± 13) mm	(3303 ± 5) mm	(3732 ± 11) mm
			2 mm	(3762 ± 11) mm	(3305 ± 4) mm	(3745 ± 9) mm

Table 9.4.: Simulated signal attenuation length of the BCF-92 WLS fibre for several fibre layouts. "Rough" refers to the roughness of the outer fibre cladding and stands for a σ_α of $5\,^\circ$, whereas "smooth" means $0\,^\circ$. n_{ambient} is the refractive index of the material surrounding the fibre and "$n_{\text{ambient}} = n_{\text{clad}}$" indicates that the surrounding material has the same refractive index as the outer cladding of the fibre. This means, photons entering the outer cladding leave the fibre and are lost.

[81] If the fibre is too short for a compensation of the smaller initial losses by the shorter signal attenuation length.

- There are only minor or no significant deviations between the signal attenuation length of single-clad and double-clad fibres.

- The **diameter** of the fibres does not have a significant influence on the signal attenuation length. This is expected, as the distances in the material per distance along the fibre does not change for geometry reasons. Additionally, though there are more reflections per distance along the fibre for smaller diameters, the fraction of photons that are not trapped by total reflection should be negligible after distance of 1 m along the fibre (cf. section 9.1).

- The signal attenuation length of **square fibres** is longer than that of round fibres. The reason for this effect is the higher initial losses (lower trapping efficiency, cf. also table 9.2) of square fibres. Nevertheless, figure 9.7(b) demonstrates that as a result of the same effect, the signal of round fibres is higher despite the shorter signal attenuation length.

The results for the signal attenuation length spectra of the light-guiding fibre BCF-98 are presented in the figures 9.8 and 9.9. They show the same features as described for the attenuation length of the WLS fibre BCF-92.

As a conclusion of the studies of the signal attenuation length of optical fibres, simulating an optical fibre without surface roughness of the outer cladding leads to significant deviations in the signal attenuation length as well as the signal height. As additionally the trapping efficiency as well as the exit characteristics of the optical fibre dramatically deviate when neglecting the surface roughness, it is not recommended to do so!

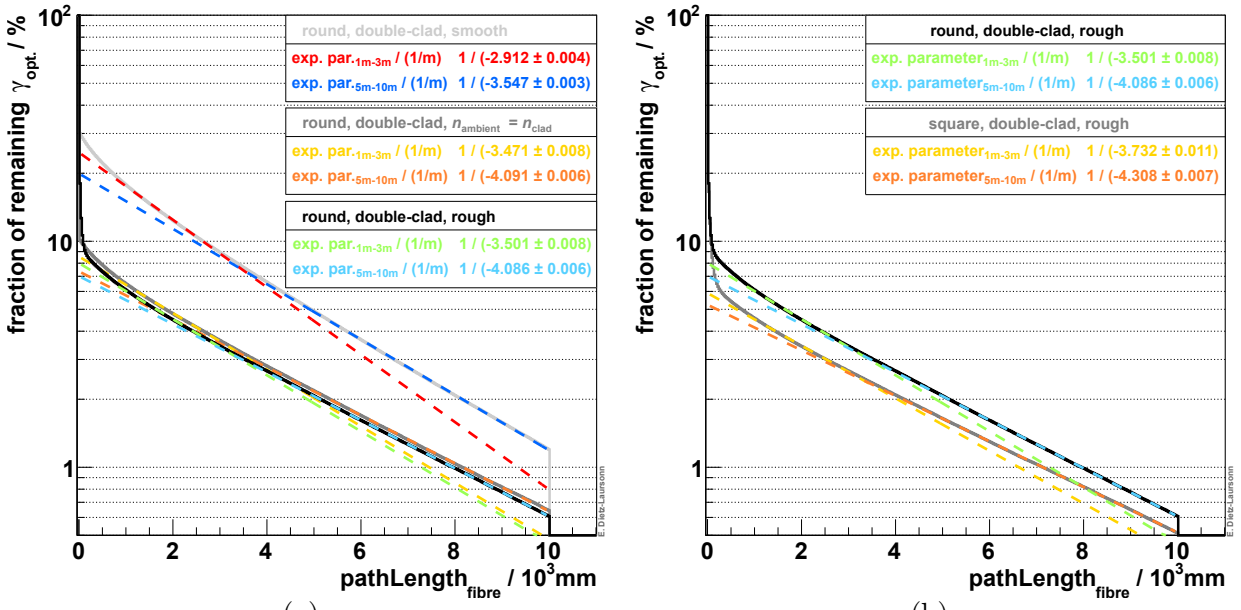

(a) (b)

Figure 9.7.: Example distributions for the determination of the simulated signal attenuation length of the BCF-92 WLS fibre with a diameter of 1 mm. The distribution for round double-clad fibres with a rough surface is compared with the distributions for round double-clad fibres with a smooth surface **(a)** and for square double-clad fibres with rough surface **(b)**, respectively.

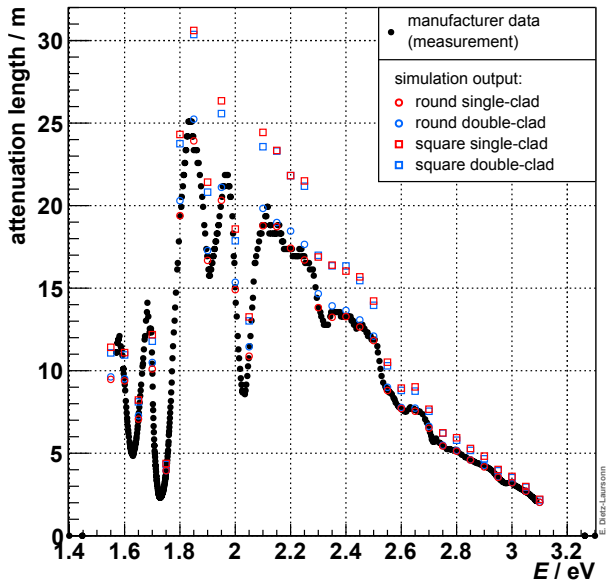

Figure 9.8.: Signal attenuation length of the light-guiding fibre BCF-98 for several fibre layouts (for a **rough surface** of the outer cladding). The statistical uncertainties (from the fits) are below 1 %.

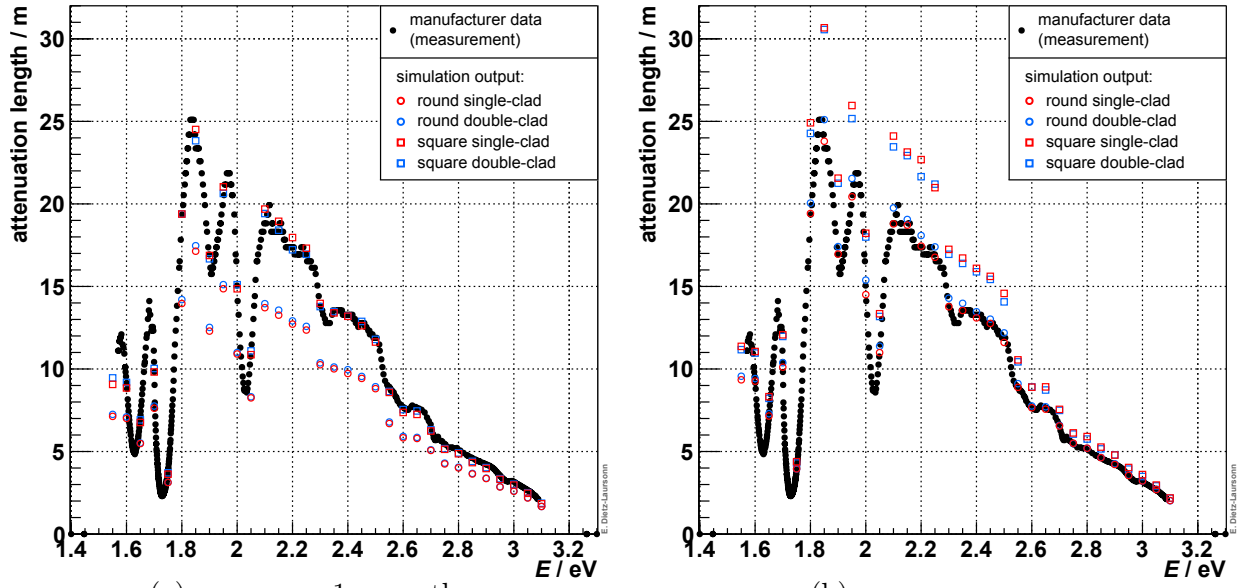

(a) $n_{\text{ambient}} = 1$, smooth

(b) $n_{\text{ambient}} = n_{\text{clad}}$

Figure 9.9.: Signal attenuation length of the light-guiding fibre BCF-98 for several fibre layouts. **(a)** shows the results for a **smooth surface** of the outer cladding. **(b)** presents the results **without** considering the **surface** between the outer cladding and the surroundings. The statistical uncertainties (from the fits) are below 1 %.

9.3. Exit Characteristics of Light from Optical Fibres

The exit characteristics of light from optical fibres as well as a corresponding comparison between simulations and measurements have been presented in section 7.1. The comparison was done to validate the implementation of optical fibres in the GODDeSS framework. The exit characteristics are important, as the position of the photons on the photodetector might influence its dynamic range and the incidence angle has influence on the PDE (due to reflections at the surface of the photodetector) [166]. To study the exit characteristics in more detail, simulations have been performed for a `G4Fibre` with the material properties of the WLS fibre BC-92 with a diameter of 1 mm and using various fibre types (round or square profile, single- or double-clad). The WLS fibre was simulated with a length of 1800 mm, a rough surface ($\sigma_\alpha = 5\,°$) between the outer cladding of the fibre and the surroundings ($n_{\text{ambient}} = 1$[82]), and cut (i.e. unprocessed) fibre end faces. It was excited with optical photons, which were isotropically emitted around the fibre, close to one of the fibre ends. At the other end of the fibre, the optical photons were detected with a `G4PhotonDetector`, which was placed behind an air gap of 1 µm to the fibre end face. The position and incidence angle of the detected photons were filled into histograms and the statistical uncertainty of the simulation output has been determined via *Poisson statistics*. In order to investigate the influence of diverse parameters, individual parameters were varied. The results will be presented in the following subsections.

9.3.1. Fibre Type

First of all, no parameter was varied, besides the fibre type. This was done to study its influence and at the same time to obtain reference results, which the results of the following subsections could be compared to. Figure 9.10 shows the position of the detected photons (after leaving the optical fibre and crossing the air gap). The position distributions of round fibres, which are presented in this section, are corrected for the different annular areas, which the individual bins are representing. The edges of the claddings, which are marked with dashed lines, can clearly be identified in the distributions. In the outer cladding, no photons reach the fibre end. In the inner cladding of double-clad fibres, the number of photons reaching the fibre end is reduced with respect to the edge of the fibre core. Within the core, the photons are homogeneously distributed (square fibres) or have a reduced intensity in the centre (round fibres). The magnitude of the relative reduction (i.e. the ratio of the minimum value in the centre and the maximum value at the edges) is lower with two claddings. The absolute number of photons is higher with two claddings (cf. the trapping efficiencies in the tables 9.1, 9.2, and 9.3).

Figure 9.11 illustrates the angular distribution of the detected photons.[83] The frequency of occurrence increases with increasing exit angle until the maximum exit angle of meridional

[82] The refractive index of the surroundings of 1 is an extreme case. If the fibre is surrounded by a material with a different refractive index, this has of course to be considered in the simulations and the results will change. This can be seen from the other extreme case ($n_{\text{ambient}} = n_{\text{clad}}$), which will be presented in subsection 9.3.5.

[83] In order to allow for comparison with the results presented in section 7.1, the angular distributions that are presented in this section, are not corrected for the solid-angle (as it was done e.g. in section 6.7).

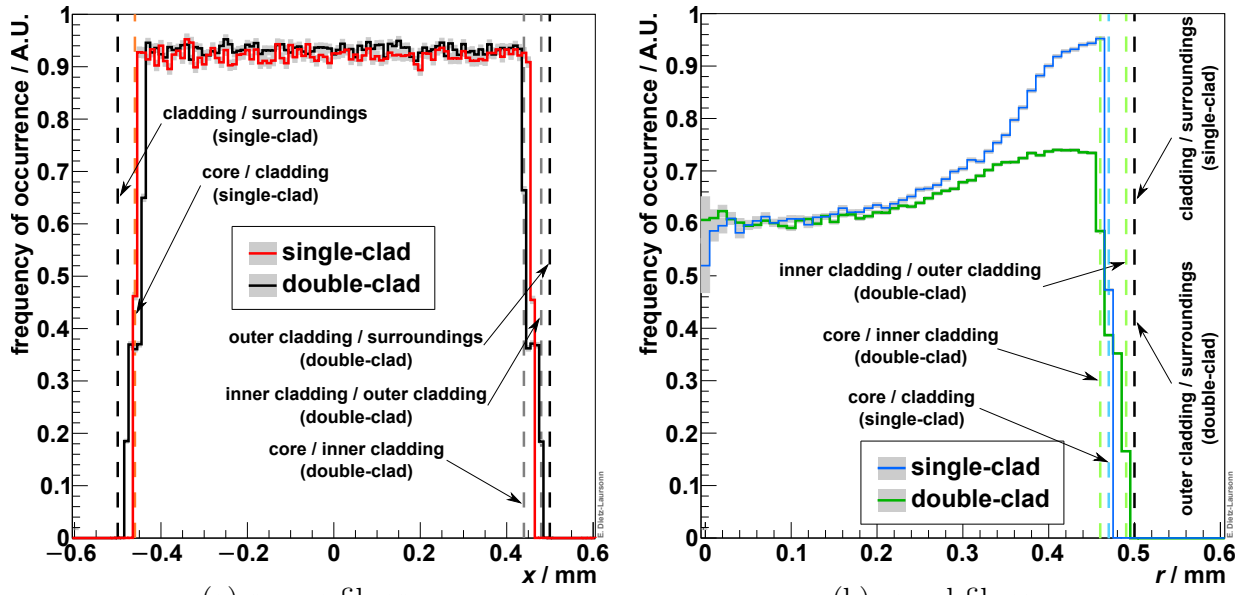

(a) square fibres (b) round fibres

Figure 9.10.: Position of photons on the photodetector after leaving an optical fibre, simulated for different fibre types and integrated over all exit angles. Illustrated are the projection to one edge of the fibre (for square fibres, **(a)**) or to the radius (for round fibres, **(b)**), respectively. The distributions have been normalised to the flat regions in the centre of the fibre ($x = 0$, $r = 0$). The dashed lines mark the edges of the core an the claddings.

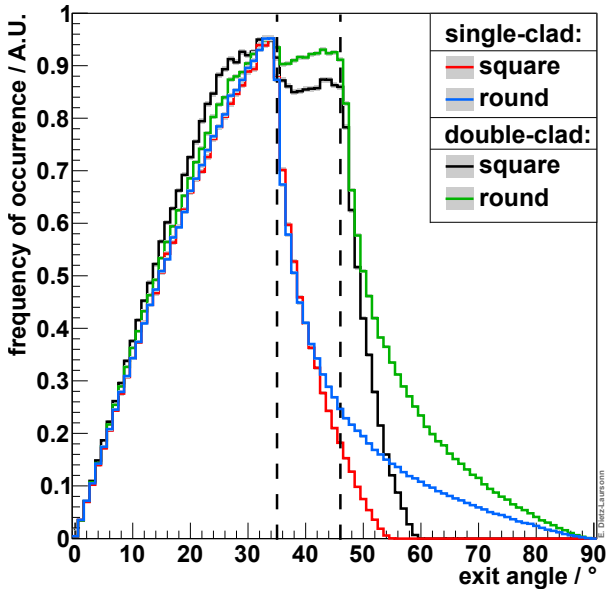

Figure 9.11.: Angular distribution of photons on the photodetector after leaving an optical fibre, simulated for different fibre types. The vertical dashed lines mark the maximum exit angle of meridional rays in the core and in the inner cladding of double-clad fibres, respectively.

rays in the core of the fibres or in the inner cladding of double-clad fibres is reached. These maximum exit angles can be calculated via equation (3.2) and are marked with vertical dashed lines. Above the maximum exit angles of meridional rays, there is a sharp drop of the frequency of occurrence, as only skew rays can contribute. The distributions for the double-clad fibres (round and square) are similar, besides the fact that large angles ($\gtrsim 60\,°$) are fully suppressed for the square profile. The same applies to the single-clad fibres. As the measurement results in figure 7.3 show, large angles should indeed be suppressed, but not fully. A possible reason for this deviation between measurement and simulation are the edges of square fibres. For available fibres, they are not sharp but rounded. This is not included in the simulation. Additionally, double-clad fibres achieve higher frequencies of occurrence for large exit angles, which is because of the smaller refractive index of the material of the outer cladding.

9.3.2. Fibre Length

If varying the fibre length, it can be recognised that the usage of fibres longer than the standard length of this section (1800 mm) does not lead to changes in the results. In contrast, the effect of the fibre length can be observed for shorter fibres (100 mm in this case). The resulting distributions are presented in figures 9.12 and 9.13, respectively. In the short fibres, the fraction of photons reaching the fibre end inside the claddings is increased and photons are also detected from the outer cladding. This corresponds to the increased trapping efficiency of short fibres (cf. tables 9.1, 9.2, and 9.3). Additionally, the relative reduction in the centre of the fibre core of round fibres seems to be decreasing for short fibres.

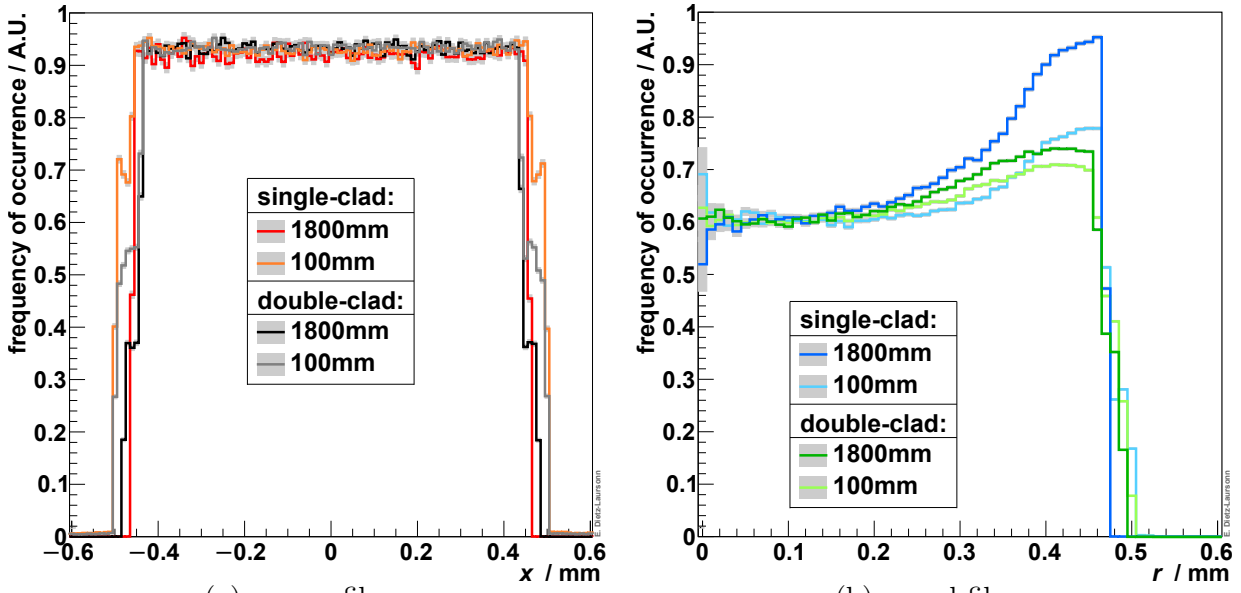

(a) square fibre (b) round fibre

Figure 9.12.: Position of photons on the photodetector after leaving an optical fibre, simulated for different fibre lengths and integrated over all exit angles. Illustrated are the projection to one edge of the fibre (for square fibres, **(a)**) or to the radius (for round fibres, **(b)**), respectively. The distributions have been normalised to the flat regions in the centre of the fibre ($x = 0$, $r = 0$).

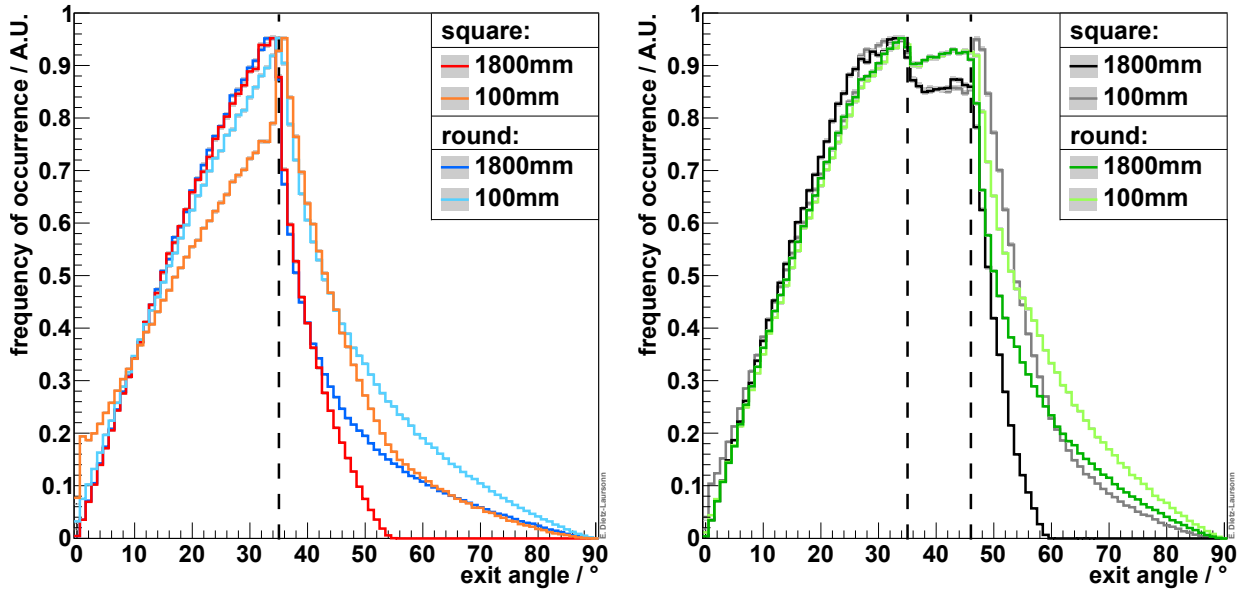

(a) single-clad (b) double-clad

Figure 9.13.: Angular distribution of photons on the photodetector after leaving an optical fibre, simulated for different fibre lengths. The vertical dashed lines mark the maximum exit angle of meridional rays in the core and in the inner cladding of double-clad fibres, respectively.

Concerning the angular distribution of the photons, a higher fraction of exit angles above the maximum exit angles of meridional rays can be observed for short fibres. The reason for this effect is the number of photons inside the outer cladding, which cannot be neglected for short fibres (cf. subsection 9.3.1). As the critical angle for total reflection at the fibre surface is very small for these photons ($\approx 38.2\,°$), they can contribute to every exit angle up to $90\,°$.

9.3.3. Finish of the Fibre End Face

The end faces of optical fibres can be cut (i.e. left unprocessed), mirrored, or roughened. To study the influence of the finish on the exit characteristics, the simulation was repeated once with a mirrored (100 % reflectivity) end face at the distant fibre end with respect to the `G4PhotonDetector` and once with a roughened ($\sigma_\alpha = 5\,°$) end face next to the `G4PhotonDetector`[84]. In these simulations, the mirrored finish did not have any significant effect on the spatial or angular distribution of the exiting photons.[85] In contrast, the roughened finish leads to a smearing of the exit angles (cf. figure 9.14), as expected. Additionally, the edges in the position distribution are sharpened instead of being smeared (cf. figure 9.15). This effect is particularly strong for short fibres and its causes are not known.

[84] In this subsection, the described roughness only corresponds to the end face of the fibre. The surface of the outer cladding of the fibre was always simulated with $\sigma_\alpha = 5\,°$.

[85] Of Course, the total number of detected photons increased when mirroring the fibre end face.

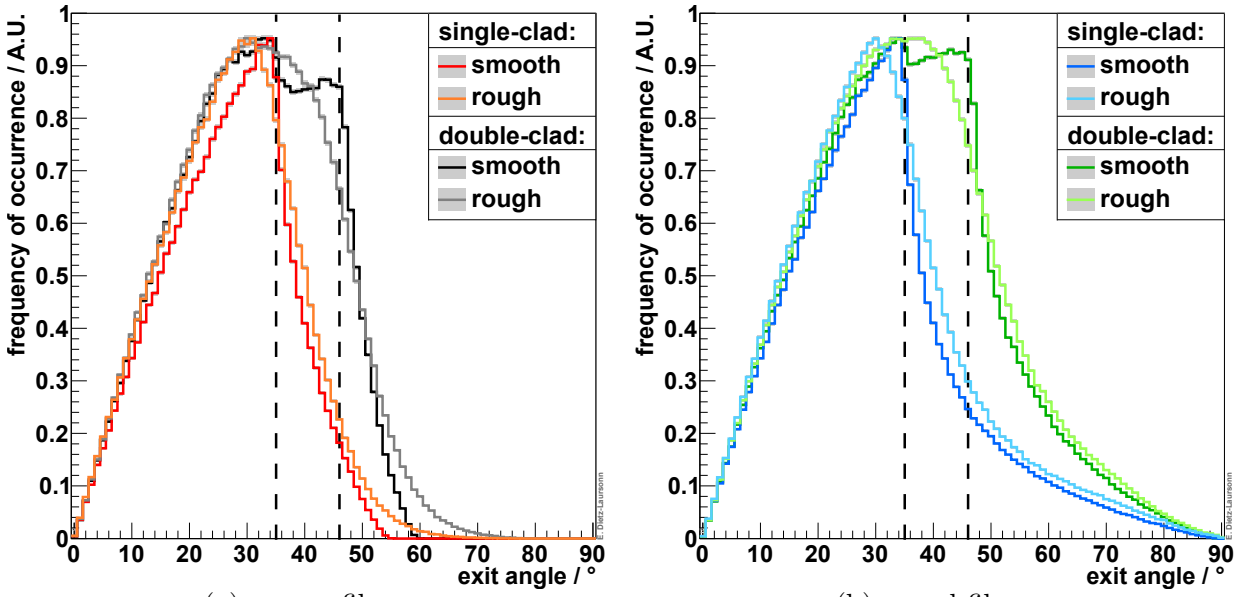

(a) square fibre (b) round fibre

Figure 9.14.: Angular distribution of photons on the photodetector after leaving an optical fibre, simulated with smooth ($\sigma_\alpha = 0\,°$) and rough ($\sigma_\alpha = 5\,°$) fibre end face close to the photodetector. The values have been integrated over all exit angles. The distributions have been normalised to the flat regions in the centre of the fibre ($x = 0$, $r = 0$). The vertical dashed lines mark the maximum exit angle of meridional rays in the core and in the inner cladding, respectively. The latter is for double-clad fibres only.

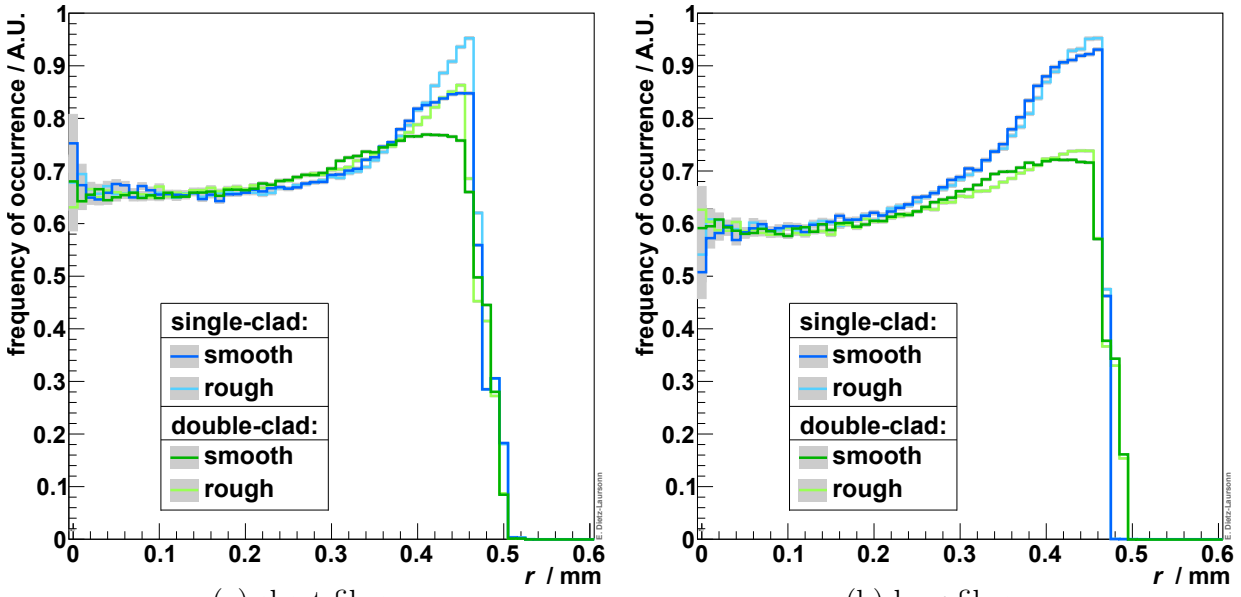

(a) short fibre (b) long fibre

Figure 9.15.: Position of photons at the end of round optical fibres, simulated with smooth ($\sigma_\alpha = 0\,°$) and rough ($\sigma_\alpha = 5\,°$) fibre end face. Illustrated is the projection to the radius for short **(a)** and long **(b)** fibres.

9.3.4. Distance between the Fibre End and the Photodetector

As the photons are not leaving the fibre parallel to its axis, the position of the photons on the photodetector naturally also depends on the distance between the fibre end and the photodetector.[86] To study this effect, the simulation was repeated with varying thicknesses of the air gap[87]. In this context, a thickness of "0 mm" actually stands for an air gap of 1 µm, as otherwise the air gap would have no extent as well as no optical surfaces and the results could not be compared to the other thickness values.

With increasing distance between the fibre end and the photodetector, the sharp edges in the distributions of the photon hit position on the photodetector are being smeared. This is illustrated for round, single-clad fibres in figure 9.16. As a result, also the relative reduction in the centre of the core of round fibres vanishes and a maximum forms in the centre. For distances of 0.5 mm for double-clad fibres or 0.75 mm for single-clad fibres, there is no longer a difference between square and round fibres with respect to the hit positions of the photons when regarding a sensitive area of the photodetector of $1\times1\,\mathrm{mm}^2$.[88] Figure 9.17 illustrates this, using the example of double-clad fibres. In case of these distances, the hit position distribution of all fibres is characterised by a maximum in the centre and a decrease to the edges, down to $\approx 20\,\%$ of the maximum value in the corners of the sensitive area of the photodetector.

Considering larger distances, the maximum value dramatically decreases with increasing distance, as the photons spread over a larger area. This can be seen from the figures 9.18

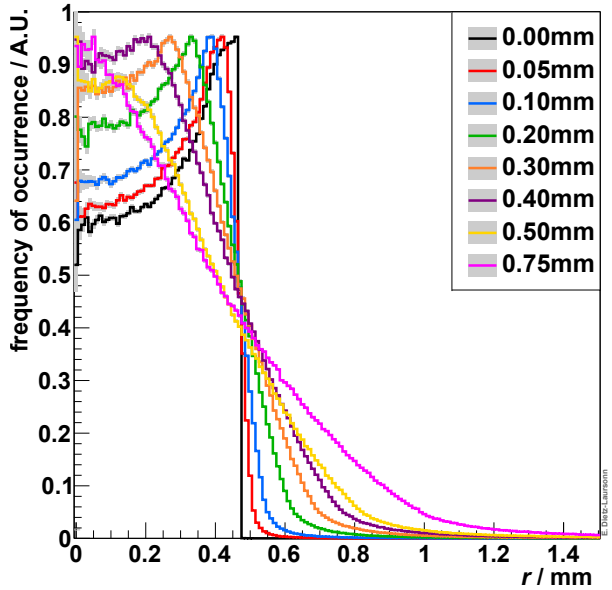

Figure 9.16.: Position of photons on the photodetector after leaving an optical fibre, simulated for different distances between the fibre and the photodetector. Illustrated is the projection to the radius of the round single-clad fibre.

[86] The finite dimensions of available photodetectors will be neglected.

[87] In the simulations in scope of this thesis, an air gap was simulated between the fibre and the photodetector. This was done for comparison to the measurements, which have been presented in section 7.1. If the gap is filled with a material with a different refractive index (e.g. optical coupling material), this has to be taken into account, i.e. the simulations have to be performed again with the alternative coupling material.

[88] The simulations were actually performed using a `G4PhotonDetector` with a sensitive area of $10\times10\,\mathrm{mm}^2$ and the results were then limited to interesting ranges.

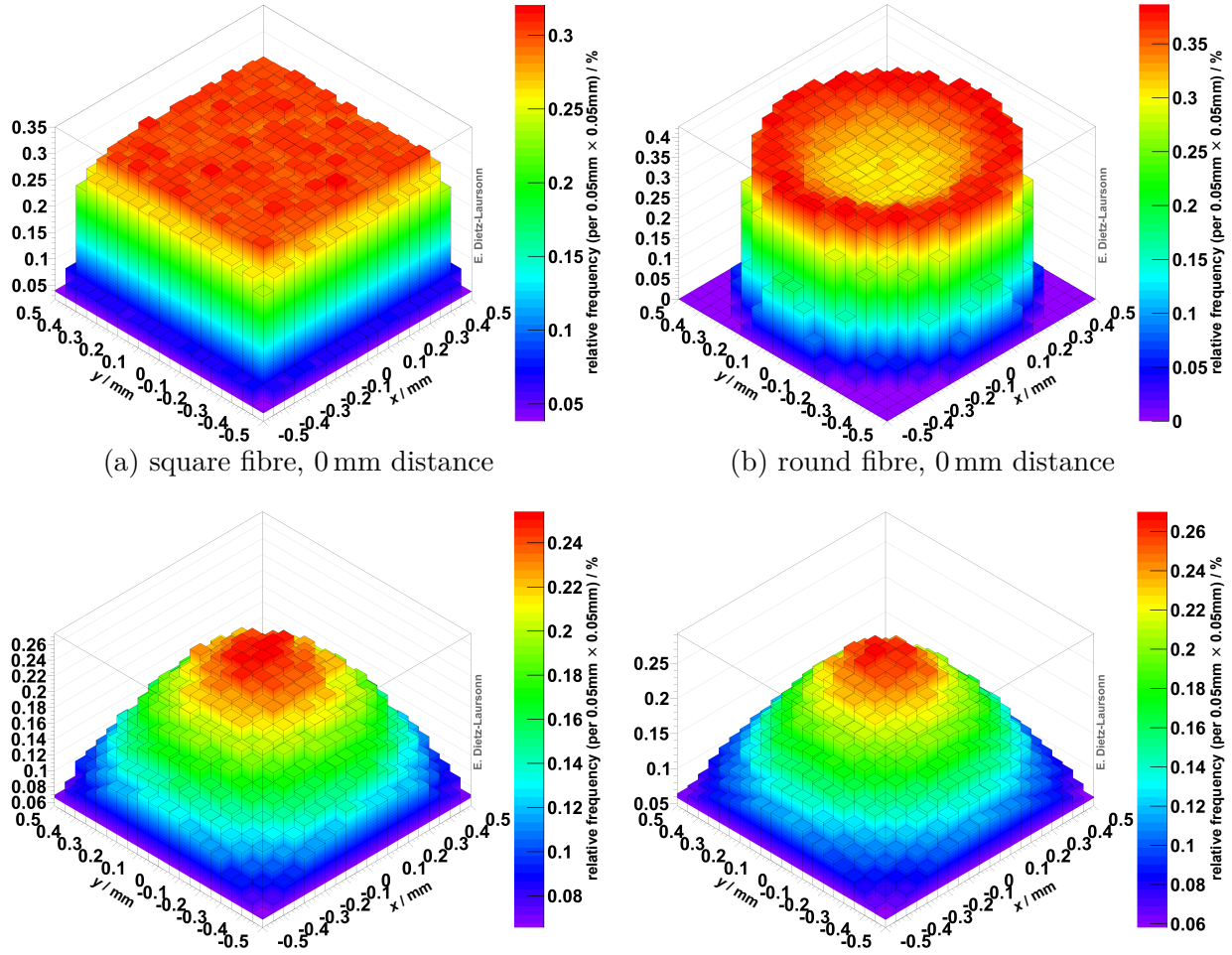

(a) square fibre, 0 mm distance

(b) round fibre, 0 mm distance

(c) square fibre, 0.5 mm distance

(d) round fibre, 0.5 mm distance

Figure 9.17.: Position of photons on the photodetector after leaving an optical fibre, simulated for distances of 0 mm and 0.5 mm between the fibre and the photodetector. The x-y-plane represents the sensitive area of a photodetector. As a fraction of the photons misses the sensitive area in case of a distance of 0.5 mm, the total numbers as well as the maximal values are smaller than in case of 0 mm.

and 9.19. If additionally taking photodetectors with larger sensitive areas into account, slight differences remain. For the areas of low hit frequency, the distribution of the photon position keeps the profile of the corresponding fibre. Furthermore, the regions that can at all be reached by (single) photons depend on the fibre type. In case of round fibres, the frequency of occurrence slowly decreases with increasing distance to the centre, whereas only sharply separated areas can be reached in case of square fibres. This might also be a result of the sharp edges of the simulated square fibres and could perhaps change when implementing rounded edges into the GODDeSS framework. The implementation as well as the corresponding studies are something that could e.g. be done in the scope of a subsequent bachelor or master thesis.

Concerning the angular distribution of the photons on the $1 \times 1\,\mathrm{mm}^2$ photodetector[89], the fraction of large exit angles decreases with increasing distance between the photodetector

[89] When using photodetectors with larger sensitive areas, of course larger distances are necessary to achieve the same changes in the angular distribution.

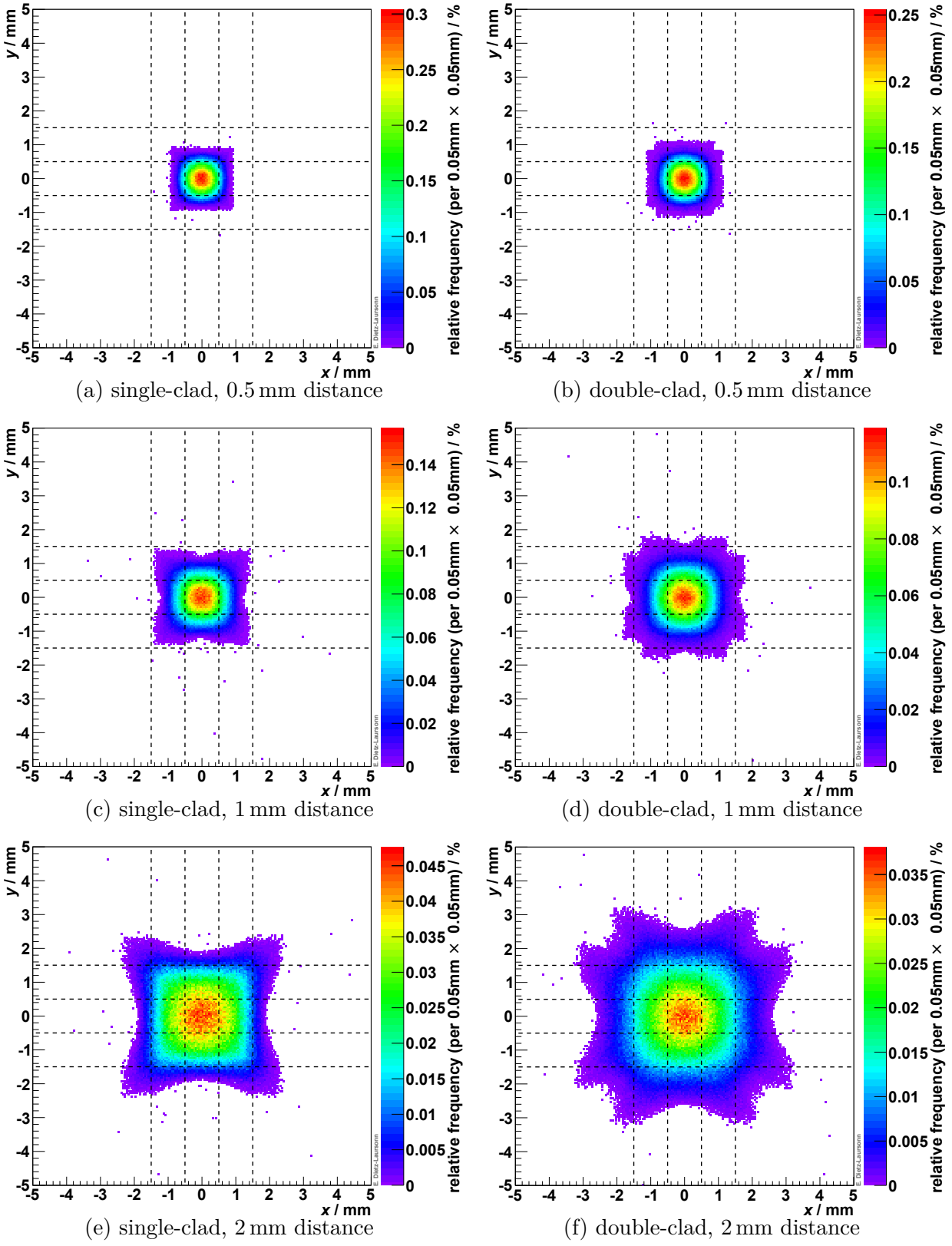

(a) single-clad, 0.5 mm distance

(b) double-clad, 0.5 mm distance

(c) single-clad, 1 mm distance

(d) double-clad, 1 mm distance

(e) single-clad, 2 mm distance

(f) double-clad, 2 mm distance

Figure 9.18.: Position of photons in the photodetector plane after leaving an optical fibre, simulated for distances of 0.5 mm, 1 mm, and 2 mm, respectively, between the **square** fibre and the photodetector. The dashed lines mark distances of 1 mm in the detector plane to allow for an easier comparison between the results and the dimensions of the sensitive area of typical SiPM types.

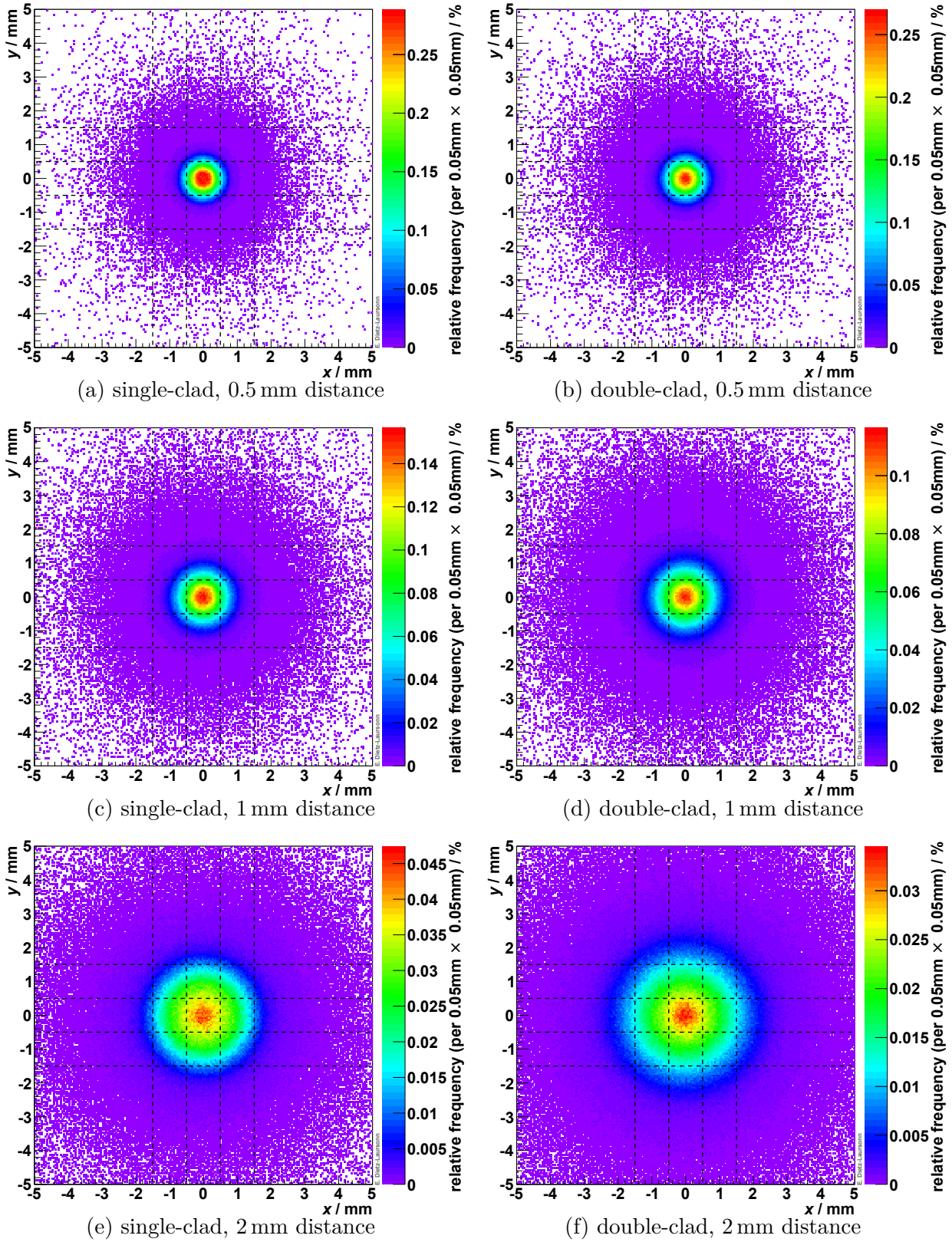

(a) single-clad, 0.5 mm distance

(b) double-clad, 0.5 mm distance

(c) single-clad, 1 mm distance

(d) double-clad, 1 mm distance

(e) single-clad, 2 mm distance

(f) double-clad, 2 mm distance

Figure 9.19.: Position of photons in the photodetector plane after leaving an optical fibre, simulated for distances of 0.5 mm, 1 mm, and 2 mm, respectively, between the **round** fibre and the photodetector. The dashed lines mark distances of 1 mm in the detector plane to allow for an easier comparison between the results and the dimensions of the sensitive area of typical SiPM types.

and the fibre end (cf. figure 9.20), as one would expect. Like for the photon hit position, this leads to an increasing agreement between the distributions of the different fibre types. For distances of 0.75 mm, there are no large deviations left.

In order to illustrate the influence of neglecting the air gap or optical cement volume, the simulation was additionally performed with the `G4PhotonDetector` (which absorbs and detects every photon hitting the sensitive surface) directly coupled to the fibre. In this case, the results significantly change, as the transition through the optical surface between the fibre and the air (or optical cement) is missing. The fraction of photons that reach the photodetector at the edge of the fibre core with respect to the fibre core centre drastically increases (cf. figure 9.21). Furthermore, the exit angles are shifted to lower values and a small peak appears at $\approx 39\,°$, in case of round fibres (cf. figure 9.22). This comes from

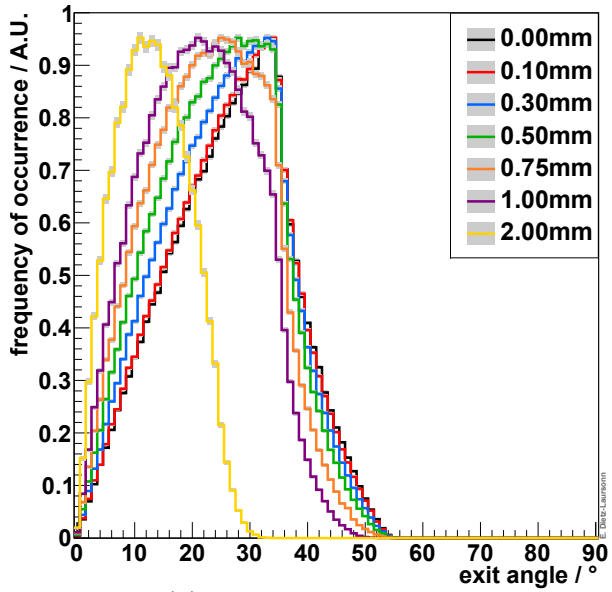

(a) square, single-clad

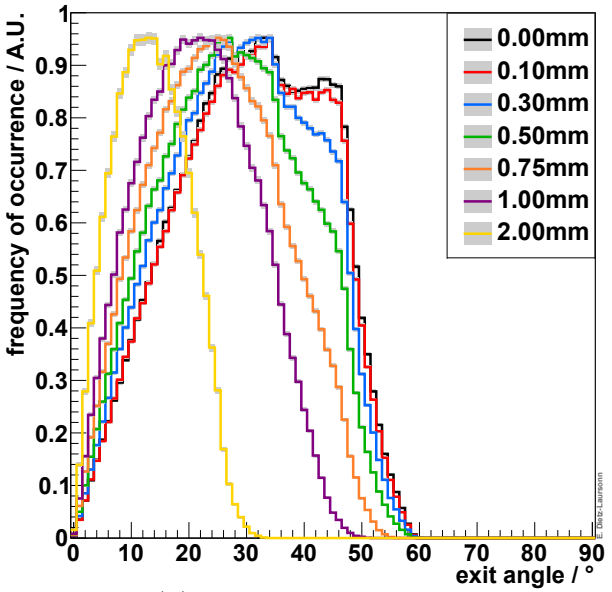

(b) square, double-clad

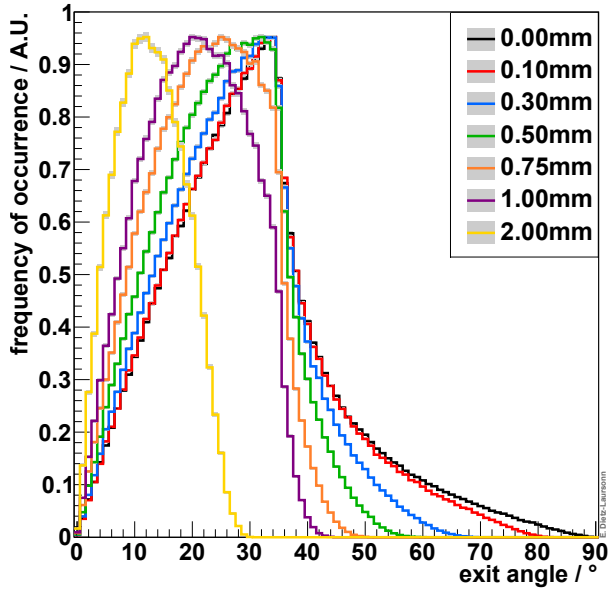

(c) round, single-clad

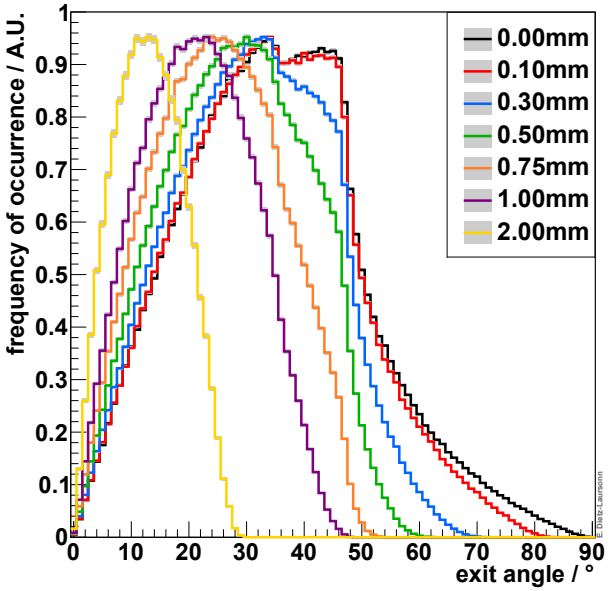

(d) round, double-clad

Figure 9.20.: Angular distribution of photons on the photodetector after leaving an optical fibre, simulated for different distances between the fibre and the photodetector.

photons that undergo total reflection at the distant fibre end (angles above $\approx 39\,°$) and are then detected at the other fibre end. These photons are not detected if there is an air gap between the photodetector and the fibre, as they undergo total reflection at both fibre ends in this case. Thus, neglecting the gap in the simulation of a detector setup will lead to unexpected results.

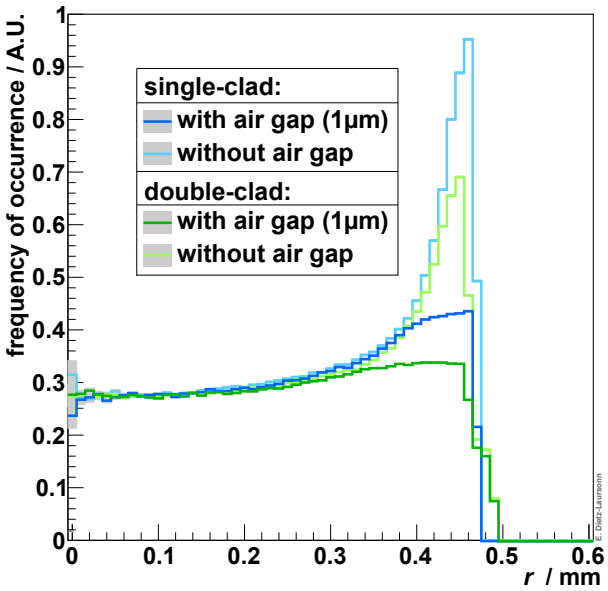

Figure 9.21.: Position of photons on the photodetector after leaving an optical fibre, simulated with and without air gap between fibre and photodetector. The values have been integrated over all exit angles. Illustrated is the projection to the radius. The distributions have been normalised to the flat regions in the centre of the fibre ($r = 0$).

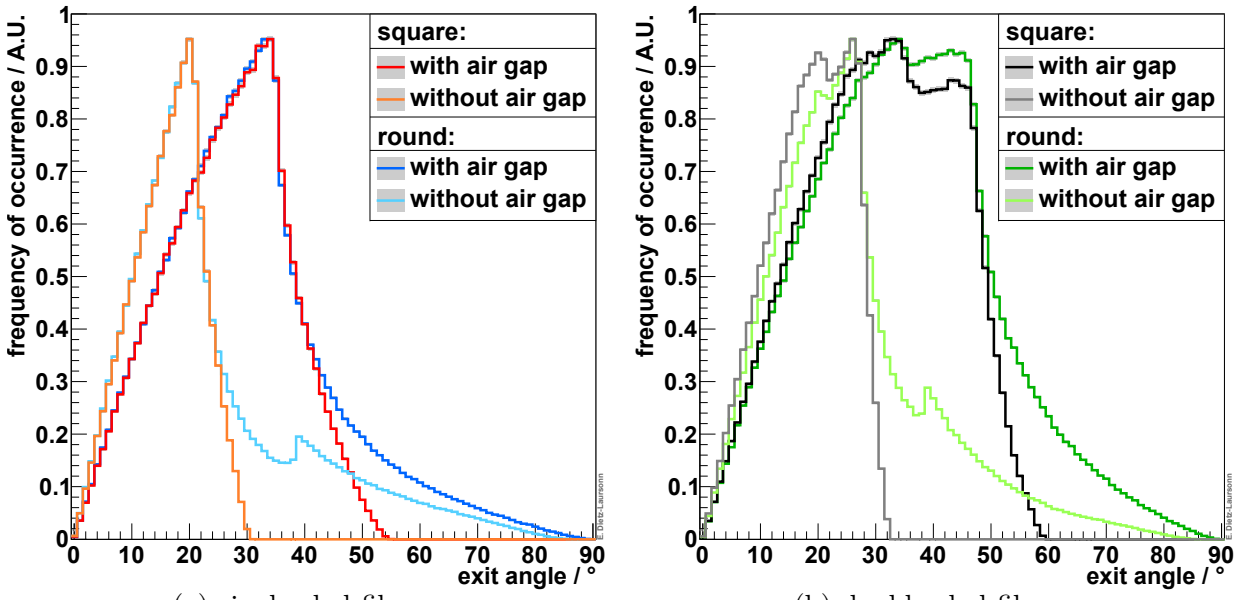

(a) single-clad fibres (b) double-clad fibres

Figure 9.22.: Angular distribution of photons on the photodetector after leaving an optical fibre, simulated with and without air gap between fibre and photodetector.

9.3.5. Equality of the Refractive Indices of Cladding and Surroundings

Besides the case of $n_{\text{ambient}} = 1$, another extreme case is when the refractive index of the surroundings equals the refractive index of the fibre's outer cladding ($n_{\text{ambient}} = n_{\text{clad}}$).[90] This can e.g. be realised if the optical fibre is embedded in scintillating material or optical glue/cement. Whereas this does not make any difference to the angular distribution of the photons, a larger fraction of the photons hits the photodetector at the edge of the core of the fibre (cf. figure 9.23).

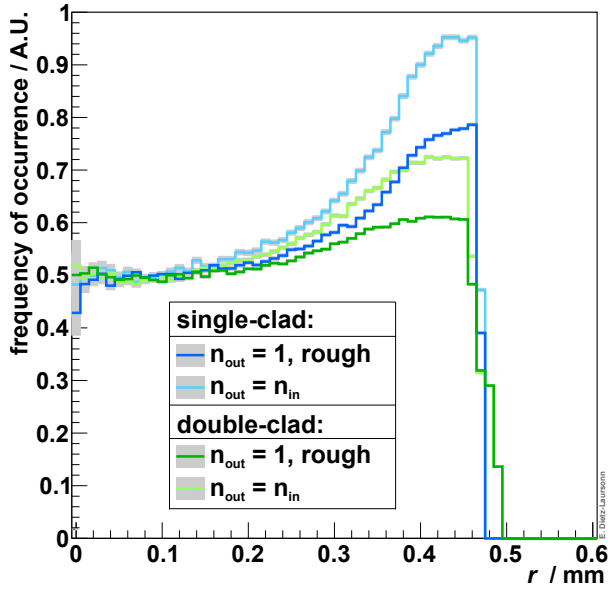

Figure 9.23.: Position of photons on the photodetector after leaving an optical fibre, simulated with $n_{\text{ambient}} = 1$ and with $n_{\text{ambient}} = n_{\text{clad}}$, respectively. The values have been integrated over all exit angles. Illustrated is the projection to the radius. The distributions have been normalised to the flat regions in the centre of the fibre ($r = 0$).

9.4. Optical Readout Options

In this section, the characteristics of the detector response of various benchmark detector setups will be investigated with GODDeSS simulations. For these setups, the number of photons (signal height), the time delay of the signal, and the pulse length were studied. The results can e.g. give a first hint, which detector setup might be the most appropriate when designing a detector with specific requirements.

The simulated setups consisted of a scintillator tile (BC-404) with or without wrapping (Tyvek with or without air gap). The scintillator tile was either read out directly with a $3\times3\,\text{mm}^2$ `G4PhotonDetecor` or with a $1\times1\,\text{mm}^2$ `G4PhotonDetecor` via a WLS fibre (BCF-92) that was coupled to the scintillator material with optical cement (BC-600). The fibre end face that was not coupled to the `G4PhotonDetecor` was mirrored (90 % reflectivity). The simple standard layouts, which have been used for studying the differences between direct

[90] At the same time, the refractive index of the air gap of course remains at 1.

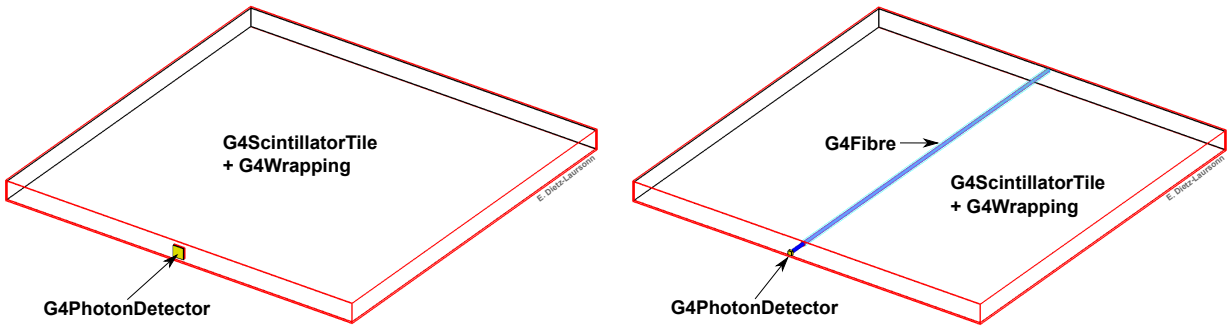

(a) (b)

Figure 9.24.: Simple detector layout with direct **(a)** or fibre **(b)** readout.

and fibre readout, are illustrated in figure 9.24. Following the studies of the standard layouts, representative special layouts with fibre readout will be presented and evaluated in subsection 9.4.3. During the simulations, scintillating material was excited with vertically traversing muons ($\beta\gamma = 3.5$). In order to take the influence of the geometry of the scintillator tiles into account (small, thick tiles versus large, thin tiles), the simulations have been performed for $100\times100\times10\,\mathrm{mm}^3$ (referred to as "thick") and for $300\times300\times5\,\mathrm{mm}^3$ (referred to as "thin") scintillator tiles for all detector setups.

As the photons were detected by a `G4PhotonDetector` during these simulations, the studies presented in this section concentrate on the influence of the detector module geometry. In particular, they do not consider the effects of the coupling of the photodetector to the scintillator material or fibre, of the geometry or the PDE of the photodetector, or potential saturation effects of the photodetector (e.g. for SiPMs). If these have to be taken into account (e.g. to determine the characteristics of a detector module with a particular geometry and photodetector), this could be done in a next simulation step.

9.4.1. Signal Height

To determine the signal height distribution, the photons, which were detected by the `G4PhotonDetector`, were counted individually for each traversing muon. Their number has then been filled into a histogram and the statistical uncertainty of the simulation output has been determined via *Poisson statistics*. An exemplary histogram is presented in figure 9.25. The distributions are characterised by a steep rise up to their MPV and a smoother fall, followed by an exponential tail. The characteristic values of this distribution are summarised for all simulated detector setups in table 9.5.

As the signal is reduced when taking the properties of the photodetector as well as its optical coupling into account (e.g. by a factor of around 5 in the simulations corresponding to the hodoscope measurements, cf. figure 8.10), a detector setup without wrapping is obviously not a good choice. This is especially true for thin scintillator tiles. The highest light yield is achieved when using a wrapping with an air gap (light yield approximately twice as high as without air gap). This is caused by the possibility of total reflection at the optical surface between the scintillator material and the air. The influence of the application of a (straight) WLS fibre for the readout depends on the dimensions of the scintillator tile. In the thin tile, the increase of the MPV is $\sim 275\,\%$ to $\sim 375\,\%$ in case of fibre readout, whereas the increase is only $\sim 40\,\%$ to $\sim 60\,\%$ for the thick tile.

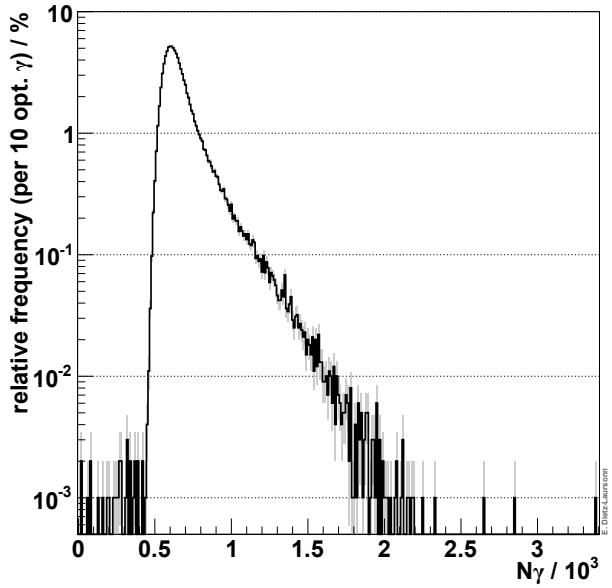

Figure 9.25.: Number of simulated optical photons reaching the photodetector (exemplary distribution).

		wrapping					
		none		without air gap		with air gap	
		min.	MPV	min.	MPV	min.	MPV
thick tiles	direct readout	10	50	150	230	300	430
	fibre readout	40	80	250	370	450	600
thin tiles	direct readout	0	8	0	15	15	40
	fibre readout	10	30	35	70	100	170

Table 9.5.: Number of optical photons reaching the photodetector in several different simulated setups. The minimum value represents the beginning of the rising slope.

To investigate the spatial distribution of the signal height across the scintillator tile, its surface was binned during the analysis. Then, the signal height distribution was created individually for each bin, only considering the muons traversing the scintillator tile at the corresponding bin position. The mean of the distributions was then assigned to the corresponding bin. The statistical uncertainty of the mean values was determined with equation (8.1) and is between 3 % and 5 %.[91] Figure 9.26 shows two representative examples of the resulting spatial distributions. They are characterised by a relatively constant base value and an increase towards the peak value at the position of the fibre or photodetector, respectively. In addition, in case of direct readout, there is a decrease of the signal height towards the corners of the scintillator tile next to the photodetector (cf. figure 9.26(a)). This is only significant for non-wrapped scintillator tiles. The characteristic values of the spatial distributions are summarised for all simulated detector setups in table 9.6. Detector layouts with direct readout feature a lower base value and a much more extreme deviation of the peak value from the base value than layouts with fibre readout do.

[91] In case of direct readout of a thin, non-wrapped scintillator tile, it is between 6 % and 8 %.

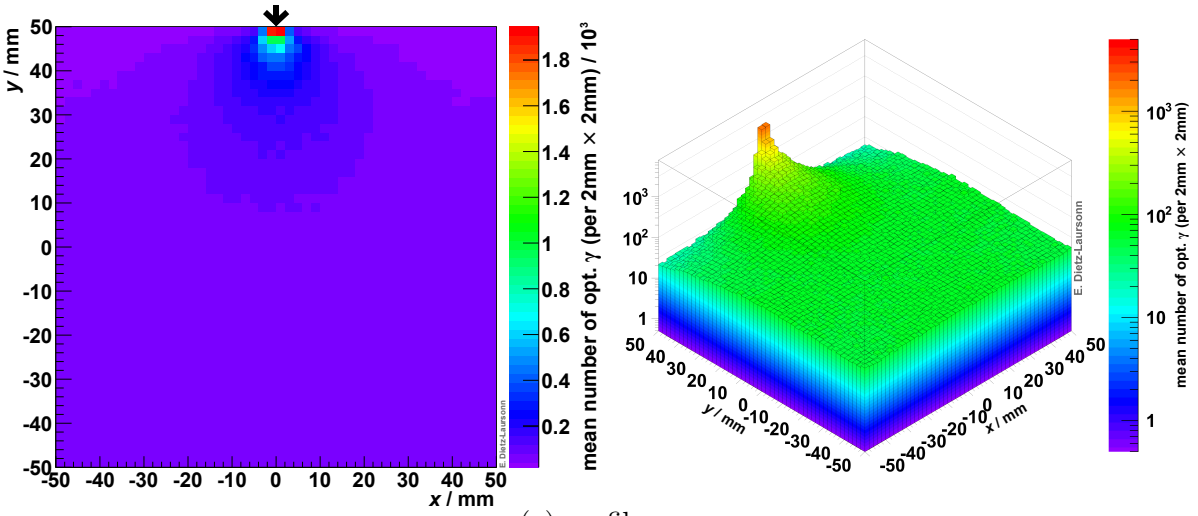

(a) no fibre

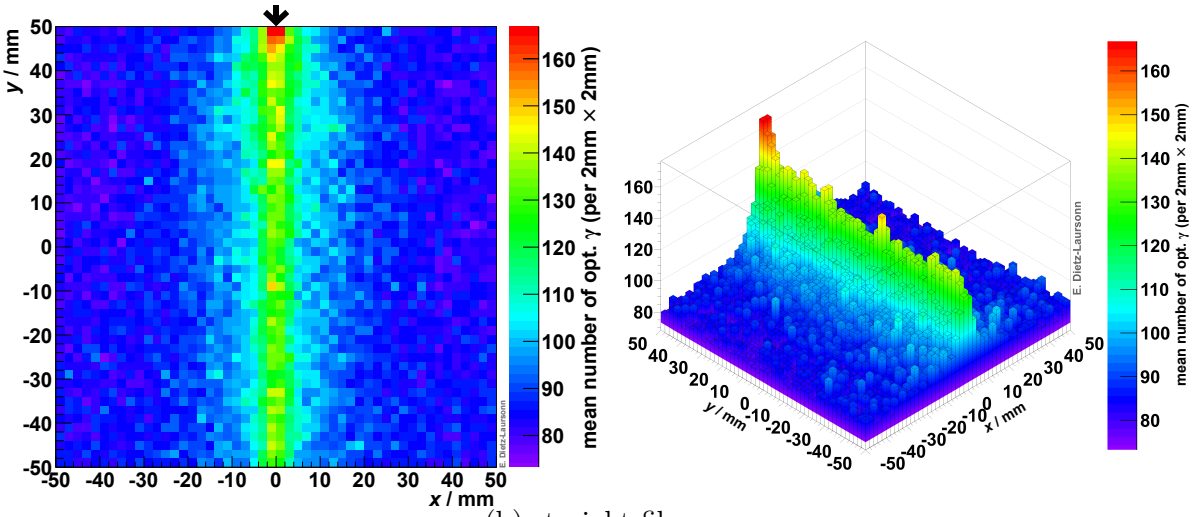

(b) straight fibre

Figure 9.26.: Simulated spatial distribution of the mean number of optical photons reaching the photodetector in case of a thick scintillator tile with wrapping with air gap. The x-y-plane represents the incidence position of the muons on the scintillator tile, the black arrows indicate the position of the `G4PhotonDetector` corresponding to the illustrated data in this plane.

		wrapping					
		none		without air gap		with air gap	
		base	peak	base	peak	base	peak
thick tiles	direct readout	40	2000	200	2500	450	2600
	fibre readout	80	140	370	490	650	750
thin tiles	direct readout	6	600	25	830	40	850
	fibre readout	30	80	70	190	170	280

Table 9.6.: Mean number of optical photons reaching the photodetector in several different simulated setups: base and peak values of the spatial distribution.

Although the installation of optical fibres creates additional potential error sources and makes the assembly of optical detectors more complex and time-consuming, the results of the simulations favour their application. They are indispensable for optical detectors with thin scintillator tiles, which can practically not be operated efficiently with direct readout, as the signal is very low in large areas of the detector. When looking at optical detectors with thick scintillator tiles, the conclusion is not that clear. The variation of the signal height due to the position on the scintillator tile is much smaller for fibre readout than for direct readout, whereas the variations are limited to a smaller part of the scintillator tile in case of direct readout. Of course, this might be different in case of very small tiles.

Another thing to be taken into account is the influence of different tile thicknesses on the signal height. Measurements with detector prototype modules at the Physics Institute III of RWTH Aachen University showed an unexpected result: When using the same detector layout and doubling the thickness of the scintillator tile, the change of the signal height is not proportional to the change of the tile thickness [161]. In these measurements, prototype modules with a $100\times100\times5\,\mathrm{mm}^3$ or with a $100\times100\times10\,\mathrm{mm}^3$ scintillator tile were used. Like in the hodoscope measurements in the scope of this thesis (cf. section 8.1), they were wrapped with Teflon and directly readout with two $3\times3\,\mathrm{mm}^2$-SiPMs (Hamamatsu S10362-33-100C). Comparing the MPV of the signal height distributions of both prototype modules, the module with the doubled thickness only provided a $\sim 14\,\%$ higher signal. Repeating the comparison with simulations (taking the geometry, the PDE, and the saturation effect of the SiPM, as well as the saturation of the pre-amplifier into account, cf. section 8.1) showed a similar result ($\sim 22\,\%$ signal increase), although the number of created photons doubled, as expected. This is illustrated in figure 9.27. Thus, whereas the number of created photons in the scintillator material is proportional to the thickness of the scintillator tile, the number of detected photons is not.

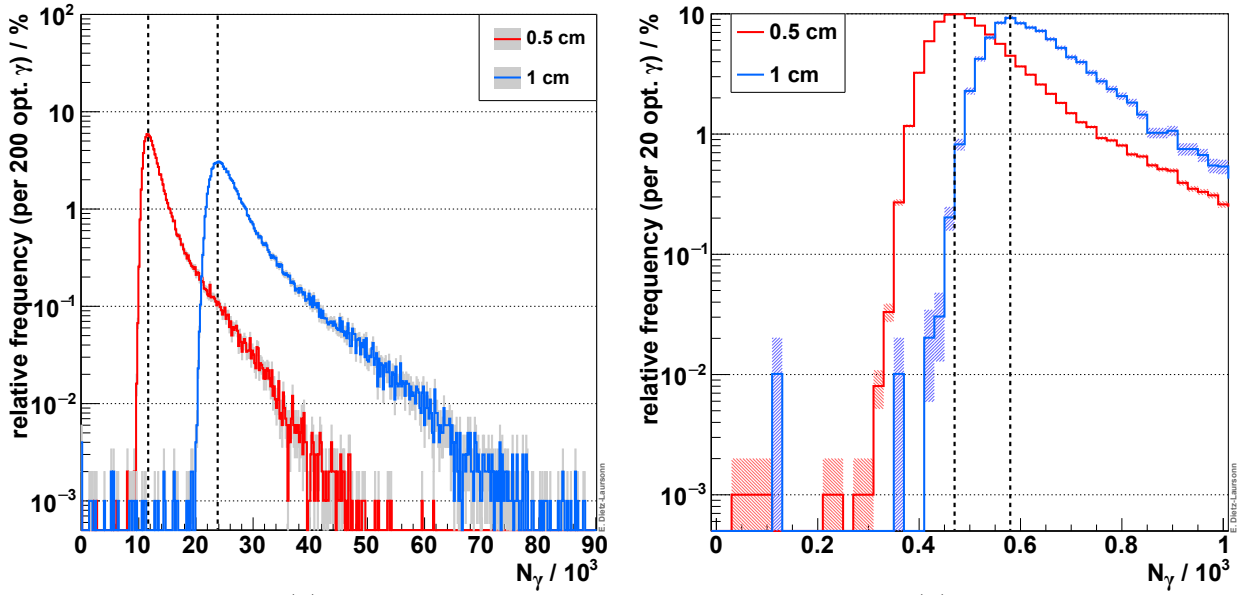

(a) (b)

Figure 9.27.: Optical photons in simulated $100\times100\times5\,\mathrm{mm}^3$ and $100\times100\times10\,\mathrm{mm}^3$ scintillator tile with Teflon wrapping and direct readout: number of created photons **(a)** and number of photons reaching the photodetector **(b)**.

In order to study this effect, the simulations were repeated with varying values of the thickness d of the tile. Additionally, this was done for small ($100\times100\times d\,\mathrm{mm}^2$) and large ($300\times300\times d\,\mathrm{mm}^2$) tiles with direct or with fibre readout. In contrast to the rest of this section, these studies were not performed with the detector layouts described at the beginning of this section, but with detector layouts following the prototype modules used for the hodoscope measurements (cf. section 8.1). This means that two photodetectors or fibres were used for direct or fibre readout. The MPV of the signal height was visually determined (bin with the maximum entry) and its uncertainty was roughly estimated from the bin width and the relative height of the neighbouring bins. The results are summarised in figure 9.28(a).

The signal height is not proportional to the thickness of the scintillator tile, but describes something like a saturation curve with increasing thickness. The magnitude of this "saturation" depends on the dimensions of the scintillator tile and on the readout method, as of course also the absolute signal height does. The normalised results (figure 9.28(b)) show that besides the absolute values, the behaviour is similar for layouts with direct readout and almost identical for layouts with fibre readout. For detector setups with direct readout, the "saturation" effect is more distinct. From the distributions presented in figure 9.28 the reasonable thickness range of scintillator tiles in optical detectors can roughly be estimated to values between 5 mm and 10 mm for direct and between 5 mm and 20 mm for fibre readout.

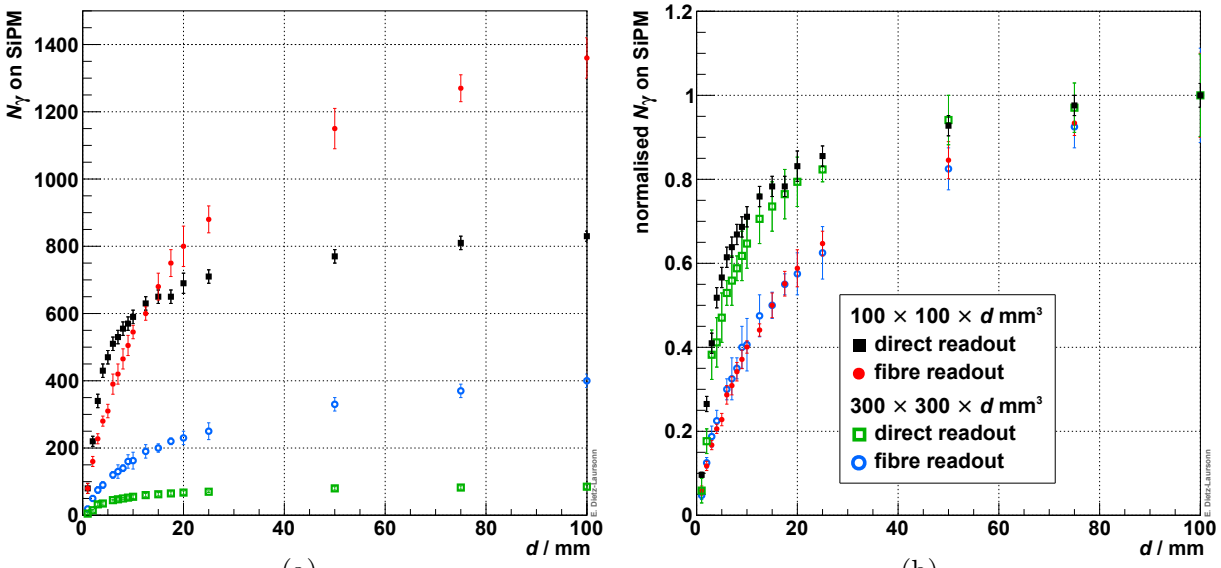

(a) (b)

Figure 9.28.: Number of optical photons reaching the photodetector in simulated $100\times100\times d\,\mathrm{mm}^3$ and $300\times300\times d\,\mathrm{mm}^3$ scintillator tiles. **(a)** shows the absolute values, **(b)** presents the same values normalised to the value at $d = 100\,\mathrm{mm}$.

9.4.2. Timing

Besides the signal height, the timing of the signal is an important property of a detector. A good knowledge of the timing is necessary e.g. for trigger application, for assigning the signal to the correct event (like the correct beam-crossing in case of the CMS detector) or for the potential application for out-of-time pile-up reduction.

The signal timing of an optical detector basically depends on the readout option (direct or fibre), the arrangement of the components, the dimensions of the components, the materials, and the wrapping. As the impact of varying the common optical detector materials (which all have rather similar material properties) is expected to be small, this was not studied in the simulations, which will be presented in this subsection. Furthermore, the scintillator tile has generally been simulated with wrapping (Tyvek) and air gap. Without wrapping, the signal is in many cases too low to be detected. With wrapping but without air gap, the results are slightly worse than with air gap (cf. figure 9.30). Therefore, the results for wrapping and air gap will be presented, as best achievable results (with respect to the wrapping). Special fibre setups will be discussed in subsection 9.4.3. Therefore, this subsection will mainly concentrate on the differences between direct and fibre readout as well as between thin ($300\times300\times5\,\mathrm{mm}^3$) and thick ($100\times100\times10\,\mathrm{mm}^3$) tiles.

The most striking difference is certainly caused by the *readout option*. This already becomes obvious, when simply filling the *time delay* Δt_γ between the muon incidence on the scintillator tile and the detection of the optical photons into a histogram. The results are illustrated in figure 9.29, using the example of the thick scintillator tile with wrapping with air gap. With fibre readout, the MPV is about twice as high as with direct readout. Additionally, the distribution for direct readout is simply exponentially decreasing for values of Δt_γ above the MPV, whereas the decrease can only be described as superposition of two exponential decreases in case of fibre readout (cf. figure 9.29(a)). This is caused by the combination of the shorter decay time of the *scintillation process* and the longer decay time of the *WLS process*. Furthermore, when closely studying the range below the MPV (cf. figure 9.29(b)), another difference becomes obvious: In case of direct readout, several peaks with low values of Δt_γ can be identified in the distribution. These are caused by *Cherenkov photons*, which reached the photodetector directly or with a very small number of reflections. In case of fibre readout,

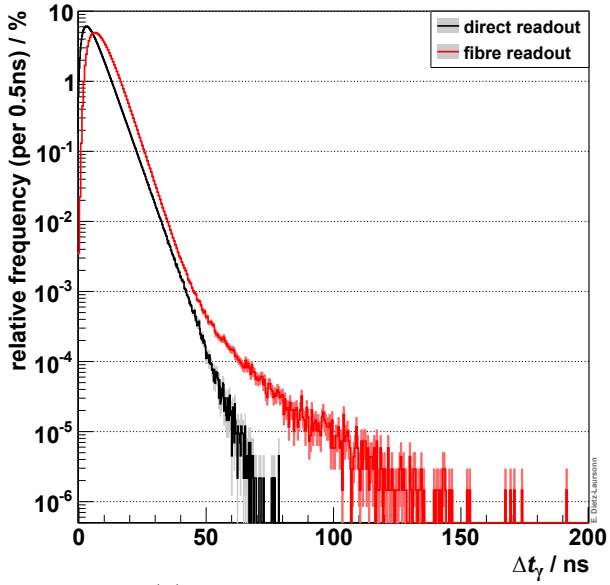

(a) logarithmic ordinate

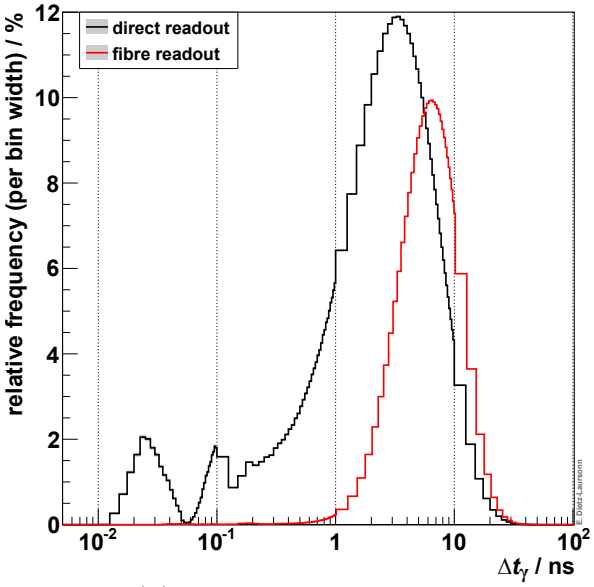

(b) logarithmic abscissae

Figure 9.29.: Exemplary distribution of the simulated photon hit time Δt_γ on the photodetector with respect to the incidence time of the muon on the scintillator tile. The distributions present the results for direct readout and for fibre readout, with a logarithmic ordinate **(a)** or abscissae **(b)**, respectively. The statistical uncertainty has been determined via *Poisson statistics*.

these peaks do not occur, as the Cherenkov photons cannot reach the photodetector, but have to be collected by the WLS fibre (as long as the fibre is protruding from the scintillator tile and thus the photodetector is not partly coupled to it).

For measurements with optical detectors, the *signal delay* Δt is more essential than the hit time Δt_γ of the individual photons. In a measurement, a signal is basically detected if the measured (i.e. integrated over a certain time) signal height exceeds a given threshold value. Thus, the signal delay can be specified as the time delay between the muon incidence on the scintillator tile and the signal exceeding the threshold. For the simulations, a threshold of 50 photons was chosen, as in the simulations in scope of the hodoscope measurements (cf. figure 8.10) the signal is reduced by a factor of around 5 when taking the properties of the photodetector as well as its optical coupling into account. Δt was determined by adding up the bin entries of the hit time distribution (starting from the low edge of the distribution) until the resulting sum exceeded the threshold. The resulting signal delay times were filled into histograms, which are illustrated in figure 9.30.

Compared to the thick detector layouts, the thin detectors possess a much wider distribution of Δt. As a result, the time resolution of thick detectors is much better. Besides providing low signals and a significant fraction of events without exceeding the threshold, the Δt distribution of detectors without wrapping is much wider than for detectors with wrapping. The resulting much worse time resolution is another reason for using wrapped detectors. This also applies to the case of the thin tile with direct readout. Here, the large majority of the events did not reach the number of 50 photons hitting the photodetector.[92] Comparing

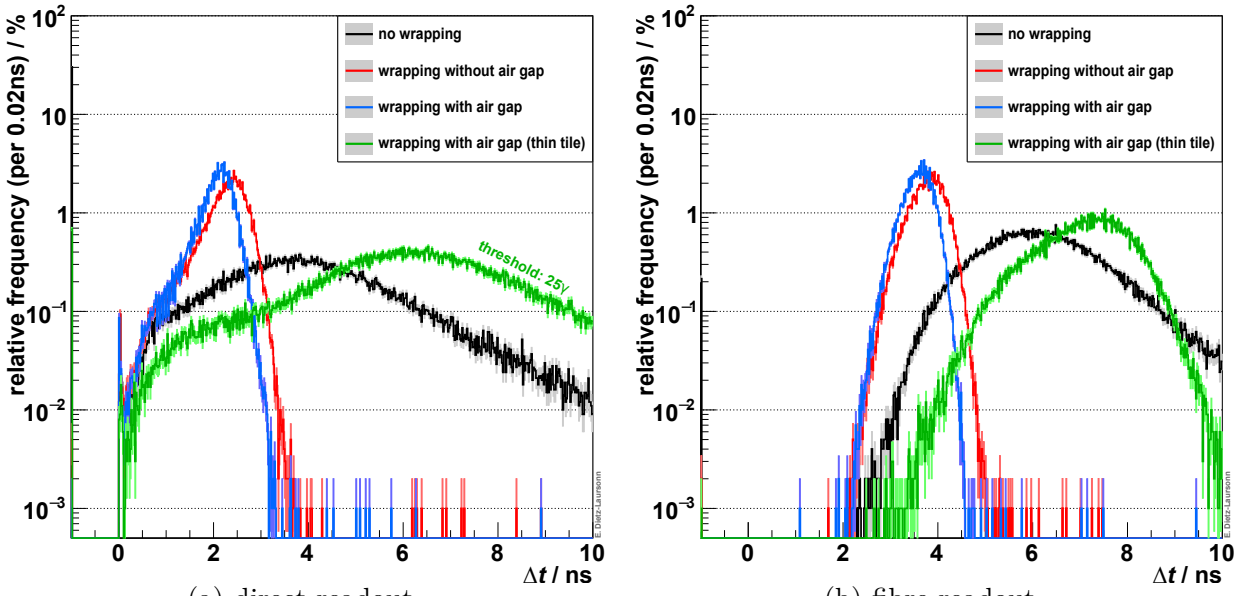

(a) direct readout (b) fibre readout

Figure 9.30.: Simulated time delay Δt between muon incidence and the corresponding signal for a threshold of 50 optical photons hitting the photodetector. In case of the thin tile with direct readout, a threshold of only 25 photons was used, as the large majority of the events did not reach the number of 50 photons hitting the photodetector. The single bin at -1 represents events in which the threshold was not reached.

[92] To allow for a rough comparison of the thin and the thick scintillator tile nevertheless, a threshold of only 25 photons was used.

wrapping with air gap and without air gap, the former leads to a slightly narrower distribution and thus to the best time resolution. Furthermore, fibre readout seems to allow for a better time resolution than direct readout.

However, in case of direct readout, there is a certain fraction of events that have significantly shorter signal delays than the other events. These are a result of particle incidences in short distances from the photodetector. In order to study the *variation of the signal delay due to the incidence position* of the muons across the scintillator tile, its surface was binned. The signal delay distribution was created for each bin and filled with the Δt of muons traversing the scintillator tile at the corresponding bin position. The mean of the distributions was then assigned to the corresponding bin of the spatial distribution. Exemplary results of detector layouts with thick scintillator tiles are presented in figure 9.31.

In case of **direct readout**, the mean signal delay is constant in the area that covers about one third of the scintillator tile and is located opposite to the photodetector position. In the other parts of the scintillator tile, it rapidly decreases with decreasing distance to the position of the photodetector. Additionally, the mean value increases with decreasing probability of the photons to hit the photodetector directly. Due to geometrical reasons, this is e.g. the case in the corners left and right of the photodetector position. For **fibre readout**, the mean signal delay is minimal for particle incidences at or very close to the position of the WLS fibre and is increasing with increasing distance. The increase is very steep next to the fibre and becomes shallower for higher distances. For detector layouts with thin scintillator tiles, the spatial distributions look like in case of thick scintillator tiles, but the signal delay is longer: a factor of about 4 for direct readout (using a threshold of only 25 photons, because of the low signal heights in this detector setup) and of about 2 for fibre readout.

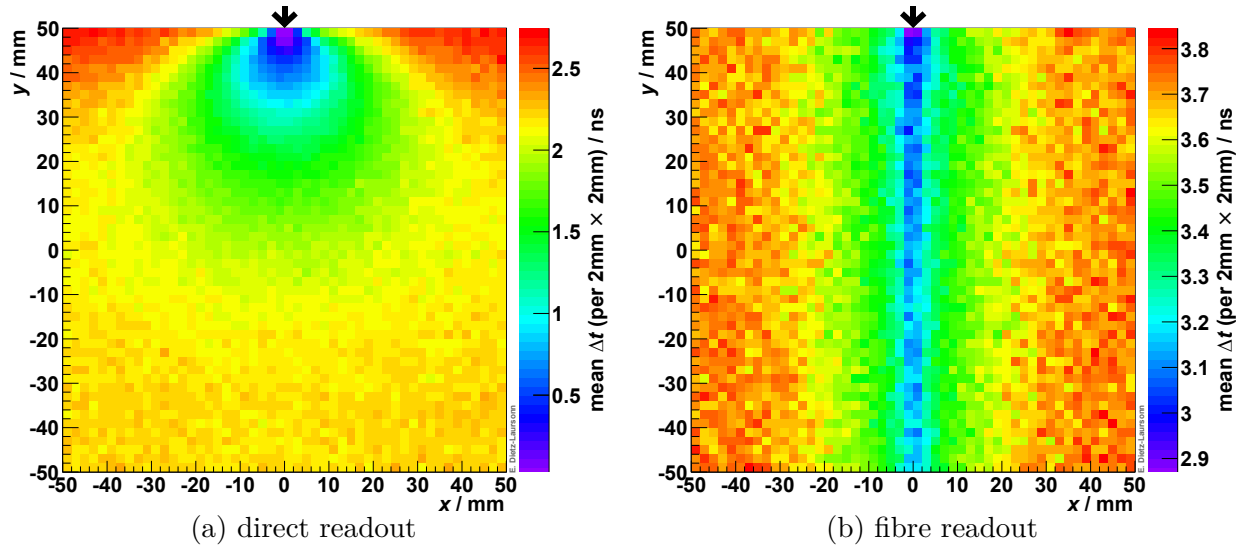

(a) direct readout (b) fibre readout

Figure 9.31.: Spatial distribution of the simulated time delay between muon transition and the corresponding signal for optical detectors with thick scintillator tiles. The x-y-plane represents the incidence position of the muons on the scintillator tile, the black arrows indicate the position of the `G4PhotonDetector` corresponding to the illustrated data in this plane. A threshold of 50 optical photons hitting the photodetectors was used to specify the beginning of the signal.

Besides on a good knowledge of the signal delay, the achievable time resolution depends on the magnitude of the variation of the signal delay. This can be determined by the *standard deviation* of the signal delay distribution. When doing this for each bin of the spatial signal delay distribution, a spatial distribution of the variation can be received. The results are illustrated in figure 9.32. For direct readout, it has the same structure as the corresponding signal delay distribution. In case of fibre readout, the distribution is predominantly plane. The characteristic values are summarised in table 9.7. Again, it is obvious that the achievable time resolution is much better for detectors with thick scintillator tiles. Additionally, it is better at the position of the photodetector or at the distant end of the fibre. The former is caused by the large number of direct hits. The latter is a result of the isotropic light emission in the WLS fibre: One half of the trapped light is traversing the fibre into each direction. The light that is going directly to the photodetector has a shorter signal delay

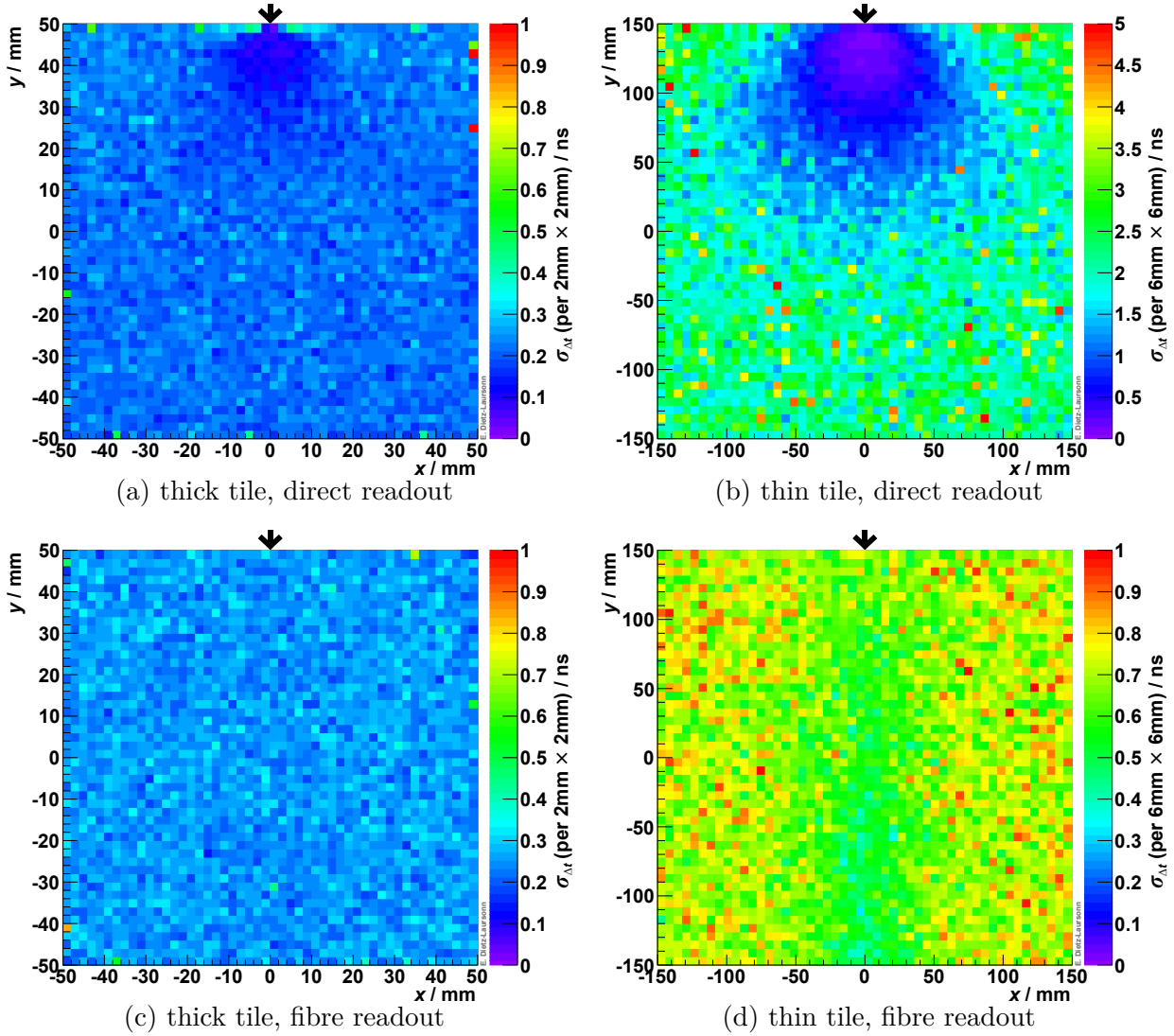

(a) thick tile, direct readout

(b) thin tile, direct readout

(c) thick tile, fibre readout

(d) thin tile, fibre readout

Figure 9.32.: Spatial distribution of the standard deviation of the simulated time delay for a threshold of 50 photons and different detector layouts. The x-y-plane represents the incidence position of the muons on the scintillator tile, the black arrows indicate the position of the `G4PhotonDetector` corresponding to the illustrated data in this plane. In case of the thin tile with direct readout, a threshold of only 25 photons was used, as the large majority of the events did not reach the number of 50 photons hitting the photodetector.

	direct readout		fibre readout	
	plane	near photodetector	plane	near fibre
thick tiles	$\sim 0.2\,\text{ns}$	$\sim 0.05\,\text{ns}$	$\sim 0.25\,\text{ns}$	$\sim 0.25\,\text{ns}$
thin tiles	$\sim 2.5\,\text{ns}$	$\sim 0.1\,\text{ns}$	$\sim 0.75\,\text{ns}$	$\sim 0.5\,\text{ns}$

Table 9.7.: Characteristic values of the simulated spatial distribution of the standard deviation of the time delay for a threshold of 50 photons. In case of the thin tile with direct readout, a threshold of only 25 photons was used, as the large majority of the events did not reach the number of 50 photons hitting the photodetector. "Plane" refers to the areas of approximately constant values, far off the fibre/photodetector.

than the light going into the other direction and being reflected at the distant fibre end before being detected. The difference decreases with decreasing distance to the distant fibre end, resulting in a smaller standard deviation.

Another important characteristic is the *pulse length* of the signal. This is especially important if the optical detector is experiencing high event rates (e.g. like the 25 ns between two bunch-crossings in case of the CMS detector at LHC). In a measurement, the pulse length of the signal can e.g. be defined as the time-over-threshold of the integrated number of detected photons. With this definition, the pulse length equals $\Delta t_{\text{end}} - \Delta t$. Here, Δt is the time delay as introduced before, i.e. the point of time when exceeding the threshold for the first time by integrating the number of photons up to this moment. Δt_{end} is the point of time when the threshold cannot be exceeded any more by integrating the number of remaining detected photons from this moment on. Thus, for the simulations, both points of time were determined in the same way (adding up the bin entries of the hit time distribution of the photons) and with the same threshold, but starting from different edges of the distribution. The resulting pulse length values were filled into histograms, which are presented in figure 9.33. The statistical uncertainty has been determined via *Poisson statistics*.

Compared to the thick detector layouts, the MPV for thin detectors is much smaller. In case of direct readout, it is even 0 ns for about two-thirds of all events (due to the very low signal height). The detector layouts with thick scintillator tiles possess larger MPV (i.e. longer pulses) but at the same time thinner distributions (i.e. lower deviations). Using fibre readout results in longer pulses, which is probably a result of the photons that are reflected at the distant fibre end (with mirrored end face) before being detected by the photodetector. Therefore, this should change when using a photodetector at each end of the fibre. All together, the pulse lengths of all the simulated detector layouts are below 20 ns (besides for few events in case of the thick detector with fibre readout).

In order to study the *variation of the pulse length due to the incidence position* of the muons across the scintillator tile, its surface was binned. The pulse length distribution was created for each bin and filled with the values of muons traversing the scintillator tile at the corresponding bin position. The mean of the distributions was then assigned to the corresponding bin. The resulting spatial distributions are presented in figure 9.34. For the **direct readout**, the mean pulse length is constant in the area that covers about one third of the scintillator tile and is located opposite to the photodetector position. In the other parts

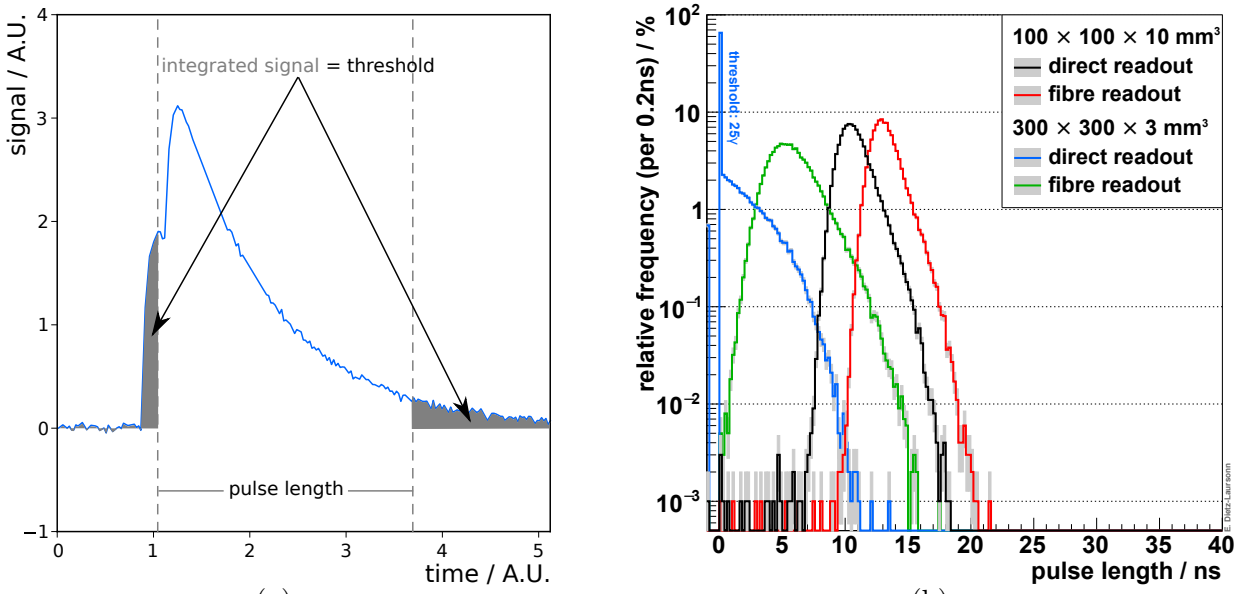

(a) (b)

Figure 9.33.: **(a):** Determination of the pulse length in the simulations, **(b):** Simulated pulse length distribution for a threshold of 50 photons and different detector layouts. In case of the thin tile with direct readout, a threshold of only 25 photons was used, as the large majority of the events did not reach the number of 50 photons hitting the photodetector. The single bin at -1 represents events in which the threshold was not reached. The bin at 0 ns also contains events for which a negative pulse length was determined, i.e. events in which the threshold was reached, but the remaining photons after Δt were not enough to exceed the threshold again.

of the scintillator tile, the pulse length increases with decreasing distance to the position of the photodetector. In case of **fibre readout**, the mean pulse length has its maximum values for particle incidences at or very close to the position of the WLS fibre and is decreasing with increasing distance. In both cases, the increase is very steep for detector layouts with thin scintillator tiles and shallower in case of detector layouts with thick scintillator tiles.

Besides the mean value of the pulse length as a function of the particle incidence position, its *standard deviation* is an important value, as it represents the magnitude of the variation of the individual values forming the mean value. Thus, a spatial distribution of the variation can be obtained by assigning the standard deviations to their corresponding bins. The results are illustrated in figure 9.35. Like for the signal delay, detectors with thick scintillator tiles allow for a better resolution of the pulse length.

As a summary, the pulse length (time-over-threshold) is longer for large signals and it is comparable for detector layouts with direct or fibre readout and is shorter for thin scintillator tiles. Although it varies across the scintillator tile (much more for direct readout than for fibre readout), it is well below 20 ns and has a standard deviation of below 1 ns to 2.5 ns.

The signal delay is comparable for thick detector layouts with direct and fibre readout. In case of thin detector layouts, the signal delay is twice as long for fibre readout and much longer for direct readout (if the threshold is exceeded at all). Besides the low signal height of thin detector layouts with direct readout, this is another reason not to use them. For the

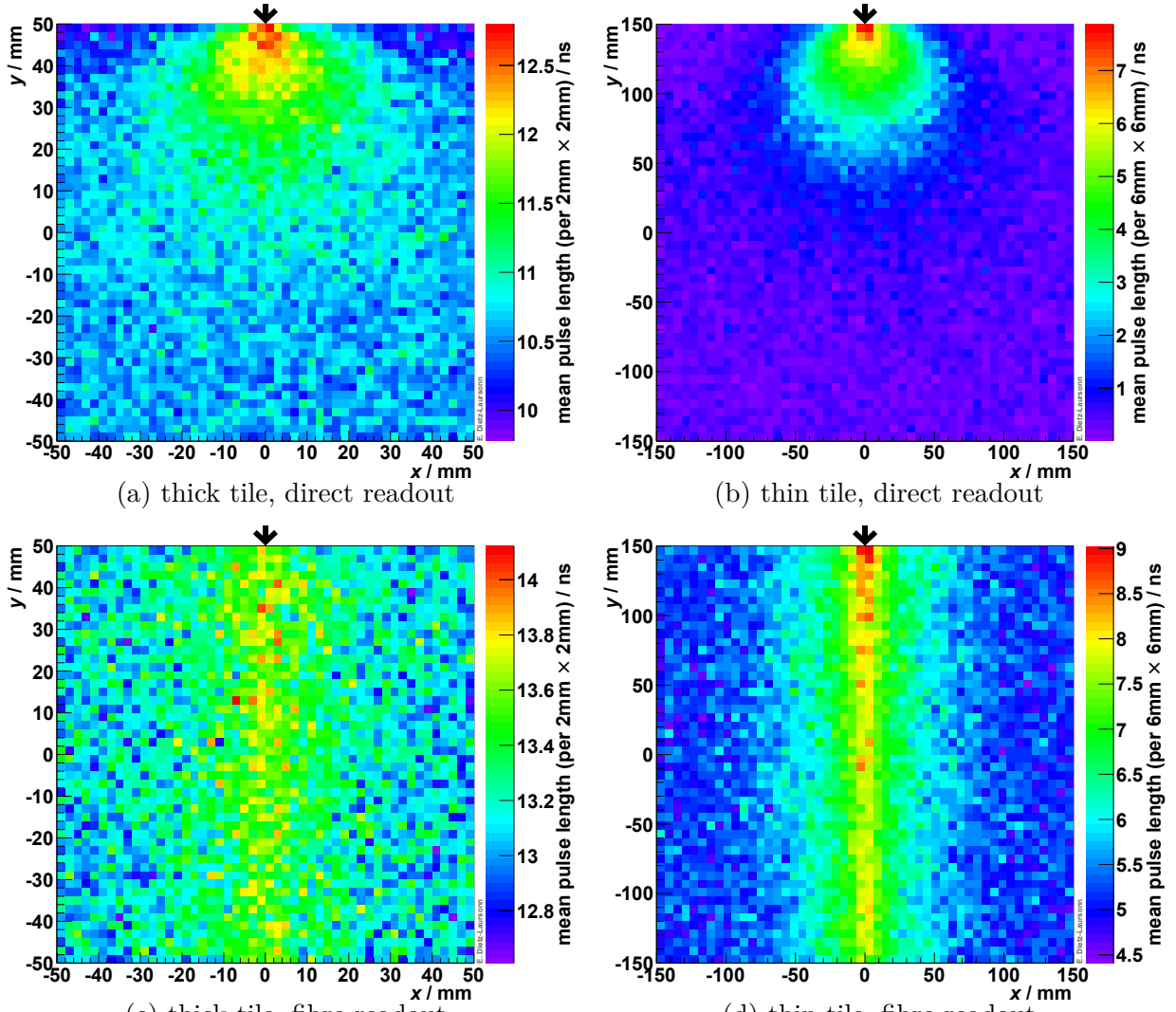

(a) thick tile, direct readout

(b) thin tile, direct readout

(c) thick tile, fibre readout

(d) thin tile, fibre readout

Figure 9.34.: Spatial distribution of the simulated pulse length for a threshold of 50 photons and different detector layouts. The x-y-plane represents the incidence position of the muons on the scintillator tile, the black arrows indicate the position of the `G4PhotonDetector` corresponding to the illustrated data in this plane. In case of the thin tile with direct readout, a threshold of only 25 photons was used, as the large majority of the events did not reach the number of 50 photons hitting the photodetector.

other layouts, the standard deviation is well below 1 ns (besides the higher standard deviation due to binning effects close to the fibre position). However, the signal delay depends on the incidence position of the particle on the scintillator tile. Using only one fibre or one directly coupled photodetector in a measurement, it is therefore not possible to determine to which extent the signal delay was influenced by the incidence position. On the other hand, the position dependence of the signal height and the signal delay might allow for an improvement of both, the position and time resolution. This could be achieved by combining the measured signal height and signal delay of at least two fibres/photodetectors.[93] In order to verify this for a certain detector layout, detailed studies on the difference between the signals of the individual photodetectors would be necessary.

[93] To get the best possible result in case of direct readout, the photodetectors should of course not be placed at the same surface of the scintillator tile.

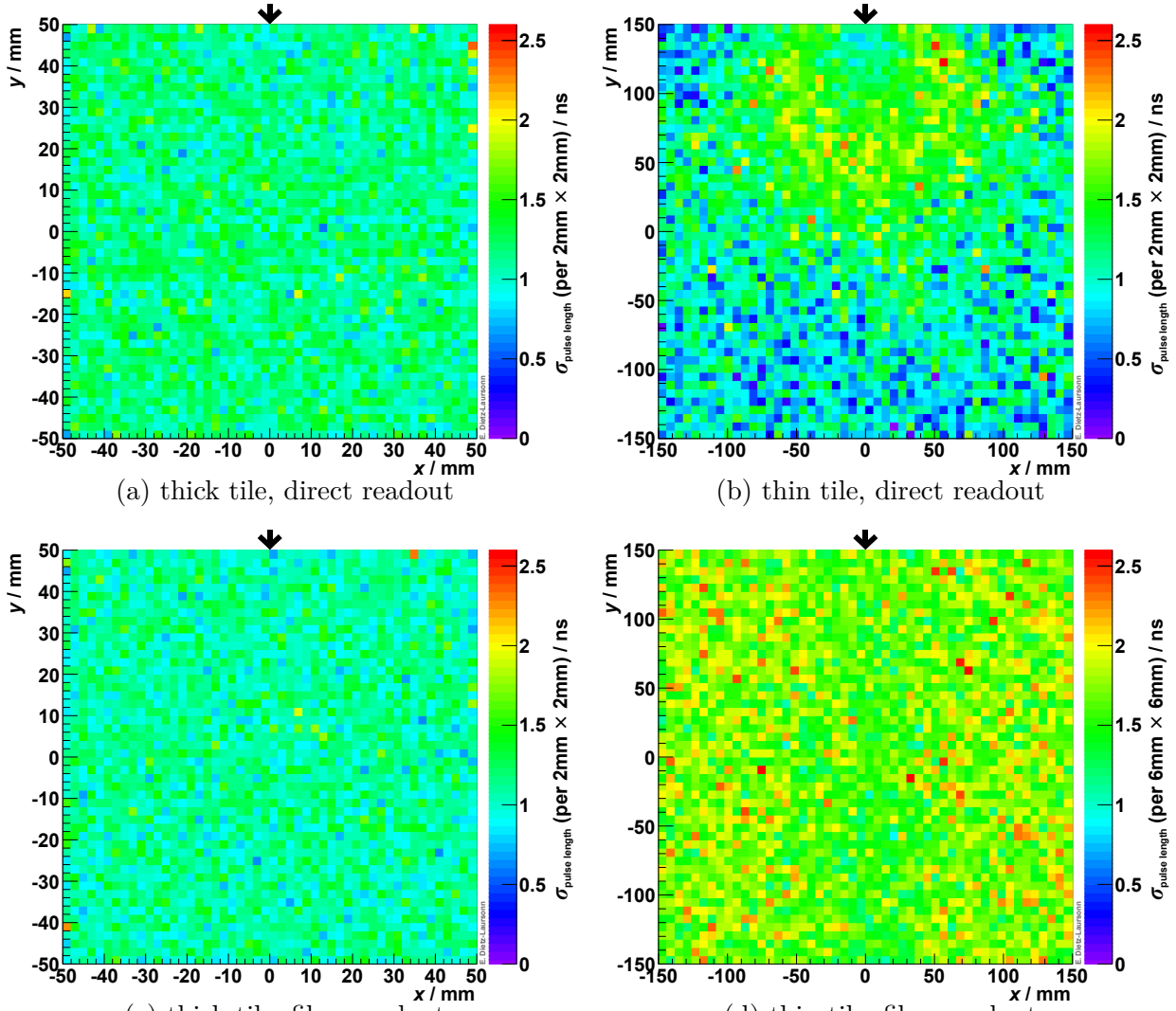

(a) thick tile, direct readout

(b) thin tile, direct readout

(c) thick tile, fibre readout

(d) thin tile, fibre readout

Figure 9.35.: Spatial distribution of the standard deviation of the simulated pulse length for a threshold of 50 photons and different detector layouts. The x-y-plane represents the incidence position of the muons on the scintillator tile, the black arrows indicate the position of the `G4PhotonDetector` corresponding to the illustrated data in this plane. In case of the thin tile with direct readout, a threshold of only 25 photons was used, as the large majority of the events did not reach the number of 50 photons hitting the photodetector.

9.4.3. Special Fibre Layouts

After the basic differences between direct and fibre readout regarding the signal height, the signal delay and the pulse length have been presented in the previous subsections, these properties will be studied in this subsection for some representative examples of special fibre layouts. For the corresponding simulations, the same materials and properties like in the previous subsection were used and only the fibre layout was varied. The results have been obtained using the same methods as described in the previous subsections. The figures 9.36 to 9.40 each show the detector layout as well as the corresponding simulation results. As the influence of the fibre layout is to be examined, only the results for detector layouts with thick scintillator tiles ($100\times100\times10\,\mathrm{mm}^3$) are presented in the figures, although they have also been performed for the thin layouts ($300\times300\times5\,\mathrm{mm}^3$). The behaviour of the detector layouts with thin scintillator tiles with respect to detector layouts with thick scintillator tiles is similar to the results described in the previous subsections. The statistical uncertainty of the signal height distributions (determined via *Poisson statistics*) has typical values of around 4 % and is not illustrated, as it does not depend on the incident position. The same applies to the standard deviation of the signal delay and of the pulse length. They have values of around 0.25 ns to 0.3 ns for the signal delay and around 1.1 ns in case of the pulse length, respectively.

The spatial distributions have the same basic features, which have been found for the detector layout with fibre readout in the previous subsection:

- The signal height has its maximum values at the position of the fibre, the value decreases with increasing distance to the fibre and the relative decrease is larger for detector layouts with thin scintillator tiles.
- The signal delay has its minimum values at the position of the fibre, the value increases with increasing distance to the fibre and the relative increase is larger for detector layouts with thin scintillator tiles.
- The pulse length is relatively constant with a slight decrease with increasing distance to the fibre, which is broader for detector layouts with thin scintillator tiles.

Additionally, some further features can be observed:

- In case of a particle incidence in regions that are surrounded by the fibre, the change of the signal height and of the signal delay with increasing distance to the fibre is smaller the more the fibre surrounds the region. As a consequence, the change is smaller on the inside of the circle-quarter in design 1 than outside. Inside the “u” of design 2 or the semi-circle of design 4, the change is even smaller (not even significant in case of the signal height).
- The same effect applies to regions in which the fibre is close to a side face of the scintillator tile. Thus, the fibre layout of design 3 (“sigma-fibre”) leads to relatively homogeneous distributions with the smallest variation across the scintillator tile.
- In case of a particle incidence in regions between two individual fibres, which are readout by separate photodetectors, the change of the signal height and of the signal

delay with increasing distance to the fibre (whose signal is examined) is steeper and the absolute change is larger. This can be observed in design 5 and especially in design 4, where the change is steeper the closer the fibres are. For particle incidences in the region on the far side of the other fibre (whose signal is not examined), the signal height or the signal delay are constant across the scintillator tile.

- The "sigma-fibre" of design 3 leads to a relatively homogeneous distribution of the pulse length, in which the fibre position cannot be identified, in contrast to the other investigated designs.
- The spatial distributions of the standard deviation show homogeneous distributions.

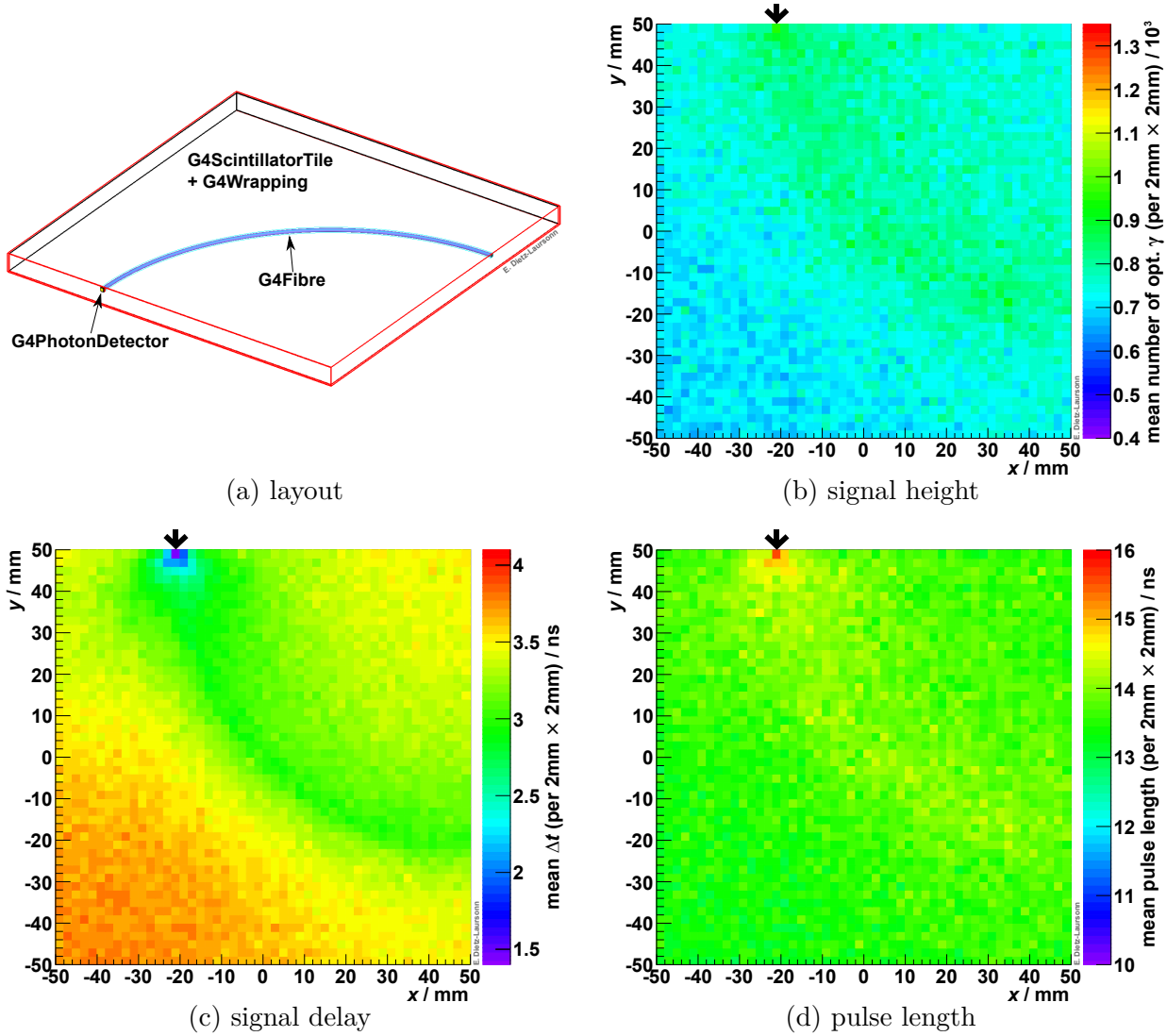

(a) layout (b) signal height

(c) signal delay (d) pulse length

Figure 9.36.: Design 1: layout and simulation results of the spatial distribution of the signal height, the signal delay, and the pulse length. The x-y-plane represents the incidence position of the muons on the scintillator tile, the black arrows indicate the position of the `G4PhotonDetector` corresponding to the illustrated data in this plane. A threshold of 50 optical photons that hit the photodetectors was used to specify the beginning of the signal as well as the pulse length.

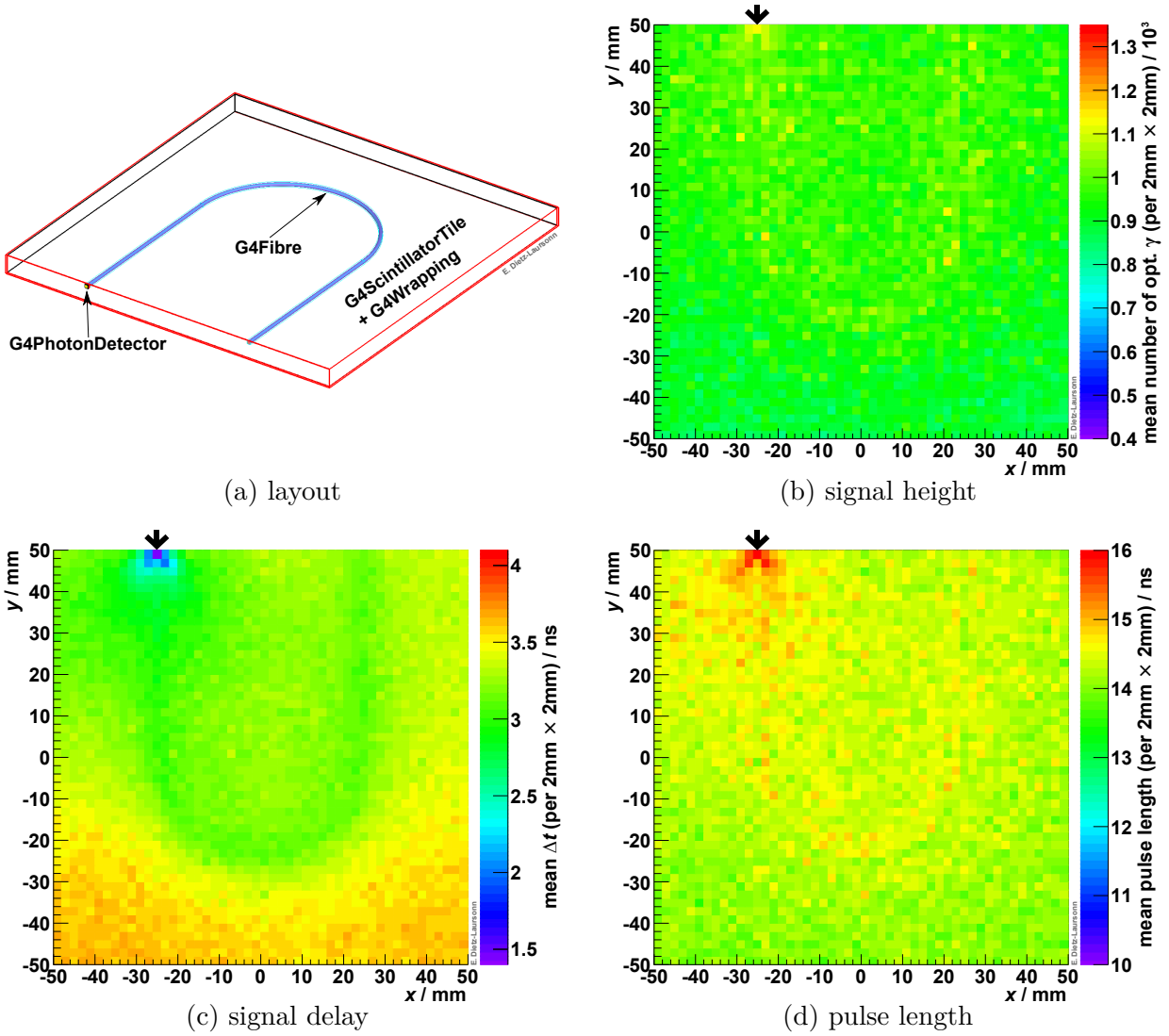

(a) layout (b) signal height

(c) signal delay (d) pulse length

Figure 9.37.: Design 2: layout and simulation results of the spatial distribution of the signal height, the signal delay, and the pulse length. The x-y-plane represents the incidence position of the muons on the scintillator tile, the black arrows indicate the position of the `G4PhotonDetector` corresponding to the illustrated data in this plane. A threshold of 50 optical photons that hit the photodetectors was used to specify the beginning of the signal as well as the pulse length.

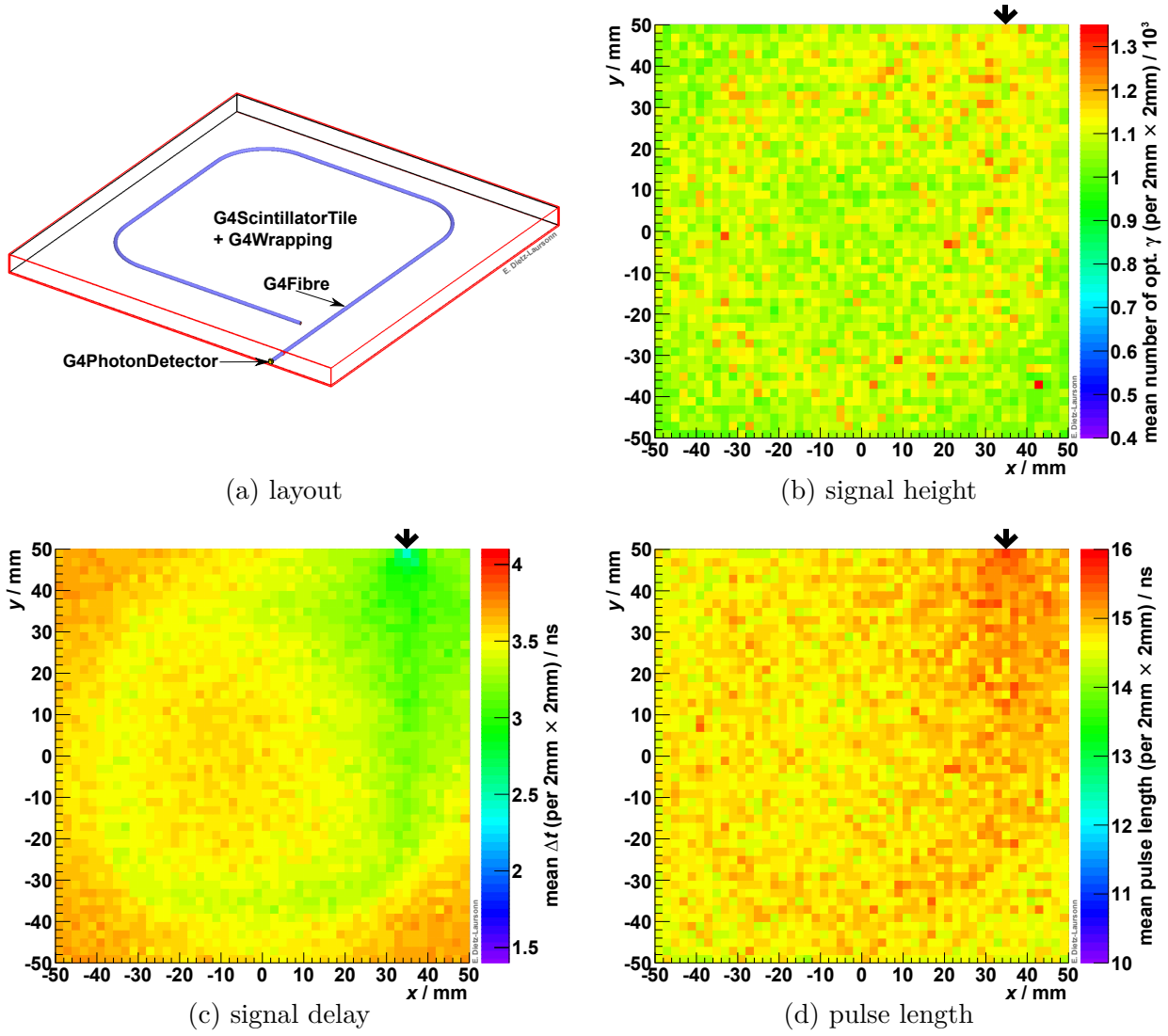

(a) layout (b) signal height

(c) signal delay (d) pulse length

Figure 9.38.: Design 3: layout and simulation results of the spatial distribution of the signal height, the signal delay, and the pulse length. The x-y-plane represents the incidence position of the muons on the scintillator tile, the black arrows indicate the position of the `G4PhotonDetector` corresponding to the illustrated data in this plane. A threshold of 50 optical photons that hit the photodetectors was used to specify the beginning of the signal as well as the pulse length.

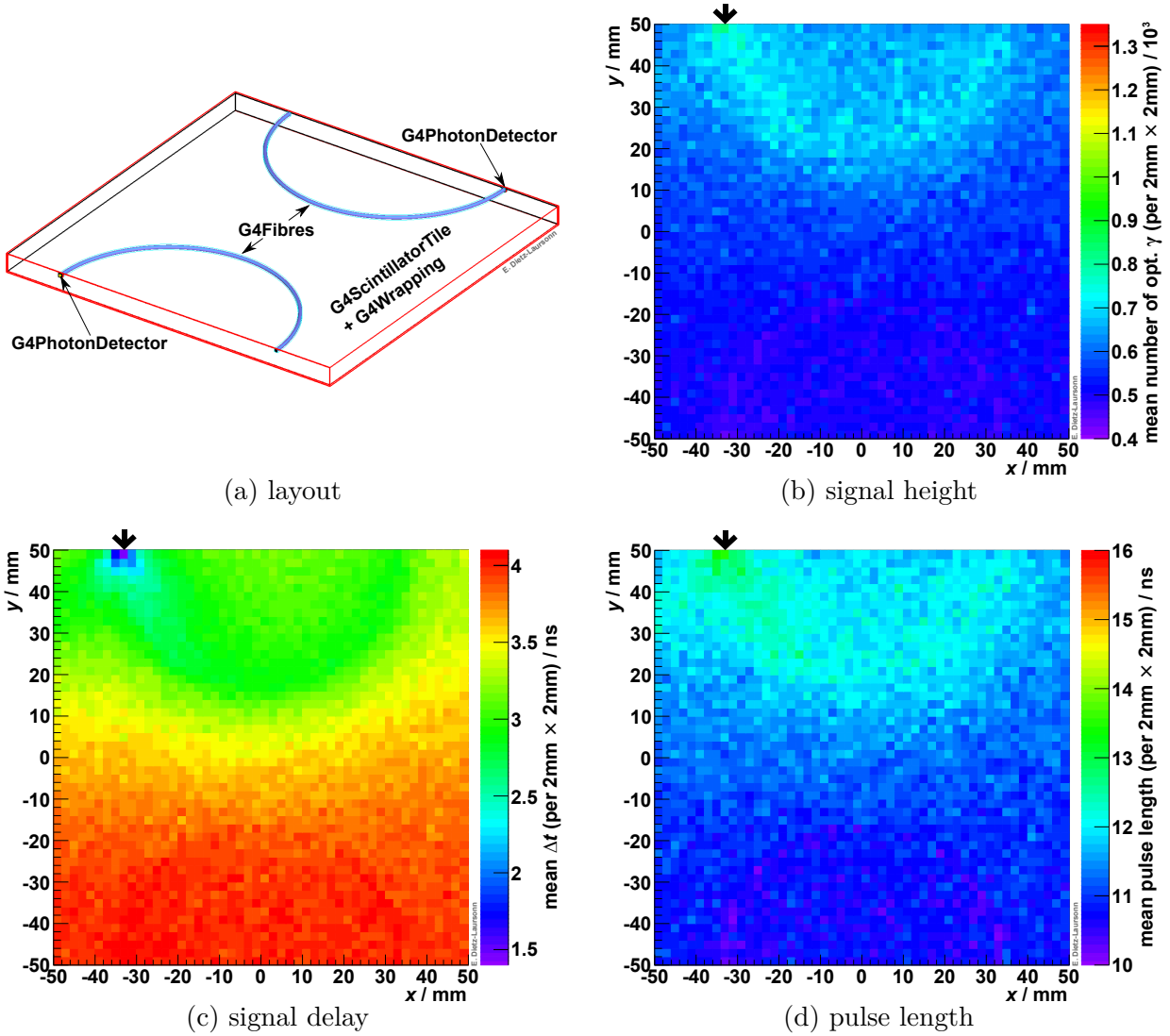

(a) layout (b) signal height

(c) signal delay (d) pulse length

Figure 9.39.: Design 4: layout and simulation results of the spatial distribution of the signal height, the signal delay, and the pulse length. The x-y-plane represents the incidence position of the muons on the scintillator tile, the black arrows indicate the position of the `G4PhotonDetector` corresponding to the illustrated data in this plane (the data of the other `G4PhotonDetector` is not illustrated, as it is mirror-symmetric to the presented data). A threshold of 50 optical photons that hit the photodetectors was used to specify the beginning of the signal as well as the pulse length.

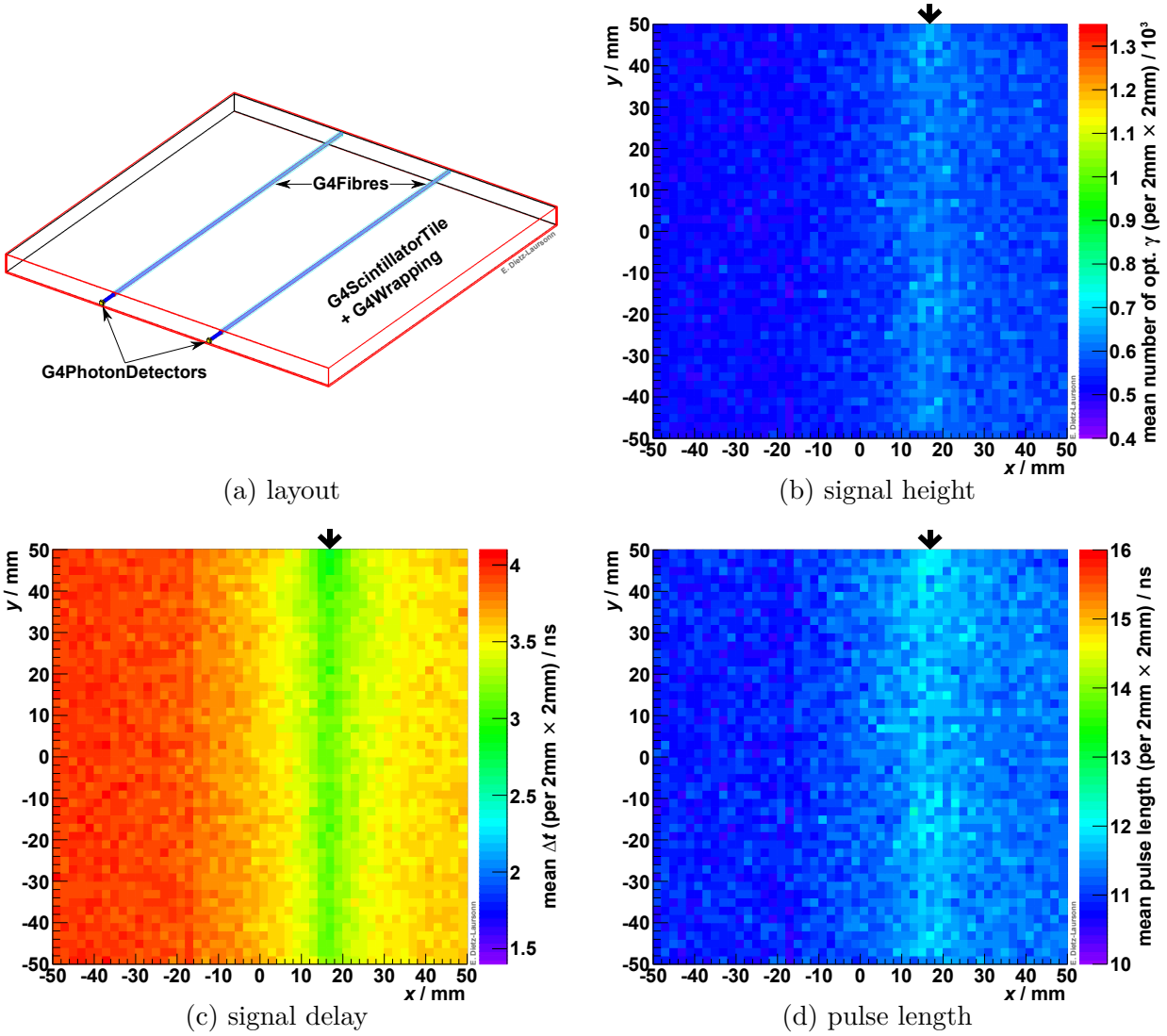

(a) layout (b) signal height

(c) signal delay (d) pulse length

Figure 9.40.: Design 5: layout and simulation results of the spatial distribution of the signal height, the signal delay, and the pulse length. The x-y-plane represents the incidence position of the muons on the scintillator tile, the black arrows indicate the position of the `G4PhotonDetector` corresponding to the illustrated data in this plane (the data of the other `G4PhotonDetector` is not illustrated, as it is mirror-symmetric to the presented data). A threshold of 50 optical photons that hit the photodetectors was used to specify the beginning of the signal as well as the pulse length.

10. Conclusion

10.1. Summary

The results of this thesis fall into three major categories, which are the creation of the GODDeSS framework, its validation, and detailed studies using GODDeSS.

First of all, the GODDeSS framework has been developed as a new extension of the Geant4 simulation framework. This was done to address the challenges and peculiarities of Geant4 with respect to the detailed simulation of optical detector components: The necessary complexity and flexibility of Geant4, which also allows for performing very detailed simulations of optical detector components, especially combinations of scintillators, optical fibres and optical photodetectors, may lead to peculiarities, which can increase the danger of incorrect simulation results due to user mistakes. This has to be avoided in order to allow for a reliable usage, also by less experienced users. Additionally, the effort that has to be invested to create or modify a detailed simulation, including detailed modelling of the optical physics, of the optical material properties and of the optical components, has to be minimised in order to allow for the fast and reliable creation of flexible simulation setups. Therefore, the creation of setups is automated as much as possible in the GODDeSS framework. New object classes allow for an easy creation of scintillator tiles, optical fibres, wrappings and paints, and photodetectors. The necessary material properties of the optical detector components are specified via easy-to-read text files. Thus, the user can create complex setups within a few lines of code and mistakes are avoided, as the peculiarities of Geant4 regarding optical physics are treated automatically by the GODDeSS framework. This makes GODDeSS an excellent approach to simplify the detailed simulations of optical detector components, which are necessary for designing and understanding the response of modern particle detectors.

The second topic combines consistency checks and comparison to manufacturer data. Much effort has been made to validate the functioning of the GODDeSS framework. On the one hand with regard to the correct operation on source code level. This includes the correct implementation of important physics processes in Geant4, the correct modelling of the optical fibres, and the correct processing of the material property input. Whereas the behaviour of most of the investigated subjects meets the expectations, some peculiarities became obvious. They were discussed in detail at the end of chapter 6. The most important results are:

- Emission spectra as well as refractive index spectra have to be specified with a high density of data points for avoiding incorrect simulation results.
- The energy range of the optical properties has to be limited to reasonable values to avoid the overestimation of the fraction of Cherenkov photons.

- Using surfaces with predefined properties from look-up tables is not recommended, due to unexpected behaviour.
- The consideration of saturation effects according to Birks' equation with respect to the light yield of scintillators is correctly implemented in Geant4, but its application requires the consideration of the measurement method of Birks' constant that is applied by the user.
- In case of "dielectric-metal" `G4OpticalSurfaces`, a modified Fresnel equation is used in Geant4 to calculate the reflectivity of the surface, which does not depend on the refractive indices of the volumes forming the surface.
- The simulation of the trapping efficiency of optical fibres as well as of the gamma ray attenuation length of the scintillators is more realistic than the values stated by the manufacturers, which are calculated using significantly limiting assumptions.

On the other hand, the functioning of the GODDeSS framework was validated by comparing simulation results with measurements. This applies to the exit characteristics of light from optical fibres as well as to the spatial signal height distribution of several complete detector prototype modules. As a consequence of the comparison of the exit characteristics, optical fibres have to be simulated with a rough surface between their outer cladding and the surroundings. The comparison of simulation and measurement of the detector prototype modules shows both, very good agreement over the full scintillator tile or large parts of it as well as some significant deviations. The latter might be explainable with possible differences between the setup used for the measurement with respect to the unrealistically accurate setup used for the simulation. These are namely, a deviating overall reflectivity of the scintillator surface in combination with its wrapping, differences as well as a limited reproducibility of the optical coupling of fibres and SiPMs, and a contamination with directly hitting photons in case of the measurements with detector prototype modules with fibre readout.

The last topic of this thesis was using the GODDeSS framework for detailed studies of the optical properties of optical fibres and of the characteristics of the response detector modules. The studies for realistic fibres show:

- The (calculated) trapping efficiency values, given by the manufacturers, are too low for round fibres but too high for square fibres. More realistic values have been determined from the simulation results.
- The signal attenuation length of square fibres is generally higher than of round fibres and neglecting the surface roughness when simulating the fibres leads to significantly lower attenuation lengths (but higher signals due to lower initial losses).
- The exit characteristics of round and square fibres features an increasing agreement for increasing air gaps with respect to the photodetector.

For the detector modules, the basic differences between direct and fibre readout as well as between large, thick and small, thin scintillator tiles was studied with respect to the three observables signal height, time delay of the signal, and pulse length. Additionally, some representative special fibre layouts were examined. The generic results are:

- For the same detector layout, the signal height is not proportional to the thickness of the scintillator tile but follows a "saturation curve". Thus, neither the usage of too

thin nor of too thick scintillator tiles makes sense and a reasonable thickness range can be determined.

- Large, thin scintillator tiles should be readout via optical fibres, because of their insufficient performance with respect to all three observables that have been investigated in case of direct readout.
- Small, thick scintillator tiles lead to more homogeneous spatial distributions of all three observables as well as a better time resolution.
- The "sigma" fibre layout shows the best results if a homogeneous response across the scintillator tile is desired.
- Using multiple fibres that are readout individually, results in an increased position dependence of the observables. Thus, combining the data of at least two fibres/photodetectors might allow for an improved resolution of the observables.

10.2. Outlook

The GODDeSS framework is publicly available [4] and can be used for the simulation of optical detector components. This has already been done in several simulation studies within Physics Institute III at RWTH Aachen University (studies of the exit characteristics of light from optical fibres [154] and on the AMD-upgrade for the Pierre Auger Observatory) as well as at the Faculty of Physics at LMU Munich (simulation studies of a position sensitive scintillation detector [167]). Additionally, there are plans to include GODDeSS directly into the Geant4 software package as an extended example of usage.

Of course, like in every newly created software framework, there is room for improvements. The two major points would be the implementation of rounded edges for square fibres into the GODDeSS framework and the improvement of the `G4Fibre` creation functions in order to reduce the usage of boolean volumes. The former point would bring the simulated square fibres nearer to the real ones, which hopefully improves the agreement between simulation and measurement. The latter point would help to reduce the computing time to create a simulated setup at the beginning of the simulation as well as the possible impact of visualisation restrictions due to boolean volumes in Geant4.

On the simulations' and measurements' side, further studies would be desirable. First of all, an extension of the hodoscope measurements in order to allow for an absolute comparison between simulation and measurement. In the scope of this, also the apparently deviating overall reflectivity of the prototype module with direct readout could be examined and the measurement could be performed before and after a renewal of the wrapping. Furthermore, an absolute measurement of the absorption spectra of WLS fibres, which strongly influences the number of created WLS photons, would be a great improvement to the relative spectra given by the manufacturers. Last but not least, the potential of improving the spatial resolution and the time resolution by combining the data of at least two individual fibres/photodetectors used for the readout of one scintillator tile should be studied.

A. Appendix: Important Quantities

symbol	equation	value and unit	quantity description
π		≈ 3.141593	ratio of a circle's circumference to its diameter
c		$= 299792458\,\mathrm{m/s}$	speed of light in vacuum
h		$\approx 6.626070 \cdot 10^{-34}\,\mathrm{J\ s}$ $\approx 4.135667 \cdot 10^{-21}\,\mathrm{MeV\ s}$	Planck constant
$\hbar$	$= \frac{h}{2\pi}$	$\approx 1.054572 \cdot 10^{-34}\,\mathrm{J\ s}$ $\approx 6.582119 \cdot 10^{-22}\,\mathrm{MeV\ s}$	reduced Planck constant
ϵ_0		$\approx 8.854188 \cdot 10^{-12}\,\mathrm{F/m}$	(absolute) permittivity of free space
α	$= \frac{e^2}{4\pi\epsilon_0\hbar c}$	$\approx 7.297353 \cdot 10^{-3}$ $\approx 1/137.035999$	fine-structure constant
m_e		$\approx 9.109383 \cdot 10^{-31}\,\mathrm{kg}$ $\approx 0.510999\,\mathrm{MeV}/c^2$	electron mass
λ_e	$= \frac{h}{m_\mathrm{e}c}$	$\approx 2.426310 \cdot 10^{-12}\,\mathrm{m}$	Compton wavelength of electrons
λ_x	$= \frac{h}{m_\mathrm{x}c}$		Compton wavelength of particle x with mass m_x
ρ	$= \frac{m}{V}$	$\frac{\mathrm{kg}}{\mathrm{m}^3}$	mass density
N_A		$\approx 6.022141 \cdot 10^{23}\,1/\mathrm{mol}$	Avogadro constant
M		$\frac{\mathrm{g}}{\mathrm{mol}}$	molar mass
A			atomic mass number
Z			atomic proton number
ω_p	$= \sqrt{N_\mathrm{A}\frac{\rho Z}{M}\frac{e^2}{\epsilon_0 m_\mathrm{e}}}$		plasma frequency of an electron gas
β	$= v/c$		ratio of a particle's velocity to the speed of light in vacuum
γ	$= 1/\sqrt{1-\beta^2}$		relativistic Lorentz factor

Table A.1.: Important quantities, which are used often within this document [1].

B. Appendix: Fibre Trapping Efficiency

The common calculation of the fibre trapping efficiency requires two *important assumptions*:

- The fibre surfaces are assumed to be *perfectly smooth*.
- The considered photons are *meridional*, i.e. their trajectory cross the fibre's axis (cf. figure 3.8).

Under these conditions, the full (i.e. considering both fibre directions) trapping efficiency can be calculated using two simple geometrical considerations:

1. The overlap between a sphere and a non-curved plane always forms a circle.
2. Every straight connection between the centre of the sphere and the circle hits the plane in the same angle α.

Therefore, the trapping efficiency $\epsilon_{\text{meridional, round}}$ for meridional photons in **round fibres** is simply twice the fraction of the surface of a sphere that is "cut off" by a plane that fulfils $\alpha = \alpha_{\text{crit}}$. In this case, the plane is parallel to the fibre's cross section and α_{crit} is the critical angle for total internal reflection. $\epsilon_{\text{meridional, round}}$ can be calculated from the full sphere surface $A_{\text{sphere}} = 4\pi R^2$ and the surface of a sphere cap A_{round} with half opening angle $\beta/2 = 90\,^\circ - \alpha_{\text{crit}}$ [168]

$$A_{\text{round}} = 2\pi R^2 \left(1 - \cos\left(\frac{\beta}{2}\right)\right) = 2\pi R^2 \left(1 - \sin\left(\alpha_{\text{crit}}\right)\right),$$

where R is the radius of the sphere. This results in a meridional trapping efficiency of

$$\epsilon_{\text{round, meridional}} = \frac{2 \cdot A_{\text{round}}}{A_{\text{sphere}}} = 1 - \sin\left(\alpha_{\text{crit}}\right). \tag{B.1}$$

For **square fibres** with **small critical angles** ($\alpha_{\text{crit}} \leq 45\,^\circ$), the same geometrical considerations can be made, but in this case, the trapping efficiency is the fraction of the surface of a sphere that remains after "cutting of" four times the sphere cap defined by a plane that fulfils $\alpha = 90\,^\circ - \alpha_{\text{crit}}$ (representing the fibre's lateral surfaces). This leads to

$$\epsilon_{\text{square, meridional, } \alpha_{\text{crit}} \leq 45\,^\circ} = 2 \cdot \cos\left(\alpha_{\text{crit}}\right) - 1. \tag{B.2}$$

In case of **larger critical angles**, equation (B.2) underestimates the trapping efficiency, as the sphere caps overlap. Thus, a different approach has to be made, which does not use these sphere caps. This leads to an integral over a surface that can be parametrised via

$$\vec{r} = \begin{pmatrix} x \\ y \\ z(x,y) \end{pmatrix} \tag{B.3}$$

The resulting surface integral (cf. [169]) is

$$A = \oiint_S \mathrm{d}S = \int_{y\in S}\int_{x\in S} \left|\frac{\partial\vec{r}}{\partial x} \times \frac{\partial\vec{r}}{\partial y}\right| \mathrm{d}x\,\mathrm{d}y \overset{(B.3)}{=} \int_{y\in S}\int_{x\in S} \sqrt{\left(\frac{\partial z(x,y)}{\partial x}\right)^2 + \left(\frac{\partial z(x,y)}{\partial y}\right)^2 + 1}\ \mathrm{d}x\,\mathrm{d}y.$$

The function $z(x,y)$ is given by the Cartesian definition of a sphere:

$$z(x,y) = \sqrt{R^2 - x^2 - y^2}$$

and results in

$$A_{\text{square}} = \int_{-d/2}^{d/2}\int_{-d/2}^{d/2} \sqrt{\frac{x^2+y^2}{R^2-x^2-y^2} + 1}\ \mathrm{d}x\,\mathrm{d}y.$$

The radius R of the sphere depends on the fibre's diameter or edge length d, respectively. It can be determined via:

$$R = \frac{d}{2\cos\left(\alpha_{\text{crit}}\right)}.$$

This integral can be solved numerically for given values of d and α_{crit}. The meridional trapping efficiency of square fibre's is then given by

$$\epsilon_{\text{meridional, square, }\alpha_{\text{crit}}>45\,^\circ} = \frac{2\cdot A_{\text{square}}}{A_{\text{sphere}}}. \tag{B.4}$$

For $\alpha_{\text{crit}} < 45\,^\circ$, the integral results in complex values, because the radius of the sphere falls below the diagonal diameter of the fibre and the parametrisation does not work. Example values for "standard" fibres are given in table B.1.

The calculated trapping efficiency values for square fibres are systematically too high (for fibres with one cladding only in case of $n_{\text{ambient}} \neq n_{\text{cladding}}$). This is due to the fact that the actual geometry of the claddings is not considered in equations (B.2) and (B.4) (cf. section 6.12 for more information). Figure B.1 summarises the trapping efficiency values calculated with the different approaches.

Additionally, also **skew photons** (i.e. photons whose trajectory does not cross the fibre's axis and which therefore has a spiral form, cf. figure 3.8) have to be taken into account. Generally, they increase the total trapping efficiency ϵ_{total} [170]. Because of the fact that in general skew photons have to traverse longer distances within the fibre material to cover the same fibre distances, their influence decreases with increasing fibre length. Thus, the actual trapping efficiency ϵ is given by $\epsilon_{\text{meridional}} \leq \epsilon \leq \epsilon_{\text{total}}$. The trapping efficiency values given by the manufacturers are only for meridional rays and thus the minimal values that can be achieved.

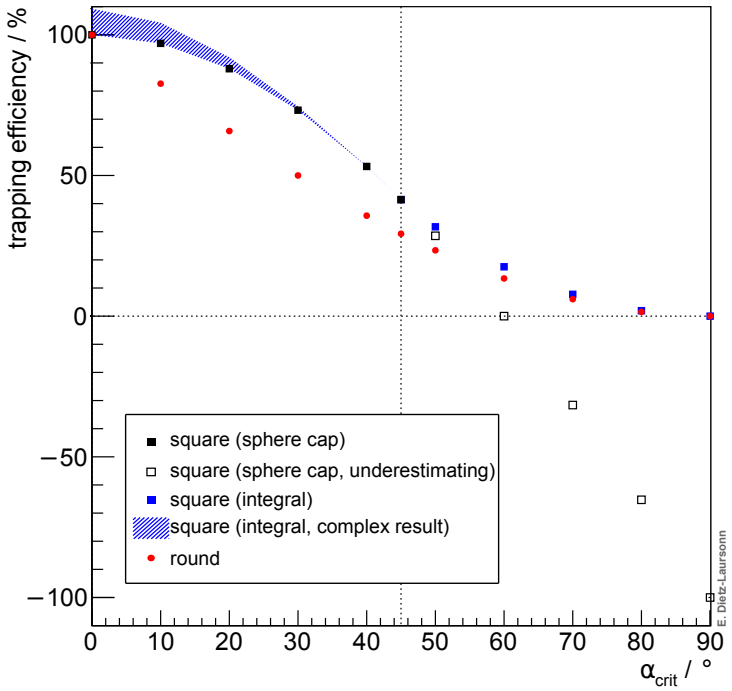

Figure B.1.: Full meridional trapping efficiency as a function of the critical angle. For $\alpha_{\text{crit}} > 45\,°$, the calculation via sphere caps underestimates the trapping efficiency because the sphere caps overlap. For $\alpha_{\text{crit}} < 45\,°$, the integral results in complex values the shaded area represents the range between the real part and the absolute value of the complex value.

	$n_{\text{ambient}} = n_{\text{clad}}$		$n_{\text{ambient}} = 1$	
	α_{crit} / °	$\epsilon_{\text{meridional}}$ / %	α_{crit} / °	$\epsilon_{\text{meridional}}$ / %
round, single-clad	68.6	6.875	38.2	37.500
round, double-clad	62.6	11.250	38.2	37.500
square, single-clad	68.6	8.866	38.2	56.125
square, double-clad	62.6	14.654	38.2	56.125

Table B.1.: Full meridional trapping efficiency values (for both fibre directions together) for "standard" fibres with $d = 1\,\text{mm}$, $n_{\text{core}} = 1.6$, $n_{\text{inner cladding}} = 1.49$, and $n_{\text{outer cladding}} = 1.42$ (only for fibres with two claddings) [153]. n_{clad} represents refractive index of the outermost cladding of the fibres. The values for $n_{\text{ambient}} = n_{\text{clad}}$ represent the extreme case when all photons entering the outermost cladding are lost (as the trapping efficiency is defined in this way, cf. subsection 3.2.3). This is reasonable, if the outermost cladding is coated with an absorbing material or if the refractive indices of the surroundings and of the outer cladding are equal (which is approximately the case for fibres that are embedded in plastic scintillators or optical glue). The other case, when photons can also be reflected at the boundary between the outermost cladding an the surroundings, is represented by the values for $n_{\text{ambient}} = 1$. Note that the calculated trapping efficiency values for square fibres - which are also used by the manufacturers - are systematically too high because of the non-consideration of the actual geometry of the claddings (for fibres with one cladding only in case of $n_{\text{ambient}} = 1$).

C. Appendix: Code Examples

This appendix summarises code examples, which illustrate some important functionalities of the Geant4 framework and the GODDeSS framework, respectively.

C.1. Geant4

Specifying optical physics options of the (before registering the optical physics class to Geant4):

```
G4OpticalPhysics* opticalPhysics = new G4OpticalPhysics();

// setting the decay time profile of the WLS process to "exponential" or "
   delta"-like (default)
opticalPhysics->SetWLSTimeProfile("exponential");

// deactivating (false) or activating (true, default) the postponed
   processing of mother particles if optical photons are created by
   different optical processes (kCerenkov, kScintillation, kWLS)
opticalPhysics->SetTrackSecondariesFirst(kScintillation, false),

// setting the rise time of the scintillation process and the WLS process
   finite values (true) or zero (false, default)
opticalPhysics->SetFiniteRiseTime(true);

// register opticalPhysics to the PhysicsList
//...
```

Specifying Birks' constant for a scintillating material:

```
G4Material* material;   // scintillator material

// create material and specify its properties
//...

// specify Birks' constant
material->GetIonisation()->SetBirksConstant(0.111*CLHEP::mm/CLHEP::MeV);
```

Specifying the reflection models for a `G4OpticalSurface` (in this example with 10 % reflection at the average (smooth) surface, 20 % reflection at a micro facet surface, 30 % back scattering, and 40 % diffuse reflection):

```
G4OpticalSurface* optSurf;

// create optSurf and specify its properties
//...

// create energy-dependent property vectors
G4double minE = 0.5*CLHEP::eV;
G4double maxE = 5.0*CLHEP::eV;

G4double spike = 0.1;
G4MaterialPropertyVector* specularspike = new G4MaterialPropertyVector();
specularspike->InsertValues(minE, spike);
specularspike->InsertValues(maxE, spike);

G4double lobe = 0.2;
G4MaterialPropertyVector* specularlobe = new G4MaterialPropertyVector();
specularlobe->InsertValues(minE, lobe);
specularlobe->InsertValues(maxE, lobe);

G4double back = 0.3;
G4MaterialPropertyVector* backscattering = new G4MaterialPropertyVector();
backscattering->InsertValues(minE, back);
backscattering->InsertValues(maxE, back);

// assign properties to optSurf
G4MaterialPropertiesTable* MPT_optSurf = new G4MaterialPropertiesTable();

// "SPECULARSPIKECONSTANT" defines the probability for reflection at the
   average surface (default is 0)
MPT_optSurf->AddProperty("SPECULARSPIKECONSTANT", specularspike);

// "SPECULARLOBECONSTANT" defines the probability for reflection at a
   micro facet surface, i.e.~the direction is smeared around the direction
    of the specular spike reflection (default is 0)
MPT_optSurf->AddProperty("SPECULARLOBECONSTANT", specularlobe);

// "BACKSCATTERCONSTANT" defines the probability of back scattering,
   caused by several reflections within a deep grove (default is 0)
MPT_optSurf->AddProperty("BACKSCATTERCONSTANT", backscattering);

// the probability of diffuse (Lambertian) reflection can not be specified
    directly but is defined via 100% = "SPECULARSPIKECONSTANT" + "
   SPECULARLOBECONSTANT" + "BACKSCATTERCONSTANT" + Lambertian (-> default
   is 1)

optSurf->SetMaterialPropertiesTable(MPT_optSurf);
```

Changing the number of segments per circle in order to solve the visualisation restrictions of round contours (GUI command):

```
/vis/viewer/set/lineSegmentsPerCircle 360
```

C.2. GOODDeSS

C.2.1. Installation and Usage

The source code presented in this subsection can also be found on [4].

Install GODDeSS and the example simulation:

1. Install Geant4 (GODDeSS is based on it):
   Geant4.9.6.p02 for GODDeSS versions before 4.0 or Geant4.10.00.p02 since version 4.0.

2. If your working environment does not have it, install `boost` [171] and `zlib` [172] (GODDeSS uses them).

3. Download the GODDeSS package [4] and extract it in your desired directory.

4. Set the environment variable `GODDESS` (the path to the directory in which you extract the package):

```
export GODDESS="/absolute/path/to/GODDESS-directory"
```

5. Create a `build` directory (usually `$GODDESS/build`) and change into it:

```
mkdir -p path/to/BUILD-directory
cd path/to/BUILD-directory
```

6. Set the environment variables of your Geant4 version:

```
source path/to/Geant4-directory/bin/geant4.sh
```

7. Use `cmake` to compile the source code:

```
cmake $GODDESS/source
make -j install
```

Run the example simulation with default/individual settings:

1. Set the environment variables of your Geant4 version:

```
source path/to/Geant4-directory/bin/geant4.sh
```

2. Set the GODDeSS environment variables (`GODDESS` is the path to the directory in which you untared the package, `BUILDDIR` is usually `$GODDESS/build`):

```
export GODDESS="/absolute/path/to/GODDESS-directory"
export SIMDIR="$GODDESS/source/Simulation"
export BUILDDIR="/absolute/path/to/BUILD-directory"
```

3. Change to the `source` directory:

```
cd $GODDESS/source
```

4. For individual settings, edit the `RunSimulation` script and save the changes. (The predefined setups as well as the primary particles and their properties can easily be changed by editing the files `$SIMDIR/src/ Preparation/DetectorConstruction.cc` and `$SIMDIR/macros/GeneralParticle- Source.mac`, respectively.)

5. Start the simulation using the `RunSimulation` script (a new window will open):

```
./RunSimulation.sh
```

6. To shoot a minimum ionising muon into the scintillator tiles (default), do:

```
/run/beamOn
```

Implement the GODDeSS object classes into your own simulation:

1. Install GODDeSS as described above (including the environment variables).

2. Link GODDeSS to your simulation in your `CMakeLists.txt` (which is creating the simulation executable):
   a) In the beginning, add:

```
#------ Boost ------#
# Find Boost package
find_package(Boost REQUIRED regex)

# Add include directories to the list of directories searched by the
    compiler for include files:
include_directories(${Boost_INCLUDE_DIRS})

# Set Boost library list
set(LIBS_BOOST boost_regex)

#------ zlib ------#
# Find zlib package
find_package(ZLIB REQUIRED)

# Add include directories to the list of directories searched by the
    compiler for include files:
include_directories(${ZLIB_INCLUDE_DIRS})

# Set zlib library list
set(LIBS_ZLIB ${ZLIB_LIBRARIES})

#------ GODDeSS ------#
# Locate GODDeSS
set(GODDESS_LIB_DIR $ENV{GODDESS}/build/G4BasicObjects/*/)
find_library(G4PropertyFileReadInTools NAMES
    G4PropertyFileReadInTools HINTS "${GODDESS_LIB_DIR}")
find_library(G4Scintillator NAMES G4Scintillator HINTS "${
    GODDESS_LIB_DIR}")
find_library(G4Fibre NAMES G4Fibre HINTS "${GODDESS_LIB_DIR}")
find_library(G4GeneralParticleSource NAMES G4GeneralParticleSource
    HINTS "${GODDESS_LIB_DIR}")
find_library(G4PhotonDetector NAMES G4PhotonDetector HINTS "${
    GODDESS_LIB_DIR}")
```

```
find_library(DataProcessing NAMES DataProcessing HINTS "${
    GODDESS_LIB_DIR}")
set(LIBS ${G4PropertyFileReadInTools} ${G4Scintillator} ${G4Fibre} ${
    G4GeneralParticleSource} ${G4PhotonDetector} ${DataProcessing})

# Add include directories to the list of directories searched by the
    compiler for include files:
set(GODDESS_INCLUDE_DIR $ENV{GODDESS}/source/G4BasicObjects/)
include_directories(${GODDESS_INCLUDE_DIR}/G4PropertyFileReadInTools/
    include)
include_directories(${GODDESS_INCLUDE_DIR}/G4Scintillator/include)
include_directories(${GODDESS_INCLUDE_DIR}/G4Fibre/include)
include_directories(${GODDESS_INCLUDE_DIR}/G4GeneralParticleSource/
    include)
include_directories(${GODDESS_INCLUDE_DIR}/G4PhotonDetector/include)
include_directories(${GODDESS_INCLUDE_DIR}/DataProcessing/include)
```

b) After your simulation executable has been specified, add:

```
target_link_libraries(${PROJECT_NAME} ${LIBS_BOOST} ${LIBS_ZLIB} ${
    LIBS_GODDESS})
add_dependencies(${PROJECT_NAME} ${LIBS_GODDESS})
```

3. Implement GODDeSS in your simulation's main file (which sets up the Geant4 framework):
   a) In the beginning of your main file, add:

```
#include <GODDeSS_Messenger.hh>
#include <ScintillatorTileConstructor.hh>
#include <FibreConstructor.hh>
#include <PhotonDetectorConstructor.hh>
```

   b) In the beginning of your `main()` function, add:

```
// GODDeSS: energy range for the property distributions
vector<G4double> energyRangeVector;
G4double energyRangeVectorSize = 10;
for(int i = 0; i < energyRangeVectorSize; i++) energyRangeVector.
    push_back( energiesMin + i * (energiesMax - energiesMin) / (
    energyRangeVectorSize - 1) );

// GODDeSS Messenger:
GODDeSS_Messenger* goddessMessenger = new GODDeSS_Messenger(
    energyRangeVector);
```

   c) Pass the goddessMessenger to all parts of your simulation, where it is needed, e.g. like:

```
DetectorConstruction* detectorConstruction = new DetectorConstruction
    (/*other parameters...,*/ goddessMessenger);
RunAction* run_action = new RunAction(/*other parameters...,*/
    goddessMessenger);
EventAction* event_action = new EventAction(/*other parameters...,*/
    goddessMessenger);
```

d) After your physicsList (G4VModularPhysicsList*) has been created (but before it is initialised by SetUserInitialization(physicsList)), add:

```
// GODDeSS Constructors:
ScintillatorTileConstructor* scintillatorTileConstructor = new
    ScintillatorTileConstructor(physicsList, goddessMessenger->
    GetPropertyToolsManager(), goddessMessenger->GetDataStorage(),
    SearchOverlaps);

goddessMessenger->SetScintillatorTileConstructor(
    scintillatorTileConstructor);

FibreConstructor* fibreConstructor = new FibreConstructor(physicsList
    , goddessMessenger->GetPropertyToolsManager(), goddessMessenger->
    GetDataStorage(), SearchOverlaps);

goddessMessenger->SetFibreConstructor(fibreConstructor);

G4String hitFile = path/to/file/which/the/hitting/photons/should/be/
    saved/in;

goddessMessenger->GetDataStorage()->SetPhotonDetectorHitFile(hitFile)
    ;

PhotonDetectorConstructor* photonDetectorConstructor = new
    PhotonDetectorConstructor(physicsList, goddessMessenger->
    GetPropertyToolsManager(), goddessMessenger->GetDataStorage(),
    SearchOverlaps);

goddessMessenger->SetPhotonDetectorConstructor(
    photonDetectorConstructor);
```

e) At the end of your main() function, add:

```
// GODDeSS
delete goddessMessenger;
delete scintillatorTileConstructor;
delete fibreConstructor;
delete photonDetectorConstructor;
```

4. Implement the goddessMessenger as parameter in the constructors of all parts of your simulation, where it is needed, and pass it to a class variable, e.g. like:

```
RunAction(/*other parameters...,*/ GODDeSS_Messenger*
    goddessMessenger)
: Messenger(goddessMessenger)
{
//...
}
```

```
EventAction(/*other parameters...,*/ GODDeSS_Messenger*
    goddessMessenger)
: Messenger(goddessMessenger)
{
//...
}
```

```
SteppingAction(/*other parameters...,*/ GODDeSS_Messenger*
    goddessMessenger)
: Messenger(goddessMessenger)
{
//...
}
```

```
DetectorConstruction(/*other parameters...,*/ GODDeSS_Messenger*
    goddessMessenger)
: Messenger(goddessMessenger)
{
//...
}
```

5. Implement the goddessMessenger in all parts of your simulation, where it is needed, e.g. like:
   a) In the function RunAction::BeginOfRunAction(const G4Run* aRun), add:

```
// write the RunID to the hit files of the G4PhotonDetectors
Messenger->GetPhotonDetectorConstructor()->WriteRunIDToHitFile(aRun->
    GetRunID());
```

   b) In the function EventAction::BeginOfEventAction(const G4Event* theEvent), add:

```
// write the EventID to the hit files of the G4PhotonDetectors
Messenger->GetDataStorage()->GetPhotonDetectorConstructor()->
    WriteEventIDToHitFile(theEvent->GetEventID());
// clean the GODDeSS_DataStorage from recorded data of the previous
    event
Messenger->GetDataStorage()->clean();
```

   c) In the function EventAction::EndOfEventAction(const G4Event* theEvent), implement processing of the recorded data, e.g.:

```
// get the time from the GODDeSS_DataStorage, when the particle with
    ID "iter" hit the scintillator
G4double scintillatorHitTime = Messenger->GetDataStorage()->
    GetScintillatorHitTime(iter);
```

   d) In the function SteppingAction::UserSteppingAction(const G4Step* theStep), add:

```
G4Track* theTrack = theStep->GetTrack();

// for optical photons, temporally save the data of this step (This
    is necessary, as it is not possible to retrieve the data of a
    previous step. If a photon hits a G4PhotonDetector, it is possible
     to write the photon data of the step before the hit into the hit
    file, when using the temporally saved data.)
if(theTrack->GetDefinition() == G4OpticalPhoton::
    OpticalPhotonDefinition()) Messenger->GetDataStorage()->
    SavePreviousStepOpticalPhotonData(theStep);
```

e) In the DetectorConstruction, add:

```
#include <ScintillatorTileConstructor.hh>
#include <FibreConstructor.hh>
#include <PhotonDetectorConstructor.hh>
```

f) In the function of the DetectorConstruction that defines the setup, add (to be able to use the GODDeSS object constructors):

```
ScintillatorTileConstructor* STConstructor = goddessMessenger->
    GetScintillatorTileConstructor();
FibreConstructor* FConstructor = goddessMessenger->
    GetFibreConstructor();
PhotonDetectorConstructor* PDConstructor = goddessMessenger->
    GetPhotonDetectorConstructor();
```

C.2.2. How To

Collecting and accessing simulation data:

- Collecting data, e.g. in the sensitive detector of the G4PhotonDetector:

```
// obtain data
//...

// pass data to the GODDeSS data storage
GODDeSS_Messenger->GetDataStorage()->SetPhotonDetectorHitPoint(G4int
    trackID, G4ThreeVector photonDetectorHitPoint);
```

- Accessing data, e.g. in the EventAction:

```
G4ThreeVector photonDetectorHitPoint = GODDeSS_Messenger->
    GetDataStorage()->GetPhotonDetectorHitPoint(G4int trackID);

// process data
//...
```

Defining material properties in property files:

- Comments can be inserted using "#".
- Constant properties:
  - Without units: "*key* = *value*" or "*key* : *value*".
  - With units: "*key* = *value* * *unit*" or "*key* : *value* * *unit*".
- Energy-dependent properties (tables):
  - The table beginning has to be specified like: "*table key* = tabular" or "*table key* : tabular".
  - The columns have to be specified in the first line of the table via "*column key*" or "*column key* / *unit*", respectively.
  - The entries of the columns in each line have to be separated by tabs or blanks.

  - The tables have to be sorted by energy in ascending order.

- Examples:

```
# constant properties:

#density
density:        0.36 * g/cm3
# roughness (width of the Gaussian distribution describing the
    distribution of the angle between average surface normal and micro
    -facet normals)
roughness:      3.5 * deg
# reflectivity
reflec:         98. * %
# refractive index
n_ref:          1.5
# attenuation length
mu_att:         0.01 * mm
# decay time
t_decay:        1.8 * ns
#Birks' constant
birks_constant:    0.111 * mm/MeV
```

```
# tables / energy-dependent properties:

# chemical components:
chemical_components: tabular
element  mass_fraction / %
Hydrogen 8.4
Carbon   91.6

# relative light output distribution:
epsilon: tabular
energy / eV     epsilon / %
2.477612466     1.71164
2.4817932743    1.70713
...
3.2502028359    4.92236
3.2537938432    4.27909
```

Changing the way how reflected optical photons are treated in by the `SensitiveDetector` of the `G4PhotonDetector` in GODDeSS:
By default, all optical photons that hit the `SensitiveDetector` are detected and "killed" (i.e. there is effectively no reflection). This behaviour changes if the third line of the following example code is uncommented inside the source code of the `G4PhotonDetector`'s `SensitiveDetector`. In this case, optical photons are neither detected nor "killed", if they are reflected at the surface of the `SensitiveDetector`.

```
1 // if optical photon was reflected at the surface of the sensitive
     detector (and if reflected optical photons are not to be counted),
     stop here (but do not kill it...)
2 // but then also the material properties (especially the refractive
     index) of the sensitive detector volume have to be defined
     correctly!!!
3 if(theStep->GetPostStepPoint()->GetPhysicalVolume() !=
     photonDetectorThatWasHit) return true;
```

Creating setups using the GODDeSS object constructors:

```
//---------- scintillator tile ----------//
G4ThreeVector ScintiDimensions = G4ThreeVector(100.*CLHEP::mm, 10.*CLHEP::
    mm, 100.*CLHEP::mm);

STConstructor->SetScintillatorTransformation(G4Transform3D(
    G4RotationMatrix(), G4ThreeVector(0., 50.*CLHEP::mm, 0.));
STConstructor->SetScintillatorName("scintillator");
STConstructor->ConstructASensitiveDetector();
G4ScintillatorTile* scintillator = STConstructor->ConstructScintillator(
    ScintiDimensions, path/to/scintillator/property/file, pointer-to-
    physical-world-volume);

///---------- fibre ----------///
G4ThreeVector FibreEndPoint = G4ThreeVector(0., 0., ScintiDimensions [2] /
     2. + 5.*CLHEP::mm);
G4ThreeVector FibreStartingPoint = G4ThreeVector(0., 0., -ScintiDimensions
     [2] / 2.);

FConstructor->SetFibreStartingPointReflective(0.98);
G4Fibre* fibre = FConstructor->ConstructFibre(path/to/fibre/property/file,
     scintillator->GetScintillator_physicalVolume(), FibreStartingPoint,
    FibreEndPoint);

///---------- SiPM ----------///
PDConstructor->SetPhotonDetectorName("SiPM");
PDConstructor->SetPhotonDetectorReferenceVolume(fibre->
    GetOutermostVolumeOutsideMother_physicalVolume());
PDConstructor->SetSensitiveSurfaceNormalRelativeToReferenceVolume(
    G4ThreeVector(0., 0., - 1.));
PDConstructor->SetSensitiveSurfacePositionRelativeToReferenceVolume(
    G4ThreeVector(0., 0., fibre->GetFibreLength() / 2.));
PDConstructor->ConstructPhotonDetector(edgeLength, pointer-to-physical-
    world-volume);

//---------- external reflector / wrapping ----------//
STConstructor->SetWrappingName("wrapping");
STConstructor->ConstructWrapping(scintillator, path/to/wrapping/property/
    file);
```

Using the GODDeSS property tools to define the properties of your own volumes, e.g. like:

- Create energy dependent distribution from a constant value:

```
#include <PropertyToolsManager.hh>
#include <Properties.hh>

G4MaterialPropertyVector* refractiveIndex_Vacuum = goddessMessenger->
    GetPropertyToolsManager()->GetPropertyDistribution(1.);
```

- Get properties from a file:

```
#include <PropertyToolsManager.hh>
#include <Properties.hh>
```

```
Properties AirProperties.load(path/to/air/property/file);

G4double density_air = AirProperties.getNumber("density");

Properties::tabular chemicalComponents_air = AirProperties.getTabular
    ("chemical_components");
G4Material* Material_air = new G4Material("Mat_air", density_air, (
    int) chemicalComponents_air["element"].size());
PropertyTools->AddElementsFromTable(Material_air,
    chemicalComponents_air);

G4MaterialPropertyVector* attenuationLength_air = PropertyTools->
    GetPropertyDistribution(AirProperties, "mu_att");
```

D. Appendix: Implementation of Material Properties

In this appendix, the elements and materials are listed, which have been used in the simulations in the scope of this thesis. Additionally, the used properties of the elements and materials as well as the realisation of these properties in the simulations are described. Furthermore, the physics processes, which have been considered in the simulations, will be listed.

D.1. Elements

The following table summarises the elements, which have been used in the scope of this thesis. Their properties have been taken from [55]. All materials used for the simulations consist of combinations of these elements.

	Z	A / g/mol		Z	A / g/mol
hydrogen (H)	1	1.00794	fluorine (F)	9	18.9984032
carbon (C)	6	12.0107	aluminium (Al)	13	26.9815386
nitrogen (N)	7	14.0067	titanium (Ti)	22	47.867
oxygen (O)	8	15.9994	lead (Pb)	82	207.2

D.2. Materials

- If not stated differently, **all optical properties** have been specified for an **energy range between 1 eV and 7 eV** in the scope of this thesis.[94] If a given property spectrum does not cover this energy range, it is extended by linear extrapolation of the two outermost data points at the affected edge of the spectrum.
- **Vacuum:**
  Vacuum has been used for the surroundings of the actual simulation setup. It has been implemented in the common Geant4-definition:

Z	A / g/mol	ρ / g/cm^3	T / K	p / Pa
1	1.01	10^{-25}	0.1	10^{-19}

Table D.1.: The material properties of vacuum as defined in the simulations.

[94] This also limits the creation of Cherenkov radiation to this energy range.

- **Air:**
  As an alternative to vacuum, air has been introduced, using the properties that are summarised in table D.2. The *refractive index* spectrum has been taken from [173] and is illustrated in figure D.1.

chemical components (mass fraction)	ρ / kg/m^3	μ_{att} / m
nitrogen (76 %), oxygen (24 %)	1.225*	1000×

* This corresponds to dry air at 1013.25 hPa and 15 °C [174].
× This is a rough estimation for high transparency, the value is two magnitudes higher than the diameter of the simulated setups.

Table D.2.: The material properties of air in the simulations.

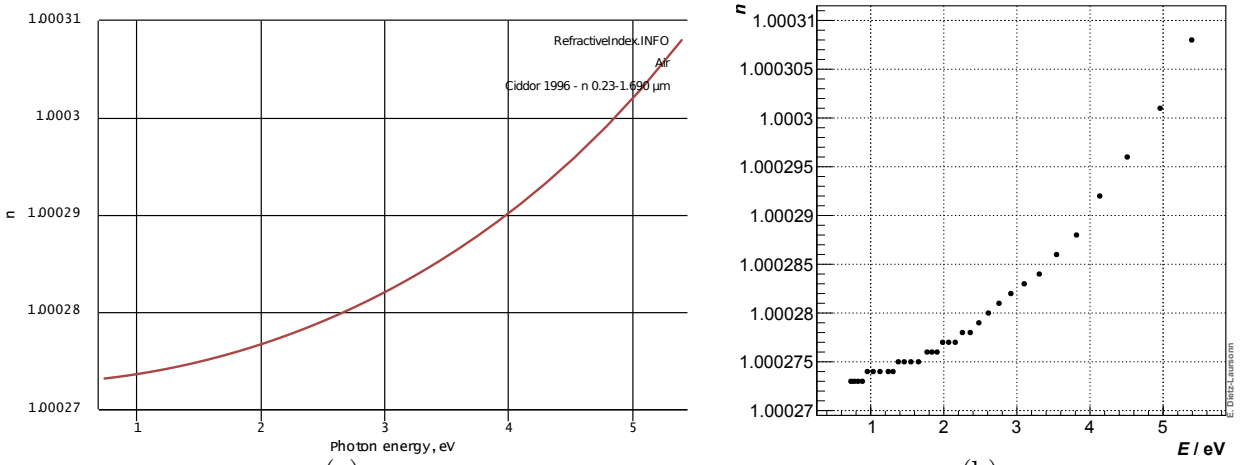

(a) (b)

Figure D.1.: Refraction index of air as function of the photon energy: diagram from [173] **(a)** and values used for the simulations **(b)**.

- **Scintillators (BC-404, BC-408, and BC-452):**
  BC-404, BC-408, and BC-452 are scintillators from Saint-Gobain. BC-452 is loaded with 2 %, 5 %, or 10 % lead (mass fraction). As its emission spectrum, refractive index, and decay time equal the corresponding properties of BC-408, it is reasonable to assume that BC-452 is a lead-loaded version of BC-408. Therefore, properties of BC-452, which are not explicitly specified by the manufacturer, have been adopted from BC-408. Table D.3 summarises the properties of all three scintillators.

  The relative *emission spectra* of BC-404 and BC-408 are illustrated in figure D.2. The spectrum of BC-452 is equal to the spectrum of BC-408 and is, therefore, not illustrated. The manufacturer data was digitised with [177]. In order to avoid unexpected effects at the edges of the wavelength ranges that are covered by the manufacturer data, the spectra have been extended linearly. For this purpose, the slope has been determined at the edges of the original spectra. As emission spectra are not interpolated by a straight line between two points of the spectrum within Geant4 (cf. subsection 4.2.7 and section 6.1), the linear extensions have been formed of several data points (instead of single points where the emission reaches zero).

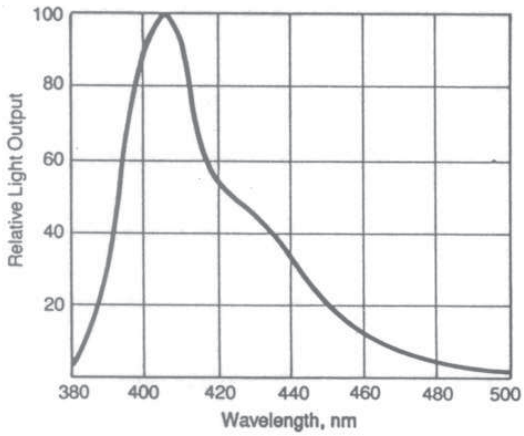

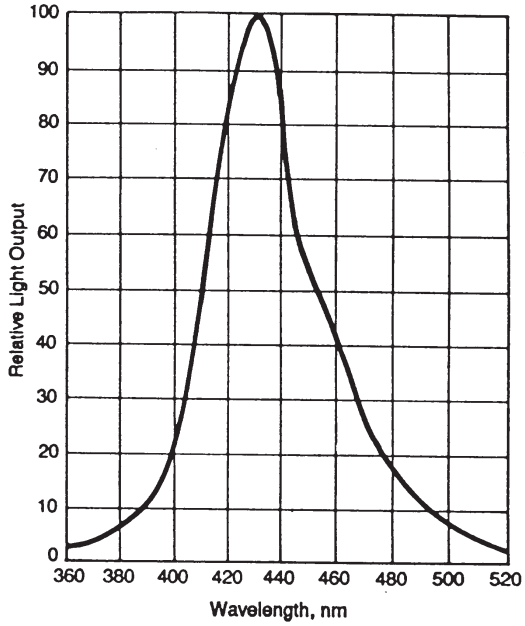

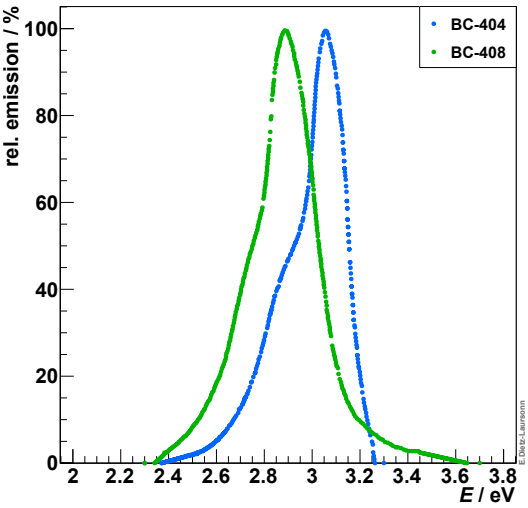

Figure D.2.: Relative emission spectra of BC-404, BC-408: manufacturer data [175] of BC-404 **(top)** and BC-408 **(middle)**, values used for the simulations **(bottom)**.

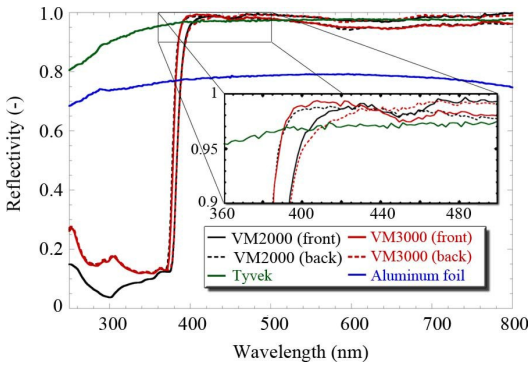

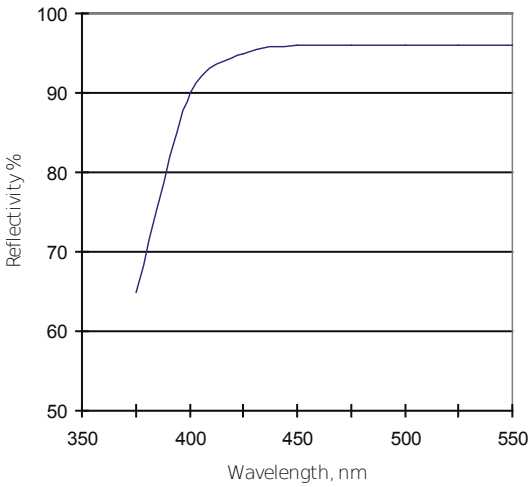

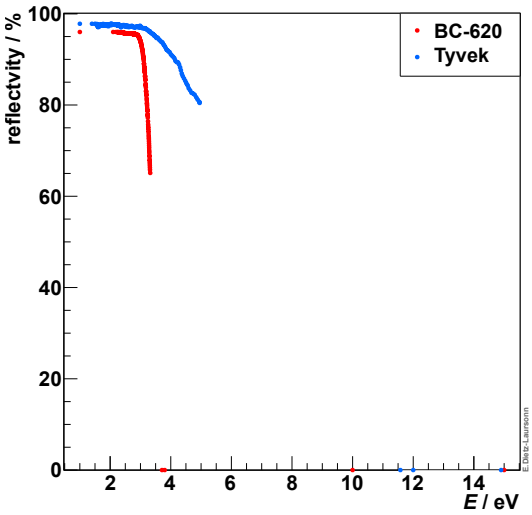

Figure D.3.: Reflectivity spectra of Tyvek and BC-620: diagram for Tyvek [178] **(top)**, manufacturer data of BC-620 [179] **(middle)**, and values used for the simulations **(bottom)**.

	BC-404 [175]	BC-408 [175]	BC-452 [150]		
			2% Pb	5% Pb	10% Pb
H: mass fraction / %*	8.4	8.5	8.33	8.075	7.65
C: mass fraction / %*	91.6	91.5	89.67	86.925	82.35
Pb: mass fraction / %	/	/	2	5	10
ρ / g/cm^3	1.032	1.032	1.05	1.08	1.17
rel. light yield / %×	68	64	48	32	20
t_{decay} / ns	1.8	2.1	2.1		
t_{rise} / ns	0.7	0.9	0.9+		
μ_{att} / mm	1600	3800	3800+		
refractive index n	1.58				
Birks' constant C_{B}	$0.0115 \frac{\text{g}}{\text{MeVcm}^2} \cdot \rho = 0.111 \frac{\text{mm}}{\text{MeV}}$ [97]				

* For BC-404 and BC-408, these values have been calculated from the corresponding atoms per unit [175]. For BC-452, they have been estimated by multiplying the corresponding values of BC-408 with 0.98, 095, or 0.9, respectively.
× The light yield is specified relative to the light yield of Anthracene (20000 photons/MeV [176]).
+ These values have been adopted from BC-408.

Table D.3.: Material properties of BC-404, BC-408, and BC-452 in the simulations.

The *surface roughness* (cf. subsection 4.2.4) of scintillator tiles has been measured at the Physics Institute III of RWTH Aachen University using atomic force microscopy [100]. The resulting value ($\sigma_\alpha = 5\,°$) has been adopted. For the *reflection* at the optical surfaces of scintillator tiles, 5 % diffuse reflection and 95 % "specular-lobe" reflection (cf. subsection 4.2.4) have been specified. This results in a predominant geometric reflection, which is smeared by the surface roughness, and a small diffuse fraction.

- **Wrapping materials (aluminium, Teflon, Tyvek, and BC-620):**
  Wrapping materials can be used to reduce the light losses of scintillator tiles. The properties that have been used to simulate the presented wrapping materials are summarised in table D.4.

  Aluminium foil can be used as wrapping with a rather geometric reflection. For the simulations, neither the optical attenuation length nor the reflectivity have to be specified. The former is not needed, as aluminium is a metal and a `G4OpticalSurface` that is declared "dielectric-metal" is impervious to photons in Geant4. The latter does not have to be specified explicitly, as it can be derived from the complex refractive index (in case of dielectric-metal `G4OpticalSurfaces`). The complex refractive index is illustrated in figure D.4.

  In contrast to aluminium and Tyvek (polyethylene, C_2H_4 [55]), **Teflon** (Polytetrafluoroethylene, C_2F_4 [55]) is a diffuse reflector. Its reflectivity spectrum is illustrated in figure D.3. In order to avoid unexpected effects at the edges of the wavelength ranges that are covered by the original data, the spectra have been extended linearly. For this purpose, the slope has been determined at the edges of the original spectra.

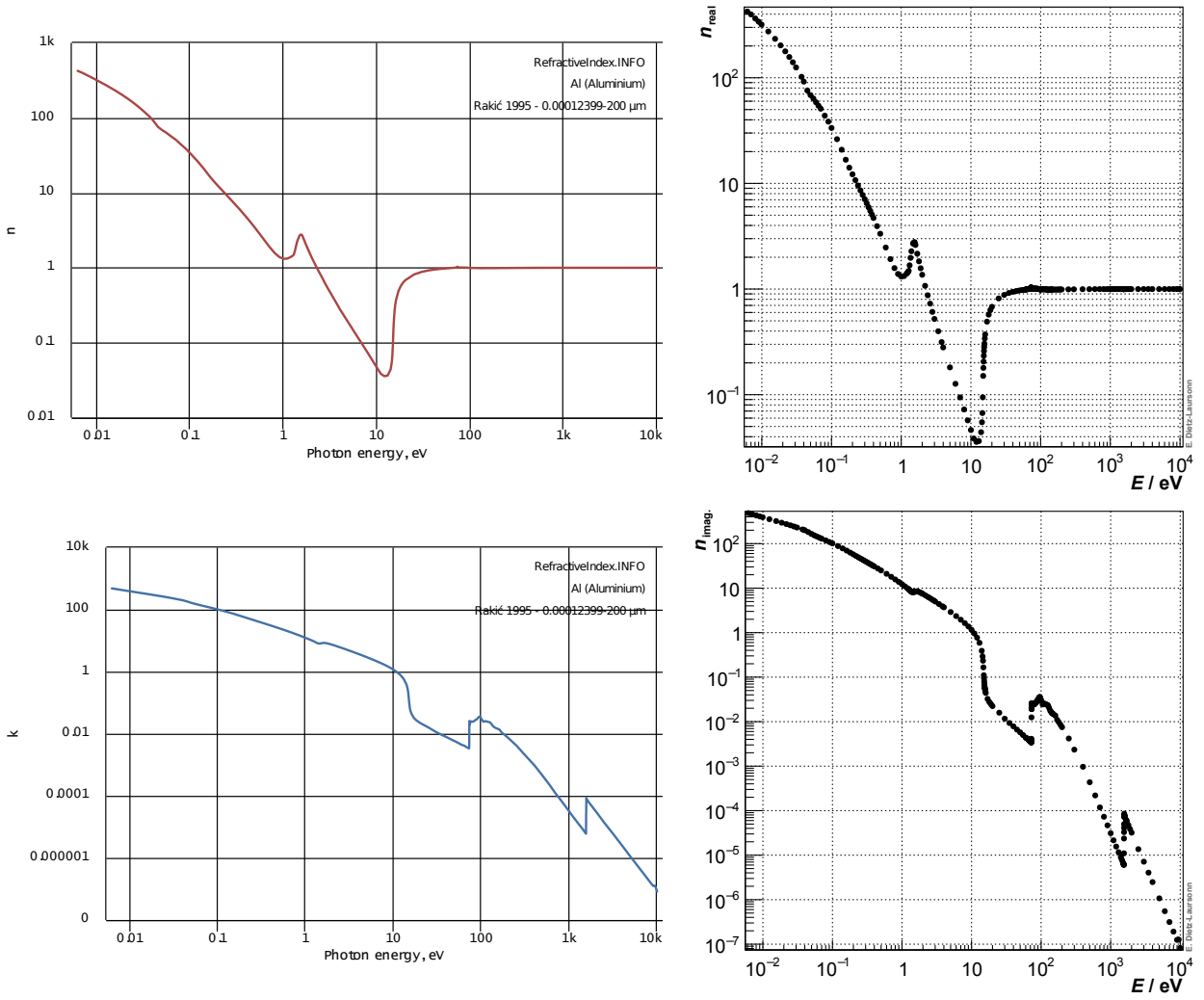

Figure D.4.: Real part **(top)** and imaginary part **(bottom)** of the complex refractive index of aluminium as function of the photon energy: diagrams from [180] **(left)** and values used for the simulations **(right)**.

BC-620 is a diffuse reflective paint from Saint-Gobain with a reflectivity spectrum that is illustrated in figure D.3. It consists of "40 % Anatase Titanium Dioxide, 24 % Acrylic Emulsion Resin, 32 % Water, 2.8 % Glycol Coalescent, and 1.2 % Surfactants & Thickeners" [181]. In order to approximate its refractive index, density, and chemical composition, the latter three can be neglected: the water evaporates and the other two components occur in negligible fractions. The properties of BC-620 can therefore be approximated by taking the weighted mean of the properties of Anatase Titanium Dioxide (TiO_2, $n = 2.488$, $\rho = 3.78\,\mathrm{g/cm^3}$ [182]) and Acrylic Emulsion Resin, which was assumed to have the same properties as acrylic glass ($C_5H_8O_3$, $n = 1.5$, $\rho = 1.2\,\mathrm{g/cm^3}$ [183]) for lack of more precise manufacturer information.

Assuming non-transparent layers, the refractive index of the three dielectric reflectors is only important for energy losses via Cherenkov radiation. As the energy loss via scintillation is usually much more important than the energy losses via Cherenkov radiation in the thin wrapping layers, unavailable data and the resulting inaccuracies of the refractive index of the wrapping material are not severe.

	aluminium	Teflon	Tyvek	BC-620
chemical composition	Al	C_2F_4	C_2H_4	$C_5H_8Ti_2O_7$ [*]
ρ / g/cm^3	2.70 [55]	2.2 [55]	0.36 [×]	2.8 [*]
refractive index n	figure D.4	1.365 [+]	1.5 [184]	2.1 [*]
"specular-lobe" reflection	95 %	0 %	85 %	0 %
diffuse reflection	5 %	100 %	15 % [185]	100 %
reflectivity	/	99 % [186]	cf. figure D.3	
μ_{att} / mm	/	0.01 [⊗]		
σ_α / °	5 [⊕]			

[*] These values have been approximated from the properties of the chemical components as described in the text.
[×] The density of Tyvek has been estimated from manufacturer data (mass per area and layer thickness) of a Tyvek membrane [187].
[+] Estimation from several values from [188].
[⊗] Rough estimation in order to realise a non-transparent layer.
[⊕] Based on the measurement of the surface roughness of scintillator tiles (cf. "Scintillators"), the same value has been adopted for wrapping material surfaces.

Table D.4.: The material properties of aluminium, Teflon, Tyvek, and BC-620 as used in the simulations.

- **Optical coupling materials (BC-600 and BC-630):**
  BC-600 and BC-630 are an optical cement and an optical silicone grease, respectively, from Saint-Gobain. They can be used to couple optical detector components, e.g. optical fibres or photodetectors to scintillator tiles. Table D.5 shows the properties of BC-600 that have been used in the simulations. The attenuation length spectrum is illustrated in figure D.5. A refractive index of 1.465 [181] has been used for BC-630. For lack of further manufacturer data of BC-630, the other properties have been adopted from BC-600. The manufacturer data was digitised with the open-source software "Engauge Digitizer" [177] and the attenuation length μ_{att} was calculated from the fraction of transmission T via

$$\mu_{\text{att}} = -\frac{0.125\,\text{mm}}{\ln(T)}.$$

  In order to avoid unexpected effects at the edges of the wavelength ranges that are covered by the manufacturer data, the spectra have been set to constant values at the edges.

chemical components (atoms per unit)	ρ / kg/m^3	refractive index: n
H (20), C (18), O (3) [*]	1.2 [*]	1.56 [189]

[*] These are a rough estimations for "epoxy resin" [190, 191].

Table D.5.: The material properties of BC-600 as implemented in the simulations.

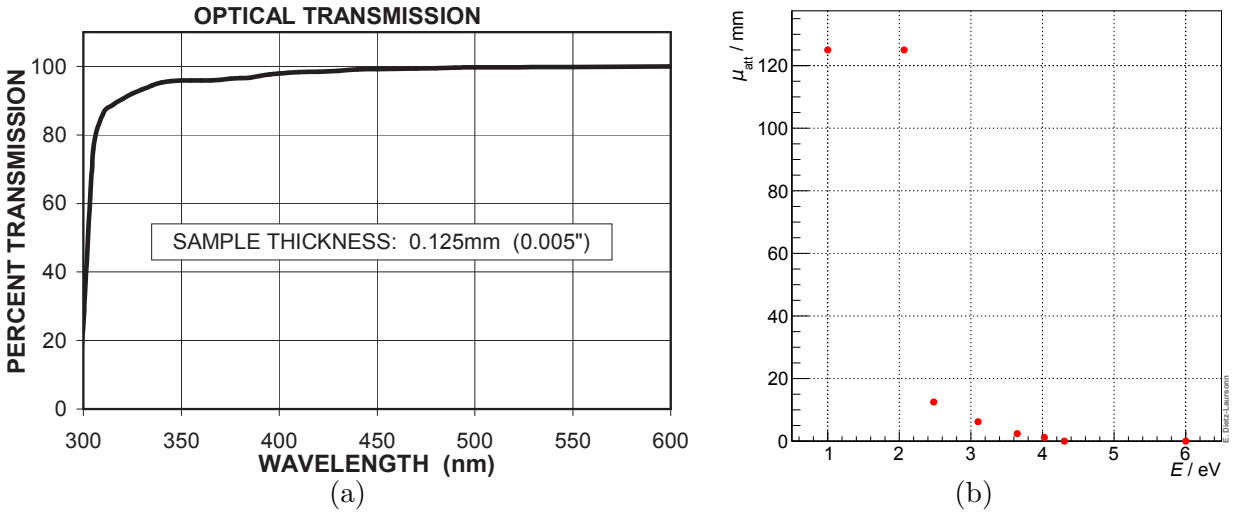

(a) (b)

Figure D.5.: Attenuation length of BC-600: manufacturer data of BC-600 [189, 192] **(a)**, and values used for the simulations **(b)**.

		BCF-92	BCF-98	Y-11
core:	chemical composition	PS [99, 153]: C_8H_8 [55]		
	ρ / g/cm^3	1.05 [99, 153]		
	refractive index n	cf. figure D.6		
	μ_{att} / mm	3500 [153]	cf. figure D.7	cf. figure D.7$^{*\times}$
	$\mu_{att,\,wls}$ / mm	cf. figure D.8^{+}	/	cf. figure D.8^{+}
	t_{decay} / ns	2.7 [153]	/	2.7 [153]
	WLS emission spectrum	cf. figure D.9	/	cf. figure D.9
1. cladding:	chemical composition	PMMA [99, 153]: $C_5H_8O_2$ [55]		
	ρ / g/cm^3	1.19 [55, 99]		
	refractive index n	cf. figure D.6		
	μ_{att} / mm	3500 [153]	cf. figure D.7	cf. figure D.7*
2. cladding:	chemical composition	"fPMMA" = fluorinated PMMA [99, 153]: $C_5H_7O_2F_1^{\otimes}$		
	ρ / g/cm^3	1.43 [99]		
	refractive index n	cf. figure D.6		
	μ_{att} / mm	3500 [153]	cf. figure D.7	cf. figure D.7*

* Outside the energy range that was covered by the manufacturer data, the attenuation length spectrum of Y-11 was set to 3500 mm [99].

$^{\times}$ Inside the energy range that was covered by the WLS absorption spectrum, the attenuation length has been set to infinity.

$^{+}$ Outside the energy range that was covered by the WLS absorption spectrum, the WLS attenuation length has been set to infinity. This was done to prevent wavelength shifting of photons with energies not matching the WLS absorption spectrum.

$^{\otimes}$ The fraction of fluorine in the material has been approximated from the increase of the materials density from PMMA to fPMMA (assuming a constant molecular density).

Table D.6.: The material properties of BCF-92, BCF-98, and Y-11 as defined in the simulations.

- **Optical Fibres (BCF-92, BCF-98, Y-11):**
  BCF-98 is a light-guiding fibre from Saint-Gobain. BCF-92 and Y-11 are WLS fibres from Saint-Gobain and Kuraray, respectively. In table D.6, their properties are summarised. As some properties of the WLS fibres are not given by both manufacturers, the corresponding data has been adopted from the manufacturer data of the respective other fibre.

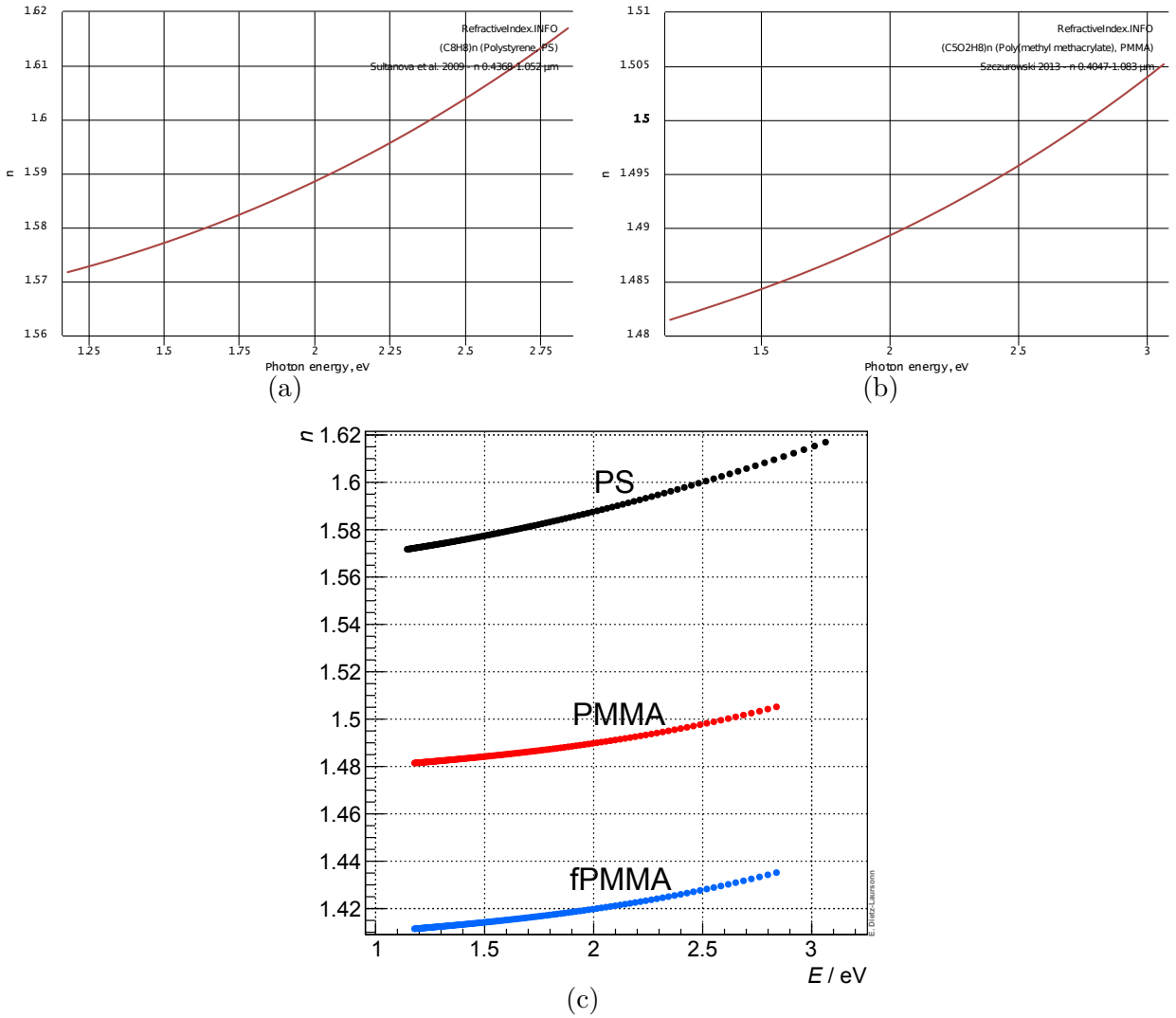

Figure D.6.: Refractive index of BCF-92, BCF-98, and Y-11 as function of the photon energy: diagrams of PS [193] (**(a)**, fibre core) and PMMA [194] (**(b)**, inner fibre cladding) and values used for the simulations **(c)**. For fPMMA, the values of PMMA have been taken and reduced by 0.7, which corresponds to the refractive index difference given by the manufacturer.

The *digitalisation* of property spectra that were only available in form of pictures (all but the refractive index spectra) was done with [177]. In order to avoid unexpected effects at the edges of the wavelength ranges that are covered by the manufacturer data, the spectra have been extended linearly. For this purpose, the slope has been determined at the edges of the original spectra.

After the digitalisation, the *attenuation length* was calculated from the "signal loss" L in dB/m (which is actually specifying the fraction of transmission) or from the relative fraction of absorption $A = 1 - T$, respectively. This was done via:

$$\mu_{\text{att}} = -\frac{1\,\text{m}}{\ln(10^{-\frac{L}{10\,\text{dB/m}}})} = -\frac{1\,\text{m}}{\ln(10)\cdot\frac{-L}{10\,\text{dB/m}}} = \frac{1\,\text{m}}{\ln(10)}\cdot\frac{10\,\frac{\text{dB}}{\text{m}}}{L}$$

or

$$\mu_{\text{att, wls}} = -\frac{1\,\text{m}}{\ln(T)} = -\frac{1\,\text{m}}{\ln(1-A)}.$$

As the manufacturer data of μ_{att} represents the signal attenuation length in the fibre whereas only the bulk attenuation length can be specified in Geant4, μ_{att} has to be adjusted before using it for simulations (cf. section 7.2). $\mu_{\text{att, wls}}$ was rescaled afterwards to ensure the maximum relative absorption to equal an attenuation length of 0.5 mm. This value was chosen (for lack of manufacturer data) to allow for a high absorption probability of optical photons crossing the fibre. This is a necessary requirement for the WLS fibre to work. Otherwise, the incident photons would just leave the fibre and no photons could be trapped and transported by the fibre. As this value is only

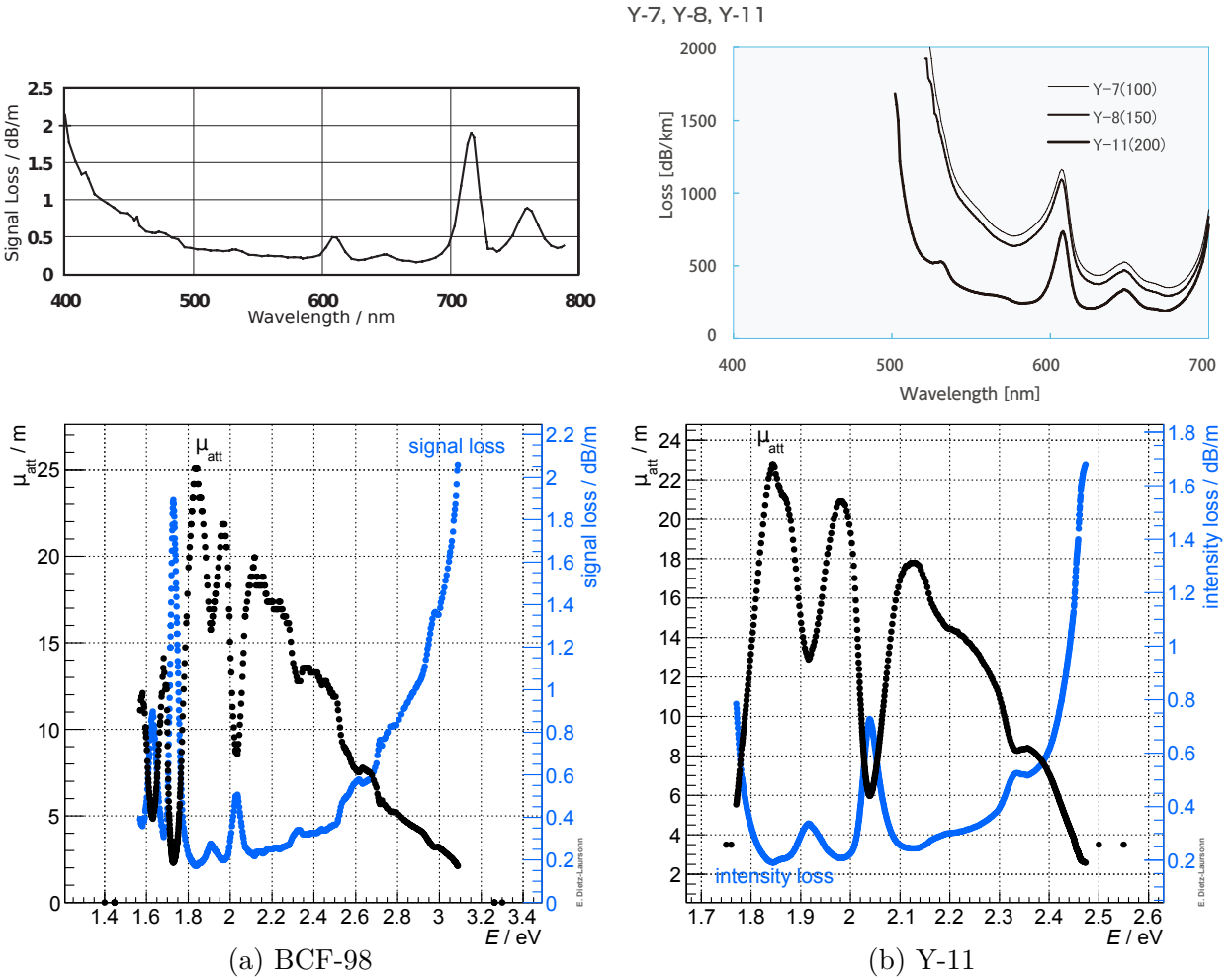

(a) BCF-98 (b) Y-11

Figure D.7.: Attenuation length spectrum of BCF-98 **(left)** and Y-11 **(right)**. **Top:** manufacturer data [99, 153] (signal attenuation). **Bottom:** digitised values and values used for the simulations (after adjusting them, cf. section 7.2).

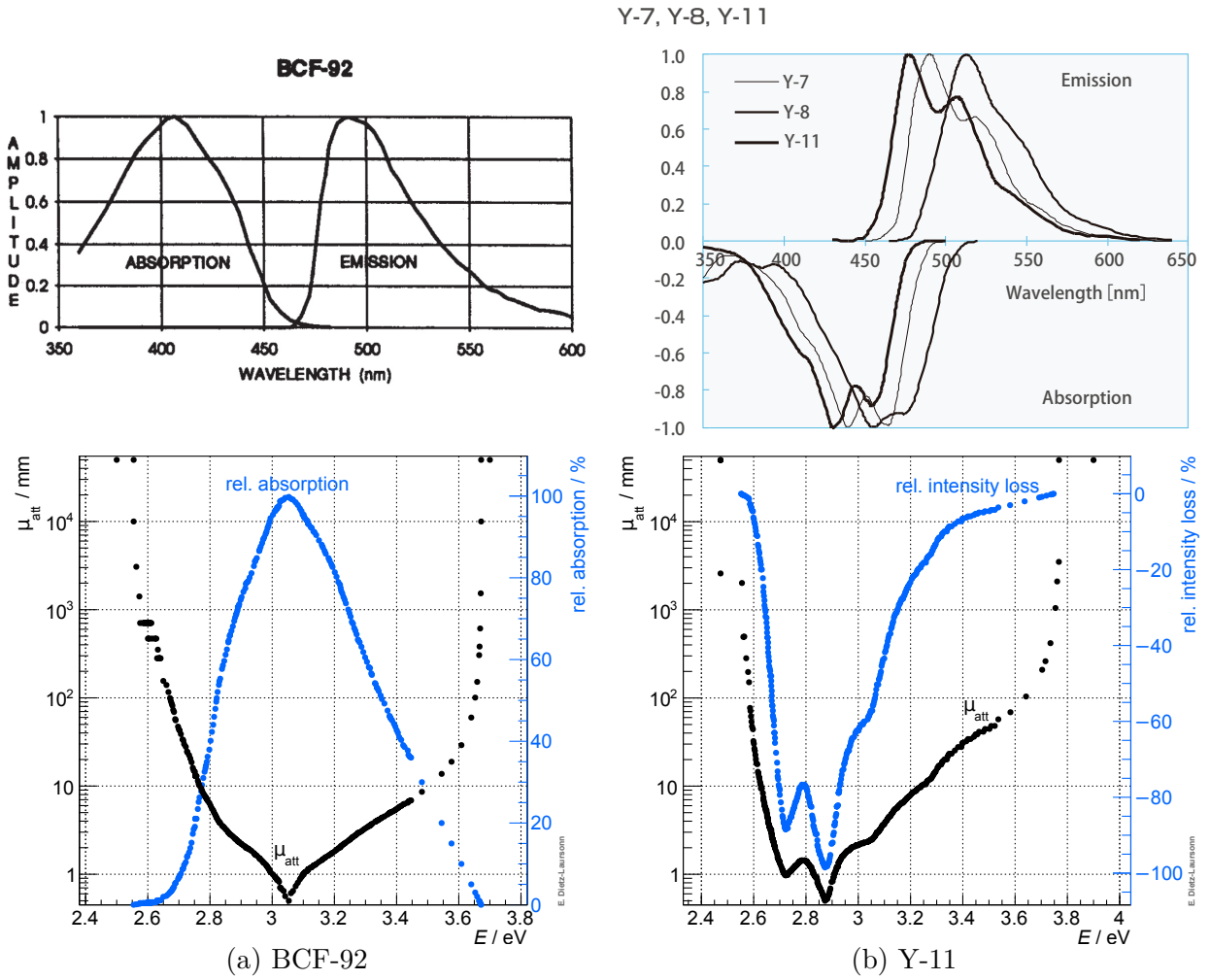

(a) BCF-92 (b) Y-11

Figure D.8.: Attenuation length spectrum of the WLS process of the WLS fibres BCF-92 **(left)** and Y-11 **(right)**. **Top:** manufacturer data [99, 153]. **Bottom:** digitised values and values used for the simulations. The cusp in the simulated WLS attenuation length spectrum of Y-11 is caused by matching this spectrum to the attenuation length spectrum of Y-11.

an estimation, a measurement of the absolute absorption spectra of $\mu_{\text{att, wls}}$ would be highly desirable, as it strongly influences the number of WLS that are created in the simulated fibres.

As a result of the comparison between simulations and measurements of the angular distribution of photons leaving the fibres at their ends (cf. section 7.1), a *roughness* of $\sigma_\alpha = 5\,^\circ$ has been applied to the surfaces of the outermost fibre cladding. Additionally, the *attenuation lengths* of the fibres had to be adjusted, as the values given by the manufacturers describe the attenuation of the signal in the fibre (including reflections etc.), in contrast to the material attenuation length that has to be specified in Geant4. This adjustment is presented in section 7.2.

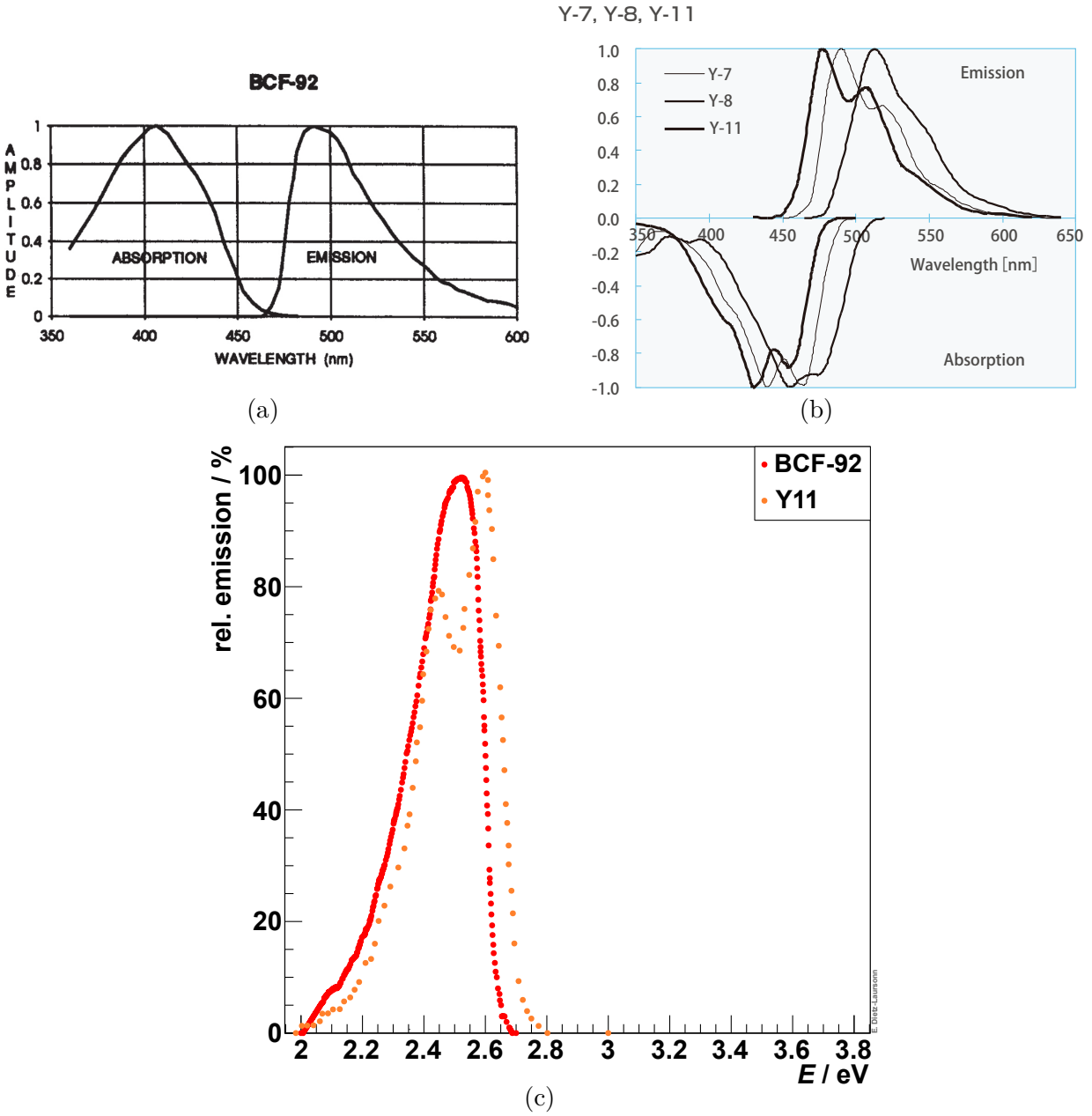

(a) (b)

(c)

Figure D.9.: Relative emission spectrum of WLS fibres: manufacturer data of BCF-92 [153] **(a)** and of Y-11 [99] **(b)**, and values used for the simulations **(c)**.

D.3. Physics Processes

The following list summarises the physics processes that have been used for the simulations in the scope of this thesis:

- **electromagnetic physics:**
  - standard electromagnetic physics (`G4EmStandardPhysics`):
    ionisation, multiple scattering, Bremsstrahlung, photoelectric effect, Compton scattering, pair production, annihilation
  - low energy standard electromagnetic physics (`G4EmLowEPPhysics`):
    like `G4EmStandardPhysics`, but only for low energies (with different models)
  - additional electromagnetic physics (`G4EmExtraPhysics`):
    synchrotron radiation, interactions with nucleus (contrary to the default, all processes have been activated)
- **optical physics** (`G4OpticalPhysics`)**:**
  Cherenkov radiation, scintillation (contrary to the default, finite rise times have been activated), absorption, optical boundary interactions, optical WLS process (contrary to the default, exponential decay time distributions have been activated), optical Rayleigh scattering, optical Mie scattering
- **particle decay physics** (`G4DecayPhysics`)
- **particle stopping physics** (`G4StoppingPhysics`)
- **ion physics:**
  - elastic scattering (`G4IonElasticPhysics`)
  - inelastic scattering (`G4IonPhysics`)
- **hadron scattering physics:**
  - elastic scattering (`G4HadronElasticPhysicsHP`)
  - inelastic scattering (`G4HadronPhysicsQGSP_BERT_HP`)
  - elastic hadron nuclear scattering (`G4ChargeExchangePhysics`)

E. Appendix: Influence of the Path Segmentation on the Birks Correction

This appendix presents the results of some simple mathematical simulations, which have been performed to study the influence of the path segmentation on the Birks correction. To verify that the resulting Birks correction is smaller when calculating it for several path segments than for calculating it for the full path, mathematical simulations have been performed for several different numbers of path segments adding up to the full path length: For each path segment, the energy deposition has been chosen randomly between 1 MeV and 2 MeV. Then, the mean number of scintillation photons of the full path has been determined three times: without Birks correction (N_γ), with Birks correction for each path segment ($N_{\gamma,\text{ per segment}}$), and with Birks correction for the total path length ($N_{\gamma,\text{ full path}}$). From these values, the Birks correction factors were calculated via

$$f_{\text{Birks, per segment}} = \frac{N_{\gamma,\text{ per segment}}}{N_\gamma}$$

and

$$f_{\text{Birks, full path}} = \frac{N_{\gamma,\text{ full path}}}{N_\gamma}.$$

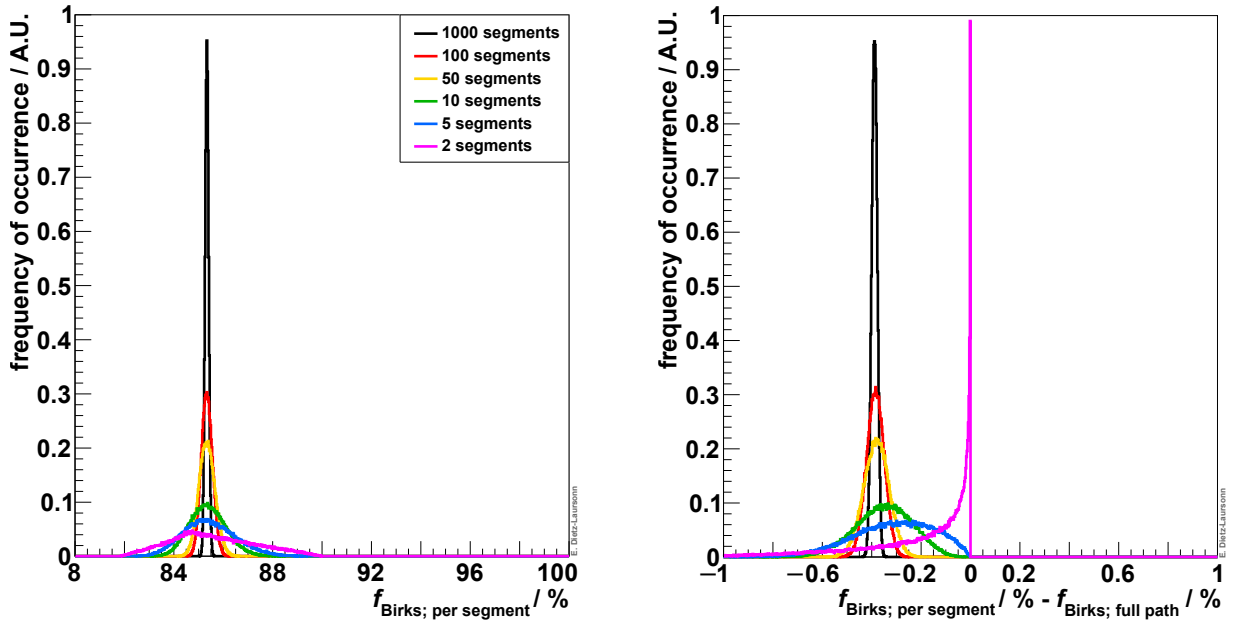

Figure E.1.: Influence of the path segmentation on the Birks correction.

For each number of path segments, the simulation has been repeated 100,000 times, the results are presented in figure E.1. The difference is always negative, i.e. applying Birks' equation at path segment level always leads to a smaller correction than the application for the full path.

F. Appendix: Adjustments to the Hodoscope Software

The hodoscope that was used in the scope of this thesis as well as its software were already existing at the Physics Institute III of RWTH Aachen University and had been tested and used before. Nevertheless, when first trying to use it for taking space-resolved measurements of the prototype modules, the results were corrupt and unusable. This can be seen from figure F.1, which illustrates the space-resolved distribution of the signal height of one SiPM of prototype module 7. In order to obtain the correct results from the measurement, several corrections had to be implemented. This appendix describes these changes for documentation purpose.

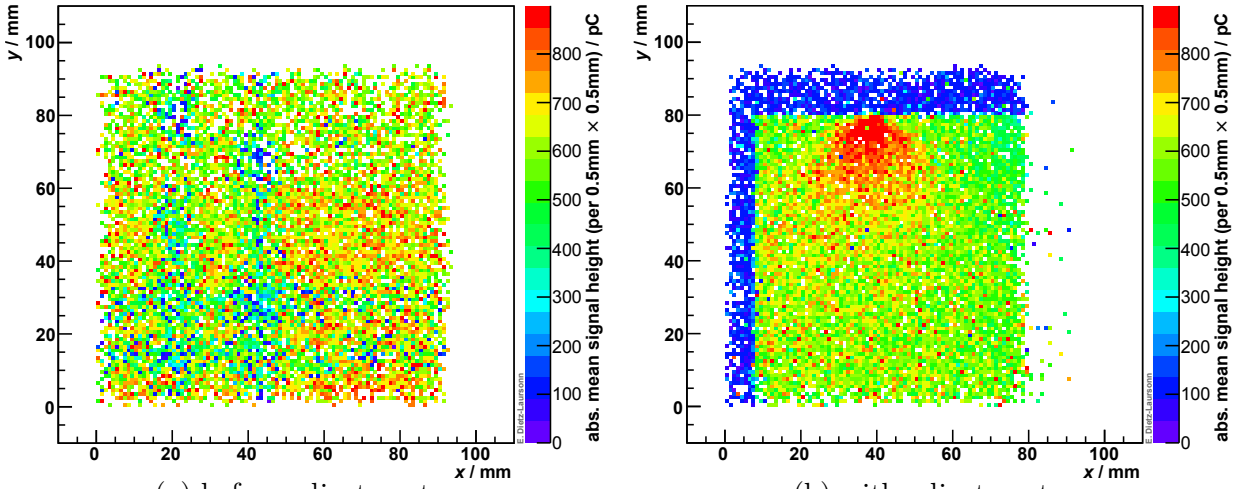

(a) before adjustments (b) with adjustments

Figure F.1.: Distribution of the signal height of prototype module 7 as a function of the transition position of the cosmic muons in the plane of the prototype module. Whereas **(a)** shows the actual result from the measurement (before the adjustments had been applied), **(b)** illustrates the result that would be expected (and is obtained after the adjustments). The sharply separated regions with low signal heights (in **(b)**) are a result of the positioning of the prototype module, which did not fully cover the sensitive area of the hodoscope. It corresponds to position A as described in subsection 8.1.1.

The following changes have been implemented (the latter three of them will be described in more detail in the following sections):

1. Separation of data acquisition and reconstruction. This allows for trying variable reconstruction procedures without having to repeat the measurement. Therefore, this approach should be a basic principle of every experiment.

2. Ensure stable APV-chip[95] order in recorded data.

3. Application of the correct counting order of the silicon strips of the individual APV-chips during the data reconstruction.

4. Application of the correct APV-chip order during the data reconstruction.

The latter three of them will be described in more detail in the following sections.

F.1. Data Acquisition

The hodoscope consists of four silicon strip modules, one for the x- as well as one for y-direction in the top and bottom detector layer, respectively [155–160]. The silicon strips of each module are readout by six APV-chips[96] (128 consecutive silicon strips per chip). The data of each two adjacent APV-chips is combined and sent to the readout electronics via one channel.

When observing the silicon strip data of each single event, it was recognised that the order of the data from the two APV-chips in the same channel switches from event to event.[97] As a result, the data obtained from the readout channels does not allow for drawing conclusions on the actual position on the silicon strip modules. Additionally, this switching of the APV-chips results in a wrong determination of the noise of the silicon strips: as the data of the two APV-chips in the same channel is also switched when acquiring the noise events, the obtained noise spectrum is the same (the average) for both APV-chips belonging to the same APV-chip pair. This is illustrated in figure F.2. The same applies to the standard deviation σ of the noise (cf. figure F.3). As these effects did not occur in previous measurements (otherwise no meaningful results could have been obtained in the scope of [155–160]), this seems to be a new problem. The reason for this is not clear.

In order to solve this problem, a stable APV-chip order has to be ensured in the acquired data. For that purpose, the mean signal of the silicon strips was calculated for each of the two APV-chips in the first APV-chip pair. This was done for each silicon strip module and each event. If the second APV-chip had the higher mean signal[98], the order of the APV-chips in all APV-chip pairs of the corresponding silicon strip module was switched. The resulting corrected spectra of the noise and of σ are presented in figures F.4 and F.5, respectively. Now, the noise spectrum is unique for every APV-chip and the magnitude of its fluctuation (represented by σ) is relatively constant for all silicon strips of the same silicon strip module. The only exceptions are some noisy strips, which produce significantly higher fluctuations and can be identified as spikes in figure F.5. The threshold for a muon signal in the silicon strips is proportional to the σ of the corresponding silicon strip. Therefore, these noisy silicon strips do not lead to spikes in the distribution of muon signals.

[95] "APV" stands for "Analogue Pipeline Voltage Mode".
[96] Module 4 has fewer silicon strips and is thus only four APV-chips are needed.
[97] At the same time, the relation between the APV-chip order in the three APV-chip pairs of each silicon strip module always remains the same. This means, the order of the APV-chips of each silicon strip module is either 1-2-3-4-5-6 or 2-1-4-3-6-5, where the digits represent the APV-chip.
[98] This is an arbitrary definition.

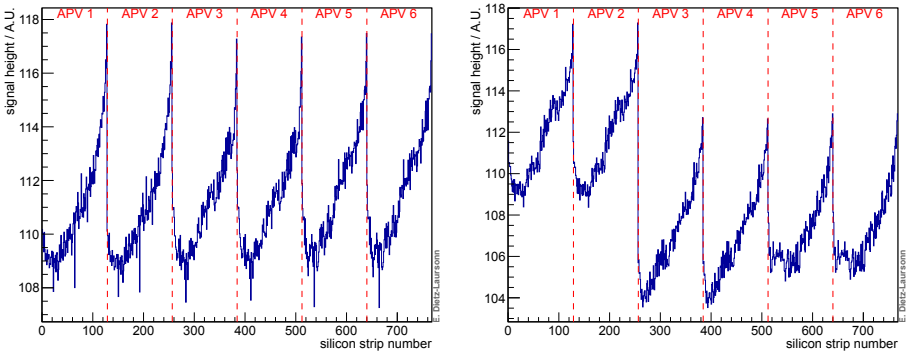

(a) module 1 (y-direction; top) (b) module2 (y-direction; bottom)

(c) module 3 (x-direction; top) (d) module 4 (x-direction; bottom)

Figure F.2.: Mean noise of the silicon strips **without** manually ensuring a stable APV-chip order in acquired data.

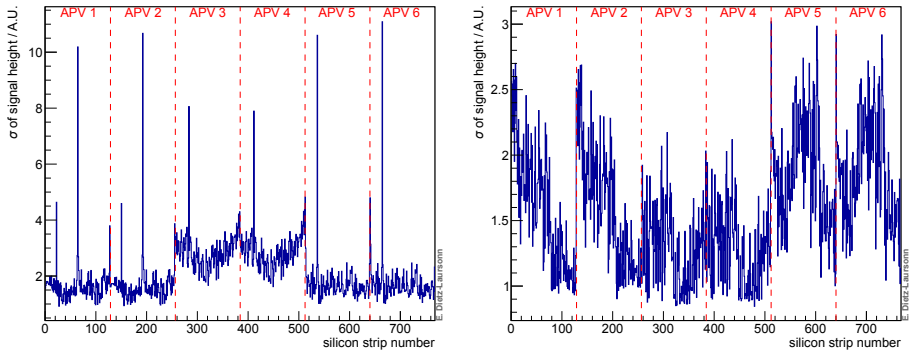

(a) module 1 (y-direction; top) (b) module 2 (y-direction; bottom)

(c) module 3 (x-direction; top) (d) module 4 (x-direction; bottom)

Figure F.3.: Standard deviation σ of the noise of the silicon strips **without** manually ensuring a stable APV-chip order in acquired data.

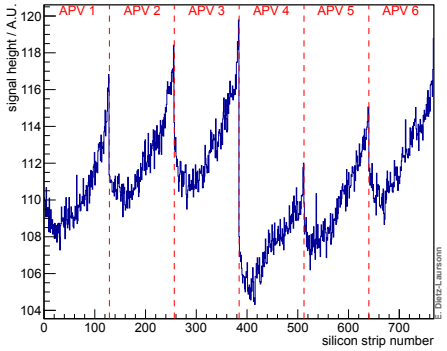

(a) module 1 (y-direction; top)

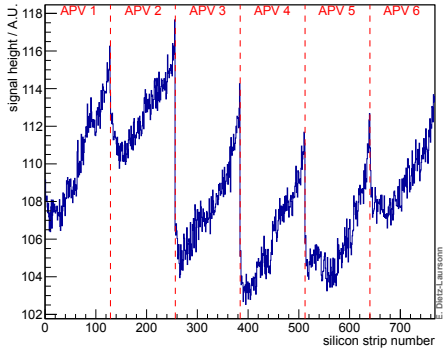

(b) module 2 (y-direction; bottom)

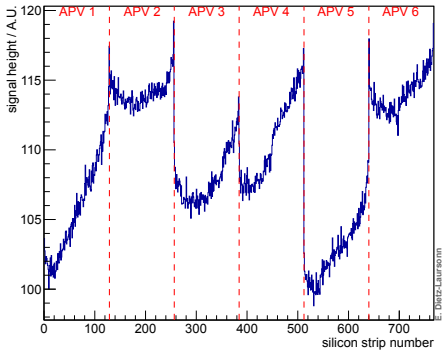

(c) module 3 (x-direction; top)

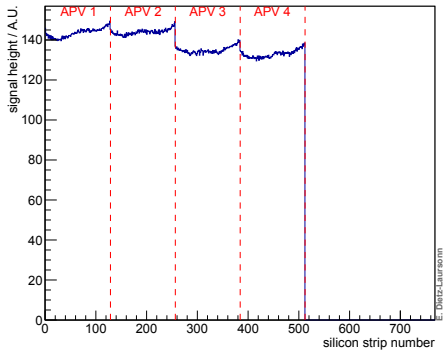

(d) module 4 (x-direction; bottom)

Figure F.4.: Mean noise of the silicon strips **with** manually ensuring a stable APV-chip order in acquired data.

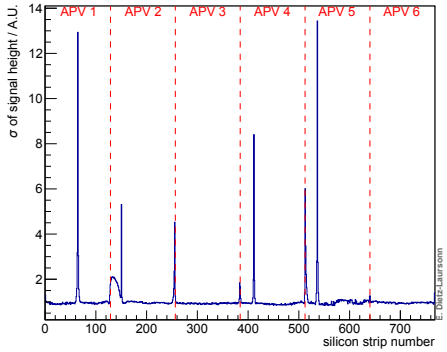

(a) module 1 (y-direction; top)

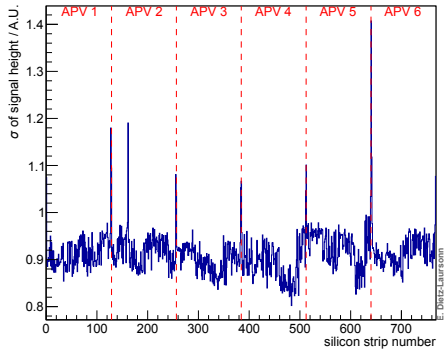

(b) module 2 (y-direction; bottom)

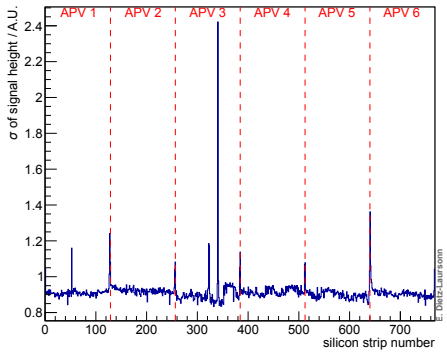

(c) module 3 (x-direction; top)

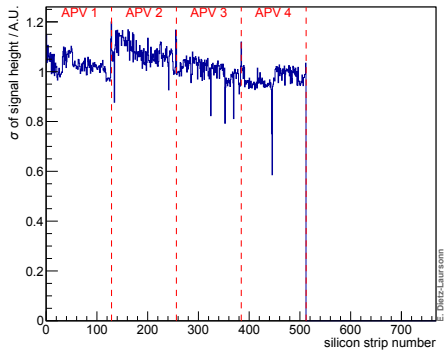

(d) module 4 (x-direction; bottom)

Figure F.5.: Standard deviation σ of the noise of the silicon strips **with** manually ensuring a stable APV-chip order in acquired data.

F.2. Data Reconstruction

Besides the problem of the switching APV-chip order in acquired data, there were two more issues that led to incorrect position data obtained from the hodoscope. As both of these issues were concerning the data reconstruction rather than the data acquisition, they could be investigated and fixed within the data reconstruction software without having to repeat the measurements.

One of the issues is a direct consequence of the switching APV-chip order: The stable APV-chip order in recorded data, which has been ensured manually as described in the previous section, is not necessarily the correct order. Therefore, all possible combinations of switched and non-switched APV-chip pairs had to be tested. The results of this survey showed that the order of all APV-chip pairs of the silicon strip modules 1 and 4 have to

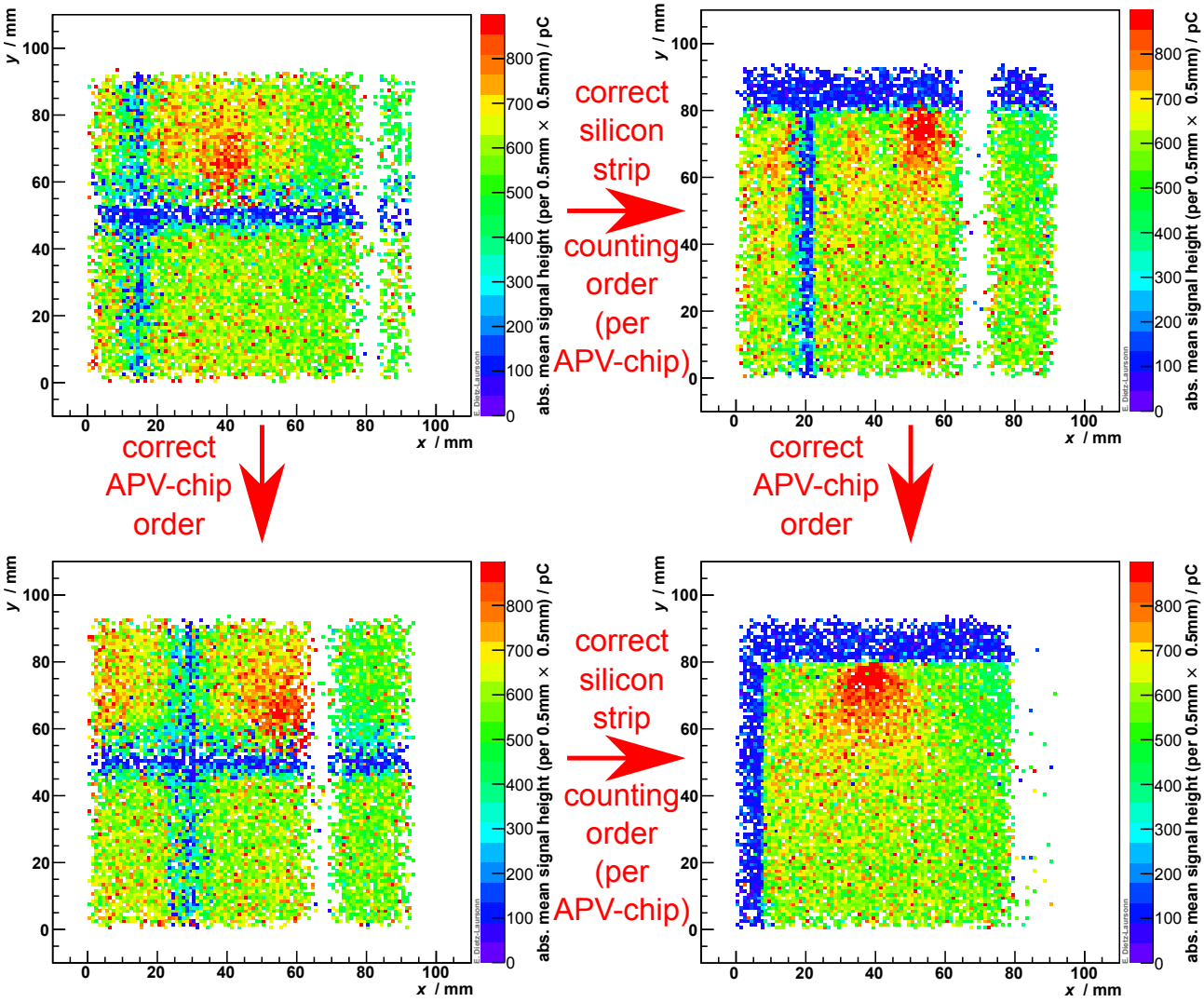

Figure F.6.: Distribution of the signal height of prototype module 7 as a function of the transition position of the cosmic muons in the plane of the prototype module. The individual plots represent different correction stages of the same recorded data. During the data acquisition, a stable APV-chip order has been ensured manually as described in the previous section.

be switched with respect to the stable APV-chip order that has been defined for the data acquisition.

The other issue concerned the conversion of the silicon strip numbers into Cartesian coordinates. During the investigations concerning the corrupt results of the hodoscope measurements, it became obvious that the counting order of the silicon strips had to be inverted within the individual APV-chip pairs to perform a correct conversion of the coordinates. This means, if the digits represent the silicon strip numbers of a silicon strip module, the silicon strip order 255-254-...-1-0-511-510-...-257-256-767-766-...-513-512 corresponds to a linear rising Cartesian coordinate, rather than the expected order 0-1-...-766-767.

The effect of the corrections is illustrated in figure F.6. It shows that applying all corrections that have been described in this appendix leads to obtaining the correct transition position of the cosmic muons from the hodoscope. Thus the result is a meaningful spatial signal distribution of the prototype module, which is also consistent with the positioning of the prototype module (position A as described in subsection 8.1.1) with respect to the position of the SiPM and the edges of the scintillator tile.

G. Appendix: Config Data for the Hodoscope Measurements

This appendix summarises the configuration that has been used for the prototype measurements with the hodoscope.

Manual hardware configurations

- gate length: 1 µs
- bias voltage of the trigger PMTs: 1920 V and 1940 V, respectively

Software based configurations

HORUS.cpp:

- bias voltage of the silicon strip modules: 200 V

```
DeppEnv[iDepp]->rampToVoltage(200, 10);
```

testHorus.cfg:

- vertical detector position (in mm) relative to the coordinate system of the hodoscope:

```
DETECTOR_Z  15;
```

- QDC base address as given on the board:

```
QDC_BASE_ADDRESS  0x00D00000;
```

- QDC readout channels (the data of `QDC_CHANNEL_SUM` has not been recorded):

```
QDC_CHANNEL_SIPM_A   9;
QDC_CHANNEL_SIPM_B   8;
QDC_CHANNEL_SUM   2;
```

- pause between events (in µs), necessary for the QDC

```
QDC_PAUSE   250;
```

- number of data points to be recorded for the pedestal measurement:

```
NOISE_EVENTS   10000;
```

- number of triggered events to be recorded per run:

```
N_EVENTS 200000;
```

horus.cfg:

- CAMAC crate slot numbers for ND16 Pulser and SEN_OR2088 Gate generator:

```
PULSER_SLOT 1;
GATE_SLOT   2;
```

- vertical position (in mm) of the silicon strip modules relative to the coordinate system of the hodoscope:

```
Z_OF_MODULE1   362;
Z_OF_MODULE2   -18;
Z_OF_MODULE3   365;
Z_OF_MODULE4   -15;
```

- signal over noise threshold (in units of the standard deviation σ of the noise) to determine hits in the silicon strip modules:

```
NOISE_CUT_SIGMA   6;
```

- ARC board addresses:

```
ARCADDR0 0x240;
ARCADDR1 0x260;
ARCSUBADDR0 0x00;
ARCSUBADDR1 0x00;
```

- DEPP board addresses:

```
DEPPADDR0   0x210;
DEPPADDR1   0x220;
DEPPSUBADDR0   0x00;
DEPPSUBADDR1   0x00;
```

- APV commands:

```
APV_IPRE 115;
APV_IPCASC  60;
APV_IPSF 50;
APV_ISHA 50;
APV_ISSF 50;
APV_IPSP 80;
APV_IMUXIN  50;
APV_ICAL 40;
APV_VFP  67;
APV_VFS  67;
APV_VPSP 30;
APV_CDRV 254;
APV_CSEL 1;
APV_MODE 0x2F;
APV_LATENCY 10;
APV_MUXGAIN 4;
```

List of Figures

1.1 scintillator tile with embedded WLS fibres 3

massive particles in matter:
2.1 mean energy loss of muons 6
2.2 mean energy loss of electrons and positrons 7
2.3 mean excitation energy of different materials 8
2.4 development of Cherenkov radiation 11
photons in matter:
2.5 dominating interaction processes 15
2.6 absorption edges of the photoelectric effect 16
optics:
2.7 secondary waves causing different speed of light in matter 23
2.8 complex refractive index of water 24
2.9 Huygens-Fresnel principle for reflection and refraction of waves 25

detector design:
3.1 the CMS detector and medical (ToF-)PET-scanners 28
3.2 the LHCb detector and the AMS-02 detector 29
3.3 the Pierre Auger Observatory and the IceCube detector 30
scintillation and wavelength-shifting:
3.4 fluorescence and Förster resonance energy transfer 32
3.5 organic scintillators: electron orbitals of chemical bond within aromatic rings 33
3.6 inorganic scintillators: energy bands 35
optical fibres:
3.7 refractive index profiles 37
3.8 meridional and skew rays 37
3.9 trapping efficiency 38
semiconductors:
3.10 energy band structure 40
3.11 p-i-n junction in thermal equilibrium 41
3.12 (G)APDs: avalanche mechanism 42
3.13 SiPMs: circuit diagram and microscopic picture 43
3.14 SiPMs: oscilloscope picture of output pulses 44
3.15 PMTs 45
3.16 microchannel plates 45

Geant4:
4.1 reflection and refraction in the Unified Model for `G4OpticalSurfaces` 52
4.2 effects of the Unified Model for `G4OpticalSurfaces` 53
4.3 peculiarity of the simulation of optical fibres 55

Geant4 visualisation problems:
4.4 optical photons seem to leave a bent fibre . . . 56
4.5 bent fibre with apparent holes . . . 57
4.6 straight fibre with apparently missing cladding parts . . . 57

GODDeSS:
5.1 workflow . . . 64
5.2 scintillator tile and optical fibre . . . 66
5.3 fibre protruding from a scintillator tile (its mother volume) . . . 67
5.4 simple photodetector . . . 68
5.5 SiPM (simulated with the G4Sipm package) . . . 68
5.6 SiPM (measured and simulated oscilloscope reading) . . . 69
5.7 wrapped scintillator tile with photodetector . . . 69

consistency checks:
6.1 emission spectra . . . 74
6.2 geometry for excitation time determination . . . 76
6.3 decay times (scintillation and WLS) . . . 76
6.4 scintillation light yield . . . 77
6.5 reflectivity spectra . . . 79
6.6 bulk attenuation length of scintillating materials . . . 81
6.7 bulk attenuation length of WLS materials . . . 81
6.8 determination of the gamma ray attenuation length of scintillating materials 83
6.9 gamma ray attenuation length of scintillating materials . . . 84
6.10 characteristics of the Geant4 reflection models . . . 86
6.11 influence of roughness on `specularlobe` reflection . . . 87
6.12 geometry considerations on the determination of reflection/refraction angles . 87
6.13 influence of roughness on refraction . . . 88
6.14 influence of roughness on diffuse reflection . . . 89
6.15 energy change during the WLS process . . . 91
6.16 Cherenkov spectra in case of constant refractive indices . . . 92
6.17 Cherenkov spectra in case of energy-dependent refractive indices . . . 93
6.18 LUT surface problems (angular distribution) . . . 96
6.19 LUT surface problems (“escaping” photons) . . . 96
6.20 fibre trapping efficiency (geometrical reason for deviations between simulation and calculation) . . . 98
6.21 fibre trapping efficiency (geometry dependence) . . . 99
6.22 fibre bending loss . . . 101

exit characteristics of light from optical fibres:
7.1 spatial distribution on the photodetector (simulation **without** roughness) . . 106
7.2 angular distribution on the photodetector (simulation with several different roughness values) . . . 106
7.3 spatial distribution on the photodetector (simulation **with** roughness) . . . 107

simulated signal attenuation length of optical fibres:
7.4 determination . . . 109
7.5 unadjusted spectra of BCF-98 and Y-11 . . . 110
7.6 adjusted spectra of BCF-98 and Y-11 . . . 110

hodoscope measurements:
8.1 prototype modules . . . 114
8.2 module positions relative to the sensitive area . . . 116
8.3 raw measurement results for the individual module positions . . . 116
8.4 coordinate transformation . . . 117
8.5 combined results of the measurements at the individual module positions . . . 117
8.6 combined results with final binning and axis ranges . . . 119
8.7 module 7: normalisation of the results . . . 119
8.8 module 7: deviations between measurement and simulation . . . 120
8.9 module 7: deviations between measurement and simulation considering SiPM effects . . . 122
8.10 module 7: deviations between measurement and simulation considering SiPM effects and amplifier saturation . . . 123
8.11 module 3: deviations between measurement and simulation considering SiPM effects . . . 124
8.12 module 3: deviations between measurement and simulation with reduced reflectivity value . . . 125
8.13 module 7: deviations between measurement and simulation with reduced reflectivity value . . . 125
test-beam measurements:
8.14 prototype modules . . . 127
8.15 prototype modules (simulation) . . . 127
8.16 module mtt1: deviations between measurement and simulation . . . 129
8.17 module mtt2: deviations between measurement and simulation . . . 130
8.18 module mtt1: signal delay . . . 131
8.19 module mtt2: signal delay . . . 131

detailed study of the fibre trapping efficiency:
9.1 influence of the photon emission angle (round fibre with smooth surface) . . . 136
9.2 influence of the photon emission angle (rough surface) . . . 136
9.3 influence of the photon emission angle (square fibre with smooth surface) . . . 137
9.4 influence of the photon emission angle (short fibre) . . . 138
9.5 initial position of WLS photons in fibres . . . 141
9.6 influence of the photon emission angle (realistic refractive index) . . . 142
detailed study of the fibre signal attenuation length:
9.7 BCF-92 . . . 144
9.8 BCF-98 . . . 145
9.9 BCF-98 (with smooth surface) . . . 145
detailed study of the exit characteristics of light from optical fibres:
9.10 different fibre types (spatial distribution) . . . 147
9.11 different fibre types (angular distribution) . . . 147
9.12 different fibre lengths (spatial distribution) . . . 148
9.13 different fibre lengths (angular distribution) . . . 149
9.14 rough fibre end face (angular distribution) . . . 150
9.15 rough fibre end face (spatial distribution) . . . 150
9.16 different distances between photodetector and fibre end (spatial distribution) 151
9.17 distances of 0 mm and 0.5 mm between photodetector and fibre end (spatial distribution) . . . 152

9.18 distances of 0.5 mm, 1 mm, and 2 mm between photodetector and fibre end (spatial distribution, square fibres) . . . 153
9.19 distances of 0.5 mm, 1 mm, and 2 mm between photodetector and fibre end (spatial distribution, round fibres) . . . 154
9.20 different distances between photodetector and fibre end (angular distribution) 155
9.21 without air gap between photodetector and fibre end (spatial distribution) . . 156
9.22 without air gap between photodetector and fibre end (angular distribution) . 156
9.23 with $n_{\text{ambient}} = n_{\text{clad}}$ (spatial distribution) . . . 157

detailed study of readout options:

9.24 simple detector layout with direct or fibre readout . . . 158
9.25 optical photons reaching the photodetector . . . 159
9.26 optical photons reaching the photodetector (spatial distribution) . . . 160
9.27 created optical photons and optical photons reaching the photodetector . . . 161
9.28 optical photons reaching the photodetector (as a function of the tile thickness) 162
9.29 photon hit time distribution on the photodetectors . . . 163
9.30 signal delay . . . 164
9.31 signal delay (spatial distribution) . . . 165
9.32 signal delay (standard deviation, spatial distribution) . . . 166
9.33 pulse length . . . 168
9.34 pulse length (spatial distribution) . . . 169
9.35 pulse length (standard deviation, spatial distribution) . . . 170
9.36 module design 1 (layout, signal height, signal delay, pulse length) . . . 172
9.37 module design 2 (layout, signal height, signal delay, pulse length) . . . 173
9.38 module design 3 (layout, signal height, signal delay, pulse length) . . . 174
9.39 module design 4 (layout, signal height, signal delay, pulse length) . . . 175
9.40 module design 5 (layout, signal height, signal delay, pulse length) . . . 176

B.1 calculated meridional fibre trapping efficiency as a function of the critical angle 185

material property simulation:

D.1 air (refractive index) . . . 200
D.2 BC-404, BC-408, BC-452 (relative emission spectra) . . . 201
D.3 Tyvek, BC-620 (reflectivity) . . . 201
D.4 aluminium (refractive index) . . . 203
D.5 BC-600 (attenuation length) . . . 205
D.6 BCF-92, BCF-98, Y-11 (refractive index) . . . 206
D.7 BCF-98, Y-11 (attenuation length) . . . 207
D.8 BCF-92, Y-11 (WLS attenuation length) . . . 208
D.9 BCF-92, Y-11 (relative WLS emission spectrum) . . . 209

E.1 influence of the path segmentation on the Birks correction . . . 211

adjustments to the hodoscope software:

F.1 corrupt hodoscope measurement results . . . 213
F.2 noise of the hodoscope silicon strips (mean, uncorrected) . . . 215
F.3 noise of the hodoscope silicon strips (standard deviation, uncorrected) . . . 215
F.4 noise of the hodoscope silicon strips (mean, corrected) . . . 216
F.5 noise of the hodoscope silicon strips (standard deviation, corrected) . . . 216
F.6 corrected hodoscope measurement results . . . 217

List of Tables

6.1 reflectivity calculation via Fresnel equations in Geant4 . . . 90
6.2 fibre trapping efficiency: consistency check . . . 97

detailed studies of the fibre trapping efficiency:
9.1 constant refractive indices . . . 134
9.2 constant refractive indices and external excitation of the fibre . . . 140
9.3 realistic refractive indices and external excitation of the fibre . . . 142
detailed study of the fibre signal attenuation length:
9.4 fibre signal attenuation length . . . 143
detailed study of readout options:
9.5 optical photons reaching the photodetector (full tile) . . . 159
9.6 optical photons reaching the photodetector (individual regions of the tile) . . . 160
9.7 standard deviation of the signal delay (individual regions of the tile) . . . 167

A.1 important quantities . . . 181

B.1 fibre trapping efficiency: calculated values . . . 185

material property simulation:
D.1 vacuum . . . 199
D.2 air . . . 200
D.3 scintillators (BC-404, BC-408, BC-452) . . . 202
D.4 wrappings (aluminium, Teflon, Tyvek, BC-620) . . . 204
D.5 optical cement (BC-600) . . . 204
D.6 optical fibres (BCF-92, BCF-98, Y-11) . . . 205

List of Equations

Bethe-Bloch equation:
2.1 heavy particles . . . 6
2.2 electrons and positrons . . . 8
2.3 density effect corrections . . . 9
2.4 Bragg's additivity rule . . . 9
2.5 mean energy loss in thick material layers . . . 9
2.6 mean energy loss in thin material layers . . . 10
multiple scattering:
2.7 total scattering angle of heavy particles in matter . . . 10
Cherenkov radiation:
2.8 Cherenkov angle . . . 11
2.9 number of created photons . . . 11
2.10 mean energy loss . . . 12
Bremsstrahlung:
2.11 mean energy loss . . . 13
2.12 radiation length in individual materials . . . 13
2.15 radiation length in material layers, mixtures, and chemical compounds . . . 13
2.16 critical energy . . . 14
transition radiation:
2.17 mean energy loss . . . 14
photon attenuation:
2.18 in individual materials . . . 15
2.19 in material layers, mixtures, and chemical compounds . . . 15
photoelectric effect:
2.20 cross section in the non-relativistic case . . . 16
2.21 cross section in the relativistic case . . . 16
Compton scattering:
2.22 cross section . . . 17
pair production:
2.23 threshold . . . 17
2.24 cross section in the Coulomb field of an unscreened nucleus . . . 17
2.25 cross section in the Coulomb field of a fully screened nucleus . . . 18
2.26 empirical cross section in the Coulomb field of an atom . . . 18
high-energy hadrons in matter:
2.27 absorption probability . . . 19
2.28 nuclear interaction length in individual materials . . . 19
2.29 nuclear interaction length in material layers, mixtures, and chemical compounds 19
2.30 Molière radius . . . 20
2.33 electromagnetic fraction of hadronic cascades . . . 22

optics:

2.35 refractive index as a function of the frequency . . . 23
2.36 refractive index as a complex number . . . 24
2.37 normal dispersion . . . 24
2.38 reflection law . . . 25
2.39 Snell's law . . . 25
2.40 Fresnel equations (reflectivity) . . . 25
2.41 Fresnel equations (transmittance) . . . 26
2.42 critical angle for total reflection . . . 26

optical detector components:

3.1 Birks' equation . . . 34
3.2 numerical aperture of optical fibres . . . 38
3.3 width of a diode's depletion zone . . . 42
3.4 counted vs. absorbed photons in case of SiPMs . . . 43

6.5 Lambert's cosine law for diffuse emittance . . . 89

8.1 statistical uncertainty of the arithmetic mean . . . 118

trapping efficiency:

B.1 round fibres . . . 183
B.2 square fibres ($\alpha_{\text{crit}} \leq 45\,^\circ$) . . . 183
B.4 square fibres ($\alpha_{\text{crit}} > 45\,^\circ$) . . . 184

Bibliography

[1] Particle Data Group. 'Review of Particle Physics'. In: *Physical Review D* 86 (1 2012). URL: http://pdg.lbl.gov/ (cit. on pp. III, 1, 2, 5–11, 13, 14, 20, 22, 31, 34–36, 42–46, 181).

[2] Erik Dietz-Laursonn, Yusuf Erdogan, et al. *Hardware development for muon track fast tag (MTT): Prototype detectors and simulation studies*. CMS Detector Note (CMS DN-2014/020). 2014. URL: http://cms.cern.ch/iCMS/user/getnote?type=DN&year=2014&files=DN2014_020.pdf (cit. on pp. III, IV, 3, 126).

[3] The Geant4 Collaboration (official homepage). URL: http://geant4.cern.ch/ (cit. on pp. III, 47–49).

[4] Public webpage of the GODDeSS framework. URL: https://forge.physik.rwth-aachen.de/projects/goddess-package/wiki (cit. on pp. III, 63, 179, 189).

[5] The ALICE experiment (official homepage). URL: http://aliceinfo.cern.ch/Public/Welcome.html (cit. on pp. III, 1).

[6] The AMS-02 experiment (official homepage). URL: http://www.ams02.org/ (cit. on pp. III, 2, 29).

[7] The ANTARES experiment (official homepage). URL: http://antares.in2p3.fr/ (cit. on pp. IV, 2).

[8] The ATLAS experiment (official homepage). URL: http://atlas.ch/ (cit. on pp. IV, 1).

[9] The European Organization for Nuclear Research (CERN) (official homepage). URL: http://home.web.cern.ch/ (cit. on pp. IV, 1, 27).

[10] The CMS experiment (official homepage). URL: http://cms.web.cern.ch/ (cit. on pp. IV, 1, 27).

[11] Official web-page about the Large Hadron Collider (LHC). URL: http://home.web.cern.ch/topics/large-hadron-collider (cit. on pp. IV, 1, 27).

[12] The LHCb experiment (official homepage). URL: http://lhcb.web.cern.ch (cit. on pp. IV, 1, 29).

[13] The MICE experiment (official homepage). URL: http://mice.iit.edu/ (cit. on pp. IV, 2, 39).

[14] Christine Peters, Thomas Bretz, et al. *The muon detector prototype AMD for the determination of the muon content in UHECRs*. ICRC 2015 conference proceeding. 2015. URL: http://pos.sissa.it/archive/conferences/236/596/ICRC2015_596.pdf (cit. on pp. IV, 3).

[15] Erik Dietz-Laursonn, Yusuf Erdogan, et al. *A possible extension of the barrel muon trigger for the CMS experiment at HL-LHC: Muon Track fast Tag (MTT)*. CMS Detector Note (CMS DN-2014/008). 2014. URL: http://cms.cern.ch/iCMS/user/getnote?type=DN&year=2014&files=DN2014_008.pdf (cit. on pp. IV, 3, 126).

[16] Carl D. Anderson. 'The Positive Electron'. In: *Physical Review* 43 (6 1933), pp. 491 –494. URL: http://dx.doi.org/10.1103/PhysRev.43.491 (cit. on p. 1).

[17] Seth H. Neddermeyer and Carl D. Anderson. 'Note on the Nature of Cosmic-Ray Particles'. In: *Physical Review* 51 (10 1937), pp. 884 –886. URL: http://dx.doi.org/10.1103/PhysRev.51.884 (cit. on p. 1).

[18] F.J. Hasert, S. Kabe, et al. 'Observation of neutrino-like interactions without muon or electron in the Gargamelle neutrino experiment'. In: *Nuclear Physics B* 73.1 (1974), pp. 1 –22. URL: http://dx.doi.org/10.1016/0550-3213(74)90038-8 (cit. on p. 1).

[19] C.M.G.Lattes, G.P.S.Occhialini, and C.F.Powell. 'Observation on the Tracks of Slow Mesons in Photographic Emulsions'. In: *Nature* 160 (1947), pp. 453 –456, 486 –492. URL: http://dx.doi.org/10.1038/160453a0 (cit. on p. 1).

[20] Wikipedia web-page about the Geiger-Müller tube. URL: http://en.wikipedia.org/wiki/Geiger%E2%80%93M%C3%BCller_tube (cit. on p. 1).

[21] The CMS Collaboration. 'The CMS experiment at the CERN LHC'. In: *Journal of Instrumentation* 3.08 (2008), S08004. URL: http://dx.doi.org/10.1088/1748-0221/3/08/S08004 (cit. on pp. 1, 28).

[22] Leonardo Milano. 'Measurement of identified charged hadron spectra with the ALICE experiment at the LHC'. In: *Journal of Physics: Conference Series* 316.1 (2011). URL: http://dx.doi.org/10.1088/1742-6596/316/1/012019 (cit. on p. 1).

[23] The CMS Collaboration. *Particle-Flow Event Reconstruction in CMS and Performance for Jets, Taus, and MET*. CMS Physics Analysis Summary (CMS PAS PFT-09/001). 2009. URL: http://cds.cern.ch/record/1194487/files/PFT-09-001-pas.pdf (cit. on p. 1).

[24] The ATLAS Collaboration. 'Observation of a new particle in the search for the Standard Model Higgs boson with the ATLAS detector at the LHC'. In: *Physics Letters B* 716 (1 2012), pp. 1 –29. URL: http://dx.doi.org/10.1016/j.physletb.2012.08.020 (cit. on pp. 2, 47).

[25] The CMS Collaboration. 'Observation of a new boson at a mass of 125 GeV with the CMS experiment at the LHC'. In: *Physics Letters B* 13 (20 2012), pp. 30 –61. URL: http://dx.doi.org/10.1016/j.physletb.2012.08.021 (cit. on pp. 2, 47).

[26] The CMS Collaboration. 'Measurement of the properties of a Higgs boson in the four-lepton final state'. In: *Physical Review D* 89 (9 2014). URL: http://dx.doi.org/10.1103/PhysRevD.89.092007 (cit. on p. 2).

[27] The CMS Collaboration. *Search for Large Extra Dimensions in Dimuon Events in pp Collisions at* $\sqrt{s} = 8\,\text{TeV}$. CMS Physics Analysis Summary (CMS PAS EXO-12/027). 2013. URL: https://cms-physics.web.cern.ch/cms-physics/public/EXO-12-027-pas.pdf (cit. on p. 2).

[28] The CMS Collaboration. *Search for Narrow Resonances in Dilepton Mass Spectra in pp Collisions at* $\sqrt{s} = 8\,\text{TeV}$. CMS Physics Analysis Summary (CMS PAS EXO-12/061). 2013. URL: https://cds.cern.ch/record/1519132/files/EXO-12-061-pas.pdf (cit. on pp. 2, 47).

[29] G. Muehllehner and J. S. Karp. 'Positron emission tomography'. In: *Physics in Medicine and Biology* 51.13 (2006), R117. URL: http://dx.doi.org/10.1088/0031-9155/51/13/R08 (cit. on pp. 2, 27, 29, 36).

[30] R. Jr. Davis and D. S. Harmer. 'Solar neutrino detection by the Cl37-Ar37 method'. In: *Informal Conference on Experimental Neutrino Physics, CERN* (1965), pp. 201 –212. URL: http://dx.doi.org/10.5170/CERN-1965-032.201 (cit. on p. 2).

[31] The IceCube experiment (official homepage). URL: http://icecube.wisc.edu/ (cit. on pp. 2, 19, 30).

[32] The Super-Kamiokande experiment (official homepage). URL: http://www-sk.icrr.u-tokyo.ac.jp/sk/index-e.html (cit. on pp. 2, 19).

[33] The KM3NeT experiment (official homepage). URL: http://www.km3net.org/home.php (cit. on p. 2).

[34] Claus Grupen and Boris A. Shwartz. 'Chapter 10 - Neutrino detectors'. In: *Particle Detectors*. 2nd ed. Cambridge University Press, 2008, pp. 307 –325. ISBN: 978-0-521-84006-4 (cit. on pp. 2, 18, 19).

[35] Claude Leroy and Pier-Giorgio Rancoita. 'Chapter 5 - Scintillating Media and Scintillator Detectors'. In: *Principles of Radiation Interaction in Matter and Detection*. 2nd ed. World Scientific Publishing, 2009, pp. 419 –450. ISBN: 978-981-281-827-0 (cit. on pp. 2, 31, 34, 36).

[36] Official homepage with the CMS Technical Design Reports. URL: http://cmsdoc.cern.ch/cms/cpt/tdr/ (cit. on pp. 2, 21, 28, 36).

[37] LHCb collaboration. 'The LHCb Detector at the LHC'. In: *Journal of Instrumentation* 3.08 (2008), S08005. URL: http://dx.doi.org/10.1088/1748-0221/3/08/S08005 (cit. on p. 2).

[38] LHCb collaboration. *LHCb Tracker Upgrade Technical Design Report*. 2014. URL: https://cds.cern.ch/record/1647400/files/LHCB-TDR-015.pdf (cit. on pp. 2, 29, 39).

[39] Claus Grupen and Boris A. Shwartz. 'Chapter 5 - Main physical phenomena used for particle detection and basic counter types'. In: *Particle Detectors*. 2nd ed. Cambridge University Press, 2008, pp. 90 –159. ISBN: 978-0-521-84006-4 (cit. on pp. 2, 31, 35, 36, 42, 44, 45).

[40] Claude Leroy and Pier-Giorgio Rancoita. 'Chapter 8 - Ionization Chambers'. In: *Principles of Radiation Interaction in Matter and Detection*. 2nd ed. World Scientific Publishing, 2009, pp. 585 –610. ISBN: 978-981-281-827-0 (cit. on p. 2).

[41] Claude Leroy and Pier-Giorgio Rancoita. 'Chapter 6 - Solid State Detectors'. In: *Principles of Radiation Interaction in Matter and Detection*. 2nd ed. World Scientific Publishing, 2009, pp. 451 –537. ISBN: 978-981-281-827-0 (cit. on pp. 2, 31).

[42] S. M. Sze and Kwok K. Ng. *Physics of Semiconductor Devices*. 3rd ed. John Wiley & Sons, 2007. ISBN: 0-471-14323-5 (cit. on pp. 2, 31, 40, 42).

[43] The Pierre Auger Observatory (official homepage). URL: https://www.auger.org/ (cit. on pp. 3, 30).

[44] The MINOS experiment (official homepage). URL: http://www-numi.fnal.gov/ (cit. on p. 3).

[45] Official homepage with the MINOS Technical Design Reports. URL: http://cmsdoc.cern.ch/cms/cpt/tdr/ (cit. on p. 3).

[46] The PAMELA experiment (official homepage). URL: http://pamela.roma2.infn.it/index.php (cit. on p. 3).

[47] PAMELA collaboration. *PAMELA - A Payload for Antimatter Matter Exploration and Light-nuclei Astrophysics*. 2008. URL: http://arxiv.org/pdf/astro-ph/0608697v2.pdf (cit. on p. 3).

[48] The Fermi Gamma ray Space Telescope experiment (official homepage). URL: http://fermi.gsfc.nasa.gov/ (cit. on p. 3).

[49] Fermi collaboration. *The Large Area Telescope on the Fermi Gamma-Ray Space Telescope Mission*. 2009. URL: http://arxiv.org/pdf/0902.1089v1.pdf (cit. on p. 3).

[50] The CALICE experiment (official homepage). URL: https://twiki.cern.ch/twiki/bin/view/CALICE/WebHome (cit. on p. 3).

[51] V. Andreev, V. Balagura, B. Bobchenko, P. Buzhan, J. Cvach, et al. 'A high granularity scintillator hadronic-calorimeter with SiPM readout for a linear collider detector'. In: *Nuclear Instruments and Methods* A540 (2005), pp. 368–380. URL: http://dx.doi.org/10.1016/j.nima.2004.12.002 (cit. on p. 3).

[52] The Geant4 Collaboration. *Physics Reference Manual, Version: geant4 10.1*. 2014. URL: http://geant4.web.cern.ch/geant4/UserDocumentation/UsersGuides/PhysicsReferenceManual/fo/PhysicsReferenceManual.pdf (cit. on pp. 5, 49).

[53] Claus Grupen and Boris A. Shwartz. 'Chapter 1 - Interactions of particles and radiation with matter'. In: *Particle Detectors*. 2nd ed. Cambridge University Press, 2008, pp. 1 –55. ISBN: 978-0-521-84006-4 (cit. on pp. 5, 6, 8–11, 13, 15–19).

[54] Claude Leroy and Pier-Giorgio Rancoita. 'Chapter 2 - Electromagnetic Interaction of Radiation in Matter'. In: *Principles of Radiation Interaction in Matter and Detection*. 2nd ed. World Scientific Publishing, 2009, pp. 31 –216. ISBN: 978-981-281-827-0 (cit. on pp. 5, 8–10, 12–18, 20).

[55] Particle Data Group. *Webpage "Atomic and Nuclear Properties of Materials for more than 300 materials"*. URL: http://pdg.lbl.gov/2012/AtomicNuclearProperties/ (cit. on pp. 7–9, 13, 14, 19, 21, 36, 199, 202, 204, 205).

[56] Chary Rangacharyulu. *Physics of Nuclear Radiations: Concepts, Techniques and Applications*. 1st ed. Taylor & Francis, 2013. ISBN: 978-1-43-985777-9 (cit. on p. 9).

[57] Simon R. Cherry, James A. Sorenson, and Michael E. Phelps. *Radiation Physics for Nuclear Medicine*. 4th ed. Elsevier Saunders, 2012. ISBN: 978-1-4160-5198-5 (cit. on p. 9).

[58] D.E. Groom, N.V. Mokhov, and S.I. Striganov. 'Muon stopping-power and range tables, 10 MeV-100 TeV'. In: *Atomic Data and Nuclear Data Tables* 78.2 (2001), pp. 183 –356. URL: http://pdg.lbl.gov/2012/AtomicNuclearProperties/adndt.pdf (cit. on p. 9).

[59] Chitrlada Settakorn. 'Generation and Use of Coherent Transition Radiation from Short Electron Bunches'. PhD thesis. Stanford Linear Accelerator Center / Stanford University, 2001. URL: http://www.slac.stanford.edu/cgi-wrap/getdoc/slac-r-576.pdf (cit. on p. 14).

[60] Claude Leroy and Pier-Giorgio Rancoita. *Principles of Radiation Interaction in Matter and Detection*. 2nd ed. World Scientific Publishing, 2009. ISBN: 978-981-281-827-0 (cit. on pp. 17, 18).

[61] Claus Grupen and Boris A. Shwartz. *Particle Detectors*. 2nd ed. Cambridge University Press, 2008. ISBN: 978-0-521-84006-4 (cit. on p. 17).

[62] Claude Leroy and Pier-Giorgio Rancoita. 'Chapter 3 - Nuclear Interactions in Matter'. In: *Principles of Radiation Interaction in Matter and Detection*. 2nd ed. World Scientific Publishing, 2009, pp. 217 –286. ISBN: 978-981-281-827-0 (cit. on pp. 19–22).

[63] Claus Grupen and Boris A. Shwartz. 'Chapter 8 - Calorimetry'. In: *Particle Detectors*. 2nd ed. Cambridge University Press, 2008, pp. 230 –272. ISBN: 978-0-521-84006-4 (cit. on pp. 19, 20, 22).

[64] Richard P. Feynman, Robert B. Leighton, and Matthew Sands. 'Chapter 31 - The Origin of the Refractive Index'. In: *The Feynman Lectures on Physics, Volume 1*. California Institute of Technology / Basic Books, Perseus Books Group, 1963, 2006, 2013. ISBN: 978-0-465-02414-8. URL: http://feynmanlectures.caltech.edu/I_31.html (cit. on pp. 22–24).

[65] German web-page with animations illustrating the microscopic origin of the refractive index. URL: http://www.mikomma.de/optik/disp/dispersion.htm (cit. on p. 23).

[66] Richard P. Feynman, Robert B. Leighton, and Matthew Sands. 'Chapter 26 - Optics: The Principle of Least Time'. In: *The Feynman Lectures on Physics, Volume 1*. California Institute of Technology / Basic Books, Perseus Books Group, 1963, 2006, 2013. ISBN: 978-0-465-02414-8. URL: http://feynmanlectures.caltech.edu/I_26.html (cit. on p. 23).

[67] Wolfgang Demtröder. 'Abb. 8.2.' In: *Experimentalphysik 2 - Elektrizität und Optik*. 3rd ed. Spinger-Verlag, 2004, p. 218. ISBN: 3-540-20210-2 (cit. on p. 23).

[68] Wolfgang Demtröder. *Experimentalphysik 2 - Elektrizität und Optik*. 3rd ed. Spinger-Verlag, 2004. ISBN: 3-540-20210-2 (cit. on p. 23).

[69] Richard P. Feynman, Robert B. Leighton, and Matthew Sands. 'Chapter 32 - Refractive Index of Dense Materials'. In: *The Feynman Lectures on Physics, Volume 2*. California Institute of Technology / Basic Books, Perseus Books Group, 1964, 2006, 2013. ISBN: 978-0-465-02416-2. URL: http://feynmanlectures.caltech.edu/II_32.html (cit. on pp. 23, 24).

[70] Refractive index of water. URL: http://refractiveindex.info/?shelf=main&book=H2O&page=Hale (cit. on p. 24).

[71] L.D. Landau and E.M. Lifshitz. 'Chapter 9 - The Electromagnetic Wave Equations'. In: *Electrodynamics of Continuous Media*. 1st ed. Pergamon Press, 1960, pp. 1 –55 (cit. on p. 24).

[72] Web page about x-ray optics by the Institute of Microstructure Technology (Karlsruhe Institute of Technology). URL: http://www.imt.kit.edu/english/236.php (cit. on p. 24).

[73] Web page about refractive x-ray optics by RXOPTICS. URL: http://www.rxoptics.de/xrayoptics.html (cit. on p. 24).

[74] Wikipedia web-page about the Huygens-Fresnel principle. URL: http://en.wikipedia.org/wiki/Huygens%E2%80%93Fresnel_principle (cit. on p. 24).

[75] German wikipedia web-page about the Huygens-Fresnel principle. URL: http://de.wikipedia.org/wiki/Huygenssches_Prinzip (cit. on pp. 24, 25).

[76] John David Jackson. 'Chapter 7 - Plane Electromagnetic Waves and Wave Propagation'. In: *Classical Electrodynamics*. 3rd ed. John Wiley & Sons, 1999, pp. 295 –351. ISBN: 0-471-30932-X (cit. on p. 25).

[77] Prof. H.-J. Kull. *private communications*. Institut für Theoretische Physik A, RWTH Aachen (cit. on pp. 25, 61).

[78] Saint-Gobain Crystals. *Organic Scintillation Materials (Brochure)*. URL: http://www.crystals.saint-gobain.com/uploadedFiles/SG-Crystals/Documents/SGC%20Organics%20Brochure.pdf (cit. on pp. 28, 33, 34, 82).

[79] Wikipedia web-page about the Positron Emission Tomography. URL: http://en.wikipedia.org/wiki/Positron_emission_tomography (cit. on p. 28).

[80] Pierre Auger collaboration. *Ultrahigh Energy Neutrinos at the Pierre Auger Observatory*. 2013. URL: http://arxiv.org/pdf/1304.1630v1.pdf (cit. on p. 30).

[81] Hamamatsu. *Technical Information - MPPC, MPPC modules*. 2013. URL: http://www.hamamatsu.com/resources/pdf/ssd/mppc_kapd9003e.pdf (cit. on pp. 31, 44).

[82] T. Yamaya, T. Mitsuhashi, et al. 'A SiPM-based isotropic-3D PET detector X'tal cube with a three-dimensional array of 1 mm 3 crystals'. In: *Physics in Medicine and Biology* 56.21 (2011), p. 6793. URL: http://dx.doi.org/10.1088/0031-9155/56/21/003 (cit. on p. 31).

[83] D. R. Schaart, S. Seifert, et al. 'LaBr3:Ce and SiPMs for time-of-flight PET: achieving 100 ps coincidence resolving time'. In: *Physics in Medicine and Biology* 55.7 (2010), N179. URL: http://dx.doi.org/10.1088/0031-9155/55/7/N02 (cit. on p. 31).

[84] D. R. Schaart, H. T. van Dam, et al. 'A novel, SiPM-array-based, monolithic scintillator detector for PET'. In: *Physics in Medicine and Biology* 54.11 (2009), p. 3501. URL: http://dx.doi.org/10.1088/0031-9155/54/11/015 (cit. on p. 31).

[85] G. Llosá, J. Barrio, et al. 'Characterization of a PET detector head based on continuous LYSO crystals and monolithic, 64-pixel silicon photomultiplier matrices'. In: *Physics in Medicine and Biology* 55.23 (2010), p. 7299. URL: http://dx.doi.org/10.1088/0031-9155/55/23/008 (cit. on p. 31).

[86] S. Seifert, G. van der Lei, H. T. van Dam, and D. R. Schaart. 'First characterization of a digital SiPM based time-of-flight PET detector with 1 mm spatial resolution'. In: *Physics in Medicine and Biology* 58.9 (2013), p. 3061. URL: http://dx.doi.org/10.1088/0031-9155/58/9/3061 (cit. on p. 31).

[87] Tim Niggemann, Thomas Hebbeker, et al. 'The Optics and Detector-Simulation of the Air Fluorescence Telescope FAMOUS for the Detection of Cosmic Rays'. In: *Proc. SPIE* 8444 (2012), pp. 844430–844430–13. URL: http://dx.doi.org/10.1117/12.925305 (cit. on p. 31).

[88] The FACT experiment (official homepage). URL: http://www.fact-project.org/ (cit. on p. 31).

[89] FACT collaboration. 'Design and operation of FACT - the first G-APD Cherenkov telescope'. In: *Journal of Instrumentation* 8.06 (2013), P06008. URL: http://dx.doi.org/10.1088/1748-0221/8/06/P06008 (cit. on p. 31).

[90] Olaf Ziemann, Jürgen Krauser, Peter E. Zamzow, and Werner Daum. 'Chapter 2 - Optical Fibers'. In: *Polymer Optical Fibers - Optical Short Range Transmission Systems*. 2nd ed. Spinger-Verlag, 2008, pp. 37 –231. ISBN: 978-3-540-76628-5 (cit. on pp. 31, 37, 38).

[91] Wikipedia web-page about fluorescence. URL: http://en.wikipedia.org/wiki/Fluorescence (cit. on p. 32).

[92] Wikipedia web-page about the Förster resonance energy transfer. URL: http://en.wikipedia.org/wiki/F%C3%B6rster_resonance_energy_transfer (cit. on p. 32).

[93] Saint-Gobain. *Physical Properties of Common Inorganic Scintillators*. 2009. URL: http://www.crystals.saint-gobain.com/uploadedFiles/SG-Crystals/Documents/Physical%20Properties%20of%20Inorganic%20Scintillators.pdf (cit. on p. 33).

[94] Wikipedia web page. URL: http://commons.wikimedia.org/wiki/File:Benzene_Representations-numbers.svg (cit. on p. 33).

[95] Theodor Förster. 'Zwischenmolekulare Energiewanderung und Fluoreszenz (Intermolecular energy migration and fluorescence, 1948)'. In: *Annalen der Physik (in German)*. Vol. 437. 2006, pp. 55 –75. URL: http://dx.doi.org/10.1002%2Fandp.19484370105 (cit. on p. 34).

[96] J. B. Birks. *The Theory and Practice of Scintillation Counting*. Pergamon, 1964. ISBN: 978-0-08-010472-0 (cit. on pp. 34, 78).

[97] ZHANG Jian-Fu, RUAN Xi-Chao, et al. 'Measurements of the light output functions of plastic scintillator using ^{9}Be(d, n)^{10}B reaction neutron source'. In: *Chinese Physics C* 34.7 (2010), pp. 988 –992. URL: http://dx.doi.org/10.1088/1674-1137/34/7/011 (cit. on pp. 34, 202).

[98] Henric Wilkens and the ATLAS LArg Collaboration. 'The ATLAS Liquid Argon calorimeter: An overview'. In: *Journal of Physics: Conference Series* 160.1 (2009). URL: http://dx.doi.org/10.1088/1742-6596/160/1/012043 (cit. on p. 36).

[99] Kuraray. *Plastic Scintillating Fibres*. URL: http://kuraraypsf.jp/pdf/all.pdf (cit. on pp. 38, 75, 100–102, 109, 205, 207–209).

[100] Paul Papacz. 'Optimisation of the Particle Detection Efficiency for Scintillation Detectors with SiPM Readout'. Diploma thesis. RWTH Aachen, 2010. URL: http://web.physik.rwth-aachen.de/~hebbeker/theses/papacz_diploma.pdf (cit. on pp. 40, 41, 43, 52, 202).

[101] Adam Nepomuk Otte. 'Observation of VHE γ-Rays from the Vicinity of magnetized Neutron Stars and Development of new Photon-Detectors for Future Ground based γ-Ray Detectors'. PhD thesis. Technische Universität München, 2007. URL: https://www.deutsche-digitale-bibliothek.de/binary/ONHY4II3ZVB776RER7FZ6MMVWKG5YSMC/full/1.pdf (cit. on p. 42).

[102] SensL. *Introduction to the SPM - Technical Note*. 2011. URL: http://www.sensl.com/downloads/ds/TN%20-%20Intro%20to%20SPM%20Tech.pdf (cit. on pp. 43, 44).

[103] Jörg Rennefeld. 'Studien zur Eignung von Silizium Photomultipliern für den Einsatz im erweiterten CMS Detektor am SLHC'. Diploma thesis. RWTH Aachen, 2010. URL: http://wwwo.physik.rwth-aachen.de/fileadmin/user_upload/www_physik/Institute/Inst_3B/Forschung/CMS/Detektorentwicklung/Diplomarbeiten/Diplomarbeit_Rennefeld_Color.pdf (cit. on p. 43).

[104] D Renker and E Lorenz. 'Advances in solid state photon detectors'. In: *Journal of Instrumentation* 4.04 (2009), P04004. URL: http://dx.doi.org/10.1088/1748-0221/4/04/P04004 (cit. on p. 43).

[105] T. Bretz, T. Hebbeker, et al. 'Dynamic Range Measurement and Calibration of SiPMs'. In: *Journal of Instrumentation* (2015) (cit. on p. 43).

[106] Excelitas Technologies Corp. *Silicon Photomultipliers with 1x1 mm^2 active area*. URL: http://www.excelitas.com/Downloads/DTS_C30742-11-050_Series_SiPM.pdf (cit. on p. 44).

[107] Wikipedia web page. URL: http://upload.wikimedia.org/wikipedia/commons/a/ab/Photomultiplier_schema_de.png (cit. on p. 45).

[108] Official webpage of the Garfield simulation tool. URL: http://garfield.web.cern.ch/garfield/ (cit. on p. 48).

[109] Official webpage of the Garfield++ simulation tool. URL: http://garfieldpp.web.cern.ch/garfieldpp/ (cit. on p. 48).

[110] J. Baró, J. Sempau, J.M. Fernández-Varea, and F. Salvat. 'PENELOPE: An algorithm for Monte Carlo simulation of the penetration and energy loss of electrons and positrons in matter'. In: *Nuclear Instruments and Methods in Physics Research (B)* 100 (1 1995), pp. 31 –46. URL: http://dx.doi.org/10.1016/0168-583X(95)00349-5 (cit. on p. 48).

[111] S España, J L Herraiz, et al. 'PeneloPET, a Monte Carlo PET simulation tool based on PENELOPE: features and validation'. In: *Physics in Medicine and Biology* 54 (6 2009), p. 1723. URL: http://dx.doi.org/10.1088/0031-9155/54/6/021 (cit. on p. 48).

[112] Official webpage of the EGS simulation tool. URL: http://rcwww.kek.jp/research/egs/ (cit. on p. 48).

[113] James F. Ziegler, M.D. Ziegler, and J.P. Biersack. 'SRIM - The stopping and range of ions in matter'. In: *Nuclear Instruments and Methods in Physics Research (B)* 268 (11 - 12 2010), pp. 1818 –1823. URL: http://dx.doi.org/10.1088/0031-9155/54/6/021 (cit. on p. 48).

[114] Official webpage of the MCNP simulation tool. URL: https://mcnp.lanl.gov/ (cit. on p. 48).

[115] Official webpage of the MCNPX simulation tool. URL: https://mcnpx.lanl.gov/ (cit. on p. 48).

[116] Official webpage of the PGS simulation tool. URL: http://www.physics.ucdavis.edu/~conway/research/software/pgs/pgs4-general.htm (cit. on p. 48).

[117] Alfredo Ferrari, Paola R. Sala, Alberto Fassò, and Johannes Ranft. *Fluka: a multi-particle transport code*. 2005. URL: https://cds.cern.ch/record/898301/files/CERN-2005-010.pdf (cit. on p. 48).

[118] The Geant4 Collaboration. 'Geant4 - a simulation toolkit'. In: *Nuclear Instruments and Methods in Physics A* 506.3 (2003), pp. 250–303. URL: http://dx.doi.org/10.1016/S0168-9002(03)01368-8 (cit. on p. 49).

[119] The Geant4 Collaboration. 'Geant4 developments and applications'. In: *Nuclear Science* 53.1 (2006), pp. 270–278. URL: http://dx.doi.org/10.1109/TNS.2006.869826 (cit. on p. 49).

[120] Official Geant4 User Documentation webpage. URL: http://geant4.cern.ch/support/userdocuments.shtml (cit. on p. 49).

[121] The Geant4 Collaboration. *Geant4 Installation Guide, Version: geant4 10.1*. 2014. URL: http://geant4.web.cern.ch/geant4/UserDocumentation/UsersGuides/InstallationGuide/fo/BookInstalGuide.pdf (cit. on p. 49).

[122] The Geant4 Collaboration. *Geant4 User's Guide for Application Developers, Version: geant4 10.1*. 2014. URL: http://geant4.web.cern.ch/geant4/UserDocumentation/UsersGuides/ForApplicationDeveloper/fo/BookForAppliDev.pdf (cit. on pp. 49, 51–53).

[123] The Geant4 Collaboration. *Geant4 User's Guide for Toolkit Developers, Version: geant4 10.1*. 2014. URL: http://geant4.web.cern.ch/geant4/UserDocumentation/UsersGuides/ForToolkitDeveloper/fo/BookForToolDev.pdf (cit. on p. 49).

[124] Official Geant4 User Support webpage. URL: http://geant4.cern.ch/support/index.shtml (cit. on p. 49).

[125] Official webpage of the Geant4 HyperNews forum. URL: http://hypernews.slac.stanford.edu/HyperNews/geant4/cindex (cit. on p. 49).

[126] Maria Grazia Pia, Tullio Basaglia, Zane W. Bell, and Paul V. Dressendorfer. *Geant4 in Scientific Literature*. 2009. URL: http://arxiv.org/pdf/0912.0360v1.pdf (cit. on p. 49).

[127] The National Institute of Standards and Technology (official homepage). URL: http://www.nist.gov/ (cit. on p. 51).

[128] Geant4 HyperNews forum discussion on deviations between visualisation and tracking. URL: http://hypernews.slac.stanford.edu/HyperNews/geant4/get/geometry/508.html (cit. on pp. 56, 58).

[129] Geant4 HyperNews forum discussion on visualisation problems with boolean volumes. URL: http://hypernews.slac.stanford.edu/HyperNews/geant4/get/geometry/1325.html (cit. on p. 58).

[130] bug report on Cherenkov radiation in Geant4 (including the answer that the generation of Cherenkov photons in Geant4 is designed for normal dispersion only). URL: http://bugzilla-geant4.kek.jp/show_bug.cgi?id=1711 (cit. on pp. 59, 95).

[131] Geant4 HyperNews forum discussion on problems with LUT surfaces. URL: http://hypernews.slac.stanford.edu/HyperNews/geant4/get/opticalphotons/494.html (cit. on pp. 59, 95).

[132] Geant4 HyperNews forum discussion on relation between physical particles and G4Tracks. URL: http://hypernews.slac.stanford.edu/HyperNews/geant4/get/eventtrackmanage/1072.html (cit. on p. 59).

[133] Geant4 HyperNews forum discussion on complex refractive index and Fresnel equations for dielectric-metal surfaces. URL: http://hypernews.slac.stanford.edu/HyperNews/geant4/get/opticalphotons/472.html (cit. on pp. 61, 90).

[134] The G4beamline project (official homepage). URL: http://www.muonsinternal.com/muons3/G4beamline (cit. on p. 61).

[135] Thomas J. Roberts and Daniel M. Kaplan. 'G4beamline simulation program for matter-dominated beamlines'. In: *Particle Accelerator Conference, 2007* (2007), pp. 3468 –3470. URL: http://dx.doi.org/10.1109/PAC.2007.4440461 (cit. on p. 61).

[136] The GATE collaboration (official homepage). URL: http://www.opengatecollaboration.org/ (cit. on p. 62).

[137] G. Santin, D. Strul, et al. 'GATE: a Geant4-based simulation platform for PET and SPECT integrating movement and time management'. In: *Nuclear Science* 50.5 (2003), pp. 1516 –1521. URL: http://dx.doi.org/10.1109/TNS.2003.817974 (cit. on p. 62).

[138] The GAMOS project (official homepage). URL: http://fismed.ciemat.es/GAMOS/ (cit. on p. 62).

[139] P. Arce, Pedro Rato, M. Cañadas, and J.I. Lagares. 'GAMOS: A Geant4-based easy and flexible framework for nuclear medicine applications'. In: *Nuclear Science Symposium Conference Record, 2008* (2008), pp. 3162 –3168. URL: http://dx.doi.org/10.1109/NSSMIC.2008.4775023 (cit. on p. 62).

[140] The Geant4-DNA project (official homepage). URL: http://geant4-dna.org/ (cit. on p. 62).

[141] S. Incerti, G. Baldacchino, et al. 'The Geant4-DNA project'. In: *International Journal of Modeling, Simulation, and Scientific Computing* 1.2 (2010), pp. 157 –178. URL: http://dx.doi.org/10.1142/S1793962310000122 (cit. on p. 62).

[142] S. Incerti, A. Ivanchenko, et al. 'Comparison of GEANT4 very low energy cross section models with experimental data in water'. In: *Medical Physics* 37.9 (2010), pp. 4692 –4708. URL: http://dx.doi.org/10.1118/1.3476457 (cit. on p. 62).

[143] The MEGAlib project (official homepage). URL: http://megalibtoolkit.com/ (cit. on p. 62).

[144] A. Zoglauer, R. Andritschke, and F. Schopper. 'MEGAlib - The Medium Energy Gamma-ray Astronomy Library'. In: *New Astronomy Reviews* 50.7-8 (2006), pp. 629 –632. URL: http://dx.doi.org/10.1016/j.newar.2006.06.049 (cit. on p. 62).

[145] Official ESA homepage of the Geant4 Space Users. URL: http://geant4.esa.int/index.php/resources.html (cit. on p. 62).

[146] private communication Tim Niggemann (cit. on p. 69).

[147] Tim Niggemann, Erik Dietz-Laursonn, et al. 'G4SiPM: A novel silicon photomultiplier simulation package for Geant4'. In: *Nuclear Instruments and Methods in Physics Research Section A: Accelerators, Spectrometers, Detectors and Associated Equipment* 787 (2015), pp. 344 –347. URL: http://dx.doi.org/10.1016/j.nima.2015.01.067 (cit. on p. 68).

[148] Public webpage of the G4SiPM software package. URL: https://forge.physik.rwth-aachen.de/projects/g4sipm (cit. on p. 68).

[149] C. J. Clopper and E. S. Pearson. *The Use of Confidence or Fiducial Limits illustrated in the Case of the Binomial*. 1934. URL: http://dx.doi.org/10.1093/biomet/26.4.404 (cit. on p. 80).

[150] Saint-Gobain. *BC-452 - Lead-loaded Plastic Scintillators*. URL: http://www.crystals.saint-gobain.com/uploadedFiles/SG-Crystals/Documents/SGC%20BC452%20Data%20Sheet.pdf (cit. on pp. 82, 202).

[151] Web page about x-ray absorption edges by the National Physical Laboratory (United Kingdom). URL: http://www.kayelaby.npl.co.uk/atomic_and_nuclear_physics/4_2/4_2_1.html (cit. on p. 84).

[152] Web page about x-ray absorption edges by the Biomolecular Structure Center (University of Washington). URL: http://skuld.bmsc.washington.edu/scatter/AS_periodic.html (cit. on p. 84).

[153] Saint-Gobain Crystals. *Scintillating Optical Fibers (Brochure)*. URL: http://www.crystals.saint-gobain.com/uploadedFiles/SG-Crystals/Documents/SGC%20Fibers%20Brochure.pdf (cit. on pp. 97, 103, 109, 185, 205, 207–209).

[154] Simon Nieswand. 'Measurement of the exit characteristics of light from optical multimode plastic fibres'. Master thesis. RWTH Aachen, 2014. URL: http://web.physik.rwth-aachen.de/~hebbeker/theses/nieswand_master.pdf (cit. on pp. 105–107, 142, 179).

[155] Gordon Kaußen. 'Aufbau eines Hodoskops aus Siliziumstreifendetektoren'. Diploma thesis. RWTH Aachen, 2005. URL: http://wwwo.physik.rwth-aachen.de/fileadmin/user_upload/www_physik/Institute/Inst_3B/Forschung/CMS/Detektorentwicklung/Diplomarbeiten/Diplomarbeit_Gordon_Kaussen.pdf (cit. on pp. 113, 214).

[156] Patrick Schmitz. 'Inbetriebnahme eines Hodoskops für kosmische Höhenstrahlung mit Siliziumstreifendetektoren'. Bachelor thesis. RWTH Aachen, 2010. URL: http://wwwo.physik.rwth-aachen.de/fileadmin/user_upload/www_physik/Institute/Inst_3B/Forschung/CMS/Detektorentwicklung/Bachelorarbeiten/Bachelorarbeit_Patrick_Schmitz.pdf (cit. on pp. 113, 214).

[157] Paul Maanen. 'Inbetriebnahme eines Hodoskops für kosmische Höhenstrahlung mit Siliziumstreifendetektoren'. Bachelor thesis. RWTH Aachen, 2010. URL: http://wwwo.physik.rwth-aachen.de/fileadmin/user_upload/www_physik/Institute/Inst_3B/Forschung/CMS/Detektorentwicklung/Bachelorarbeiten/Bachelorarbeit_Paul_Maanen.pdf (cit. on pp. 113, 214).

[158] Nadine Bey. 'Szintillationsdetektoren ausgelesen mit Silizium-Photomultipliern als Trigger für kosmische Myonen in einem Hodoskop'. Bachelor thesis. RWTH Aachen, 2011. URL: http://wwwo.physik.rwth-aachen.de/fileadmin/user_upload/www_physik/Institute/Inst_3B/Forschung/CMS/Detektorentwicklung/Bachelorarbeiten/Bachelorarbeit_Nadine_Bey.pdf (cit. on pp. 113, 114, 214).

[159] Martin Lipinski. 'Szintillationsdetektoren ausgelesen mit Silizium-Photomultipliern als Trigger für kosmische Myonen in einem Hodoskop'. Bachelor thesis. RWTH Aachen, 2011. URL: http://wwwo.physik.rwth-aachen.de/fileadmin/user_upload/www_physik/Institute/Inst_3B/Forschung/CMS/Detektorentwicklung/Bachelorarbeiten/Bachelorarbeit_Martin_Lipinski.pdf (cit. on pp. 113, 114, 214).

[160] Milena Quittnat. 'A Testbench for the Optimization of Scintillation Detectors read out by Silicon Photomultipliers for the MTT System at CMS'. Diploma thesis. RWTH Aachen, 2012. URL: http://wwwo.physik.rwth-aachen.de/fileadmin/user_upload/www_physik/Institute/Inst_3B/Forschung/CMS/Detektorentwicklung/Masterarbeiten/Masterarbeit_Milena_Quittnat_low_res.pdf (cit. on pp. 113, 114, 118, 214).

[161] Simon Weingarten. 'Prototypdetektoren für das geplante Upgradeprojekt "Muon Track Fast Tag" am CMS-Experiment'. Master thesis. RWTH Aachen, 2013. URL: http://wwwo.physik.rwth-aachen.de/fileadmin/user_upload/www_physik/Institute/Inst_3B/Forschung/CMS/Detektorentwicklung/Bachelorarbeiten/WeingartenMasterarbeit.pdf (cit. on pp. 114, 118, 126, 161).

[162] web-page of the ROOT data analysis framework. URL: https://root.cern.ch (cit. on p. 118).

[163] O. Pooth, T. Radermacher, S. Weingarten, and L. Weinstock. 'Scintillator tiles read out with silicon photomultipliers'. In: *Journal of Instrumentation* 10.10 (2015). URL: http://dx.doi.org/10.1088/1748-0221/10/10/T10007 (cit. on p. 126).

[164] R. Maier. 'Cooler synchrotron COSY - Performance and perspectives'. In: *Nuclear Instruments and Methods in Physics Research Section A: Accelerators, Spectrometers, Detectors and Associated Equipment* 390.1 - 2 (1997), pp. 1 –8. URL: http://dx.doi.org/10.1016/S0168-9002(97)00324-0 (cit. on p. 126).

[165] Oliver Pooth, Simon Weingarten, and Lars Weinstock. 'Efficiency and timing resolution of scintillator tiles read out with silicon photomultipliers'. In: *Journal of Instrumentation* (2016). URL: http://dx.doi.org/10.1088/1748-0221/11/01/T01002 (cit. on pp. 126–128, 130, 131).

[166] M. V. Nemallapudi, S. Gundacker, et al. 'SiPM angular response and enhanced light extraction'. In: *Nuclear Science Symposium and Medical Imaging Conference (NSS/MIC), 2013 IEEE* (2013), pp. 1–5. URL: http://dx.doi.org/10.1109/NSSMIC.2013.6829586 (cit. on p. 146).

[167] Felix Kröger. 'Simulationsstudien zu einem ortsauflösenden Szintillations-Detektors mit Geant4'. Bachelor thesis. LMU München, 2014. URL: http://www.etp.physik.uni-muenchen.de/publications/bachelor/download_auth_etp/bac14_fkroeger.pdf (cit. on p. 179).

[168] German Wikipedia web-page about spherical caps. URL: http://de.wikipedia.org/wiki/Kugelsegment (cit. on p. 183).

[169] Wikipedia web-page about surface integrals. URL: http://en.wikipedia.org/wiki/Surface_integral (cit. on p. 184).

[170] Carsten Patrick Achenbach. *Active optical fibres in modern particle physics experiments*. 2004. URL: http://arxiv.org/pdf/nucl-ex/0404008v1.pdf (cit. on p. 184).

[171] Official webpage of the boost libraries. URL: http://www.boost.org/ (cit. on p. 189).

[172] Official webpage of the zlib libraries. URL: http://www.zlib.net/ (cit. on p. 189).

[173] Refractive index of air. URL: http://refractiveindex.info/?shelf=other&book=air&page=Ciddor (cit. on p. 200).

[174] Wikipedia web-page about the density of air. URL: https://en.wikipedia.org/wiki/Density_of_air (cit. on p. 200).

[175] Saint-Gobain. *BC-400, BC-404, BC-408, BC-412, BC-416 - Premium Plastic Scintillators*. URL: http://www.crystals.saint-gobain.com/uploadedFiles/SG-Crystals/Documents/SGC%20BC400-404-408-412-416%20Data%20Sheet.pdf (cit. on pp. 201, 202).

[176] DETEC. *Scintillating Products*. URL: http://detecsciences.com/api/files/535012e58cd6be252e000081-Scint_Brochure.pdf (cit. on p. 202).

[177] web-page of the Engauge Digitizer. URL: http://digitizer.sourceforge.net/ (cit. on pp. 200, 204, 206).

[178] Martin Janecek. 'Reflectivity Spectra for Commonly Used Reflectors'. In: *Nuclear Science* 59.3 (2012), pp. 490–497. URL: http://dx.doi.org/10.1109/TNS.2012.2183385 (cit. on p. 201).

[179] Saint-Gobain. *BC-620 - Reflector Paint for Plastic Scintillators*. URL: http://www.crystals.saint-gobain.com/uploadedFiles/SG-Crystals/Documents/SGC%20BC620%20data%20sheet.pdf (cit. on p. 201).

[180] Refractive index of aluminium. URL: http://refractiveindex.info/?shelf=main&book=Al&page=Rakic-1995 (cit. on p. 203).

[181] Saint-Gobain. *Detector Assembly Materials*. URL: http://www.crystals.saint-gobain.com/uploadedFiles/SGdetectors/Documents/Product_Data_Sheets/SGC_Detector_Assembly_Materials_Data_Sheet.pdf (cit. on pp. 203, 204).

[182] Wikipedia web-page about titanium dioxide. URL: https://en.wikipedia.org/wiki/Titanium_dioxide (cit. on p. 203).

[183] Wikipedia web-page about acrylic glass. URL: https://en.wikipedia.org/wiki/Acrylic_glass (cit. on p. 203).

[184] Refractive index of polyethylene. URL: http://www.filmetrics.com/refractive-index-database/Polyethylene/PE-Polyethene (cit. on p. 204).

[185] Wang Ling-Yu, Lu Hao-Qi, et al. 'Study of Tyvek reflectivity in water'. In: *Chinese Physics C* 36.7 (2012), pp. 628–632. URL: http://dx.doi.org/10.1088/1674-1137/36/7/011 (cit. on p. 204).

[186] Martin Janecek and William W. Moses. 'Measuring Light Reflectance of BGO Crystal Surfaces'. In: *Nuclear Science* 55.5 (2008), pp. 2443–2449. URL: http://dx.doi.org/10.1109/TNS.2008.2003253 (cit. on p. 204).

[187] Web page about the Dupont Tyvek products. URL: http://www.dupont.co.uk/products-and-services/construction-materials/tyvek-building-envelope/brands/tyvek-breather-membrane/products/tyvek-soft-breather-membrane-for-walls.html (cit. on p. 204).

[188] Wikipedia web-page with a list of refractive indices. URL: https://en.wikipedia.org/wiki/List_of_refractive_indices (cit. on p. 204).

[189] Saint-Gobain. *BC-600 - Optical Cement*. URL: http://www.crystals.saint-gobain.com/uploadedFiles/SG-Crystals/Documents/SGC%20BC600%20Data%20Sheet.pdf (cit. on pp. 204, 205).

[190] Wikipedia web-page about Epoxy. URL: https://en.wikipedia.org/wiki/Epoxy (cit. on p. 204).

[191] Wikipedia web-page about Bisphenol A. URL: https://en.wikipedia.org/wiki/Bisphenol_A (cit. on p. 204).

[192] Eljen Technology. *EJ-500 Optical Cement*. URL: http://www.eljentechnology.com/images/stories/Data_Sheets/Accessories/EJ500%20data%20sheet.pdf (cit. on p. 205).

[193] Refractive index of polystyren. URL: http://refractiveindex.info/?shelf=organic&book=polystyren&page=Sultanova (cit. on p. 206).

[194] Refractive index of Polymethylmethacrylate. URL: http://refractiveindex.info/?shelf=organic&book=poly%28methyl_methacrylate%29&page=Szczurowski (cit. on p. 206).

Acknowledgements

Now that five years of working on my Ph.D. thesis are coming to an end, I want to seize the opportunity to thank the people who supported me during this time. First of all, I want to thank all my current and former colleagues at Physics Institute III for the pleasant working atmosphere, for their support, for fruitful discussions, as well as for the critical reviewing of this thesis. Special thanks go to:

- Prof. Dr. Thomas Hebbeker for giving me the opportunity to perform the scientific work for my Ph.D. thesis at Physics Institute III and for being my doctoral adviser.

- Dr. Oliver Pooth for reviewing my Ph.D. thesis and for evaluating it as second referee.

- Dr. Markus Merschmeyer for being very dedicated in his role as my main supervisor. He always supported me by taking time for valuable discussions, by providing new perspectives and ideas, by patiently answering all physical or organisational questions, by reviewing my thesis, and by much more.

- My office colleague Carsten Heidemann for always being open to many questions and discussions of several hours. When a problem came up, he was willing to drop everything at any time to help me solving it.

- Andreas Künsken for his invaluable support during the initiation and troubleshooting of the hodoscope. Besides not being part of his work, he invested much time in this support and without it, the hodoscope measurements as presented in this thesis could not have been realised.

- Christine Peters for her great commitment in allowing for the consideration of SiPM effects in the simulations in the scope of the comparison between measurements and simulation. She extremely eased my workload by taking over the task of running the `G4SiPM` simulations with the results of my `GODDeSS` simulations.

- All the members of the hardware-groups of Physics Institute III for helping whenever support was needed as well as for the unique working atmosphere in the “Halle”.

- The people of the IT-support of Physics Institute III for the quick solution of occurring IT problems.

Additionally, I would like to thank the Geant4 experts who patiently answered my questions in the Geant4 Hypernews and thus helped me finding my way into the complex world of the Geant4 source code. In this context, special thanks go to Peter Gumplinger, Ph.D., from TRIUMF (the national laboratory for particle and nuclear physics and accelerator-based science in Canada).

Furthermore, I thank Anna-Maria Panitz for reviewing my thesis with respect to English diction as well as my family for laying the foundations for my academic education by im-

parting the necessary character, social skills and attitude to me and for their great support over the past years.

Last but not least I want to thank all the billions of photons, which took their time to participate in my studies, although they have enough other problems themselves:

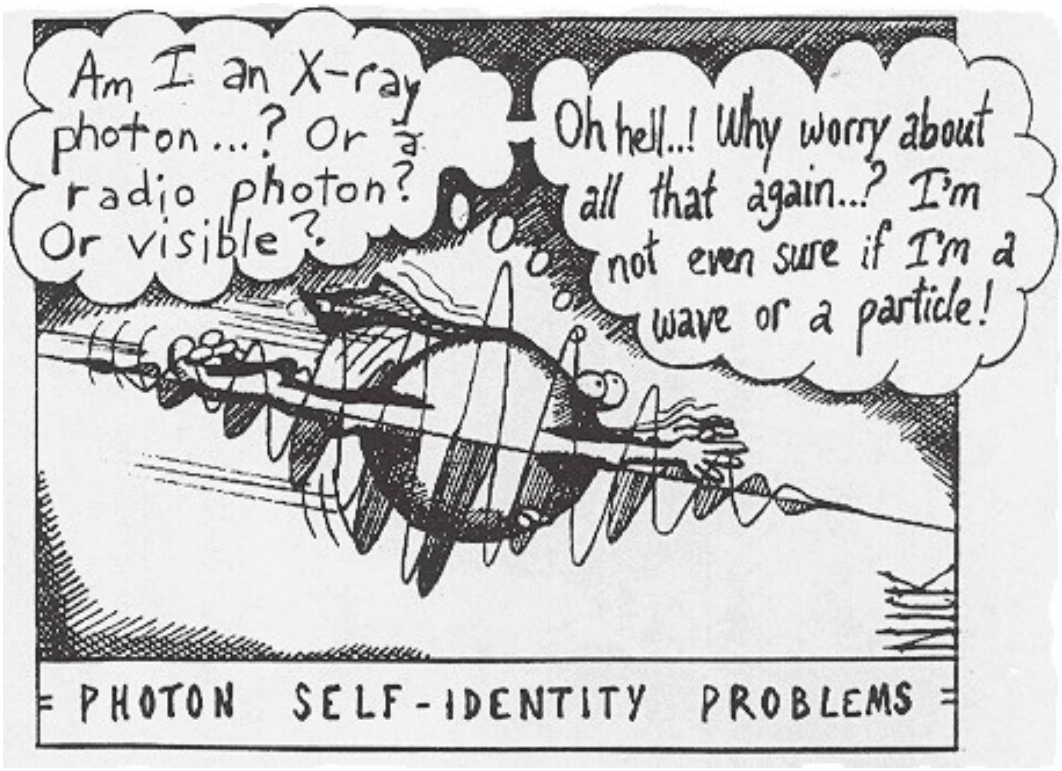

Figure G.1.: Taken from http://www.thephysicsmill.com/2015/01/18/whats-particle/, the original source is unknown.